Quantum chemical studies in catalysis

Document Version:
Publisher's PDF, also known as Version of Record (includes final page, issue and volume numbers)

Please check the document version of this publication:

• A submitted manuscript is the version of the article upon submission and before peer-review. There can be important differences between the submitted version and the official published version of record. People interested in the research are advised to contact the author for the final version of the publication, or visit the DOI to the publisher's website.
• The final author version and the galley proof are versions of the publication after peer review.
• The final published version features the final layout of the paper including the volume, issue and page numbers.
Link to publication

Quantum Chemical Studies in Catalysis

Willem Biemolt

QUANTUM CHEMICAL STUDIES IN CATALYSIS

PROEFSCHRIFT

ter verkrijging van de graad van doctor aan de
Technische Universiteit Eindhoven, op gezag van
de Rector Magnificus, prof.dr. J.H. van Lint,
voor een commissie aangewezen door het College
van Dekanen in het openbaar te verdedigen op
dinsdag 13 juni 1995 om 16.00 uur

door

WILLEM BIEMOLT

geboren te Groningen

Dit proefschrift is goedgekeurd door de promotoren:

prof.dr. R.A. van Santen

en

prof.dr. E.J. Baerends

copromotor:

dr. A.P.J. Jansen

para Solange Regina

Contents

1

General introduction and methodology

1.1   CATALYSIS

This thesis is a collection of studies into fundamental aspects of some catalytic reactions. Catalysis involves the creation of a reaction path with a lower activation energy, thus increasing the rate of a reaction. There exists three different types of catalysis: enzymatic, homogeneous and heterogeneous catalysis. While in enzymatic and homogeneous catalysis the reactant(s) and catalyst are in the same phase in heterogeneous catalysis both are in a different phase. Nowadays catalysis is an essential part of many chemical industrial processes, which can minimize raw material and energy usage or reduce pollution. Important examples of catalytic reactions are hydrocarbon cracking, oxidation, synthesis gas conversion and NO reduction. This explains the large number of experimental and theoretical studies in various aspects of catalysis. Some studies focus on the catalyzed reaction, while others deal with the catalyst preparation or characterization, thus giving insight in catalysis at a microscopic, mesoscopic and macroscopic level [1].

This thesis focuses especially on heterogeneous catalysis at the microscopic level. Using theoretical chemical techniques, discussed in the next section, (parts of) catalytic reactions were modeled and characterized. The principle of a heterogeneous catalysis reaction is shown in fig. 1.1. In this figure the gas phase atoms or molecules A and B form products C and D, also gas phase atoms or molecules, over a solid catalyst surface M. The gas phase reaction has an activation energy E_a which is much higher than the catalyzed reaction. The overall catalytic reaction breaks down into a number of elementary reaction steps. Every step indicates which bonds between catalyst surface atoms and substrate atoms or molecules are formed or broken. Fig. 1.1 shows first the adsorption of the reactants A and B on the surface M followed by the reaction of A and B to produce C and D. Finally, the products C and D desorb from the surface. This leaves empty sites on the surface where the following reactant molecules can adsorb. The regeneration of the catalyst is an essential property of catalysis.

However, in practice the catalysts may deteriorate for various reasons and the catalytic activity then declines. An example of this is the poisoning of rhodium in the three-way catalyst controlling automotive pollution by lead. Another feature of a catalytic reaction is that the overall change in free energy (ΔH) for the reaction shown in fig. 1.1 is the same for the uncatalyzed and the catalyzed reaction. This means that catalysis changes reaction kinetics, but has no effects on the thermodynamics.
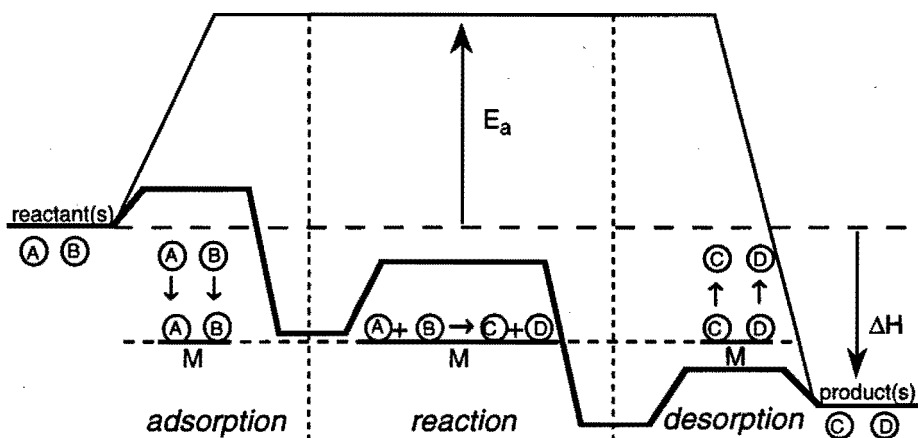
Fig. 1.1   *The principle of catalysis; gas phase molecules (A and B) over a metal catalyst (M).*

An important step in most heterogeneous catalytic reactions is the chemisorption of reactants to the catalyst, e.g., a transition metal surface. Chemisorption is a strong adsorption process (greater than about 40 kJ/mol) in which bonding occurs by 'ordinary' chemical bonds (of ionic and covalent character). The adsorption process may involve an activation energy. Although many adsorption geometries are possible, usually only one particular configuration is preferred. This is known as the catalytic active site. The idea of chemisorption as a function of atom arrangement implies a relation between substrate reactivity and catalytic site arrangement. One example of this is that surfaces containing atoms of an increasing unsaturated coordination usually appear more reactive. Chemical reactivity also depends on particle size. An increasing particle size may first result in a decrease in reactivity, but slowly increases for larger particle sizes [2]. The differences relate to changes in electronic structures as well as changes in exposed surface geometry. Related to particle size is shape selectivity, only molecules small enough to enter will be converted. Long-range interactions are changes in the environment of the catalytic reactive site that are due to alterations in composition or geometry of atoms in the second coordination shell with respect to the chemisorbed molecule.

An example is the shift of an adsorbate to higher coordination sites due to the presence of a cation [3]. Catalysis studies need to relate to the surface composition rather than the bulk composition. Surface and bulk composition of a material may significantly differ. Due to the phenomenon of the minimization of surface energy the surface composition may change. This may favor enrichment of surface atoms with the lowest sublimation energy. Consequently small metal particles will have particular shapes that may depend on gas-phase composition.

One of the early ideas about heterogeneous catalysis was that the catalytic activity relates to the number of d-valence electron holes, the 'electronic factor'. The behavior of metals with a filled d-valence electron band is different from the ones who have partially filled d-valence electron band. Of the metal catalysts the group VIII and IB metals are the most important. A reason for this is that the bonding between reacting molecules and metal surface is such that the interaction is strong enough for reactant molecules to adsorb (and rearrange) and weak enough for the product molecules to desorb.
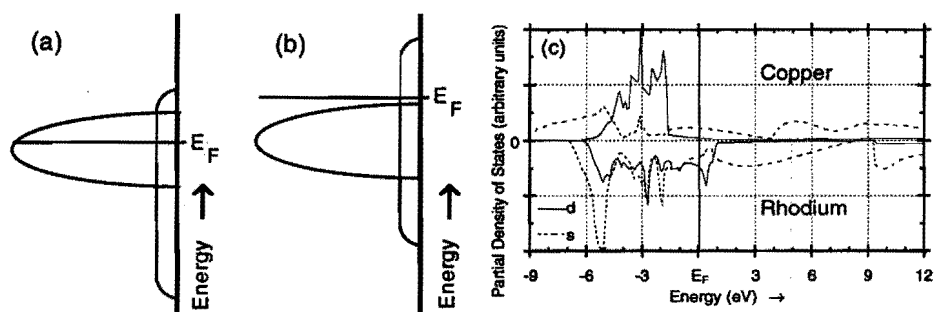
Fig. 1.2   *Distribution of valence electrons over the d- and s, p-electron bands. Schematic view for (a) group VIII and (b) group IB metals, and (c) PDOS from s- and d-electrons for bulk Cu and Rh.*

This thesis presents studies involving the transition metals copper, rhodium and iridium. Rhodium and iridium are group VIII metals. This group of metals all have their d-valence electrons distributed over a narrow nearly filled d-valence electron band and a broader s-, p-valence electron band (fig. 1.2a). Rhodium has a low electrical resistance and is highly resistant to corrosion. Iridium is very hard, brittle and the most corrosion-resistant metal. Both rhodium and iridium are used as an alloying or hardening agent for platinum. Copper is a group IB metal. These metals have a completely filled d-valence electron-band (fig. 1.2b). Copper is a good conductor of heat and electricity, and widely used in the electrical industry. Fig. 1.2(c) shows the calculated density due to valence d- and s-electrons for bulk rhodium and copper. Some properties of all three elements are given in table 1.1.

Table 1.1 *Properties of the elements copper, rhodium and iridium.*

Element (symbol)	Copper (Cu)	Rhodium (Rh)	Iridium (Ir)
(l=latin ; g=greek)	cuprum (l) from Cyprus	rhodon (g) rose	iris (l) rainbow
atomic number	29	45	77
atomic weight	63.546(3)	102.90550(3)	192.22(3)
melting point (°C)	1083.4	1966	2410
boiling point (°C)	2567	3727	4130
density (kg dm^{-3})	8.96 (20°C)	12.41 (20°C)	22.42 (17°C)
bond length (Å)	2.5560 (20°)	2.6901 (20°)	2.714 (room temp.)
electron configuration	[Ar] $3d^{10} 4s^1$	[Kr] $4d^8 5s^1$	[Xe] $4f^{14} 5d^7 6s^2$
ionization potential (eV)	7.726	7.46	9.1

1.2   THEORETICAL METHODS

Theoretical studies can provide information that can not or hardly be obtained experimentally and/or provide a better understanding of experimental results. Thus a better understanding of catalysis at the microscopic level can be achieved by employing theoretical models. Due to the enormous advancements in computational resources, more and better theoretical studies appear. Faster computers with more memory allow larger problems and more realistic models. Theoretical treatments of adsorbate-surface interactions have thus rapidly advanced to a stage where detailed qualitative understandings of structural and electronic features are available. In many cases, even reliable quantitative predictions of structures and energies can be made. First we will give a short survey of some of the theoretical methods that are used in studies in the field of catalysis.

1.2.1   Empirical methods

The Bond Order Conservation method (BOC), with atomic adsorption energies and bond strengths of molecules in the gas phase as parameters, is a very successful empirical treatment of catalysis. Pioneered by Shustorovich [4], it provides simple analytical expressions to estimate adsorption and interaction energies. It can even estimate activation barriers and yield important chemical insights. Others have proposed extensions to the method to treat real catalytic systems [5]. Despite some severe limitations we will use some of the basic BOC rules to express some concepts. More details about BOC can be found elsewhere [1].

1.2.2 Semi-empirical methods

The most elementary of the semi-empirical methods is the tight-binding or Hückel method. This approach, originally introduced to treat electronic structure problems in organic chemistry, can be useful to study clusters or slabs [6]. The absence of non-orthogonality of atomic orbitals is a major limitation of the simple Hückel method. Extended Hückel tries to treat this non-orthogonality, and is thus a more realistic approach for modeling transition metal systems. With this model relevant systems can be studied, and it has been applied successfully to small metal clusters and elementary surface reactions [6, 7]. However, due to the level of approximation in this one-particle theory only qualitative and no quantitative results can be obtained. More advanced semi-empirical methods are generally not parametrized for transition metal systems, making them useless for the treatment of most catalytic problems. The complete neglect of differential overlap (CNDO) and intermediate neglect of differential overlap (INDO) offer little more than just qualitative insight and are hard to justify over the simple EHT method. The ZINDO package [8], based upon the INDO method, is an exception to this, and was successfully applied in a number of catalytic studies.

More recent, and maybe also more promising, methods to study larger problems are the effective medium (EM) theory [9] and the embedded atom method (EAM) [10]. Both these techniques have been developed for the analysis of extended metal systems. The basic idea behind it is very simple. The change in the electron density within an atom is determined upon embedding it in the surrounding atoms. A difference is made between contributions to bonding by highly delocalized electrons, the s- and p-valence electrons, and the more localized and lower density d-valence electrons (see fig. 1.2). The contributions of the s- and p-valence electrons are computed by assuming the density to behave as a free electron gas. The contributions of the d-valence electrons are computed within the tight binding approximations using the Anderson-Newns approach [11] to solve the surface problem. The EM approach is based upon embedding techniques, in which the surroundings of the site of interest are not considered directly but via an embedding potential and local density theory. It employs a number of additional approximations in the embedding technique. With the EM method it becomes possible for example to compute sticking coefficients at surfaces or to study diffusion processes at surfaces. EAM is a many-atom potential for computing the total energy of a metallic system. It is especially useful for systems with large unit cells, and is appropriate for metals with empty of filled d bands. With EAM many problems have been investigated: point defects, melting, alloying, dislocations, segregation, surface structure, and epitaxial growth. For simple metals and early and late transition metals (e.g., Al and Cu) the EM method is mathematically equivalent to the EAM.

1.2.3 First principle methods

Computational quantum chemistry has reached a level of sophistication that currently provides quantitatively reliable predictions of interaction energies, geometric structure, and electronic properties. Both ab initio molecular orbital methods as well as density functional methods, which are derived from first principles, have been successful in the prediction of electronic and energetic properties of systems containing transition metals. The inherent difficulty is in the treatment of electron correlation. First principle methods give not always better results than (semi)empirical methods. Especially for systems involving transition metals simple first principle methods may fail to yield accurate quantitative descriptions, mainly because electron correlation effects are lacking from some first principle methods.

Ab initio molecular orbital methods

The most basic ab initio molecular orbital approach is the Hartree-Fock self-consistent field method (HF-SCF). It is known to yield poor geometries and energetics for transition metal systems due to the improper treatment of electron correlation. Additional configuration interaction (CI) is, even with today's large and efficient computer power, difficult to perform on a routine basis for catalytic systems of interest. Furthermore, the interpretation of CI results in terms of simple concepts is also difficult since the one-electron MO picture is lost.

A more recent and promising method to study larger problems is the Car and Parrinello method [12]. This approach is based upon the idea of combining simulated annealing [13] with energy density functional theory [14]. It is a mix between quantum chemistry for the electrons and classical mechanics for the atoms in a system. This method allows, for example, for a time dependent description of atomic adsorption or to determine reaction mechanisms at surfaces. However, additional approximations are used, making it less ab initio.

Density functional methods

Some very successful methods to study larger problems or systems are based upon the density functional theory (DFT) [15, 16], mainly the local density approximation (LDA). This is the method used throughout this thesis. The DFT approach combines the capacity to incorporate exchange-correlation effects of electrons with reasonable computational costs and high accuracy. In DFT the electron density is the basic variable, instead of the wave function. This reduces the computational burden of treating electron-electron interaction terms, which are treated explicitly as a functional of the density. For larger systems DFT methods may well prove superior to conventional methods. Calculations based upon this model successfully predict molecular and transition-state structures, frequencies, and activation barriers.

1.3   DENSITY FUNCTIONAL THEORY

In principle, all properties of a many electron system can be derived from solving the time-independent Schrödinger equation

$$H \Psi(r_1,...,r_N) = E \Psi(r_1,...,r_N) \qquad (1.1)$$

Here Ψ is the wave-function which depends on the coordinate positions r of the N electrons. DF theory is an exact reformulation of eq. (1.1) based on the Hohenberg-Kohn theorem [17]. According to this theorem the ground state energy is uniquely determined by the electronic density $\rho(r)$. Using the Kohn-Sham method [18] the energy can be expressed as

$$E[\rho] = T_S[\rho] + E_N[\rho] + E_C[\rho] + E_{XC}[\rho] \qquad (1.2)$$

Here, the first term represents the kinetic energy of N non interacting electrons. The second term accounts for the electron nucleus attraction. The third term is the Coulomb attraction between two charge distributions. The last term is the exchange-correlation energy. The exact dependence on the density is not known, and thus has to be approximated.

DFT offers a practical computational scheme. By solving the Kohn-Sham orbital equation

$$h_{eff}\phi_i = (-\frac{1}{2}\nabla^2 + V_N + V_C + V_{XC})\phi_i = \varepsilon_i\phi_i \qquad (1.3)$$

it is possible to determine the optimal density $\rho(r)$ for which the total energy has a minimum. In principle DFT is restricted to ground states.

1.3.1   The Local Density Approximation

The search for an accurate exchange-correlation potential has encountered tremendous difficulty and continues to be one of the great challenges in DF theory. The simplest and most widely employed approximation is known as the local density approximation (LDA) [15]. In this approximation, electronic properties are determined as functionals of the electron density by applying locally relations appropriate for a homogeneous electronic system. The LDA for exchange and correlation energy is given by

$$E_{xc}^{LDA}[\rho] = \int \rho(r)\varepsilon_{xc}(\rho)dr \qquad (1.4)$$

Here $\varepsilon_{xc}(\rho)$ is the exchange and correlation energy per particle of a uniform electron gas of density ρ. From this a corresponding exchange-correlation potential can be derived which can be used in the KS orbital equation, eq. (1.3). The self-consistent solution of this is usually called the LDA method.

$$\varepsilon_{xc}(\rho) = \varepsilon_x(\rho) + \varepsilon_c(\rho) \qquad (1.5)$$

The exchange energy, $\varepsilon_x(\rho)$, is the stabilization energy resulting from the interaction of each electron with N-1 other electrons. The correlation energy, $\varepsilon_c(\rho)$, is the stabilizing energy

due to the Coulomb repulsion between electrons of different spin. One of the first DFT-based schemes used for many atoms studies is the Hartree-Fock-Slater or Xα method. This method [17, 19] retains only the exchange part of the total expression for the exchange-correlation energy given in eq. (1.5) and adopts usually values for the exchange scaling factor around 2/3.

LDA results for molecular properties such as bond energies and equilibrium geometries are in good agreement with experiment [20]. Bonding energies are usually overestimated. Bond lengths and angles are predicted to within 0.05 Å and 1-2° accuracy, respectively. The precision for vibrational frequencies is about 75 cm^{-1}. Transition metal systems are typically predicted with somewhat less accuracy than all organic systems.

All calculation described in this thesis are based on the LDA, as implemented in program packages developed in the group of Baerends at the Vrije Universiteit Amsterdam [21, 22]. The program package for electronic structure calculations on molecules and clusters is called ADF (see 1.4.1). Except in chapter 2, were we used the LDA in its simplest, exchange-only Hartree-Fock-Slater (Xα) form, the parameterization of Vosko, Wilk and Nussair [23] was used for the exchange correlation potential. The program package for electronic structure calculations on periodic systems is (ADF-)BAND (see 1.4.2). It is quite similar to ADF.

1.3.2 Extensions

Spin restricted or spin unrestricted

The aufbau or building-up principle states that, starting from the lowest, all electronic levels are filled with alpha (= spin up) and beta (= spin down) electrons, until all electrons are distributed. However, sometimes this principle does not hold. For example rhodium has a ground state occupation of $4d^8 5s^1$ (table 1.1), whereas simple aufbau would suggest $4d^9$. Density functional theory can, just like Hartree-Fock, cover spin. Separate equations for alpha and beta electrons can be derived. These equations are coupled through terms which contain the total electron density. The total exchange terms are split into an alpha and a beta part. Alpha and beta electrons will thus experience a different effective potential. This is taken care of by enabling alpha and beta space orbitals to differ. This is called (spin) unrestricted LDA. Since the wave function can exploit more degrees of freedom, an unrestricted calculation will lower the energy. However, for closed shell systems restricted calculations are usually sufficient. The resulting N-electron wave function from an unrestricted calculation is in general not an eigenfunction of S^2. Consequently, unrestricted calculations do not describe correct multiplets. The obtained one determinant wave functions may be mixtures of several states e.g., a singlet with a triplet.

Non-local or Gradient corrections

An obvious way to improve LDA is by taking into account small fluctuations in the density, instead of assuming a locally constant density: non-local or gradient corrections. With these corrections the density functional potential is evaluated not only from the local value of the charge density, but also from the gradient of the charge density. The best known non-local or gradient corrections are due to Becke [24] for the exchange and due to Perdew for the correlation [25]. Calculating gradient corrections during the SCF procedure increases the computational effort, however, the incorporation after SCF convergence usually suffices.

It is known that LDA overestimates the correlation energies by 100%. The major part of this error comes from correlation between electrons of the same spin. Same-spin correlation is much smaller in finite systems than in the homogeneous electron gas. A correction to remove the same spin correlation was formulated by Stoll et. al. [26, 27]. The Stoll correction is considered to be a correction to the correlation of LDA. It is not correct to use the Stoll correction together with non-local gradient corrections to the correlation.

The optimal density functional is still a subject of extensive research. Applying corrections usually gives better results in comparison with experimental data. Especially bonding energies improve significant. Geometries are also reproduced better, but here the difference is less pronounced. It has become clear that for chemisorption calculations reasonably accurate results can be obtained so long as non-local corrections to the exchange-correlation potential, along with the proper adsorbate-surface geometry, are included.

Non-relativistic, scalar-relativistic or quasi-relativistic

An important effect in chemistry involving heavy atoms, like transition metal atoms, is relativity. Quite a few methods have been developed to deal with relativistic effects. The implementation of relativity in quantum mechanical programs is less straightforward than the implementation of spin, but not impossible. However, for most systems full inclusion of relativity is computationally too expensive. An alternative is to include relativity as a perturbation. The first approach is the quasi-relativistic approach. The Foldy-Wouthuysen transformation [28] gives the first order relativistic perturbation in the hamiltonian. So-called scalar relativistic Darwin and mass-velocity can thus be incorporated. The treatment is not strictly first-order. The first-order scalar relativistic corrections, the Pauli Hamiltonian, is diagonalized in the space of the non-relativistic solutions, i.e. in the non-relativistic basis set. The quasi-relativistic approach considerably improves the results over a first-order treatment. Another possibility is the use of the zeroth-order regular approximate relativistic hamiltonian (ZORA) [29]. Valence energy levels from the ZORA formalism are almost indistinguishable from fully relativistic levels, however, it requires adapted basis sets to show this advantage.

1.4   DENSITY FUNCTIONAL IMPLEMENTATIONS

One of the earliest practical implementations of self-consistent (SCF) DF theory employed scattered-plane waves, the SW-Xα method [30]. In addition a muffin-tin approximation [31] was used. It is computationally more favorable than standard ab initio techniques and has been used with considerable success to elucidate the electronic structure in complexes and clusters of transition metals. This approach is well suited for solids, but less appropriate in molecules. Moreover, the use of the muffin-tin approximation makes accurate calculations of total energies almost impossible. The method has for this reason not been successful in studies involving molecular structures and bond energies. The first implementations without the muffin-tin approximation were due to Ellis and Painter [32], Baerends et al. [21], Sambe and Felton [33], and Dunlap [34]. The first two are both based on Slater-type basis functions, while the last two are based on Gaussians. The linear combination of atomic orbitals (LCAO) methods opened the possibility of geometry optimizations, vibrational analysis, etc. Furthermore the LCAO approach involves numerical approximations that could, at least for small systems, be expanded to reasonably converged limits. Building on these pioneering works, several practical DF software packages were developed. Some of the nowadays more common used codes are ADF [35], deMon [36], DGauss [37], DMol [38]. More recent implementations are of Becke [39], who developed the fully numerical NUMOL program, and of Pople et al. [40], which is part of the well known GAUSSIAN92 quantum chemistry software package [41]. The availability of these codes results in a rapid growth in the number of people using density functional methods in chemistry.

1.4.1   ADF - the Amsterdam density functional package

The program ADF emerged from HFS (later also known as AMOL), a suite of various FORTRAN programs (FRAGMN, HFS/SCF/AMOL, ETS and PAIRPOT). These programs were combined into one single program: the Amsterdam density functional package or ADF. The ADF program is characterized by extensive use of symmetry, relativistic extensions, geometry optimizations, pseudo potentials, embedding procedures and an accurate energy decomposition scheme. Recently the ADF code has undergone major revisions [42]. Implementation of geometry optimizations, frequency computations, search of transition state, and tracing reaction paths were improved or added. Also user friendliness has undergone major improvements. While the code was already well vectorized, work on parallelization is in progress.

In ADF the molecular orbitals are represented as a linear combinations of atomic Slater type orbitals, LCA(ST)O:

$$\Psi_{nlm_1}(r,\theta,\phi) = r^{n-1}e^{-\alpha r}Y_{lm_1}(\theta,\phi). \tag{1.6}$$

The integrals that thus appear can not be solved analytically, so they are computed by an accurate numerical technique [43]. The level of precision in the integration is chosen such that the calculated bonding energies are stable within 5 kJ/mol. ADF is equipped with a database containing several basissets for all elements of the periodic table.

ADF has a fragment oriented approach. A fragment may be a single atom or a larger molecule or cluster. The polyatomic system is built up from one or more fragments. The molecular one-electron orbitals are calculated as linear combinations of fragment orbitals, and the bonding energy is in terms of fragment properties. The bonding energy is thus defined relative to the sum of fragments. Bond energies are computed with what is known as the Ziegler transition state (or field) method [44]. The energy difference between the sum of the separate fragments and the polyatomic system is determined from the corresponding initial and final charge densities. Total energies are not so easily obtained by ADF.

Bond energy analysis

An important feature of ADF is the way in which the bond energy, ΔE_b, is evaluated. ADF uses the fragment picture, the building up of more complicated molecules from simpler ones. This method allows the interpretation of quantitative results in conceptually useful terms as for example Pauli repulsion, pair bonding and the donor/acceptor interaction between physically meaningful fragments (fig. 1.3) [45].
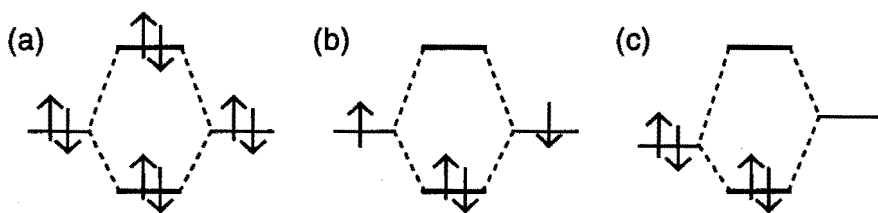
Fig. 1.3   *(a) Pauli repulsion, (b) pair bonding and (c) donor/acceptor interaction.*

For the adsorption process, where two fragments, the adsorbent A and the metal surface M, combine to form the overall system MA, the bond energy is defined as the difference between the fragments and the overall system M-A.

$$\Delta E_b = E(M-A) - E(M) - E(A), \tag{1.7}$$

The adsorption energy can be decomposed in two main contributions:

$$\Delta E_b = \Delta E_{steric} + \Delta E_{int}. \tag{1.8}$$

Here ΔE_{steric} is the energy change due to superposition of M and A without changing their molecular orbitals. This can be considered the contribution due to steric repulsion. ΔE_{int} represents the energy change upon the formation of the molecular orbitals of A-B. It includes charge transfer, polarization and relief of steric repulsion. According to the irreducible representations of the point group of M-A, ΔE_{int} can be symmetry decomposed. The steric interaction can be split as

$$\Delta E_{steric} = \Delta E_{elstat} + \Delta E_{xrep}. \tag{1.9}$$

Where ΔE_{elstat} is the classical electrostatic interaction of the unperturbed interpenetrating charge distributions of A and M, and ΔE_{xrep} is the exchange repulsion as a consequence of the anti-symmetry requirement. This is also known as overlap or Pauli repulsion.

1.4.2   ADF-BAND - DF program for periodic systems

The n-dimensional (n=1,2,3) crystal calculations were performed using the band structure program ADF-BAND or BAND, by te Velde and Baerends [46, 47]. This program is very similar in set up to the molecule program ADF. It also employs the same, highly optimized, numerical Gaussian integration scheme [43] for the Hamilton matrix elements, together with a quadratic tetrahedron method for the k-space integration [48]. A relevant difference between the two density functional programs involves the basis sets. The band structure program contains a Hermann-Skillman type subprogram [49], which solves the DF equations for the free atoms of the system. The numerical atomic orbitals (NAOs) can be used in the crystal valence set, together with, or instead of Slater-type exponential functions. ADF does not include this option, but it has the possibility to employ specific linear combinations of STOs as basis functions. Another difference is that ADF-BAND does not include the Stoll and the (scalar) relativistic corrections that we used in some of our studies with the molecule program. This makes direct comparison of results from both programs sometimes difficult.

Computational resources required for the ADF-BAND program makes that this program up till now has not been applied so much as ADF. Studies of CO chemisorption on copper are promising for the field of surface-molecule interactions [50, 51]. In contrast with the poor convergence of cluster calculations, slab calculations show a reasonable convergence for the bonding energy, showing that some erroneous results are due to finite cluster effects, rather than the underlying density functional approximation. Slab calculations offer the prospect of quantitative first principle theoretical determination of the surface-molecule interaction.

1.5   SCOPE OF THIS THESIS

Advances in heterogeneous catalysis and catalyst design are directly tied to a detailed understanding of the mechanism of the elementary steps which make up the overall catalytic cycle. Progress in this area depends upon the ability to determine the rate constants and overall equilibria of reaction intermediates for a complex series of adsorption, desorption, and surface reactions steps. Direct experimental information on intermediate surface species which take part in the mechanism of the catalytic reaction cycle is difficult to obtain due to their low surface concentrations and short residence times. In this thesis the DF-LDA method described in the previous sections will be applied to some heterogeneous catalytic systems, obtaining information about adsorption, activation and desorption, of stable surface intermediates and transient precursors which control the catalytic mechanism.

1.5.1   Iridium

The first part (chapters 2 and 3) focuses on heterogeneous catalysis involving iridium. In particular the influence of a coadsorbed Mg^{2+} cation on atomic hydrogen and atomic sulphur adsorption on small iridium particles was studied. Fig. 1.4 shows the influence of a Mg^{2+} cation on a tetrahedral iridium cluster. Model studies for the adsorption on small metal clusters deposited in the pores of a zeolite in which part of the silicon has been replaced by aluminum. Charge compensation cations are present in the pores close to the metal particles.
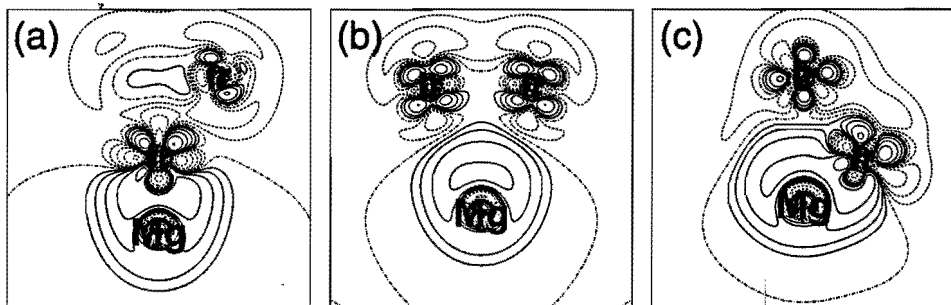
Fig. 1.4   Contour plots of the electron density difference $\rho(Ir_4\text{-}Mg^{2+}) - \rho(Ir_4) - \rho(Mg^{2+})$. Shown are (a) onefold Mg^{2+}, (b) twofold Mg^{2+}, and (c) threefold Mg^{2+} on a tetrahedral Ir_4 cluster. Dashed lines are a decrease, solid lines an increase, and dashed-dotted lines depict nodal surfaces. Subsequent contours correspond to 0.00, ±0.01, ±0.02, ±0.04, ±0.08, ±0.16, ±0.32, and ±0.64 e/Å³.

• **Chapter 2**   Catalytic activity can be modified due to alteration of the electron density of transition metal cluster atoms because of charge transfer or polarization at the interface between a very small cluster and a support. Previous calculations of the adsorption of a hydrogen molecule on a tetrahedral Ir_4 cluster showed an increased interaction in the presence of a Mg^{2+} cation [52]. In order to estimate the effect of the cation on the dissociation of the hydrogen molecule, we studied the bonding of hydrogen atoms to the same Ir_4 cluster. It is predicted that the overall activation energy for dissociative molecular hydrogen adsorption, with respect to the gas phase, decreases in the presence of the Mg^{2+} cation.

• **Chapter 3**   A related problem to changed catalyst activity is the poisoning of a catalyst by sulphur when converting reactants containing traces of sulphur. Not only the catalytic activity but also the resistance against poisoning depends on the charge of coadsorbed cations. In order to estimate the effect of the cation on sulphur poisoning, we studied the bonding of sulphur to the same tetrahedral Ir_4 cluster. Results seem to indicate a larger sulphur sensitivity for metal particles in close contact with cations.

1.5.2   Rhodium

The second part (chapters 4-6) focuses on heterogeneous catalysis involving rhodium and carbon monoxide. The chemical bonding of CO with rhodium is presented in fig. 1.5, that of carbon with oxygen within a CO molecule in fig. 1.6. It is known that CO molecules adsorb on group VIII metals with the carbon oriented towards the metal and the oxygen into the vacuum, and that CO almost always adsorbs perpendicular to the surface. This is because of the higher energy of the 5σ orbital located on carbon, compared to the lower energy of the 4σ orbital.
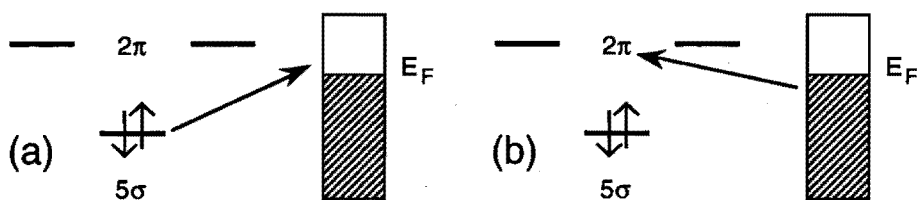
Fig. 1.5   *The Blyholder mechanism of CO adsorption on metal surfaces. (a) Donation of electrons from CO 5σ to empty metal levels. (b) Backdonation of electrons from the metal to CO $2\pi^*$.*

According to the Blyholder mechanism [53], the adsorption of carbon monoxide to the metal surface is due to two electrons flows, shown in fig. 1.5. In the first flow (see fig. 1.5a)

the occupied 5σ molecular orbital will donate electrons into the empty d band of the metal surface. As a result, a M-C bond is formed. At the same time electrons are withdrawn from the 5σ orbital which is bonding in C-O. This will lead to a weakening of the C-O bond. In the second flow (see fig. 1.5b) the metal will donate electrons into the empty $2\pi^*$ orbital of carbon monoxide. This so called back donation also results in a stronger M-C bond and, as the $2\pi^*$ MO is an antibonding orbital of carbon monoxide, also in a weakening of the C-O bond. The net effect of donation and back donation is the formation of a metal-CO bond and a weakening of the C-O bond.

Fig. 1.6   *MO scheme of CO, and contour plots of molecular orbitals of carbon monoxide. Dashed lines are negative and solid lines positive, the dashed-dotted lines depict nodal surfaces. Subsequent contours correspond to 0.00, ±0.01, ±0.02, ±0.04, ±0.08, ±0.16, ±0.32, and ±0.64 e/Å³.*

• *Chapter 4*   We started this series of studies by developing PESs for the interaction of carbon monoxide with a rhodium atom for two electronic states of Rh-CO. The construction of a reasonable accurate atom-atom potential for Rh-CO was not possible. More successful was the construction of the potential energy surfaces by representing the potential as a spherical expansion. The expansion coefficients, which are functions of the distance between the rhodium atom and the carbon monoxide center-of-mass, can be represented by different functions, with a reasonable error of the fit (± 10 kJ/mol). The potential energy surfaces, using

Morse functions, predict that the electronic ground state of Rh-CO is a doublet, which has a linear geometry. Further this PES predict that the first-excited state is a quartet, which has a bent geometry. The predictions are in good agreement with actual calculations.

• *Chapter 5*   In this study we are mainly interested in applying density-functional theory to small rhodium clusters. One of the objectives is to determine how large a cluster is needed to realistically simulate a rhodium surface, in order to permit the investigation of chemisorption and catalytic processes. Knowledge of the electronic structure of bare transition metal clusters is important for the understanding of heterogeneous catalysis. After all, we need to understand the chemistry and the physics of bare clusters before we can understand their interaction with atoms and molecules. Quantities like the binding energy per atom (or cohesive energy of the metal), bond strength and the ionization potential can be used to determine the convergence of finite clusters to an infinite bulk metal. Once the cluster requirements are known, one is able to investigate electronic properties and to study the kinetics and thermodynamics of adsorption processes.

• *Chapter 6*   We herein present an investigation of the interaction of a carbon monoxide molecule with small and medium sized rhodium clusters. The simplest approach is assuming that the interaction of carbon monoxide with a rhodium cluster can be approximated by a sum of interactions of the carbon monoxide molecule with each one rhodium atom. These so called PES results are compared with calculations on the actual small clusters systems. The agreement between PES predictions and actual calculations is rather poor. It seems that our PES for Rh-CO is not anisotropic enough. The n-fold adsorption of carbon monoxide on rhodium calculated with the PES is roughly about n times the onefold adsorption energy. Rh_{10} and Rh_{13} cluster models gave use reasonable reliable results for the rhodium-CO interaction. Calculations of CO adsorption on much larger rhodium cluster were difficult to the large computational requirements, and the very slow convergence.

1.5.3   Copper

The third and last part of this thesis (chapters 7-10) focuses on heterogeneous catalysis involving copper. Especially the adsorption, dissociation and oxidation of ammonia on/over a copper surface. The chemical bonding within an ammonia molecule is shown in fig. 1.7. The highest occupied orbital of ammonia is the lone pair orbital. The lowest unoccupied molecular orbitals are high energy antibonding orbitals between nitrogen and hydrogen. The chemisorptive bond is therefore dominated by the interaction with the ammonia lone pair orbital with little activation of the N-H bond. Lone pair orbital energies are lower in energy than the highest occupied metal surface orbitals and contribute to binding.

MO scheme of NH₃   selected orbitals of NH₃
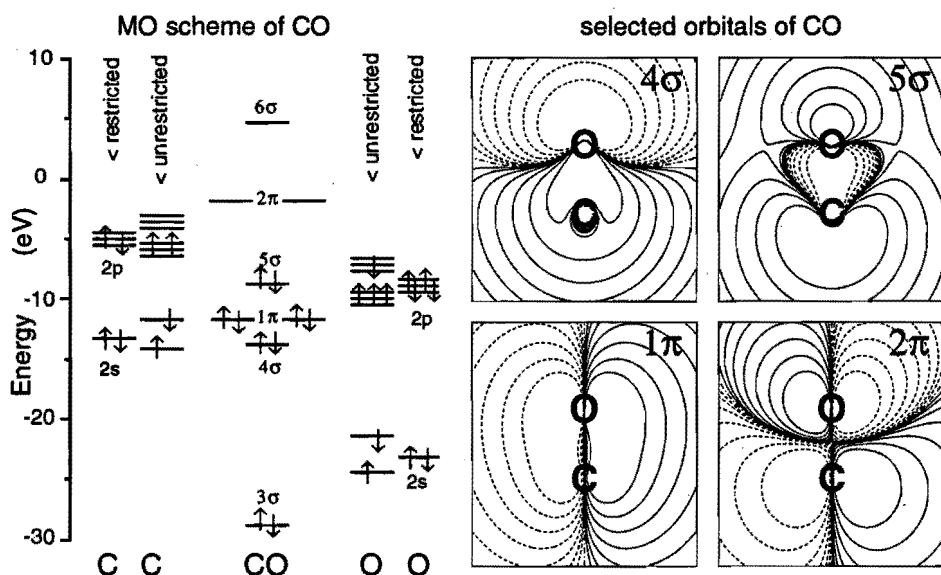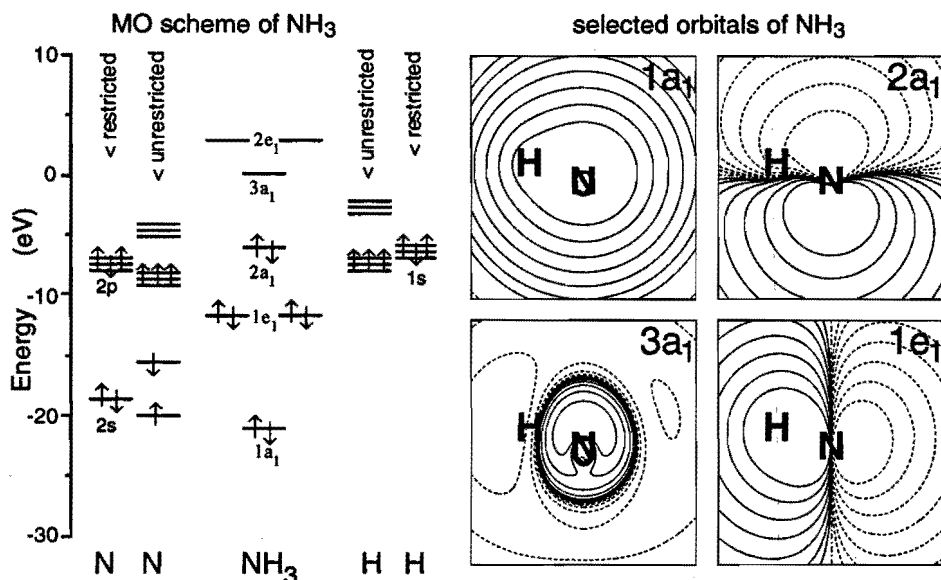

Fig. 1.7 *MO scheme of ammonia, and contour plots of some molecular orbitals of ammonia. Dashed lines are negative and solid lines positive, the dashed-dotted lines depict nodal surfaces. Subsequent contours correspond to 0.00, ±0.01, ±0.02, ±0.04, ±0.08, ±0.16, ±0.32, and ±0.64 e/Å³.*

Ammonia is thought to interact with copper through electrostatic and weak covalent binding. Ammonia is bound to surface through the nitrogen atom with the hydrogens directed away from the surface. The interaction between ammonia and copper is rather weak, therefore it is a reasonable approximation to fix the Cu-Cu distance in the cluster to the bulk value, while allowing the geometry of ammonia on the surface to be optimized.

• *Chapter 7* We started this series of studies by examining the chemisorption of ammonia on copper. Copper clusters of different sizes modeling the (100) and (111) surface. Using for some of the copper atoms only one instead of eleven electrons explicitly in the calculation, did not always work satisfactorily. Comparison of adsorption energies for clusters of related geometry indicates a preference for onefold adsorption. This is due to the Pauli repulsion of the lone-pair orbital of ammonia with the copper 3d electrons, which is minimal for onefold adsorption, as well as an interaction with 4s electrons, which is most attractive in the onefold position. The predicted bond lengths, adsorption energies and frequencies were sensitive to the smaller cluster sizes. At least the adsorption site and complete nearest neighbor is required to mimic the electronic properties of the adsorbate-surface

• *Chapter 8* The next step in this series of studies was to determine the role of preadsorbed oxygen. Fig. 1.8 shows the influence of an oxygen atom adsorbed on an eleven atom model cluster of Cu(111), eight atoms in the first layer and three in the second: Cu(8, 3). A rather small polarization of the copper atom on which ammonia will adsorb can be seen. Second layer copper atoms are almost not influenced by the threefold adsorbed oxygen atom. The adsorption and initial dissociation pathways of ammonia on this model cluster of the copper (111) surface, and the effects of preadsorbed oxygen were analyzed.
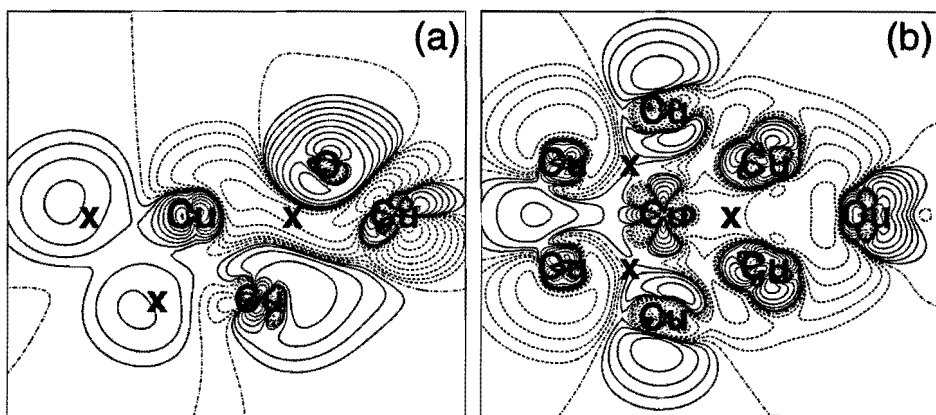
Fig. 1.8 Contour plots of the electron density difference $\rho(Cu(8,3)\text{-}O) - \rho(Cu(8,3)) - \rho(O)$. Shown are (a) cross-section, and (b) first layer. The second layer is almost not influenced by oxygen. Dashed lines are a decrease, solid lines an increase, and dashed-dotted lines depict nodal surfaces. Subsequent contours correspond to 0.000, ±0.001, ±0.002, ±0.004, ±0.008, ±0.016, ±0.032, ±0.064, ±0.128, ±0.256, 0.512, and 1.024 e/Å³. A "X" denotes a projection of a copper atom on the plane.

The presence of preadsorbed oxygen increases the adsorption energy and promotes the dissociation of ammonia over copper. All examined dissociation reactions of ammonia to NH₂ were endothermic. Dissociation in the absence of oxygen has the highest activation barrier of all steps analyzed and is the most endothermic. In presence of oxygen, however, the energy needed for the dissociation of ammonia is considerably lower. The dissociation of ammonia in the presence of oxygen has the same overall reaction energy regardless of whether the ammonia was initially adsorbed onefold or threefold. The activation energies demonstrate that system favors the pathway where ammonia is initially onefold. It is concluded that ammonia dissociation proceeds via the intermediate formation of adsorbed hydroxyl.

• **Chapter 9**   Herein a short study into the ammonia oxidation over copper is presented. It builds on the previous adsorption and dissociation studies of ammonia on Cu(8, 3) as a model of the Cu(111) surface. Preadsorbed oxygen increases the adsorption energy of ammonia, and promotes the dissociation of ammonia. All examined dissociation reactions in the absence of oxygen are endothermic. Dissociation of ammonia to NH_2 with oxygen is also found to be endothermic, but less than for systems without oxygen. Subsequent dissociation to NH is thermally neutral, whereas NH dissociation to nitrogen is exothermic. The most endothermic steps in the catalytic reaction cycle of the ammonia oxidation reaction appears to be the dissociation of ammonia and the desorption of water.

• **Chapter 10**   We conclude this series of studies with a complete theoretical analysis of the structure and energetics of transient chemical precursors for the oxidation of ammonia. Different reaction mechanisms and catalytic cycles for the oxidation reaction catalyzed by copper are compared, and the role of O and O_2 precursors in the overall catalytic cycle for NH_3 dissociation is analyzed. Attractive and repulsive lateral interactions were important in accessing accurate adsorption energies. O enhances N-H bond activation, however, it also acts to poison active surface sites and inhibit NH_3 dissociation kinetics. Transient O_2 adsorbs weakly in parallel (precursor for O_2 dissociation) and perpendicular (precursor for NH_3 dissociation) orientation. The mechanism in which H atoms are abstracted sequentially to form an OOH^* intermediate is favored over that in which two H atoms are simultaneously transferred to form water directly. The non-activated transient molecular path in which H is abstracted sequentially is the most favored of all of the four paths studied. In light of the experimental O_2 dissociation energy over Cu(111), transient O_2 is more likely than "hot" O as the dominant chemical precursor for NH_3 dissociation. Subsequent dissociation of the NH_x fragments lead to N^*. While enthalpy considerations favor recombinative desorption of N_2, at reaction conditions the most abundant reaction intermediate is O, making the recombinative desorption of NO a more likely reaction path.

1.6   REFERENCES

[1] R.A. van Santen, *Theoretical Heterogeneous Catalysis* (World Scientific, Sigapore, 1991).

[2] Studies in Surface Science and Catalysis 79: *Catalysis: an integrated approach to homogeneous, hetrogeneous and industrial catalysis* J.A. Moulijn, P.W.N.M. van Leeuwen and R.A. van Santen, Eds., (Elsevier, Amsterdam, 1993).

[3] E.L. Garfunkel, M.H. Farias and G.A. Somorjai, *J.Am. Chem. Soc.* **107** (1985) 349.

[4] E.M. Shustorovich, *Surf. Sci. Rep.* **6** (1986) 1; E.M. Shustorovich, *Adv. Catal.* **37** (1990) 101.

[5] E.M. Shustorovich and A.T. Bell, *Surf. Sci.* 268 (1992) 397.

[6] R. Hoffmann, *Solids and Surfaces* (VCH Publishers, New York, 1988).

[7] R.A. van Santen and E.J. Baerends, in: Theoretical models of chemical bonding, Part 4. Theoretical treatment of large molecules and their interactions, ed. Z.B. Maksic (Springer, Berlin, 1991) p. 323.

[8] M.C. Zerner, ZINDO Package, Quantum Theory Project, University of Florida, Gainesville, FL.

[9] J.K. Nørskov and N.D. Lang, *Phys. Rev. B* 21 (1980) 2131; J.K. Nørskov, *Phys. Rev. B* 26 (1982) 2875; K.W. Jacobsen, J.K. Nørskov and M.J. Puska, *Phys. Rev. B* 35 (1987) 7423.

[10] M.S. Daw, S.M. Foiles and M.I. Baskes, *Mat. Sci. Rep.* 9 (1993) 251.

[11] P.W. Anderson, *Phys. Rev.* 124 (1961) 41; D.M. Newns, *Phys. Rev.* 178 (1969) 1123.

[12] R. Car and M. Parrinello, *Phys. Rev. Lett.* 55 (1985) 2471; M. Parrinello, in *MOTECC-91*, ed. E. Clementi (ESCOM, Leiden, 1991), p. 833.

[13] S. Kirkpatrick, J.C.D. Gelatt and M.P. Vecchi, *Science* 220 (1983) 671.

[14] E.S. Kryachko and E.V. Lundeña, Energy Density Functional Theory of Many Electrons Systems (Kluwer, Dordrecht, 1990).

[15] R.G. Parr and W. Yang, *Density-functional theory of atoms and molecules* (Oxford University Press, New York, 1989).

[16] R.O. Jones, O. Gunnarsson, *Rev. Mod. Phys.* 61 (1989) 689.

[17] P. Hohenberg and W. Kohn, *Phys. Rev. B* 136 (1964) 864.

[18] W. Kohn and L.S. Sham, *Phys. Rev. A* 140 (1965) 1133.

[19] K. Schwarz, *Phys. Rev. B* 5 (1972) 2466; M.S. Gopinathan and M.A. Whitehead, *Phys. Rev. A* 14 (1976) 1.

[20] T. Ziegler, *Chem. Rev.* 91 (1991) 651.

[21] E.J. Baerends, D.E. Elis and P. Ros, *Chem. Phys.* 2 (1973) 41; E.J. Baerends and P. Ros, *Chem. Phys.* 2 (1973) 52; E.J. Baerends and P. Ros, *Chem. Phys.* 8 (1975) 412.

[22] P.M. Boerrigter, G. te Velde and E.J. Baerends, *Int. J. Quantum Chem.* 33 (1988) 87.

[23] S.H. Vosko, L. Wilk, and M. Nusiar, *Can. J. Phys.* 58 (1980) 1200.

[24] A.D. Becke, *Int. J. of Quant. Chem.* 23 (1983) 1915; A.D. Becke, *Phys. Rev. A* 38 (1988) 3098.

[25] J.P. Perdew, *Phys. Rev. B* 33 (1986) 8822; J.P. Perdew, *Phys. Rev. B* 34 (1986) 7406.

[26] H. Stoll, C.M.E. Pavlidou and H. Preuß, *Theor. Chim. Acta*, 49 (1978) 143; H. Stoll, E. Golka and H. Preuß, *Theor. Chim. Acta*, 55 (1980) 29.

[27] J.P. Perdew and A. Zunger, *Phys. Rev. B* 23 (1981) 5048.

[28] L.L. Foldy and S.A. Wouthuysen, *Phys. Rev.* 78 (1950) 29.

[29] E. van Lenthe, J.G. Snijders and E.J. Baerends, *J. Chem. Phys.* 99 (1993) 4597.

[30] J. Korringa, *Physica* 13 (1947) 392.

[31] K.H. Johnson, *J. Chem. Phys.* 45 (1966) 3085.

[32]   D.E. Ellis and G.S. Painter, *Phys. Rev. B* **2** (1970) 2887.

[33]   H. Sambe and R.H. Felton, *J. Chem. Phys.* **62** (1975) 1122.

[34]   B.I. Dunlap, J.W.D. Connolly and J.F. Sabin, *J. Chem. Phys.* **71** (1979) 4993; B.I. Dunlap, J.W.D. Connolly and J.F. Sabin, *J. Chem. Phys.* **78** (1983) 4787.

[35]   ADF is available from the Department of Theoretical Chemistry, Vrije Universiteit, Amsterdam.

[36]   A. St-Amant and D.R. Salahub, *Chem. Phys. Lett.* **169** (1990) 387; A. St-Amant, Ph. D. Thesis, Université de Montréal (1991).

[37]   DGauss, part of the UniChem Chemistry Codes, Cray Research, Inc., Eagan, MN.

[38]   B. Delley, *J. Chem. Phys.* **92** (1990) 508 (DMol is available from BioSym Technologies, San Diego, CA).

[39]   A.D. Becke, *Int. J. Quantum Chem. Symp.* **23** (1989) 599.

[40]   B.G. Johnson, P.M.W. Gill and J.A. Pople, *J. Chem. Phys.* **98** (1993) 5612.

[41]   Gaussian 92/DFT, Revision F.2, M.J. Frisch, G.W. Trucks, H.B. Schlegel, P.M.W. Gill, B.G. Johnson, M.W. Wong, J.B. Foresman, M.A. Robb, M. Head-Gordon, E.S. Replogle, R. Gomperts, J.L. Andres, K. Raghavachari, J.S. Binkley, C. Gonzalez, R.L. Martin, D.J. Fox, D.J. Defrees, J. Baker, J.J.P. Stewart, and J.A. Pople, Gaussian, Inc., Pittsburgh PA, 1993.

[42]   G. te Velde, ADF user's guide, Vrije Universiteit, Amsterdam (1993)

[43]   G. te Velde and E.J. Baerends, *J. Comput. Phys.* **99** (1992) 84.

[44]   T. Ziegler and A. Rauk, *Theoret. Chim. Acta* **46** (1977) 1.

[45]   T.A. Albrigh, J.K. Burdett and M.H. Whangbo, *Orbital Interactions in Chemistry* (Wiley, NY, 1985).

[46]   G. te Velde and E.J. Baerends, *Phys. Rev. B* **44** (1991) 7888.

[47]   G. te Velde, PhD. thesis, Vrije Universiteit Amsterdam (1990).

[48]   G. Wiesenekker, G. te Velde and E.J. Baerends, *J. Phys. C* **21** (1988) 4263.

[49]   F. Hermann and S. Skillman, Atomic structure calculations (Prentice-Hall, Englewood Cliffs, 1963).

[50]   G. te Velde and E.J. Baerends, *Chem. Phys.* **177** (1993) 399.

[51]   P.H.T. Philipsen, G. te Velde and E.J. Baerends, *Chem. Phys. Lett.* **226** (1994) 583.

[52]   E. Sanchez Marcos, A.P.J. Jansen and R.A. van Santen, *Chem. Phys. Lett.* **167** (1990) 399.

[53]   G. Blyholder, *J. Phys. Chem.* **68** (1964) 2772.

2

Bonding of hydrogen atoms to Ir$_4$ clusters: the effect of Mg^{2+} ions

ABSTRACT

In this chapter we[*] present local density approximation calculations of atomic hydrogen adsorption on a tetrahedral Ir$_4$ cluster. The hydrogen atom prefers twofold or threefold coordination. The effect of the presence of a Mg^{2+} cation next to the Ir$_4$ cluster on the adsorption of a hydrogen atom is studied. It changes the calculated adsorption energy by less than 10%, but the Ir-H stretch frequencies may change as much as 25%. A comparison with earlier results of molecular hydrogen adsorption on the same tetrahedral Ir$_4$ cluster supports the hypothesis that polarization of the metal particle by a Mg^{2+} cation in zeolites promotes molecular hydrogen dissociation.

2.1   INTRODUCTION

The chemical reactivity of small metal clusters in zeolites is of practical and fundamental interest [1]. They are active hydrocarbon-conversion catalysts. Zeolites are alumino-silicates having a large internal surface. The negative charge of the zeolite-lattice is compensated for by positively charged ions in the zeolite micropore. The catalytic activity of metal particles embedded in zeolite cavities has been reported to be a strong function of cation charge [2]. If cations of low charge are replaced by cations of high charge, the rate of hydrocarbon conversion may increase by an order of magnitude. This has been found especially for the zeolites X and Y [3, 4].

In order to explore a possible explanation, we have initiated a quantum-chemical study of carbon monoxide, molecular and atomic hydrogen adsorption on a tetrahedral Ir$_4$ particle in the presence and absence of a Mg^{2+} cation. Earlier, we reported the results of local density approximation calculations on the effect of Mg^{2+} on CO and H$_2$ adsorption [5-7]. For a configuration with the carbon monoxide adsorbed to the Ir$_4$ cluster opposite of the Mg^{2+} cation, we found significant changes in the CO stretch frequencies but no change in the carbon monoxide adsorption energy. Different from carbon monoxide, the adsorption energy of molecular hydrogen was found to be significantly affected by the presence of a Mg^{2+} cation.

For the particular adsorption geometry chosen, changes in adsorption energy are due to polarization of the metal particle by the cation. The Mg^{2+} cation polarizes the Ir$_4$ particle such that a negative charge develops on the cluster atoms close to the Mg^{2+} cation screening the Mg^{2+} cation. The resulting electron-density reduction between metal particle and adsorbate decreases repulsion between doubly occupied adsorbate and cluster orbitals. This is the dominating effect in the case of molecular hydrogen adsorption and results in an increase of the adsorption energy. For chemisorbed carbon monoxide, this effect is counteracted by a reduced interaction with the $2\pi^*$ orbital. In order to estimate the effect of a Mg^{2+} cation on the dissociation of the hydrogen molecule, the molecular hydrogen adsorption calculation will be compared with results for the atomic hydrogen adsorption.

2.2   METHOD

We have done non-relativistic, restricted local density approximation (LDA) calculations with the Xα exchange-correlation potential (α=0.7) using the implementation developed in

the group of Baerends (HFS-LCAO) [8]. Molecular orbitals are represented as linear combinations of atomic Slater-type orbitals (STO's). Integrals are computed numerically [9], and adsorption energies are computed with the Ziegler transition state method [10].

Table 2.1   *Exponents ζ of the STO's for iridium, magnesium and hydrogen.*

type		ζ		type	ζ		type		ζ	
Ir	1s	26.55	core	4d	10.65	core		2s	4.35	valence
	2s	26.55	core	4f	7.59	core		2p	2.35	valence
	3s	22.40	core	5d	1.55	valence		2p	3.90	valence
	4s	8.85	core	5d	2.75	valence		2p	7.10	valence
	5s	6.95	core	5d	4.75	valence		3s	0.75	valence
	2p	35.24	core	6s	1.30	valence		3s	1.10	valence
	3p	18.47	core	6s	2.35	valence		3s	1.75	valence
	4p	9.99	core	6p	1.81	valence	H	1s	1.28	valence
	5p	4.57	core	Mg 1s	10.00	core		1s	0.76	valence
	3d	22.15	core	2s	2.70	valence		2p	1.00	valence

For magnesium the 1s core is kept frozen. For iridium electrons up to 4f are kept frozen. The exponents of the STO basis sets we used in our calculations can be found in table 2.1. They are the same basis sets that were used for the molecular hydrogen calculations [6]. Single-ζ functions are used for core orthogonalization. The valence functions are of double-ζ quality with a triple-ζ d for iridium and triple-ζ p as well as. triple-ζ s for magnesium. Polarization functions have been added for iridium and hydrogen.
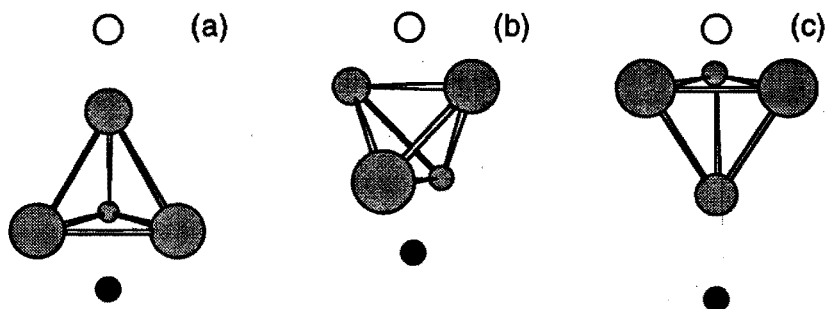
Fig. 2.1   *The structures of (a) onefold, (b) twofold, and (c) threefold H on Mg^{2+}-Ir_4. The structures of H on Ir_4 are the same except that the Mg^{2+} is absent.* ● = Ir, ● = Mg^{2+} and ○ = H.

Fig. 2.1 shows the three Mg^{2+}-Ir_4-H clusters studied. The distance between two iridium atoms is taken equal to the nearest-neighbour distance in the bulk, 2.714 Å [11]. For this Ir-Ir distance the calculated heat of formation of an Ir_4 cluster is -2771 kJ/mol. The calculated cluster equilibrium distance from a quadratic fit is 2.695 Å with a calculated heat of formation of -2773 kJ/mol, indicating that the cluster equilibrium Ir-Ir distance is in good agreement with the nearest-neighbour distance in the bulk. The distance between the iridium atoms and the Mg^{2+} cation is taken to be equal to 2.02 Å, which is the ionic radius (0.66 Å) of magnesium [12] plus half the Ir-Ir distance (1.36 Å). The distance between the hydrogen atom and nearest neighbour iridium atom(s) of the Ir_4 cluster has been optimized. The Mg^{2+} cation is located on the opposite side of the metal particle that is accessible to the adsorbing atom.

An estimate of the numerical error in the calculated adsorption energies one gets from calculating the adsorption energy of a hydrogen atom and a Mg^{2+} cation on the Ir_4 cluster in two different ways. In one case the Mg^{2+} cation is first adsorbed on Ir_4 and then the hydrogen atom on Mg^{2+}-Ir_4. In the other case the hydrogen atom is first adsorbed on Ir_4 and then the Mg^{2+} cation on Ir_4-H. The sum of the two adsorption energies thus obtained should be the same in both cases. We found that the maximum difference between the two adsorption energies is 10 kJ/mol, and thus estimate the error in our calculation at about 10 kJ/mol.

2.3 RESULTS AND DISCUSSION

The results of the atomic hydrogen adsorption in the geometries of minimal energy are shown in tables 2.2 (without the Mg^{2+} cation) and 2.3 (with the Mg^{2+} cation). The adsorption energy is defined as

$$\Delta E_{ads} = E(Ir_4\text{-}H) - E(Ir_4) - E(H), \qquad (2.1)$$

for the calculations without the Mg^{2+} cation, and as

$$\Delta E_{ads} = E(Mg^{2+}\text{-}Ir_4\text{-}H) - E(Mg^{2+}\text{-}Ir_4) - E(H), \qquad (2.2)$$

for the calculations with the Mg^{2+} cation. When comparing the three adsorption geometries, we see that the hydrogen atom has a strong preference for the twofold or threefold adsorption site over the onefold adsorption site. The adsorption energy for the twofold and the threefold sites are very close. The adsorption energy does not depend much on the presence of a Mg^{2+} cation. For the onefold adsorption geometry this dependence is the largest, and is shown in fig. 2.2(a). For the threefold adsorption geometry this dependence is much smaller, as is shown in fig. 2.2(b). The contribution of the zero-point energy to the adsorption energy is of the same order as the error in our calculations (~10 kJ/mol), and is ignored in this discussion.

The $X\alpha$ method generally suffers from overestimating adsorption energies. Together with the fact that the surface is modeled by a small cluster, the agreement between the calculated adsorption energies and the experimental values is expected to be poor.

The adsorption energy can be decomposed in two main contributions:

$$\Delta E_{ads} = \Delta E_{steric} + \Delta E_{int}. \qquad (2.3)$$

Here ΔE_{steric} is the energy change due to superposition of Ir_4 and the hydrogen atom without changing their molecular orbitals. This can be considered the contribution due to steric repulsion. The steric repulsion is much larger for twofold and threefold adsorption than for the onefold, simply because the hydrogen atom in the twofold and threefold position is in contact with more iridium atoms than in the onefold position.

The other term ΔE_{int} is the interaction energy, which can be split into various symmetries:

$$\Delta E_{int} = \Delta E_{\sigma} + \Delta E_{\pi} + \Delta E_{\delta} \qquad (2.4)$$

The changes in the orbital interaction energies shown in tables 2.2 and 2.3 are partly due to the fact that the number of electrons in an orbital with a certain symmetry changes with respect to Ir_4 and atomic hydrogen or Mg^{2+}-Ir_4 and atomic hydrogen at infinite separation. We can estimate the various symmetry contributions by transferring the electrons back to their original orbital [5]. The resulting values are the ones in parentheses in tables 2.2 and 2.3. We see that the σ orbitals are stabilized the most, the π orbitals are stabilized very little and the δ orbitals not at all. The latter orbitals do not participate actively in the bond formation.

Table 2.2 *Calculated properties of Ir_4-H for three geometries. Values in parentheses obtained by transferring electrons to the original configuration of Ir_4 and H at infinite separation.*

Ir_4-H	onefold		twofold		threefold	
Electronic configuration	$a_1^{10}a_2^2e^{25}$		$a_1^{14}a_2^6b_1^9b_2^8$		$a_1^{10}a_2^{2.57}e^{24.43}$	
d(Ir-H) (Å) [height (Å)]	1.64	[1.64]	1.82	[1.21]	1.91	[1.08]
ΔE_{steric} (kJ/mol)	195		380		499	
ΔE_{σ} (kJ/mol)	-123	(-460)	-430	(-742)	-548	(-842)
ΔE_{π} (kJ/mol)	-347	(-11)	-335	(-23)	-151	(-23)
ΔE_{δ} (kJ/mol)	0	(0)	-1	(-1)	-176	(-9)
ΔE_{int} (kJ/mol)	-471		-765		-874	
ΔE_{ads} (kJ/mol)	-276		-388		-377	
Gross population H(1s)	0.93		0.81		0.84	
ω of H (cm^{-1})	2337		1975		2538	

Table 2.3 *Calculated properties of Mg^{2+}-Ir_4H for three geometries. Values in parentheses obtained by transferring electrons to the original configuration of Mg^{2+}-Ir_4 and H at infinite separation.*

Mg^{2+}-Ir_4-H	onefold		twofold		threefold	
Electronic configuration	$a_1^{14}a_2^2e^{29}$		$a_1^{18}a_2^6b_1^{10.14}b_2^{10.86}$		$a_1^{14.95}a_2^2e^{28.05}$	
d(Ir-H) (Å) [height (Å)]	1.64	[1.64]	1.81	[1.20]	1.91	[1.08]
ΔE_{steric} (kJ/mol)	182		298		322	
ΔE_σ (kJ/mol)	927	(-406)	628	(-661)	-617	(-685)
ΔE_π (kJ/mol)	-1359	(-26)	-1320	(-31)	-84	(-16)
ΔE_δ (kJ/mol)	0	(0)	0	(0)	0	(0)
ΔE_{int} (kJ/mol)	-432		-692		-701	
ΔE_{ads} (kJ/mol)	-251		-397		-380	
Gross population H(1s)	0.75		0.79		0.86	
ω of H (cm⁻¹)	1733		2002		2384	

In contrast to the adsorption energy, both the steric repulsion and the orbital interaction show a strong dependence on the presence of the Mg²⁺. In the presence of the cation the steric repulsion as well as the (attractive) orbital interaction decreases. These changes cannot be explained from a change in the adsorption geometry, the Ir-H distance is not found to change. The reduction of the steric repulsion is caused by the polarization of the cluster by the cation, which moves electrons away from the adsorption site. This polarization also makes it harder for the iridium cluster orbitals to interact with the hydrogen 1s orbital, as the formation of a chemical bond has to shift the electron density in the cluster to a less favorable one for the interaction with the cation. The cancellation of the two effects is accidental.
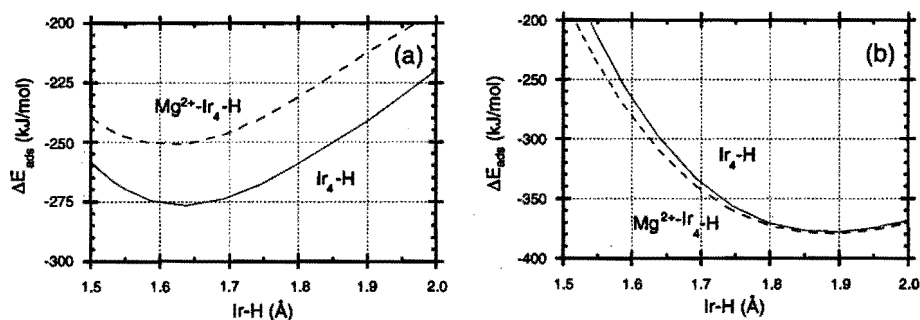
Fig. 2.2 *Adsorption energy as a function of Ir-H for (a) onefold and (b) threefold H on $[Mg^{2+}]Ir_4$.*

The calculated hydrogen stretch frequency for the onefold and threefold hydrogen adsorption shows also a strong dependence when a Mg^{2+} cation is present. For carbon monoxide adsorption we showed that the polarization of the cluster leads to a flatter well for the metal-carbon bond. The same mechanism is working here. The effect is however subtle, and for twofold adsorption hardly any change in stretch frequency is found. For hydrogen adsorption on iridium there exists no known experimental value for the stretch frequency. The calculated stretch frequencies for the twofold en threefold geometries seems to be rather large when compared to adsorption on other transition metals, for example the frequencies obtained with inelastic neutron scattering spectroscopy for the hydrogen adsorption on nickel [13], on palladium [14], and on platinum [15].

Fig. 2.3 presents the local density of states of the hydrogen 1s orbital for the three different adsorption geometries. Of interest is the upward shift in average peak position for occupied levels when the coordination of the hydrogen atom decreases. This agrees with the trend predicted based on the concept of group orbitals [16]. The hydrogen 1s orbital interacts with cluster orbitals, σ symmetric with respect to the hydrogen-metal particle symmetry axis. In high coordination this constraints the interaction to low energy-orbitals, whereas in lower coordination also higher energy orbitals contribute [17].
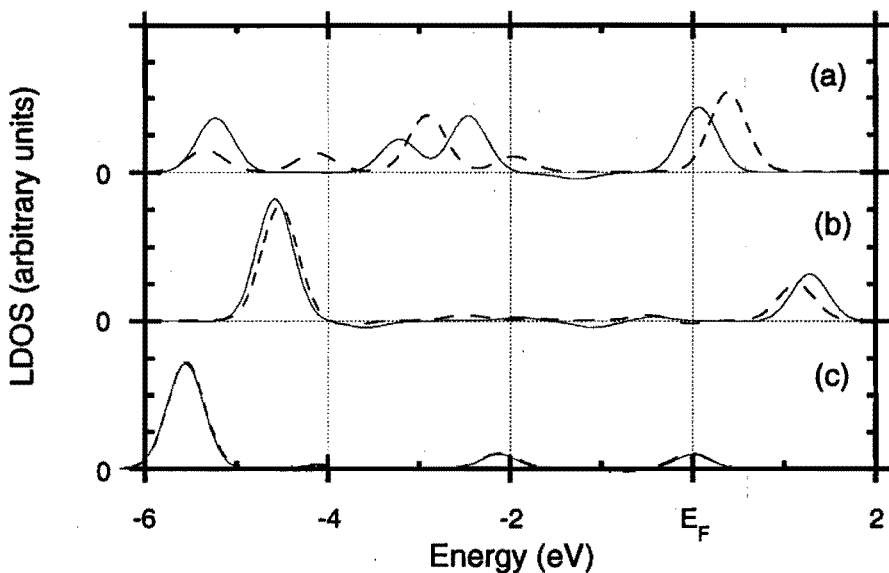
Fig. 2.3   *LDOS of H(1s) for (a) onefold, (b) twofold, and (c) threefold H on Ir₄ without (_____)*
and with (_ _ _) Mg²⁺. For threefold H, the calculated LDOS without and with Mg²⁺ almost coincide.

The shift, show in fig. 2.3, in average local density for onefold adsorption to higher energies when a Mg^{2+} cation is present, agrees with the observed bond weakening. It is due to the increased energy difference between cluster and adatom orbitals that weakens the covalent interaction. For the twofold and threefold adsorption this energy difference increases much less, as the distance between hydrogen and Mg^{2+}, and between Mg^{2+} and the iridium atoms that interact with hydrogen is almost the same. Hence the small change in the LDOS for these adsorption geometries.

Additional information on the bonding of hydrogen on iridium, and the influence of the Mg^{2+} cation is given by electron-density difference plots. These plots show the change in electron density of the system (e.g. Ir_4-H) and its separate fragments (e.g. Ir_4 and H). Electron-density difference maps of all the geometries studied, without and with the Mg^{2+} cation, are shown in figs. 2.4 (hydrogen adsorbed onefold), 2.5 (hydrogen adsorbed twofold) and 2.6 (hydrogen adsorbed threefold). Some polarization of the hydrogen metal bond density towards the Ir_4 cluster by the Mg^{2+} cation can be seen from these figures. However, these effects are small, in accord with the LDOS figures (fig. 2.3). The substantial polarization caused by the Mg^{2+} cation can be seen by comparing the figure in the absence of the Mg^{2+} (on the left) with the figure in the presence of the Mg^{2+} (on the right).
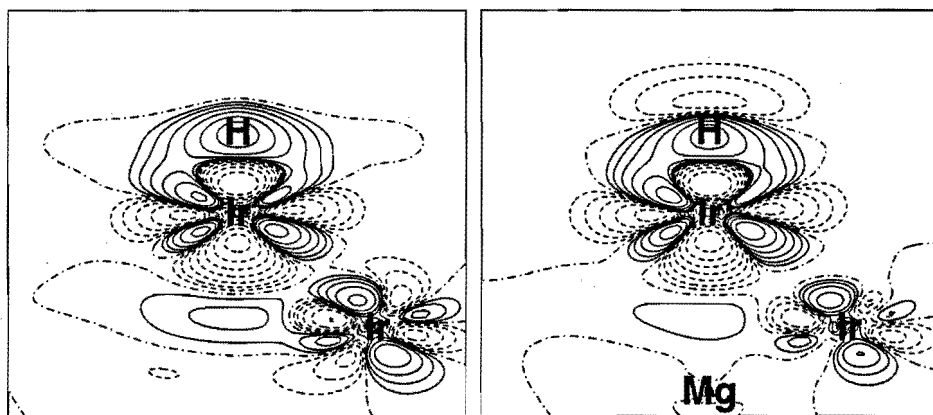
Fig. 2.4   *Contour plot of the electron density difference $\rho(Ir_4$-H$) - \rho(Ir_4) - \rho(H)$ (on the left) and $\rho(Mg^{2+}$-Ir_4-H$) - \rho(Mg^{2+}$-$Ir_4) - \rho(H)$ (on the right) for onefold H. Dashed lines show a decrease and solid lines an increase of the electron density, the dashed-dotted lines depict nodal surfaces. Subsequent contours correspond to 0.00, ±0.01, ±0.02, ±0.04, ±0.08, ±0.16, ±0.32, and ±0.64 e/Å³ (electrons per cubic Ångstrom).*
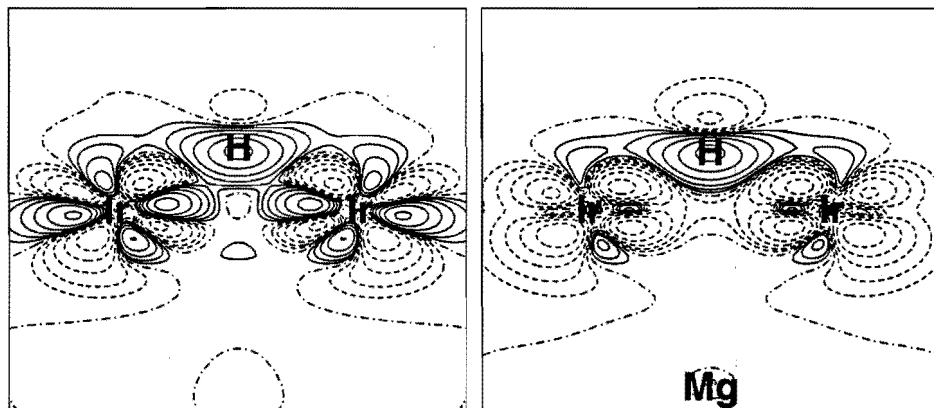
Fig. 2.5   Contour plot of the electron density difference $\rho(Ir_4\text{-}H) - \rho(Ir_4) - \rho(H)$ (on the left) and $\rho(Mg^{2+}\text{-}Ir_4\text{-}H) - \rho(Mg^{2+}\text{-}Ir_4) - \rho(H)$ (on the right) for twofold H. Values at the contours as in fig. 2.4.

The polarization of the Ir_4 particle by the Mg^{2+} cation such that a negative charge develops on the cluster atoms close to the Mg^{2+} cation can also be seen from table 2.4. This table shows the Mulliken population analysis by atomic orbitals. Although the Mulliken population analysis is somewhat arbitrary in the way it divides electrons between bonded atoms, electrons clearly move from the iridium atom(s) to which hydrogen adsorbs to the iridium atom(s) to which the Mg^{2+} cation adsorbs. The charge of the cation decreases from 2.00 to 1.78, 1.64, and 1.32 for onefold, twofold, and threefold hydrogen, respectively.
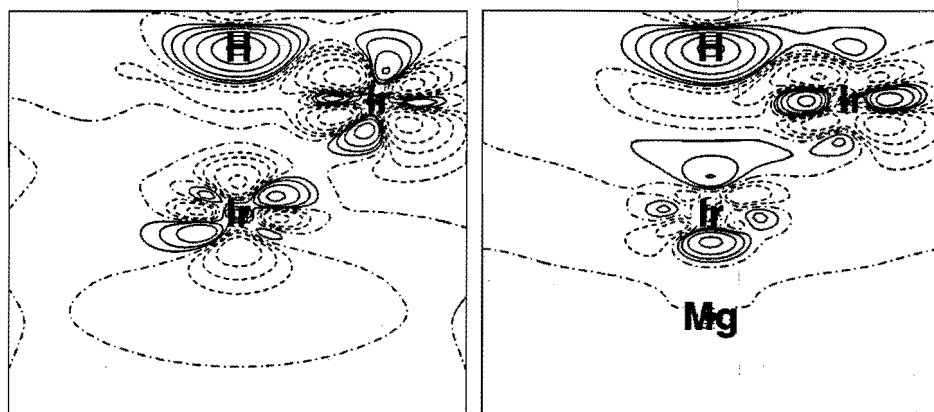
Fig. 2.6   Contour plot of the electron density difference $\rho(Ir_4\text{-}H) - \rho(Ir_4) - \rho(H)$ (on the left) and $\rho(Mg^{2+}\text{-}Ir_4\text{-}H) - \rho(Mg^{2+}\text{-}Ir_4) - \rho(H)$ (on the right) for threefold H. Values at the contours as in fig. 2.4.

Table 2.4 Mulliken population analysis by atomic orbitals for hydrogen adsorbed on [Mg^{2+}-]Ir$_4$

Atom	l	onefold			twofold			threefold		
		without	with	Δ	without	with	Δ	without	with	Δ
Ir†	s	0.90	0.48	-0.42	0.72	0.53	-0.19	0.65	0.54	-0.11
	p	-0.17	-0.18	-0.01	0.07	0.04	-0.03	0.08	0.08	0.00
	d	8.13	8.09	-0.04	8.25	7.94	-0.31	8.31	7.96	-0.35
	total	8.86	8.39	-0.47	9.04	8.51	-0.53	9.04	8.58	-0.46
Ir††	s	0.66	0.81	0.15	0.67	0.84	0.17	0.61	1.06	0.45
	p	0.07	0.15	0.08	0.08	0.18	0.10	0.07	0.09	0.02
	d	8.34	8.26	-0.08	8.32	8.39	0.07	8.35	8.59	0.24
	total	9.07	9.22	0.15	9.07	9.41	0.34	9.03	9.74	0.71
H	s	0.91	0.76	-0.15	0.75	0.75	0.00	0.78	0.81	0.03
	p	0.00	-0.01	-0.01	0.04	0.04	0.00	0.06	0.06	0.00
	total	0.91	0.75	-0.16	0.79	0.79	0.00	0.84	0.87	0.03
Mg	s		2.15			2.31			2.65	
	p		6.07			6.05			6.03	
	total		8.22			8.36			8.68	

† Iridium atom(s) to which hydrogen adsorbs

†† Iridium atom(s) to which the Mg^{2+} cation adsorbs.

In a previous paper we found that the adsorption energy of molecular hydrogen on the tetrahedral Ir$_4$ cluster increases (in absolute sense) when the Mg^{2+} cation is present [6]. Together with the results for the hydrogen atom presented here we find, that the overall activation energy for molecular hydrogen adsorption and dissociation with respect to the gas phase should decreases, as predicted by the relation of Polanyi [2]. This agrees with the observed activation of saturated hydrocarbons, which contain H$_2$ type bonds, in zeolites containing metal particles and highly charged cations [2, 3].

2.4   CONCLUSIONS

The local density approximation studies of hydrogen adsorbed to Ir$_4$ clusters show a small decrease in hydrogen bond strength in the presence of a Mg^{2+} cation. The maximum decrease is 25 kJ/mol for onefold adsorbed hydrogen. For stronger bounded hydrogen atoms adsorbed in high coordination sites only very small changes in bond strength are found.

As a result the heat of dissociative adsorption for the particular clusters studied of hydrogen to Ir_4 particles will not change. For the particular cluster studied the overall activation energy with respect to the gasphase is predicted to decrease due to the increased heat of adsorption of the hydrogen molecule.

2.5   REFERENCES

[1]   I. Maxwell, *Adv. Catal.* **31** (1982) 1.

[2]   M. Boudart and G. Djéga-Mariadassou, *Kinetics of Hetrogenous Catalic Reactions* (Princeton University Press, Princeton, 1984); T.R. Hughes, W.C. Buss, P.W. Tamm and R.L. Jacobson, in: *Proceedings of the 7th Int. Zeolite Conference*, eds. Y. Murakami, A. Iijima and J.W. Ward (Elsevier, Amsterdam, 1986).

[3]   P. Gallezot, Catal. *Rev. - Sci. Eng.* **20** (1979) 121.

[4]   C. Besoukhanova, J. Guidot and D. Barthomeuf, *J. Chem. Soc., Faraday Trans. I* **77** (1981) 1595; A. De Mallman and D. Barthomeuf, in: *Studies in Surface Science and Catalysis*, Vol. 46, eds. H.G. Karge, and J. Weitkamp (Elsevier, Amsterdam, 1989).

[5]   A.P.J. Jansen and R.A. van Santen, *J. Phys. Chem.* **94** (1990) 6764.

[6]   E. Sanchez Marcos, A.P.J. Jansen and R.A. van Santen, *Chem. Phys. Lett.* **167** (1990) 399.

[7]   A.P.J. Jansen and R.A. van Santen, in: *Structure-Activity Relationships in Heterogeneous Catalysis*, eds. R.K. Grasselli and A.W. Sleight (Elsevier, Amsterdam, 1991).

[8]   E.J. Baerends, D.E. Elis and P. Ros, *Chem. Phys.* **2** (1973) 41; E.J. Baerends and P. Ros, *Chem. Phys.* **2** (1973) 52; E.J. Baerends and P. Ros, *Chem. Phys.* **8** (1975) 412; P.M. Boerrigter, G. te Velde and E.J. Baerends, *Int. J. Quantum Chem.* **33** (1988) 87.

[9]   G. te Velde and E.J. Baerends, *J. Comput. Phys.* **99** (1992) 84.

[10] T. Ziegler and A. Rauk, *Theoret. Chim. Acta* **46** (1977) 1.

[11] R.W.G. Wychoff, *Crystal Structures*, Vol I, 2nd edition (Wiley, New York, 1963).

[12] R.C. Weast , ed., *Handbook of Chemistry and Physics*, 64th Ed. (CRC Press, Boca Raton, 1983).

[13] H. Jobic and A. Renouprez, *J. Chem. Soc., Faraday Trans. I* **80** (1984) 1991.

[14] I.J. Braid, J. Howard and J. Tomkinson, *J. Chem. Soc., Faraday Trans. II* **79** (1983) 263; H. Jobic, J.P. Candy, V. Perrichon and A. Renouprez, *J. Chem. Soc., Faraday Trans. I* **81** (1985) 1955; J.M. Nicol, J.J. Rush and R.D. Kelley, *Surf. Sci.* **197** (1988) 67.

[15] J.J. Rush, R.R. Cavanagh, R.D. Kelley and J.M. Rowe, *J. Chem. Phys.* **83** (1985) 5339.; A. Renouprez, and H. Jobic, *J. Catal.* **113** (1988) 509.

[16] R.A. van Santen, *J. Chem. Soc. Far. Trans. I* **83** (1987) 1915; R.A. van Santen, *Progr. Surf. Sci.* **25** (1987) 253; R.A. van Santen, *J. Mol. Struct.* **173** (1988) 157.

[17] R.A. van Santen, *Rec. Trav. Chim. Pays Bas* **101** (1982) 157.

3 Cation-induced changes in the adsorption of sulphur on Ir₄ clusters

ABSTRACT

In this chapter we[*] present the results of density functional calculations, including relativistic effects, for the adsorption of a sulphur atom on a tetrahedral Ir_4 cluster. We used the formulas of Vosko-Wilk-Nussair for the exchange-correlation potential, including the Stoll correction (to improve the correlation part) and the gradient correction according Becke (to improve the exchange part). The sulphur atom is found to prefer a twofold coordination. Introducing a Mg^{2+} cation at the opposite side of the Ir_4 cluster lowers the adsorption energy for the onefold geometry, but increases it for the threefold geometry. The twofold geometry is influenced only slightly. We analyze the results in terms of the steric repulsion and orbital interactions, as a function of the electronic configuration and the distance between sulphur and the cluster.

3.1   INTRODUCTION

The chemical reactivity of small metal clusters is of considerable fundamental as well as practical interest. When dispersed in the micro cavities of zeolites, they form active hydrocarbon conversion catalysts. A common problem in these processes is the rapid poisoning of the catalyst when converting reactants containing traces of sulphur. The resistance against this poisoning, as well as the catalytic activity of the catalyst has been reported to be a strong function of the cation charge [1-3]. Quantum chemical methods have reached a stage that the basis of this phenomenon can be studied using chemically relevant model systems. Earlier we reported the results of local density approximation (LDA) calculations using the $X\alpha$ potential, on the adsorption of carbon monoxide, molecular and atomic hydrogen, on iridium clusters [4-7]. When introducing a cation we found changes in the geometry (optimized distance between the adsorbate and the cluster), the adsorption energy and the stretch-frequencies.

The $X\alpha$ method has been shown to give reasonably accurate results for diatomic molecules. But in general, it is found to overestimate the bond energy for carbonyl complexes, whereas bond lengths are predicted somewhat too short. Various improvements have been suggested, mainly concerning a better description of the exchange-correlation potential. In the calculations we are reporting, we have incorporated some of these.

We studied the adsorption of sulphur on a cluster in three different adsorption geometries and in the absence or presence of the Mg^{2+} cation on the opposite side of the cluster. That the Mg^{2+} cation will influence the adsorption of sulphur is due to the fact that it will polarize the cluster [5]. Negative charge will develop on the iridium atoms close to the cation, and a reduction of the electron density between the cluster and the adsorbate will result. The way this influences the strength of the bond between adsorbate and the cluster, depends on the extend in which repulsive and interactive forces are affected by the cation. LDA gives us a powerful tool to analyze these often competing changes.

3.2   METHOD

We have performed restricted calculations using the local density approximation (LDA). We used the Amsterdam density-functional (ADF) program suite developed by Baerends and coworkers, which is an implementation of the Kohn-Sham equations [8-10]. For the adsorption of sulphur, we followed an approach that differed slightly from our first LDA

calculations. We used the Vosko-Wilk-Nussair (VWN) potential [11], based on homogeneous electron gas calculations, to describe the exchange-correlation energy. Since VWN is known to underestimate the exchange energy and to overestimate the correlation energy, we used the correction as proposed by Stoll [12], to repair the correlation error, and a correction due to Becke [13] to repair the exchange error. Another point where our calculations differ from the former ones is that relativistic effects have been included [14, 15]. We used a relativistic frozen core, obtained by Dirac-Slater calculations, and included relativistic effects on the valence electrons as a first order perturbation.

The molecular orbitals are represented as linear combinations of atomic Slater-type orbitals (STO's). Integrals are computed numerically, using the Te Velde integration [16]. Adsorption energies are computed with the Ziegler transition-state method [17]. For magnesium the 1s orbital is kept frozen, for sulphur the 1s, 2s, and 2p orbitals, and for iridium electrons up to the 4f. The exponents of the STO basis set for sulphur are shown in table 3.1. The basis sets for iridium and magnesium can be found in earlier reports [4, 5]. The basis sets we used are of double ζ quality with a triple ζ 5d for iridium. Polarization functions have been added for iridium and sulphur.

Table 3.1   *Exponents ζ of the STO's for sulphur.*

	type	ζ		type	ζ		type	ζ	
S	1s	13.25	core	3s	1.60	valence	3p	2.15	valence
	2s	5.35	core	3s	2.60	valence	3d	2.20	valence
	2p	6.25	core	3p	1.15	valence			

Fig. 3.1 shows the three Mg^{2+}-Ir_4-S clusters studied. The distance between two iridium atoms is taken equal to the nearest neighbour distance in the bulk; 2.714 Å. We found that this is very close to the distance for the geometry optimized cluster. The distance between the iridium atoms and the Mg^{2+} cation is taken to be equal to the ionic radius (0.66 Å) plus half the Ir-Ir distance (1.36 Å), 2.02 Å. With this distance we tried to compromise between a maximum influence on the sulphur adsorption and still retaining the ionic character of Mg^{2+}. The distance between the sulphur atom and the cluster has been optimized. The Mg^{2+} cation is located on the opposite side of the cluster where the sulphur is adsorbed (see fig. 3.1).

Earlier we reported that we had to reckon with a numerical error in the calculations of the adsorption energy of about 10 kJ/mol. We expect that this estimate is also valid for the results presented here.
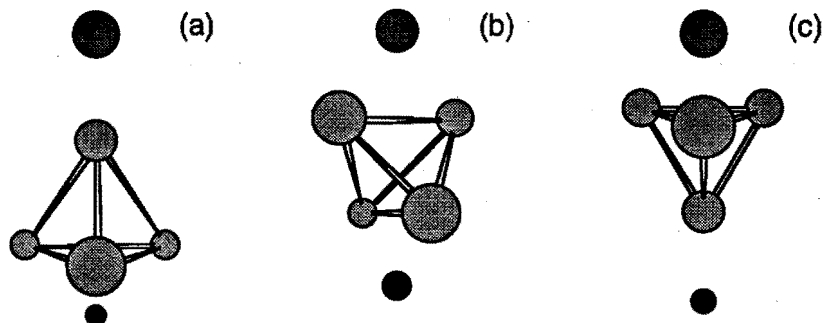
Fig. 3.1 *The structures of (a) onefold, (b) twofold, and (c) threefold S on Mg^{2+}-Ir_4. The structures of S on Ir_4 are the same except that the Mg^{2+} is absent.* ⊘ = Ir, ● = Mg^{2+} and ● = S.

3.3   RESULTS AND DISCUSSION

Before discussing the Ir_4-S results we will briefly address the results of calculations on a single iridium atom to show the changes related with the new potentials and the relativistic corrections. We found that a non-relativistic calculation, just like the Xα calculation [5], gave d^9 as ground state whereas the calculations with the relativistic corrections show a preference for d^8s^1 (which was 68 kJ/mol lower in energy then d^7s^2, the true ground state). When doing an unrestricted calculation for iridium we found that the energies of d^7s^2 and d^8s^1 are very close. LDA with non-local and relativistic corrections seems to give a better description of a single iridium atom than calculations with the Xα potential. An unrestricted calculation for the sulphur atom shows an energy of -69 kJ/mol with respect to the restricted state. We observed no significant changes in unrestricted calculations for the closed shell fragments Ir_4 and Mg^{2+}. We found that relativistic corrections for S and Mg are much smaller than for Ir, as expected. Nevertheless, we incorporated relativistic corrections for all atoms.

Table 3.2 summarizes the results of sulphur adsorption for the optimized geometries with the electronic configuration of the ground state. The adsorption energies are defined as:

$$\Delta E_{ads} = E(Ir_4\text{-}S) - E(Ir_4) - E(S), \qquad (3.1)$$

for the calculations without the Mg^{2+} cation, and for the calculations with the Mg^{2+} cation as:

$$\Delta E_{ads} = E(Mg^{2+}\text{-}Ir_4\text{-}S) - E(Mg^{2+}\text{-}Ir_4) - E(S). \qquad (3.2)$$

The difference between restricted and unrestricted sulphur has been included in the tables in ΔE_{ads}, but not in its decomposition, which is with respect to the restricted state. We see that the sulphur atom has a preference for the twofold adsorption site. The adsorption energies for the onefold and the threefold position are very close, however.

Table 3.2 *Calculated properties for Ir₄-S and Mg²⁺-Ir₄-S: electronic configuration of the ground state, geometrical parameters, adsorption energies (including Becke, Stoll and relativistic corrections, and difference between restricted and unrestricted sulphur [69 kJ/mol]) and Ir₄-S stretch frequencies.*

geometry	onefold		twofold		threefold	
system	Ir₄-S	Mg²⁺-Ir₄-S	Ir₄-S	Mg²⁺-Ir₄-S	Ir₄-S	Mg²⁺-Ir₄-S
elec. config.	$a_1^{13}a_2^1e^{28}$	$a_1^{17}a_2^2e^{31}$	$a_1^{16}a_2^6b_1^{10}b_2^{10}$	$a_1^{20}a_2^6b_1^{12}b_2^{12}$	$a_1^{12}a_2^2e^{28}$	$a_1^{18}a_2^2e^{30}$
d(Ir-S) (Å)	2.15	2.12	2.37	2.25	2.54	2.42
ΔE_{ads} (kJ/mol)	-296	-251	-335	-335	-284	-374
ω (cm⁻¹)	550	480	710	310	355	305

We see for the onefold geometry that the cation is destabilizing the bond. For the twofold geometry there is no change in adsorption energy, whereas for the threefold geometry the Mg^{2+} is stabilizing the bond. We also see that for the twofold and the threefold geometry the distance between the cluster and the sulphur atom is decreased by approximately 0.12 Å. For the onefold geometry the adsorption distance is changed only slightly.

We also calculated Ir₄-S stretch frequencies. For all geometries we found that the stretch frequency decreases upon introduction of the Mg^{2+} cation, as was also found for CO and H_2. We did not find experimental values for these vibrations. However, our values are of comparable magnitude as calculated sulphur stretch frequencies on nickel clusters [20].

In order to understand the site dependence and the effect of Mg^{2+} we have decomposed the adsorption energy into two main contributions [21]:

$$\Delta E_{ads} = \Delta E_{steric} + \Delta E_{int}. \qquad (3.3)$$

Here ΔE_{steric} is defined as the energy change due to superposition of Ir₄ and sulphur without changing their molecular orbitals. It can be split in an electrostatic and an exchange repulsion:

$$\Delta E_{steric} = \Delta E_{elstat} + \Delta E_{xrep} + \Delta E_{rest}. \qquad (3.4)$$

The term ΔE_{rest} contains the non-local Becke correction, which the ADF program does not incorporate in the decomposition of ΔE_{steric}. For the systems studied this term is almost constant. The second term in the decomposition of ΔE_{ads} is the interaction energy, which gives the energy change due to orbital relaxation. It can be split into various symmetries

$$\Delta E_{int} = \Delta E_{\sigma} + \Delta E_{\pi} + \Delta E_{\delta} + \Delta E_{rest}. \qquad (3.5)$$

The point group symmetry is C_{3v} for the onefold and the threefold geometry, and is C_{2v} for the twofold geometry. With σ we mean a_1, and with δ we mean a_2 for both point group symmetries. With π we mean e symmetry in C_{3v} and b_1 and b_2 in C_{2v} (in that case we will refer to it as π_1 and π_2 respectively). Again ΔE_{rest} contains the non-local Becke correction, that is not incorporated in the decomposition of ΔE_{int}, and again it is almost constant.

The decomposition of the adsorption energy is presented in tables 3.3, 3.4 and 3.5. The electronic configurations in column I and III are due to the ground state of the separate fragments at infinity, and in column II, IV and V due to the ground state of the overall system. The iridium-sulphur distance is only optimized in the case of columns II and V.

Table 3.3 *Onefold geometry: Energies (in kJ/mol) include Stoll and relativistic corrections. ΔE_{steric}, ΔE_{int}, and ΔE_{ads} also include Becke correction and the difference between restricted and unrestricted sulphur. Decomposition of ΔE_{steric} and ΔE_{int} as defined in the text.*

	Without Mg^{2+}		With Mg^{2+}		
	I	II	III	IV	V
elec. config.	$a_1^{13.3}a_2^2e^{26.7}$	$a_1^{13}a_2^1e^{28}$	$a_1^{17.3}a_2^2e^{30.7}$	$a_1^{17}a_2^2e^{31}$	$a_1^{17}a_2^2e^{31}$
d(Ir-S) (Å)	2.15	2.15	2.15	2.15	2.12
ΔE_{elstat}	-623	-623	-477	-477	-524
ΔE_{xrep}	945	945	755	755	837
ΔE_{steric}	428	428	379	379	418
ΔE_{σ}	-389	-239	-329	143	132
ΔE_{π}	-481	-969	-425	-892	-919
ΔE_{δ}	0	382	0	0	0
ΔE_{int}	-815	-794	-704	-698	-738
ΔE_{ads}	-317	-296	-257	-250	-251

Table 3.4 *Twofold geometry: Energies (in kJ/mol) / decomposition as in table 3.3.*

	Without Mg^{2+}		With Mg^{2+}		
	I	II	III	IV	V
elec. config.	$a_1^{17.3}a_2^6b_1^{9.3}b_2^{9.3}$	$a_1^{16}a_2^6b_1^{10}b_2^{10}$	$a_1^{21.3}a_2^6b_1^{11.3}b_2^{11.3}$	$a_1^{20}a_2^6b_1^{12}b_2^{12}$	$a_1^{20}a_2^6b_1^{12}b_2^{12}$
d(Ir-S) (Å)	2.37	2.37	2.37	2.37	2.25
ΔE_{elstat}	-1007	-1007	-806	-806	-1137
ΔE_{xrep}	1595	1595	1331	1331	1907
ΔE_{steric}	721	721	655	655	919
ΔE_{σ}	-519	-73	-508	1213	1086
$\Delta E_{\pi 1}$	-347	-604	-339	-1217	-1309
$\Delta E_{\pi 2}$	-218	-480	-198	-1093	-1142
ΔE_{δ}	-19	-20	-14	-14	-25
ΔE_{int}	-1051	-1125	-998	-1048	-1324
ΔE_{ads}	-261	-335	-273	-323	-335

Table 3.5   *Threefold geometry: Energies (in kJ/mol) / decomposition as in table 3.3.*

	Without Mg^{2+}		With Mg^{2+}		
	I	II	III	IV	V
elec. config.	$a_1^{13.3}a_2^2e^{26.7}$	$a_1^{12}a_2^2e^{28}$	$a_1^{18.3}a_2^2e^{29.7}$	$a_1^{18}a_2^2e^{30}$	$a_1^{18}a_2^2e^{30}$
d(Ir-S) (Å)	2.54	2.54	2.54	2.54	2.42
ΔE_{elstat}	-890	-890	-780	-780	-1116
ΔE_{xrep}	1427	1427	1369	1369	1967
ΔE_{steric}	677	677	724	724	1008
ΔE_σ	-416	20	-522	-149	-266
ΔE_π	-606	-1112	-621	-1059	-1240
ΔE_δ	-3	-3	-2	-2	-5
ΔE_{int}	-959	-1030	-1092	-1155	-1452
ΔE_{ads}	-212	-284	-299	-362	-374

The decomposition of the adsorption energy for the ground state of the geometry optimized systems is shown in columns II and V of tables 3.3, 3.4 and 3.5. Apart from the steric repulsion and the orbital relaxation these columns also contain the effect of a change in the electronic configuration when the sulphur atom is brought close to the Ir$_4$ cluster. This leads to $\Delta E_\delta = 382$ kJ/mol for the onefold adsorption without the Mg^{2+} ion, even though no orbitals of δ symmetry form chemical bonds. Moreover, when comparing systems with and without the Mg^{2+} ion we have an effect of the change in the Ir-S distance.

In order to split off these effects we performed calculations on intermediately configurated systems. Column I shows the results for the system without the cation, that differs from the optimized system only in that it has the electronic configuration of the ground state of the separate fragments at infinity. E.g., for the onefold geometry we did a calculation with the configuration $a_1^{13.33}a_2^2e^{26.67}$, being the combined configuration of Ir$_4$ ($a_1^{10}a_2^2e^{24}$, which is derived from $a_1^4e^8t_1^6t_2^{18}$ in T_d symmetry by reducing the representations) and sulphur ($a_1^{3.33}a_2^0e^{2.67}$, which is derived from s^{2}p^4). Although it does not comply with the basic idea of Kohn and Sham, it can be very instructive to work with fractional occupation numbers. We have separated now the effects of the shifts of the molecular orbital levels on the one hand (column I), and the effect of electron transfer on the other (column I to II). The decomposition shows clearly the various symmetry contributions to the interactions. We see in column I that for the Ir$_4$-S system the interactions are, as expected, predominantly with the σ and π orbitals for all geometries; with the π interactions somewhat stronger. The change in electronic configuration lowers ΔE_{ads} only substantially for high coordination sites. For the onefold

adsorption the configuration with fractional occupation numbers is slightly more stable. This is a consequence of the fact that we use an approximation for the exchange-correlation potential [22]. We conclude that the optimization of the electronic configuration for onefold adsorption has little effect. The steric repulsion in columns I and II are necessarily the same as they relate only to the orbitals of the Ir$_4$ and the sulphur atom, and not to the final orbitals.

For the systems with Mg^{2+} we did comparable calculations. Column III show results of calculations that differ from the ones in column IV only in electronic configuration. For the onefold geometry we did a calculation with the configuration $a_1^{17.33}a_2^2e^{30.67}$, being the combined configuration of the ground state of the Mg^{2+}-Ir$_4$ fragment ($a_1^{14}a_2^2e^{28}$) and the sulphur atom ($a_1^{3.33}a_2^0e^{2.67}$). The Ir-S distance in column III and IV is the same as in the systems without Mg^{2+}. Again we see (column III) that the interaction is with the π orbitals, and to a somewhat lesser extent with the σ orbitals. The effect of the change of the electronic configuration is the same as without the Mg^{2+} cation.

The difference between columns IV and V is the relaxation of the Ir-S bond, which lowers the adsorption energy for the twofold and threefold geometry by approximately 10 kJ/mol, involving a decrease of the bond length of about 0.12 Å. Such an reduction in adsorbate-metal distance has also been found before for molecular hydrogen resulting from the reduction in electron-density between adsorbate and metal atom [4]. For onefold geometry these changes are almost negligible. The contribution to the adsorption energy from the optimization of the Ir-S bond length is rather small; the decomposition, however, changes a lot. As expected the steric repulsion increases, but this is compensated by a more favorable interaction of especially the π orbitals.

Fig. 3.2 shows sulphur s, p_σ and p_π local density of states (LDOS) for the threefold geometries. We see that there is only one large peak for sulphur s orbitals, whereas the p_σ and p_π orbitals show a broad band. These plots are characteristic for all geometries. They indicate that the bonding is mainly a result of interaction with the sulphur p_σ in combination with the sulphur p_π orbitals. For twofold adsorption the plots for the two p_σ orbitals differ. This is because the p_x, which points in the direction of the two closest iridium atoms, interacts strongly. The p_y orbital on the other hand, perpendicular to the line connecting the two closest iridium atoms, interacts less.

As the change in Ir-S distance when Mg^{2+} cation is added has only a small effect on the adsorption energy we look at the effect of Mg^{2+} by comparing columns II and IV. For onefold and twofold adsorption we see the same trend as we found in previous studies [4-7]. The cation polarizes the Ir$_4$ cluster, thus decreasing the electron density at the site where the sulphur atom adsorbs. This reduces the steric repulsion, but also the interaction between the Ir$_4$ cluster and the sulphur atom. The two effects, reduced interaction and steric repulsion,

tend to cancel. This is indeed the case for the twofold adsorption. For onefold adsorption the interaction energy is reduced more than the steric repulsion so that the net effect is a smaller adsorption energy. The relative importance of the σ and π interaction does not change.
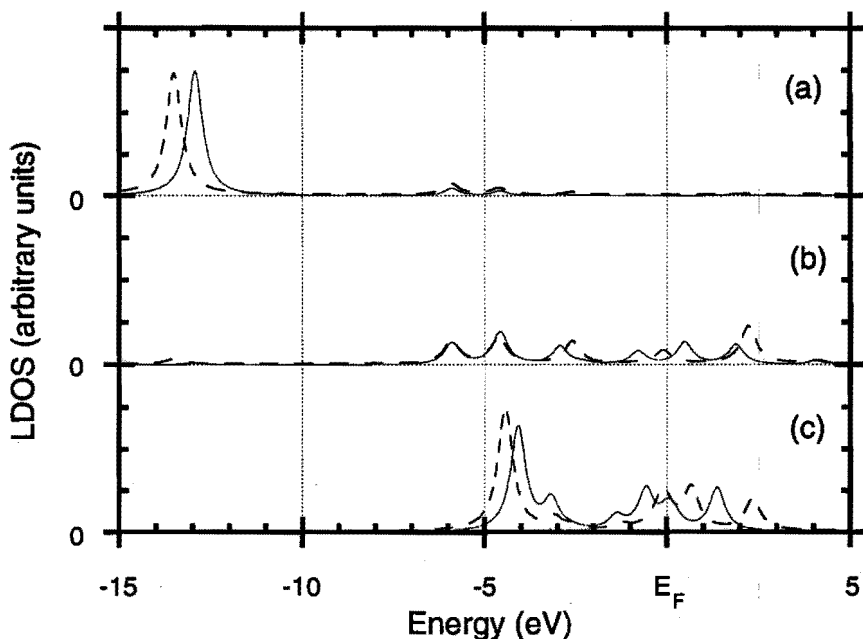
Fig. 3.2   *The local density of states for threefold sulphur without (_____) and with (_ _ _) Mg²⁺. LDOS of the sulphur (a) s, (b) pσ, and (c) pπ orbital. Energies are with respect to the Fermi level (EF).*

The threefold adsorption is different. The steric repulsion increases. As for the other sites it changes, because the exchange repulsion and the electrostatic interaction both decrease in absolute value. Usually the effect in the exchange repulsion dominates, but for threefold adsorption the electrostatic change is more important. At the same time the interaction energy increases; primarily via the σ orbitals. The net effect is an increased adsorption energy. Such an increase we have found before for H_2 adsorption [4]. However, there this increase was accompanied by a large change in geometry. Apparently, the effect of the Mg^{2+} cation on the threefold adsorption of a sulphur atom is not just electrostatic, but the cation also changes the chemical bond between the Ir_4 cluster and the sulphur atom in a qualitative way.

Additional information on the nature of the bonding is given by density difference plots. The plots for the twofold geometry without and with the Mg^{2+} cation are shown in fig. 3.3.

We see, in the absence of Mg^{2+}, an increase of the electron density in the region the sulphur p_π orbitals, and a decrease just below the sulphur atom. The increase in the p_π region indicates the formation of bonding orbitals of the p_x orbital. The decrease just below the sulphur atom points to a reduction of the steric repulsion between the partially filled p_σ orbital and filled cluster orbitals. Such an effect we found previously for carbon monoxide adsorption [5, 7]. In the presence of Mg^{2+} we do not see the decrease just below the sulphur atom because the Mg^{2+} cation polarizes the Ir_4 cluster, thus decreasing the electron density and the steric repulsion at the site where the sulphur atom adsorbs. The interaction with the metal d orbitals is also very clear from the cloverleaf structure in this figure. The polarization due to the cation is substantial, as can be seen by comparing the two figures.
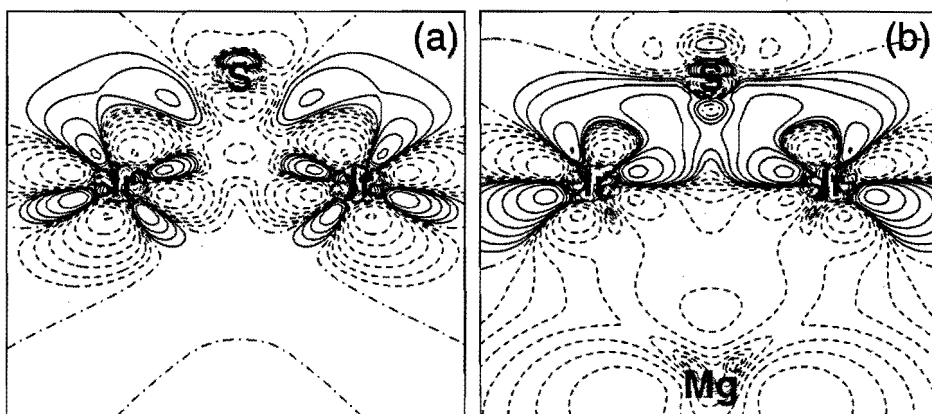
Fig. 3.3   Contour plot of the electron density difference $\rho(Ir_4\text{-}S) - \rho(Ir_4) - \rho(S)$ (on the left) and $\rho(Mg^{2+}\text{-}Ir_4\text{-}S) - \rho(Mg^{2+}\text{-}Ir_4) - \rho(S)$ (on the right) for twofold S. Dashed lines show a decrease and solid lines an increase of the electron density, the dashed-dotted lines depict nodal surfaces. Subsequent contours correspond to 0.00, ±0.01, ±0.02, ±0.04, ±0.08, ±0.16, ±0.32, and ±0.64 $e/Å^3$.

Another way to analyze the adsorption is to promote fragments so that electrons already occupy orbitals of the same symmetry as the final system. The main advantage of this analysis is that the decomposition of the interaction energy directly reflects the orbitals that form chemical bonds. Misleading results as $\Delta E_\delta = 382$ kJ/mol for onefold Ir_4-S are not found. The results for the threefold geometry for the systems without and with the Mg^{2+} cation are given in table 3.6. We promoted the fragments by primarily rearranging the sulphur p electrons, thus keeping the promotion energy minimal. For the system without the Mg^{2+} cation we promoted the sulphur atom from $a_1^{3.33}a_2^0e^{2.67}$ to $a_1^2a_2^0e^4$, which combines with the Ir_4 cluster $(a_1^{10}a_2^2e^{24})$ to the ground state configuration of Ir_4-S $(a_1^{12}a_2^2e^{28})$. The

corresponding energy cost was 69 kJ/mol. For the system with the Mg^{2+} cation, the sulphur was promoted to $a_1^3a_2^0e^3$, which costed only 4 kJ/mol. We see that the steric repulsion and its decomposition change, because of the different fragment electron configuration. The steric repulsion of the system with the Mg^{2+} ion is much larger than for the system without the Mg^{2+} ion, because the p_σ orbital of the sulphur atom is (partially) occupied. The system with the Mg^{2+} cation shows also a much larger π interaction. As Ir_4-S has one more π electron, the smaller π interaction indicates that this electron occupies an anti-bonding orbital. Consequently, the interaction must be with filled Ir_4 π orbitals. This result is less important for the onefold and twofold adsorption, because of the smaller overlap of the π orbitals. This may explain the difference between the onefold and twofold adsorption on the one, and the threefold adsorption on the other hand.

Table 3.6 *Threefold geometry: Energies in kJ/mol. Decomposition of ΔE_{steric} and ΔE_{int}, for optimized systems from table 3.5, built from promoted fragments. Results for systems from columns II and IV from table 3.5, which are built from ground state fragments, are given for comparison.*

fragments	Without Mg^{2+}		With Mg^{2+}	
	promoted with $S(a_1^2a_2^0e^4)$	ground state	promoted with $S(a_1^3a_2^0e^3)$	ground state
elec. config.	$a_1^{12}a_2^2e^{28}$	$a_1^{12}a_2^2e^{28}$	$a_1^{18}a_2^2e^{30}$	$a_1^{18}a_2^2e^{30}$
d(Ir-S) (Å)	2.54	2.54	2.54	2.54
ΔE_{elstat}	-708	-890	-728	-780
ΔE_{xrep}	963	1427	-1307	1369
ΔE_{steric}	399	677	713	724
ΔE_σ	-659	20	-642	-149
ΔE_π	-235	-1112	-562	-1059
ΔE_δ	-5	-3	-3	-2
ΔE_{int}	-817	-1030	-1147	-1155
ΔE_{ads}	-347	-284	-365	-362

We finally want to make some comparisons between our results and experimental results. Chan and Weinberg [23] found with LEED spectroscopy an Ir-S bond length of 2.28 Å for a threefold coordinated position. McCarty and Wise [24] published heats of adsorption from equilibrium measurements and found for sulphur adsorption on alumina-supported iridium ΔH_f^0 = -219 to -149 kJ/mol. In view of the probable differences between the experimentally studied system and ours we think that our results are in good agreement with these results.

3.4   CONCLUSIONS

We have performed density functional calculations using the Vosko-Wilk-Nussair exchange-correlation potential, including relativistic and non-local corrections, on the adsorption of sulphur on a tetrahedral Ir_4 cluster. LDA with non-local and relativistic corrections seems to give a better description than the $X\alpha$ method we used in earlier studies. We have studied the influence of a Mg^{2+} cation at the opposite end of the cluster with the sulphur atom adsorbed in three different geometries. We analyzed the results in terms of the steric repulsion and orbital interactions, as a function of the electronic configuration and the distance between the sulphur atom and the Ir_4 cluster. This gave us a tool to obtain from the decomposition of the interaction energy the contributions of the various symmetries.

We have found adsorption energies for the cluster without the cation between -289 kJ/mol for onefold and threefold geometries and -338 kJ/mol for the twofold geometry. These values are in good agreement with values found from equilibrium measurements [24]. The bonding between the metal cluster and the sulphur atom is found to be mainly caused by interaction with the p orbitals of sulphur; the interaction of p_π is slightly stronger than p_σ. The s orbitals do not play a role in the bond formation. The effect of introducing the Mg^{2+} ion is geometry dependent. The bond strength of the onefold geometry is weakened, whereas that of the threefold geometry is strengthened. The effect on the adsorption energy of the twofold geometry is small. For the twofold and threefold geometries the distance between the sulphur atom and the metal is decreased by approximately 0.12 Å. For the onefold geometry the bond length remains almost unchanged.

In previous papers, studying the adsorption of carbon monoxide, molecular and atomic hydrogen, we have explained the changes in the adsorption due to the Mg^{2+} cation, with a relatively simple electrostatic model. We could do this because the Mg^{2+} electrostatic field was dominating the changes. In the present study of sulphur the influence of the cation appears to be very similar for the onefold and the twofold geometry. For the threefold geometry however, chemical bonding effects are of more importance, which forced us to a more extensive analysis. The changes for threefold adsorption can be explained using a promoted sulphur atom which has for this geometry a more favorable π interaction with Ir_4 when Mg^{2+} is present. The overall finding that the sulphur bond strength increases when a cation is added. This is compatible with the observed larger sulphur sensitivity for metal particles in close contact with Ba^{2+} ions.

3.5   REFERENCES

[1] M. Boudart and G. Djega-Mariadassou, in: Proceedings of the 3rd International Congress on Catalysis, Vol. 2, eds. W.M.H. Sachtler, G.C.A. Schuit and P. Zwietering (North-Holland, Amsterdam, 1965).

[2] P. Gallezot, *Catal. Rev. Sci. Eng.* **20** (1979) 121.

[3] T.R. Hughes, W.C. Buss, P.W. Tamm and R.L. Jacobson, in: Proceedings of the 7th International Zeolite Conference, eds. Y. Murakami, A. Iijima and J.W. Ward (Elsevier, Amsterdam, 1986)

[4] E. Sanchez Marcos, A.P.J. Jansen and R.A. van Santen, *Chem. Phys. Lett.* **167** (1990) 399.

[5] A.P.J. Jansen and R.A. van Santen, *J. Phys. Chem.* **94** (1990) 6764.

[6] W. Biemolt, A.P.J. Jansen and R.A. van Santen, *Chem. Phys. Lett.* **180** (1991) 95 (chapter 2 of this thesis).

[7] A.P.J. Jansen and R.A. van Santen, in: Structure-Activity Relationships in Heterogeneous Catalysis, eds. R.K. Grasselli and A.W. Sleight (Elsevier, Amsterdam, 1991), 221.

[8] E.J. Baerends, D.E. Ellis and P. Ros, *Chem. Phys.* **2** (1973) 41.

[9] P.M. Boerrigter, G. te Velde and E.J. Baerends, *Int. J. Quantum Chem.* **33** (1988) 87.

[10] G. te Velde and E.J. Baerends, *J. Comput. Phys.* **99** (1992) 84.

[11] S.H. Vosko, L. Wilk, and M. Nussair, *Can. J. Phys.* **58** (1980) 1200.

[12] H. Stoll, C.M.E. Pavlidou, and H. Preuß, *Theoret. Chim. Acta* **49** (1978) 143.

[13] A.D. Becke, *J. Chem. Phys.* **88** (1988) 1053.

[14] J.G. Snijders and E.J. Baerends, *Mol. Phys.* **36** (1978) 1789.

[15] J.G. Snijders, E.J. Baerends, and P. Ros, *Mol. Phys.* **38** (1979) 1909.

[16] G. te Velde, Ph.D. Thesis (Free University of Amsterdam, Amsterdam, 1990).

[17] T. Ziegler and A. Rauk, *Theoret. Chim. Acta* **46** (1977) 1.

[18] R.W.G. Wychoff, Crystal Structures, Vol. 1, 2nd Ed. (Wiley, New York, 1963).

[19] R.C. Weast, ed. Handbook of chemistry and physics, 64th Ed. (CRC Press, Boca Raton, 1983).

[20] T.H. Upton and W.A. Goddard III, *CRC Cri. Rev. Solid State Mater. Sci.* **10** (1981) 261.

[21] D. Post and E.J. Baerends, *J. Chem. Phys.* **78** (1983) 5663.

[22] J.P. Perdew, in: Density functional methods in physics, eds. R.M. Dreizler and J. da Providencia (Plenum Press, New York, 1985).

[23] C.-M. Chan and W.H. Weinberg, *J. Chem. Phys.* **71** (1979) 3988.

[24] J.G. McCarty and H. Wise, *J. Catal.* **94** (1985) 543.

4

Potential energy surfaces for Rh-CO from DFT calculations

ABSTRACT

In this chapter we[*] present potential energy surfaces for Rh-CO obtained from density functional theory for two electronic states of Rh-CO. We have performed local spin-density calculations including relativistic as well as gradient corrections. The construction of a reasonable accurate atom-atom potential for Rh-CO is not possible. We were more successful in constructing the potential energy surfaces by representing the potential as a spherical expansion. The expansion coefficients, which are functions of the distance between the rhodium atom and the CO center of mass, can be represented by Lennard-Jones, Buckingham or Morse functions, with an error of the fit within 10 kJ/mol. The Morse potential energy surfaces predict that the electronic ground state of Rh-CO is $^2\Sigma^+$ or $^2\Delta$. This is a linear structure with an equilibrium distance of rhodium to the CO center of mass of 0.253 nm. The bonding energy is -184 kJ/mol. Further, they predict that the first-excited state is $^4A'$. This is a bent structure ($\angle$ Rh-CO = 14°) with an equilibrium distance of rhodium to the CO center of mass of 0.298 nm. The bonding energy of this state is -60 kJ/mol. Both these predictions are in good agreement with actual calculations. We found 0.250 nm with -205 kJ/mol for $^2\Sigma^+$ and 0.253 nm with -199 kJ/mol for $^2\Delta$. For $^4A'$ we found 0.271 nm, $\angle$ Rh-CO = 30° with -63 kJ/mol. The larger deviation for $^4A'$ than for $^2\Sigma^+$ or $^2\Delta$ is a consequence of the fact that the minimum for $^4A'$ is a very shallow well.

4.1   INTRODUCTION

The interaction of carbon monoxide with a transition metal surface is of enormous technological importance and of great catalytic interest. Examples where this interaction plays a crucial role are the Fischer-Tropsch synthesis of hydrocarbons [1], the catalytic production of methane [2], and automobile exhaust catalysis [3]. Because of this, the interaction between carbon monoxide and transition metals is both experimentally and theoretically intensively studied [4]. It is generally described by the Blyholder model [5]. In this model the bonding is the result of the (repulsive) donation of the 5σ orbital of carbon monoxide to empty metal levels and the (attractive) back donation from the metal to the empty $2\pi^*$ orbital of CO.

In theoretical studies, the chemisorption processes (assuming that the interaction of carbon monoxide with the surface is mainly of a local nature) has been investigated using various transition metal clusters to model the surface. The most commonly studied transition metals are nickel, copper and platinum [6]. When one is interested in quantitative correct properties the cluster model shows its limitations and care must be taken when comparing the results to experiments involving real surfaces. The calculated results will depend largely on cluster size, and the convergence as a function of cluster size is usually slow. Although the shortcomings of the cluster model are apparent, the model proves to be useful when one is interested in a qualitative description rather than quantitative accuracy. Also, the results of cluster calculations can often directly be compared with molecular beam experiments [7]. Because we only performed calculations with one transition metal atom, the calculated properties are quantitatively not correct for the carbon monoxide chemisorption on a surface. Nevertheless, it is possible to draw interesting conclusions from such model calculations, as has been shown in previous calculations using various *ab initio* methods [8, 9]. We will focus on the interaction of carbon monoxide with rhodium using density functional theory (DFT) [10]. Within DFT it is possible to obtain molecular properties which compare well with measured properties. Rhodium has a partial filled 3d shell, which is nearly degenerate with the 4s shell. This partially filled d shell gives rise to interesting catalytic properties. Carbon monoxide adsorbs molecularly on rhodium at room temperature, but dissociative adsorption occurs at reaction temperatures [11]. Because of this, rhodium is a catalyst for the synthesis of oxygenated compounds and hydrocarbons. Particular promoters, like ThO_2, MoO_3, and V_2O_5, enhance the selectivity to oxygenated compounds [12] Rhodium is also used in catalysts for motor cars for the total oxidation of carbon monoxide by incomplete oxidation of hydrocarbons. These facts motivates experimental [13] and theoretical [8, 14-17] studies of the rhodium-carbon monoxide system.

The structures of carbon monoxide adsorbed on surfaces can be probed by infrared spectroscopy. The vibrational frequencies of carbon monoxide can provide significant insight on the nature of the adsorbed carbon monoxide on the surface. The vibrational properties of CO on the surface reflect the strength of the metal-CO bonding at different sites. On rhodium, carbon monoxide adsorbs onefold, resulting in the formation of gem-dicarbonyl species.

We will present an analytic potential energy surface (PES) for Rh-CO [18, 19]. The concept of a PES, which is based on the assumption that in a molecule, electronic motion and nuclear motion are separable, is one of the important ideas in chemical physics. Much research effort is directed both to determining PES from spectroscopic data and by the methods of quantum chemistry, and to using such surfaces for dynamical calculations and the simulation of spectra. In our understanding of the dynamics of chemical reactions, at the most qualitative level the activation barrier can be understood in terms of the variation of potential energy along the reaction coordinate. At a more detailed and quantitative level, the dynamics of a chemical reaction can be understood fully in terms of motion of the nuclei on a potential energy surface. Although methods are being developed which do not use the Born-Oppenheimer surface [20], most theoretical treatment of the dynamics, whether classical, semi-classical, or quantum, still uses some form of PES. These potentials are used extensively in molecular dynamics (MD) studies. With MD methods we will be able to study, for example, the kinetics of carbon monoxide dissociation on a rhodium surface. These kinds of studies would be much more difficult, if not impossible, with the conventional cluster approach. An example of investigating the dynamics of chemisorptive processes is a trajectory study of carbon monoxide on a small copper cluster [21].

The PESs we will present here are only the first step in our attempt to describe the interaction of carbon monoxide with a rhodium surface. The interaction of carbon monoxide with only one rhodium atom is most likely not able to describe quantitatively the interaction of the substrate with the surface. We find, for example, that our PESs are not very anisotropic. For rhodium, however (like for most elements from the middle of the transition series), directional bonding is important. Preliminary calculations of carbon monoxide adsorption on some rhodium clusters indeed show larger anisotropy. We will try to achieve an improved PES by including results of the interaction of carbon monoxide with small and large rhodium clusters [22]. There are already some schemes available to incorporate an approximation to the many-atom interactions that are currently neglected by our PESs [23]. We expect that employing such a scheme to the PESs presented here will enable us to obtain a more quantitative PES for the interaction of carbon monoxide with a rhodium surface.

4.2   THEORY

4.2.1   Computational details

We performed, within the density functional formalism, spin-unrestricted calculations using the Vosko-Wilk-Nusair (VWN) local spin-density functional [24] as implemented in the Amsterdam density-functional (ADF) program system developed by Baerends et al. [25]. ADF represents the molecular orbitals as linear combinations of atomic Slater- type orbitals (STOs), computes the integrals numerically [26], and computes the bonding energies with the Ziegler transition state method [27]. The bonding energy ΔE_b is defined as the energy difference between the fragments (A and B) and the overall molecule (AB)

$$\Delta E_b = E(AB) - E(A) - E(B). \qquad (4.1)$$

It can be separated into two different contributions

$$\Delta E_b = \Delta E_{steric} + \Delta E_{int}. \qquad (4.2)$$

Here ΔE_{steric}, referred to as the steric repulsion, is the energy change due to superposition of the fragments A and B without changing their molecular orbitals. ΔE_{int}, the interaction energy, represents the energy change upon the formation of the molecular orbitals of A-B. The steric interaction can be split as

$$\Delta E_{steric} = \Delta E_{xrep} + \Delta E_{elstat}, \qquad (4.3)$$

which are the exchange repulsion and the electrostatic interactions, respectively. This decomposition of the bonding energy can be useful for analyzing a chemical bond [28].

Table 4.1   *Exponents ζ of the STO's for rhodium, carbon and oxygen.*

	type	ζ		type	ζ		type	ζ	
Rh	1S	29.25	core	4D	1.30	valence	2P	0.96	valence
	2S	19.00	core	4D	2.50	valence	2P	2.20	valence
	3S	7.85	core	4D	4.40	valence	3D	2.50	valence
	4S	6.05	core	5S	1.05	valence O	1S	7.36	core
	2P	19.47	core	5S	1.95	valence	2S	1.70	valence
	3P	9.09	core	5P	1.45	valence	2S	2.82	valence
	4P	4.07	core C	1S	5.40	core	2P	1.30	valence
	3D	11.00	core	2S	1.24	valence	2P	3.06	valence
				2S	1.98	valence	3D	2.00	valence

To go beyond the local spin-density approximation (LSDA), we used gradient corrections (or non-local corrections) to the bonding energy by Becke [29, 30] for the exchange and by Perdew [31] for correlation, or we used the correlation self-interaction correction due to Stoll et al. [32, 33] Relativistic corrections were included by using a relativistic core, including relativistic effects on the valence electrons as perturbation to first order [34].

For rhodium we tested two different basis sets. In the first set, the electrons up to and including the 4p core were frozen, leaving nine valence electrons. The valence functions were of double-ζ quality with a triple-ζ d. In the second set, the electrons up to and including the 3d core were frozen, leaving 17 valence electrons. In this set, the valence functions were of triple-ζ quality with a double-ζ s function. The basis sets show only small differences. We thus decided to use the first one for all the further calculations because it is smaller. For carbon and oxygen the 1s core was frozen. Here the valence functions are again of double-ζ quality. For all three atoms, a polarization function was added to the basis set. Single-ζ functions were used for core orthogonalization. Table 4.1 shows the exponents of the STO basis sets for rhodium, carbon, and oxygen we used.

4.2.2 The representation of the potential

There are a number of methods for constructing analytical potential energy surfaces (PESs) for triatomic systems [35]. The simplest is the construction of an atom-atom potential [see fig. 4.1(a) for the coordinates].

$$\Delta E_b = V_{RhC}(R_{RhC}) + V_{RhO}(R_{RhO}) + C. \tag{4.4}$$

We have added a parameter C in eq. (4.4) to describe excited states.
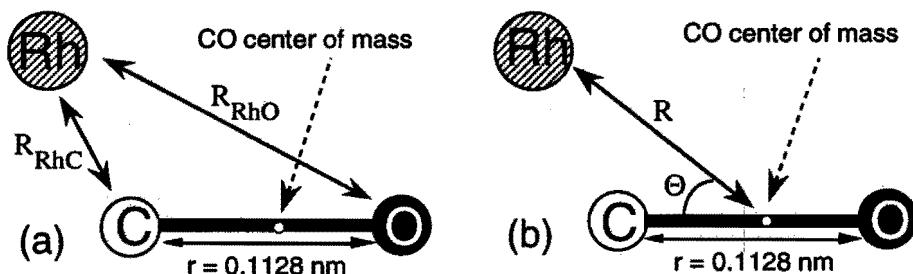
Fig. 4.1 *The Rh-CO system with the definition of (a) R_{RhC} and R_{RhO} as used in the development of an atom-atom potential, and (b) R and Θ as used in a spherical expansion.*

The second method is the spherical expansion. Fixing the carbon monoxide bond length, we can specify the Rh-CO system by a distance R and an angle Θ [fig. 4.1(b)]. In general, an energy $V(R, \Theta)$ [e.g., bonding energy, exchange repulsion, electrostatic or orbital interaction, eqs. (4.1)-(4.3)] can then be expanded in an infinite sum of Legendre polynomials,

$$V(R, \Theta) = \sum_{\ell=0}^{\infty} a_\ell(R)\, P_\ell(\cos\Theta). \tag{4.5}$$

Using a Gauss-Legendre (GL) quadrature [36, 37] of order n, we can compute all expansion coefficients *exactly* for ℓ = 0, 1, 2, ..., n-1. We use n = 10. This is slightly larger than necessary. Within the accuracy of our DFT calculations, an "exact" representation is obtained by restriction on the summation in eq. (4.5) to terms $\ell \leq 8$. The R dependence of the expansion coefficients is determined in a least-squares fit with weights. For the bonding energy, we tried three different functions: a Lennard-Jones form,

$$a_\ell(R) = \frac{A_\ell}{R^{12}} - \frac{B_\ell}{R^6} + C\delta_{0\ell}, \tag{4.6a}$$

a Buckingham form,

$$a_\ell(R) = A_\ell\, e^{-\alpha_\ell R} - \frac{B_\ell}{R^6} + C\delta_{0\ell}, \tag{4.6b}$$

and a Morse form

$$a_\ell(R) = A_\ell\, e^{-2\alpha_\ell R} - B_\ell\, e^{-\alpha_\ell R} + C\delta_{0\ell}. \tag{4.6c}$$

In our case, the least-squares fit with weights to obtain the parameters in these functions was done on the coefficients a_ℓ calculated for ten distances (R = 0.150, 0.175, 0.200, 0.225, 0.250, 0.275, 0.300, 0.325, 0.350 and 0.375 nm). The term $C\delta_{0\ell}$ in these functions originates from the fact that for R $\rightarrow \infty$ the excited state PES should converge to the excitation energy of rhodium from the ground state ^4F ($4d^8\, 5s^1$) to the first excited state ^2D ($4d^9$).

4.3   RESULTS AND DISCUSSION

4.3.1   The rhodium atom and the carbon monoxide molecule

Before starting with DFT calculations on Rh-CO, some variations of DFT were tested on rhodium and carbon monoxide. We concentrated on the electronic ground state and excitation energies of the rhodium atom, and bonding energy, equilibrium distance, vibration frequency, and dipole moment of the carbon monoxide molecule. All these properties are experimentally well known. Results for a number of excitation energies and the ionization potential of rhodium are listed in table 4.2. The results for carbon monoxide are shown in table 4.3.

Table 4.2   *Rh excitation energies (in kJ/mol) calculated at the local and non-local level.*

atom/ion	config.	State	local level	Perdew+Becke	Stoll+Becke	Exp.[a]
Rh	$s^1 d^8$	^4F	0	0	0	0
	$s^0 d^9$	^2D	3	12	7	34
	$s^2 d^7$	^4F	190	187	177	163
Rh$^+$	$s^0 d^8$	^3F	0	0	0	0
	$s^1 d^7$	^5F	209	207	199	206
IP			789	780	743	720

[a] Experimental values are averaged over J-states.

From table 4.2 we can see that our unrestricted calculations, including relativistic corrections, are able to yield the correct ground state for the rhodium atom: Rh($d^8 s^1$; ^4F), whereas LSDA usually gives a $4d^9$ configuration as ground state [38]. This would lead to underestimates of the metal-carbon monoxide bonding energy [39]. The first-order relativistic approach used here is adequate for the calculation of bond energies in compounds containing elements as heavy as gold (Z = 79) [40], so we expect that the use of more sophisticated relativistic methods would not greatly alter our results. The result obtained without any gradient corrections shows little difference between the two states. When gradient corrections for the exchange (Becke) and correlation (Perdew) are included, the excitation energy improves. Replacing the Perdew correction with the Stoll correction lowers the calculated excitation energy somewhat. Table 4.2 also shows the excitation energy from the ground state to Rh($d^7 s^2$; ^4F), and from the ionic ground state Rh$^+$(d^8; ^3F) to Rh$^+$($d^7 s^1$; ^5F) and the ionization potential. In general, the best agreement is obtained when we use VWN with Stoll and Becke correction.

Table 4.3   *Equilibrium distance (R_e), dissociation energy (D_e), dipole moment (μ) and stretch frequency (ω_e) for CO calculated at the local and non-local level.*

LSD & corrections	R_e (nm)	D_e (kJ/mol)	μ (Debye)	ω_e (cm^{-1})
VWN	0.1130	-1247	0.05	2209
VWN+Perdew+Becke	0.1138	-1148	0.02	2146
VWN+Stoll+Becke	0.1144	-1151	0.04	2096
Experiment [42] [a]	0.1128	-1077	0.11	2143[b]-2170[c]

[a] D.R. Lide, *Handbook of Chemistry and Physics*, 71st ed. (CRC Press, Boca Raton, 1990).

[b] Measured; [c] Harmonic: K.P. Huber and G. Herzberg, *Molecular Spectra and Molecular Structure. Constants of Diatomic Molecules* (Van Nostrand-Reinhold, New York, 1979).

Table 4.3 shows the calculated equilibrium distance, dissociation energy, dipole moment and stretch frequency for carbon monoxide. Except for the dissociation energy, these properties do not vary much with the various methods or corrections we used. The influence of relativistic corrections for light atoms such as carbon and oxygen is negligible. Spin-orbit effects do occur, but as our implementation only includes relativistic effects as a first-order perturbation on the core electrons, spin-orbit effect are neglected. The basis set effects in carbon monoxide were already studied in detail [41]. This demonstrated the need of adding a single 3d-polarization to get close to converged basis results. Using a triple-ζ (TZ) or quadruple-ζ (QZ) basis for carbon monoxide did not have as much effect as adding a single 3d polarization function. Only for the dipole moment TZ or QZ bases are necessary. For the remaining calculations on Rh-CO, we have used VWN with Stoll and Becke correction.

4.3.2 The rhodium-carbon monoxide system

For ten different distances, and for ten different angles Θ, the cosines of which are the roots of the tenth-order Legendre polynomial [36], we calculated for both electronic configurations the exchange repulsion [eq. (4.3)], the electrostatic interaction [eq. (4.3)], the orbital interaction [eq. (4.2)], and the bonding energy [eq. (4.1)]. The smallest distance ($R = 0.150$ nm) was chosen so that the interaction of carbon monoxide with the rhodium at each of the ten angles Θ was repulsive. For small Rh-CO distances the ground state is a doublet ($^2\Sigma^+$ or $^2\Delta$ for the linear geometry, ^{2}A' otherwise), corresponding to the 4d^9 configuration of rhodium. For larger Rh-CO distances the quartet ($^4\Delta$ for linear geometries, ^{4}A' otherwise), corresponding to the 4d^8 5s^1 configuration of rhodium, is the lowest. This is in agreement with the ground states of the rhodium atom and the carbon monoxide molecule separated at infinity. In contrast to earlier calculations by Koutecky et al., who found that the $^4\Delta$ state was repulsive at every distance [8], we find the ^{4}A' state to be slightly bonding. Mains and White [15] have found an optimized linear geometry for the quartet, which they call ^{4}X, but they only report on the total energy.

The C-O distance (r) was fixed at 0.1128 nm [42] in all of our calculations on the rhodium-carbon monoxide system. Neglecting different r's for carbon monoxide might be a source of error to the PES that we want to develop because the carbon monoxide bond is expected to relax upon the bond formation of carbon monoxide with the rhodium (because of the electron donation from rhodium into the $2\pi^*$ orbitals of carbon monoxide). Therefore, we tested the approximation of fixing r by calculating near the equilibrium geometry of the $^2\Sigma^+$ ground state of Rh-CO (the $^2\Delta$ state lies 7 kJ/mol higher near the equilibrium geometry) the formation energy of Rh-CO from the separate atoms for several C-O distances. We found that

the carbon oxygen bond indeed relaxes significantly, from 0.1128 nm to approximately 0.117-0.118 nm. However, the change in bonding energy is relatively small. For geometries further away from the equilibrium geometry of the $^2\Sigma^+$ ground state (or of the $^2\Delta$ state) of Rh-CO, we expect that the influence of CO relaxation is even smaller, concluding that we do not introduce a large error when we neglect this degree of freedom in our PES development. Also, at this moment we are not interested in the dissociation of carbon monoxide.

4.3.3 The rhodium-carbon monoxide potential energy surfaces

We tried to obtain an atom-atom potential [eq. (4.4), where both V_{RhC} and V_{RhO} are Lennard-Jones form functions, eq. (4.6a)] because they are widely used and more easy to apply in molecular dynamics (MD) calculations. The development of such an atom-atom potential was less successful than the results we obtained by representing the potential as a spherical expansion. The parameters for the atom-atom potential we obtained are shown in table 4.4, and those for the spherical expansion in tables 4.5 and 4.6. These results are obtained by a least-squares fit with weights. The weights are proportional to $e^{-E/\varepsilon}$, where $\varepsilon = 81$ kJ/mol. The weights were necessary because, especially for $R = 0.150$ nm and small or large Θ, the rhodium atom is close to the carbon or the oxygen atom. This yields a strong repulsion, which would completely determine a fit without the weights. While using weights, the fit is only incorrect at the irrelevant geometries where there is an extremely strong repulsion. The value of ε is somewhat arbitrary. The initial value we used was 324 kJ/mol, but we also tried 243 kJ/mol, 162 kJ/mol and 81 kJ/mol. We tried to find the best value for ε that gives a good fit around the minima and for large R, whereas all essential characteristics of the repulsive part of the PESs are retained. In the weighted fit of our atom-atom potential, $\varepsilon = 81$ kJ/mol seems to be the best value. For larger values of ε, we get a very bad fit, whereas for smaller values of ε the repulsive part of the PESs vanishes completely. Despite the use of weights, the root-mean-square (rms) deviation of this Lennard-Jones type of fit was around 35 kJ/mol for the doublet and 9 kJ/mol for the quartet. For the doublet this is too large. Moreover, the equilibrium geometry for the doublet and the quartet is inaccurate. This can be seen from table 4.7, which shows a poor comparison between the PESs and the actual calculated minima. Other analytical forms do not really yield a better result. It is possible to derive expressions, using variational calculus, for the optimal atom-atom potentials V_{RhC} and V_{RhO} in terms of the bonding energy ΔE_b by minimization of

$$\int dR_{RhC}\, dR_{RhO}\, w(R_{RhC}, R_{RhO}) \times$$

$$\left[\Delta E_b(R_{RhC}, R_{RhO}) - V_{RhC}(R_{RhC}) - V_{RhO}(R_{RhO}) \right]^2 \qquad (4.7)$$

where $w(R_{RhC}, R_{RhO})$ is some weight function. The integral is over all realizable combinations of R_{RhC} and R_{RhO}. The resulting expressions can be evaluated numerically, yielding numerical representations for V_{RhC} and V_{RhO} [43]. We found that this procedure gave only potentials that were marginally better than the atom-atom Lennard-Jones, thus proving that an atom-atom potential is not suited for Rh-CO.

Table 4.4 Atom-atom potential parameters for the LJ expansion functions. C is 0 for ^{4}A' and 10 kJ/mol for ^{2}A'. The rms errors are 35 and 9 kJ/mol for the doublet and quartet, respectively.

Parameter	^{2}A' state	^{4}A' state
A_{RhC} (kJ/mol·nm^{12})	$1.302 \cdot 10^{-7}$	$8.502 \cdot 10^{-8}$
B_{RhC} (kJ/mol·nm^6)	$8.986 \cdot 10^{-3}$	$1.571 \cdot 10^{-3}$
A_{RhO} (kJ/mol·nm^{12})	$-4.553 \cdot 10^{-8}$	$-4.505 \cdot 10^{-8}$
B_{RhO} (kJ/mol·nm^6)	$-7.276 \cdot 10^{-3}$	$-1.039 \cdot 10^{-3}$

We tried with the functional forms of eqs. (4.6a)-(4.6c) to fit our data with a global rms error lower than 10 kJ/mol. The results for the separate contributions to the bonding energy [eqs. (4.2) and (4.3)] are not presented here because our attempts to fit these were not satisfactory. The exchange repulsion could be fitted to a high degree of accuracy using

$$a_\ell(R) = A_\ell e^{-\alpha_\ell R}. \tag{4.8}$$

However, fits of the two other contributions to the bonding energy, the electrostatic interaction [eq. (4.3)] and the orbital interaction [eq. (4.2)], were less successful because we could not find a suitable functional form. The best rms error of both of these fits was well above 10 kJ/mol. There are functional forms that are derived for these interactions between systems at large distances [44], but these need not be appropriate when the orbitals of rhodium and carbon monoxide overlap. Damping functions have been suggested to improve the description for small R [45]. However, we find that, at least for the electrostatic interaction, the interaction increases rather than decreases for decreasing distances. Because the knowledge of the separate contributions to the bonding of carbon monoxide on rhodium is not essential for our further study, we will focus only on the bonding energy.

The results of the fit of the total bonding energy with Buckingham [eq. (4.6b)] and Morse [eq. (4.6c)] are shown in tables 4.5 and 4.6, respectively. These results are obtained by a least-squares fit with weights. The weights are proportional to $e^{-E/\varepsilon}$, where $\varepsilon = 162$ kJ/mol for the Buckingham and $\varepsilon = 243$ kJ/mol for the Morse fit. Also in these cases we tried to use the largest value of ε that gives a good fit around the minima and for large R, whereas all essential characteristics of the repulsive part of the PESs are retained.

Table 4.5   Parameters for the Buckingham spherical expansion functions. C is 0 for $^4A'$ and set to 33.77 kJ/mol for $^2A'$ [46]. rms errors are 13 and 10 kJ/mol for the doublet and quartet, respectively.

ℓ	$^2A'$ state			$^4A'$ state		
	A (kJ/mol)	B (kJ/mol)	α (nm^{-1})	A (kJ/mol)	B (kJ/mol)	α (nm^{-1})
0	$4.495 \cdot 10^6$	$2.087 \cdot 10^{-2}$	$4.663 \cdot 10^1$	$9.525 \cdot 10^5$	$-7.161 \cdot 10^{-4}$	$4.097 \cdot 10^1$
1	$9.439 \cdot 10^5$	$3.653 \cdot 10^{-2}$	$3.788 \cdot 10^1$	$6.291 \cdot 10^5$	$2.211 \cdot 10^{-2}$	$3.846 \cdot 10^1$
2	$7.198 \cdot 10^6$	$2.857 \cdot 10^{-2}$	$4.626 \cdot 10^1$	$1.214 \cdot 10^7$	$6.097 \cdot 10^{-3}$	$5.109 \cdot 10^1$
3	$4.274 \cdot 10^5$	$1.347 \cdot 10^{-2}$	$3.728 \cdot 10^1$	$2.244 \cdot 10^5$	$5.912 \cdot 10^{-3}$	$3.582 \cdot 10^1$
4	$6.889 \cdot 10^5$	$8.120 \cdot 10^{-3}$	$4.069 \cdot 10^1$	$6.762 \cdot 10^5$	$-5.125 \cdot 10^{-4}$	$4.351 \cdot 10^1$
5	$9.060 \cdot 10^5$	$-1.219 \cdot 10^{-3}$	$5.978 \cdot 10^1$	$3.981 \cdot 10^4$	0	$3.602 \cdot 10^1$
6	$3.080 \cdot 10^5$	$-1.424 \cdot 10^{-5}$	$4.933 \cdot 10^1$	$4.631 \cdot 10^4$	0	$3.651 \cdot 10^1$
7	$1.566 \cdot 10^6$	$-1.193 \cdot 10^{-4}$	$6.701 \cdot 10^1$	$6.452 \cdot 10^5$	0	$6.068 \cdot 10^1$
8	$1.755 \cdot 10^6$	$-2.010 \cdot 10^{-4}$	$7.359 \cdot 10^1$	$1.005 \cdot 10^5$	$-1.209 \cdot 10^{-4}$	$5.341 \cdot 10^1$

Table 4.6   Parameters for the Morse spherical expansion functions. C is 0 for $^4A'$ and set to 33.77 kJ/mol for $^2A'$. [46] rms errors are 11 and 10 kJ/mol for the doublet and quartet, respectively.

ℓ	$^2A'$ state			$^4A'$ state		
	A (kJ/mol)	B (kJ/mol)	α (nm^{-1})	A (kJ/mol)	B (kJ/mol)	α (nm^{-1})
0	$1.865 \cdot 10^6$	$1.880 \cdot 10^4$	$2.166 \cdot 10^1$	$7.129 \cdot 10^7$	$-6.036 \cdot 10^5$	$3.873 \cdot 10^1$
1	$1.522 \cdot 10^4$	$2.236 \cdot 10^3$	$1.236 \cdot 10^1$	$1.868 \cdot 10^4$	$2.027 \cdot 10^3$	$1.404 \cdot 10^1$
2	$2.713 \cdot 10^6$	$2.338 \cdot 10^4$	$2.114 \cdot 10^1$	$4.296 \cdot 10^6$	$1.093 \cdot 10^4$	$2.292 \cdot 10^1$
3	$7.290 \cdot 10^4$	$2.250 \cdot 10^3$	$1.575 \cdot 10^1$	$7.951 \cdot 10^4$	$1.099 \cdot 10^3$	$1.613 \cdot 10^1$
4	$3.077 \cdot 10^5$	$3.456 \cdot 10^3$	$1.903 \cdot 10^1$	$4.298 \cdot 10^5$	$3.657 \cdot 10^2$	$2.028 \cdot 10^1$
5	$2.275 \cdot 10^6$	$-1.515 \cdot 10^4$	$3.298 \cdot 10^1$	$2.649 \cdot 10^5$	$-3.931 \cdot 10^3$	$2.606 \cdot 10^1$
6	$1.659 \cdot 10^7$	$-2.448 \cdot 10^5$	$4.808 \cdot 10^1$	$2.604 \cdot 10^5$	$-3.695 \cdot 10^3$	$2.562 \cdot 10^1$
7	$3.056 \cdot 10^7$	$-3.482 \cdot 10^4$	$4.525 \cdot 10^1$	$5.016 \cdot 10^6$	$-6.778 \cdot 10^3$	$3.836 \cdot 10^1$
8	$7.684 \cdot 10^5$	$-2.016 \cdot 10^3$	$3.355 \cdot 10^1$	$1.132 \cdot 10^6$	$-5.700 \cdot 10^3$	$3.648 \cdot 10^1$

We also determined a fit of Lennard-Jones type [eq. (4.6a)], with $\varepsilon = 81$ kJ/mol, but the results for the doublet and quartet states of Rh-CO are rather poor. The rms error in bonding energy was 65 kJ/mol for the doublet state, and 18 kJ/mol for the quartet state. The results using Buckingham or Morse functions are much better. For the doublet state we find rms errors of 13 and 11 kJ/mol, and for the quartet state we find rms errors of 10 and 10 kJ/mol, respectively for Buckingham (table 4.5) and Morse (table 4.6). Note that for all potential forms the usual attractive part of the potential is sometimes used to fit repulsion. For the fit

involving Buckingham functions, we were in some case unable to use both terms to fit repulsion; in such cases the R^{-6} was removed from the fit (fixed to zero). Contour plots of the two potential energy surfaces which we obtained with the Morse fit [eq. (4.6c)] are shown in fig. 4.2. The difference between the two surfaces at infinite separation of the rhodium atom from the carbon monoxide molecule is set to exactly 33.77 kJ/mol. This is the experimental difference, averaged over J states, of $Rh(d^8s^1 ; {}^4F)$ and $Rh(d^9; {}^2D)$, and we fitted with this constraint [46]. The rms deviation for the Morse fit was the smallest, around 10 kJ/mol.

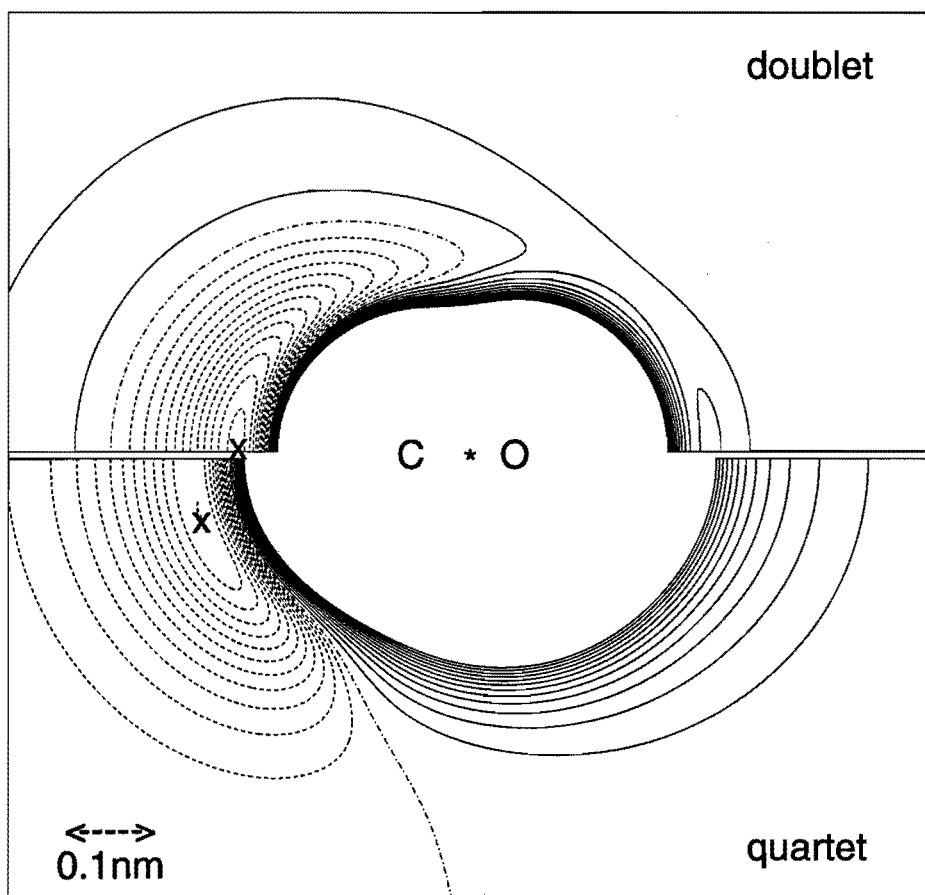**Fig. 4.2**   *Contour plot of the PESs for Rh-CO. Solid lines are positive, and dashed lines negative energies. The '*' is the CO center of mass, a 'X' is the position of a minimum. The energy difference between two neighboring contours is 15 kJ/mol for the doublet, and 5 kJ/mol for the quartet. The doublet (top) goes to 33.77 kJ/mol at infinite Rh-CO separation, the quartet (bottom) to 0 kJ/mol.*

For the remaining part of this discussion, we will concentrate on the PES which we obtained by fitting to the Morse function (table 4.6 and fig. 4.2) because this gave the best fit. We will compare our results with quantum-chemical calculations (table 4.7). This PES predicts that the ground state of Rh-CO is $^2\Sigma^+$ or $^2\Delta$, the linear geometry, with a bonding energy of -184 kJ/mol and with an equilibrium distance of rhodium to the CO center of mass of 0.253 nm. The first excited state is predicted to be ^{4}A', this is a bent structure ($\angle$ Rh-CO = 14°) with a bonding energy of -66 kJ/mol and with an equilibrium distance of rhodium to the carbon monoxide center of mass of 0.298 nm. Additional DFT calculations around the PES minima show that the fit is reasonable (compare the last two rows of table 4.7). The geometry of the quartet minimum is shallow, and larger deviations between DFT and the PES than for the doublet are to be expected.

Table 4.7   *Geometries and binding energies for Rh-CO; from previous studies and this study.*

Method	Remarks	C-O (nm)	$^2\Sigma^+$ or $^2\Delta$ state [a] ($\Theta = 0°$) Rh-C (nm)	ΔE_b (kJ/mol)	^{4}A' state Rh-C (nm)	Θ	ΔE_b (kJ/mol)
SCF-CI	Ref. [8]	0.116	0.205	-17	all	0°	repulsive
HF	Ref. [14]	0.1141[b]	0.1865[b]	-18	—	—	—
MP2	Ref. [14]	0.1141[b]	0.1865[b]	-231	—	—	—
MP3	Ref. [14]	0.1141[b]	0.1865[b]	-174	—	—	—
INDO	Ref. [16]	0.1190	0.1898	-153	—	—	—
DFT	Ref. [17]	0.1169	0.1758	-257	—	—	—
PES	Atom-Atom	0.1128[c]	0.233	-153	0.277	0°	-15
PES	Lennard-Jones	0.1128[c]	0.180	-91	—	—[d]	-34
PES	Buckingham	0.1128[c]	0.185	-188	0.231	10°	-58
PES	Morse	0.1128[c]	0.188	-184	0.236	14°	-60
DFT	ADF	0.1128[c]	0.185	-205	0.218	30°	-63
DFT	ADF [e]	0.1128[c]	0.182	-199	—	—	—

[a] Ref. [14] report that the ground state of Rh-CO is $^2\Delta$, all other studies predict $^2\Sigma^+$ as ground state.

[b] Geometry is optimized at the Hartree-Fock level only.

[c] The C-O distance was kept fixed, the optimized C-O distance is approximately 0.117 nm.

[d] The equilibrium geometry is at a very large R value. As this is clearly not correct, we did not try to determine it accurately. As the minimum in the PES is very shallow the depth could be determined.

[e] Results for the $^2\Delta$ state, we found that this state is slightly higher in energy than the $^2\Sigma^+$ state.

The values for the bonding energy of carbon monoxide to rhodium seem to be somewhat too large compared with experimental values for CO adsorption on single crystals of rhodium. On the Rh-CO molecule itself, only a few theoretical investigations have been carried out, and it has not been observed yet experimentally. The initial heat of chemisorption of carbon monoxide was measured to be approximately -180 kJ/mol [47]. However, various studies indicate that this value might be too high. More recent measurements for the desorption energy of carbon monoxide from an onefold site yielded a bonding energy of about -120 kJ/mol for the Rh(100) surface and about -130 kJ/mol for the Rh(111) surface [48-50]. Preliminary calculations of carbon monoxide adsorption on large rhodium clusters give a lower adsorption energy, in agreement with experimental results. Hence, we feel confident that our results for one rhodium atom are fair.

It seems that there are no reliable *ab initio* results available for comparison with our DFT results [51]. Former *ab initio* calculations give puzzling results. The calculations by Koutecky et al. [8] as well as by McKee and Worley [14] (who report the $^2\Delta$ state as the ground state) show also a much smaller value for the carbon monoxide bonding energy on rhodium. The first study, a non-empirical valence-only self-consistent field (SCF) configuration interaction (CI) procedure with inclusion of electron correlation effects according to the multireference double excitations (MRD) CI procedure, showed a bonding energy of only -17 kJ/mol. This is almost the same result as the second study, which showed that at the Hartree-Fock (HF) level, while using a relativistic effective core potential (RECP) for rhodium, the bonding energy of carbon monoxide on rhodium is -18 kJ/mol. Adding electron correlation via Møller-Plesset perturbation treatment increases the bonding energy to -231 kJ/mol (MP2) and -174 kJ/mol (MP3). All electron and RECP HF studies for the $^2\Sigma^+$ and $^4\Delta$ states of Rh-CO have also been presented by Mains and White [15], but no correlation effects were included in their calculations. Their unrestricted Hartree-Fock (UHF) dissociation energy into CO and the ^{2}D atom is only 7 kJ/mol. Unlike the other theoretical studies we know of, they also report on a quartet state, which they labeled ^{4}X. Their optimum geometry is, however, linear. The intermediate neglect of differential overlap (INDO) calculations of Estiu and Zerner [16] yield a bonding energy of -153 kJ/mol, after they corrected the result by 240 kJ/mol to account for the overestimation of bonding energies by the INDO method. Finally, the DFT calculation of Pápai et al. [17] resulted in a bonding energy of -257 kJ/mol. Their method, implemented in the deMon program [52], uses Gaussian-type orbitals (GTOs). The results they find for Rh, Rh$^+$, and Rh-CO compare reasonable with ours. In general, DFT results show somewhat larger bonding energies than the other calculations. At the optimized geometries for Rh-CO, we found for the doublet ($^2\Sigma^+$) a steric repulsion of 604 kJ/mol and an orbital interaction of -809 kJ/mol [eq. (4.2)] resulting in a total bonding energy of

-205 kJ/mol. For the quartet (^{4}A') we calculated 246 kJ/mol for the steric repulsion and -310 kJ/mol for the orbital interaction, yielding a total bonding energy of -64 kJ/mol. Both these bonding energy decompositions are relative to the unrestricted fragments in their ground state. For the rhodium atom, this is the ^{4}F state and for the carbon monoxide molecule it is the $^1\Sigma^+$ state.

Table 4.7 also gives the Rh-C and the C-O bond lengths. The C-O bond length indicates to some extent the amount of rhodium to carbon monoxide backbonding. Typical Rh-C bond lengths are in the range 0.178-0.201 nm [53]. This is in good agreement with the Rh-C bond length of 0.185 nm that we found for the $^2\Sigma^+$ ground state and the 0.188 nm that we found for the $^2\Delta$ state. The *ab initio* study by McKee and Worley [14] found the $^2\Delta$ state as ground state with an optimum Rh-C bond length of 0.1865 nm, but there the C-O bond length had increased to only 0.1142 nm. The INDO calculations of Estiu and Zerner [16] yield a Rh-C distance of 0.1898 nm together with a C-O distance of 0.1190 nm. The DFT calculation of Pápai et al. [17] resulted in an optimized Rh-C distance of 0.1758 nm with a C-O separation of 0.117 nm. In our calculations the C-O bond length increases to 0.117-0.118 nm.

4.4   CONCLUSIONS

We have calculated two PESs for the interaction of carbon monoxide with a rhodium atom using DFT. The PESs correspond to the electronic ground state at short and large Rh-CO distances, respectively. At short distances the system is a doublet, and at large distances it is a quartet. It was necessary to do unrestricted calculations, which include gradient as well as relativistic corrections. It could be proven that atom-atom potentials were not appropriate to describe this system. The PESs could be fitted best with a spherical expansion and Morse forms for the expansion coefficients.

It seems that no reliable *ab initio* result for Rh-CO are available for comparison and for judging the performance of our DFT results. The two previous *ab initio* studies [8, 14] give puzzling results. We found somewhat larger bonding energies than most previous calculations. This may be due to the common overestimation of bonding energies in DFT, even though we have included gradient corrections. Our results agree reasonably well with previous DFT calculations on Rh-CO[17]. We think, however, that we cannot exclude the possibility that other calculations may have underestimated the correlation in Rh-CO. The large contributions of the different orders of perturbation theory [14] seem to point in that direction. The INDO results [16] seem to be in remarkable agreement with both DFT calculations on Rh-CO.

Preliminary calculations (using the same methods as in this chapter) on the interaction of carbon monoxide with some rhodium clusters show reasonable agreement with experiments, substantiating our results for Rh-CO. Comparing the same calculations with predictions by the PESs presented here, it seems that our PESs are not anisotropic enough. This shows the need to improve the PESs presented here. Using the results for the interaction of carbon monoxide with rhodium clusters, we want to incorporate the many-atom interactions that are currently neglected by our PESs at an approximate way. We expect that this will enable us to obtain a more quantitative PES for the interaction of carbon monoxide with a rhodium surface.

4.5 REFERENCES

[1] R. Bernard, H. Koelbel and M. Ralek, *The Fischer-Tropsch synthesis* (Academic Press, London, 1984); J. Eilers, S.A. Posthuma and S.T. Sie, *Catal. Lett.* 7 (1990) 253; S.T. Sie, M.M.G. Senden and H.M.H. van Wechem, *Catal. Today* 8 (1991) 371.

[2] G.A. Mills and F.W. Steffen, *Catal. Rev.* 8 (1973)189 .

[3] K.C. Taylor, in *Catalysis*, vol. 5, edited by J.R. Anderson and M. Boudart (Springer, Berlin, 1984) p. 119; Studies in Surface Science and Catalysis 30: *Catalysis and Automotive Pollution Control*, edited by A. Crucq and A. Frennet (Elsevier, Amsterdam, 1987); Studies in Surface Science and Catalysis 71: *Catalysis and Automotive Pollution Control II*, edited by A. Crucq (Elsevier, Amsterdam, 1991).

[4] J.C. Campuzano, in *The Chemical Physics of Solid Surfaces and Heterogeneous Catalysis* (vol. 3 Chemisorption Systems, Part A) D.A. King and D.P. Woodruff, Eds. (Elsevier, Amsterdam 1990) p. 389.

[5] G. Blyholder, *J. Phys. Chem.* 68 (1964) 2772.

[6] P.S. Bagus and K. Hermann, *Surf. Sci.* 89 (1979) 588; P.S. Bagus, C.J. Nelin and C.W. Bauschlicher Jr., *Phys. Rev. B* 28, 5423 (1983); P.S. Bagus, K. Hermann and C.W. Bauschlicher Jr., *Ber. Bunsenges. Phys. Chem.* 88 (1984)302; C.W. Bauschlicher Jr., P.S. Bagus, C.J. Nelin and B. Roos, *J. Chem. Phys.* 85 (1986)354.

[7] M.R. Zakin, D.M. Cox and A.P. Kaldor, *J. Chem. Phys.* 89 (1988) 1201.

[8] J. Koutecky, G. Pacchioni and P. Fantucci, *Chem. Phys.* 99 (1985) 87.

[9] G.W. Smith and E.A. Carter, *J. Phys. Chem.* 95 (1990) 2327; R. Fournier, *J. Chem. Phys.* 98 (1993) 8041.

[10] R.G. Parr and W. Yang, *Density-functional theory of atoms and molecules* (Oxford University Press, New York, 1989).

[11] J.R. Katzer, A.W. Sleigh, P. Gajardo, J.B. Michel, E.F. Gleason and S. McMillan, *Faraday Disc. Chem. Soc.* **72** (1981) 121.

[12] T. Koerts, W.J.J. Welters and R.A. van Santen, *J. Catal.* **134** (1992) 1; T. Koerts and R.A. van Santen, *J. Catal.* **134** (1992) 13; T. Koerts and R.A. van Santen, *Catal. Lett.* **6** (1990) 49.

[13] K.C. Cannon, S.K. Jo and J.M. White, *J. Am. Chem. Soc.* **111** (1989) 5064; R. Dictor, S. Roberts, *J. Phys. Chem.* **93** (1989) 5846; M. Bowker, Q. Guo and R.W. Joyner, *Surf. Sci.* **280** (1993) 50; M. Bowker, Q. Guo, Y. Li and R.W. Joyner, *Catal. Lett.* **18** (1993) 119; V.R. Dhanak, A. Baraldi, G. Comelli, G. Paolucci, M. Kiskinova and R. Rosei, *Surf. Sci.* **295** (1993) 287.

[14] M.L. McKee, C.H. Dai and S.D. Worley, *J. Phys. Chem.* **92** (1988) 1056; M.L. McKee and S.D. Worley, *J. Phys. Chem.* **92** (1988) 3699.

[15] G.J. Mains and J.M. White, *J. Phys. Chem.* **95** (1991) 112.

[16] G.L. Estiu and M.C. Zerner, *Int. J. Quantum Chem.: Quantum Chem. Sym.* **26** (1992) 587.

[17] I. Pápai, A. Goursot, A. St-Amant and D.R. Salahub, *Theoret. Chim. Acta* **84** (1992) 217.

[18] D.M. Hirst, *Potential Energy Surfaces* (Taylor & Francis, Basingstoke, 1984).

[19] J.N. Murrell, S. Carter, S.C. Farantos, P. Huxley and A.J.C. Varandas, *Molecular Potential Energy Functions* (John Wiley & Sons, Chichester, 1984).

[20] R. Kosloff, *J. Phys. Chem.* **92** (1988) 2087.

[21] J.E. Adams, *J. Chem. Phys.* **92** (1990) 1849.

[22] W. Biemolt, A.P.J. Jansen and R.A. van Santen, in chapter 6 of this thesis.

[23] A. Carlsson, in *Solid State Physics*, Vol 43, H. Ehrenreich and D. Turnbull, Eds. (Academic Press, New York, 1990) p. 1.

[24] S.H. Vosko, L. Wilk and M Nusair, *Can. J. Phys.* **58** (1980) 1200.

[25] E.J. Baerends, D.E. Ellis and P. Ros, *Chem. Phys.* **2** (1973) 41; E.J. Baerends and P. Ros, *Chem. Phys.* **2** (1973) 52; E.J. Baerends and P. Ros, *Chem. Phys.* **8** (1975) 412; P.M. Boerrigter, G. te Velde and E.J. Baerends, *Int. J. Quantum Chem.* **33** (1988) 87.

[26] G. te Velde and E.J. Baerends, *J. Comput. Phys.* **99** (1992) 84.

[27] T. Ziegler and A. Rauk, *Theoret. Chim. Acta* **46** (1977) 1.

[28] W. Biemolt, A.P.J. Jansen and R.A. van Santen, *Chem. Phys. Lett.* **180** (1991) 95 (chapter 2 of this thesis); M.A. van Daelen, A.P.J. Jansen, W. Biemolt and R.A. van Santen, *Chem. Phys. Lett.* **190** (1992) 190 (chapter 3 of this thesis); W. Biemolt, G.J.C.S. van de Kerkhof, P.R. Davies, A.P.J. Jansen and R.A. van Santen, *Chem. Phys. Lett.* **188** (1992) 477 (chapter 7 of this thesis).

[29] A.D. Becke, *Int. J. Quant. Chem.*, **23** (1983) 1915.

[30] A.D. Becke, *Phys. Rev. A* **38** (1988) 3098.

[31] J.P. Perdew, *Phys. Rev. B* **33** (1986) 8822, J.P. Perdew, *Phys. Rev. B* **34** (1986) 7406.

[32] H. Stoll, C.M.E. Pavlidou and H. Preuß, *Theor. Chim. Acta* **49** (1978) 143; H. Stoll, E. Golka and H. Preuß, *Theor. Chim. Acta* **55** (1980) 29.

[33] J.P. Perdew and A. Zunger, *Phys. Rev. B* **23** (1981) 5048.

[34] P.M. Boerrigter, Ph.D. thesis, Free University of Amsterdam, Amsterdam (1987); J.G. Snijders and E.J. Baerends, *Mol. Phys.* **36** (1978) 1789; J.G. Snijders, E.J. Baerends and P. Ros, *Mol. Phys.* **38** (1979) 1909.

[35] N. Sathyamurthy, *Comput. Phys. Rep.* **3** (1985) 1; A. Aguado and M. Paniagua, *J. Chem. Phys.* **96** (1992) 1265.

[36] M. Abramowitz and I.A. Stegun, *Handbook of Mathematical Functions*, (Dover Publications, Inc., New York, 1990).

[37] G.A. Parker, R.L. Snow and R.T. Pack, *J. Chem. Phys.* **64** (1976) 1668; D.M. Silver, *J. Chem. Phys.* **72** (1980) 6445.

[38] O. Gunnarsson and R.O. Jones, *Phys. Rev. B* **31** (1985) 7588; F.W. Kutzler and G.S. Painter, *Phys. Rev. B* **43** (1991) 6865.

[39] H. Jörg and N. Rösch, *Chem. Phys. Lett.* **120** (1985) 359.

[40] T. Ziegler, V. Tschinke, E.J. Baerends, J.G. Snijders and W. Ravenek, *J. Phys. Chem.* **93** (1989) 3050.

[41] E.J. Baerends, P. Vernooijs, A. Rozendaal, P.M. Boerrigter, M. Krijn, D. Feil, D. Sundholm, *J. Molec. Struct. (THEOCHEM)* **133** (1985) 147.

[42] W.J. Hehre, L. Radom, P.v.R. Schleyer, J.A. Pople, *Ab Initio Molecular Orbital Theory*, (John Wiley & Sons, Chichester, 1986).

[43] A.P.J. Jansen, unpublished results.

[44] A. van der Avoird, P.E.S. Wormer, F. Mulder and R.M. Berns, *Topics in Current Chemistry* **93** (1980) 1.

[45] K.T. Tang and J.P. Toennies, *J. Chem. Phys.* **80** (1984) 3726; K.T. Tang and J.P. Toennies, *Chem. Phys. Lett.* **151** (1988) 301.

[46] C.E. Moore, *Atomic Energy Levels*, Vol. 3, Circular of the National Bureau of Standards 467 (U.S. Government Printing Office, Washington, 1958).

[47] D. Brennan and F.H. Hayes, *Philos. Trans. R. Soc. London Ser. A* **258** (1965) 347.

[48] D.G. Castner, B.A. Sexton and G.A. Somorjai, *Surf. Sci.* **71** (1978) 519.

[49] P.A. Thiel, E.D. Williams, J.T. Yates Jr and W.H. Weinberg, *Surf. Sci.* **84** (1979) 54.

[50] H.C. Peebles, D.D. Beck, J.M. White and C.T. Cambell, *Surf. Sci.* **150** (1985) 120.

[51] D. Dai and K. Balasubramanian, *J. Chem. Phys.* **101** (1994) 2148 (This complete active space multiconfiguration self-consistent field follow by multireference singles+doubles configuration interaction study for Rh-CO and Rh-OC appeared after the completion of this manuscript).

[52] A. St-Amant and D.R. Salahub, *Chem. Phys. Lett.* **169** (1990) 387.

[53] V.G. Albano, A. Ceriotti, G. Ciani, S. Martinengo and W.M. Anker, *J. Chem. Soc., Chem. Comm.* (1975) 859.

5   A DF study into properties of bare rhodium clusters

ABSTRACT

In this chapter we present density-functional calculations on a number of bare rhodium clusters to investigate the electronic structure and interatomic interactions of these systems. We examined a number of linear chains, small clusters, and clusters modeling the Rh(111) surface. The smallest cluster consists of only two atoms, the largest of over forty. For all of these clusters we determined properties like formation energy, cohesive energy, and ionization potential. The density-of-states and bond distances were also determined for some of the rhodium clusters. Most of these calculated properties show a strong dependence on clusters size. Although rhodium is a non magnetic solid, the small and medium rhodium clusters showed a preference for high spin multiplicity. This magnetic behavior only disappeared slowly for the (in three dimensions) larger clusters. The cluster results are compared with density-functional calculations on periodic systems (periodicity in one, two, or three dimensions). Now only the linear chain, and a one-layer slab show significant magnetic moments. The results are in good agreement with the available experimental data and with other high-level calculations.

5.1   INTRODUCTION

Small transition metal clusters are applied in a wide variety of chemically and physically relevant processes. In recent years, it has become possible, using such methods as density functional theory (DFT), to provide a description of electronic properties of systems of a reasonable size. Knowledge of the electronic structure of transition metals can be useful for the understanding of heterogeneous catalysis [1]. It is important, after all, to understand the chemistry and physics of the bare clusters before we can understand their interaction with atoms and molecules. Although it is still not known for sure whether small transition metal clusters resemble a real surface, they are often used as surface models. Quantities like the binding energy per atom or cohesive energy of the metal (CE) [2], equilibrium bond distance, electron affinity, density of states (DOS) and the ionization potential (IP) [3], among others, can be used to determine the convergence of finite clusters to an infinite bulk metal. Once the cluster requirements are known, one is able to investigate electronic properties and to study the kinetics and thermodynamics of adsorption processes.

Due to the more complex nature of the bonding and the higher computational cost, large transitional metal clusters have not been studied so often yet with high-level calculations. An exception is maybe nickel, which has been studied by various quantum chemical methods [4, 5, 6, 7]. Most studies indicate that properties like the IP of the bare metal are strongly dependent on the cluster size. Although the availability of modern super computers enables us to use quite large clusters, converged results with respect to cluster size are still very hard to obtain. However, the cluster size dependence is not necessarily due to the theoretical model. Experimental results for the IP of Ni_{3-90} clusters show also a dependence on cluster size [8]. The experimental results could be well reproduced with theoretical calculations [4, 9].

Our interest will focus specifically on the element rhodium, an element of the 4d block, which is used as an alloying agent to harden platinum and palladium. As it has a low electrical resistance as well as a low and stable contact resistance, and is highly resistant to corrosion it is also useful as an electrical contact material. Nowadays rhodium is, together with platinum, an important element in catalysts for removing pollution from exhaust fumes. Due to its good efficiency in dissociating NO it is effective in removing NO_x pollution. Theoretical investigation of rhodium clusters is also a challenging task. The open d shell of the rhodium atom results in a great number of low lying states for the bare rhodium clusters, which causes serious convergence problems. One of our objectives is to determine how large a cluster is needed to realistically simulate a rhodium surface, to permit a better investigation of carbon monoxide chemisorption on rhodium [10].

5.2   METHODS

Cluster calculations were performed using the density-functional (DF) theory within the local density approximation (LDA) with the Vosko-Wilk-Nusiar (VWN) local spin density potential [11], as implemented in the Amsterdam-density-functional (ADF) program [12]. The molecular orbitals are represented as linear combinations of atomic Slater type orbitals (STOs). Integrals are computed numerically [13], and energies with the generalized transition state method [14]. We employed spin unrestricted, quasi-relativistic [15] calculations, and included gradient or non-local (NL) corrections due to Becke for the exchange [16] and due to Stoll for the correlation self-interaction [17, 18].

The n-dimensional (n=1, 2, 3) crystal calculations were performed using the band structure program ADF-BAND, by te Velde and Baerends [19, 20]. It is very similar in set up to the molecular ADF program. A relevant difference between the two programs involves the basis sets. The band structure program contains a Hermann-Skillman type subprogram [21], which solves the DF equations for the free atoms of the system. The numerical atomic orbitals (NAOs) are used in the crystal valence set, together with, or instead of Slater-type exponential functions. ADF does not include this option, but it has the possibility to employ specific linear combinations of STOs as basis functions. Another difference is that ADF-BAND does not include the quasi-relativistic, and the Stoll correction, which we both used with ADF.

In the cluster and band structure calculations the electrons up to and including 4p are kept frozen (nine valence electrons). The basis and fit set is the same as we used before [10], except that in the band structure calculations only the valence, and no core, STOs are used.

5.3   RESULTS AND DISCUSSION

5.3.1   The rhodium atom

The ground-state of the rhodium atom is known to be the $4d^8 5s^1$ configuration. However, theoretical calculations usually show that the $4d^9$ configuration is lower in energy. This gives rise to problems when one would like to determine dissociation energies. Earlier we showed that by including non-local and relativistic corrections, and performing spin unrestricted calculations the correct ground-state for the rhodium atom is reproduced [10]. The true ground-state is 7 kJ/mol more stable than the first excited state. This is much lower than the experimental difference of 34 kJ/mol. The calculated ionization potential (IP) is 743 kJ/mol,

close to the experimental value of 720 kJ/mol, and the Fermi level is -431 kJ/mol. Unfortunately, calculations with ADF-BAND show again a preference for $4d^9$, possibly due to the absence of relativistic corrections. The Fermi level lies now at -338 kJ/mol.

When we use a spin unrestricted instead of spin restricted calculation for the rhodium atom, the atom stabilizes by 85 kJ/mol when the gradient correction due to Becke is included. All the energies we report herein are with respect to the spin unrestricted rhodium atom. Our rhodium ground-state configuration corresponds with a spin-multiplicity $M = 2S + 1 = 4$. In the DFT implementation we use, the open shell rhodium atom is described by a single configuration with $M_S = S$ with spherical averaging over M_L. The spherical charge density is enforced by use of fractional electron occupations.

Recently it was argued that another important issue in obtaining accurate atomic energies is removing the spherical charge density constraint, and use non-spherical atoms [22]. Removing this constraint lowers the atomic energies significantly if non-local functions are used [23], thus improving molecular bonding energies. Pápai *et al.* found that the rhodium atom becomes as much as 50 kJ/mol more stable when the spherical charge density constraint was removed. Atomic multiplets can be calculated approximately with the sum method [24]. We also applied this method, and thus determined non spherical atomic energies. Instead of determining pure states, we restricted ourselves in determining only the lowest energy value, which resulted from the use of integer occupations and breaking the degeneracy of partially filled orbitals. Without the non-local correction the atom becomes more stable by only 7 kJ/mol, but including Becke's non-local correction the atom becomes more stable by 26 kJ/mol. This stabilization is not quite as large as the one found by Pápai *et al.* [22], but still considerable. Nevertheless, for all remaining calculations we used spherical atoms.

5.3.2 The rhodium dimer

The simplest system to study the rhodium-rhodium interaction is the rhodium dimer, Rh_2. Diatomic rhodium is a good system to test our results with those obtained by different computational methods. This system has been studied before with various methodologies, yielding a number of different ground states (see table 5.1). Many of the early ab initio calculations yielded non bonded or little bonded dimers. Only configurations with an even number of electrons in the σ, π, and δ orbitals give symmetrical dissociation, excluding all the states of ungerade symmetry. The ab initio calculations of Balasubramanian and Liao [27], who have included spin-orbit and other relativistic effects directly into their calculations, resulted in $^5\Delta_g$ as the lowest lying state with Rh-Rh = 2.28 Å. Illas *et al.* [28] found a $^5\Delta_u$ configuration with Rh-Rh = 2.67 Å as the most stable state. Mains and White [29], as well as

Estiu and Zerner [30] calculated the lowest energy state of Rh_2 as $^5\Sigma_u^-$. The first found an interatomic separation 2.28 Å, while the latter found a slightly larger value, 2.35 Å. Our ground state of Rh_2 is $^5\Delta_g$, with an interatomic separation (R_e) of 2.297 Å, and a dissociation energy (D_e) of 330 kJ/mol. The *aufbau* principle was not satisfied for our lowest energy state, $^5\Delta_g$. By removing the D_{lin} symmetry constraint, we were able to obtain a solution that satisfies the *aufbau* principle. This increases the dissociation energy by 10 kJ/mol. Our values compare well with high level ab initio results and with the experimental result. A Mulliken population analysis shows $4d^{7.97}\ 5s^{1.01}\ 5p^{0.02}$ as the atomic configuration for each rhodium atom, in good agreement with Balasubramanian and Liao [27] ($4d^{7.92}\ 5s^{1.04}\ 5p^{0.04}$) and Goursot et al. [31] ($4d^{7.86}\ 5s^{1.13}\ 5p^{0.01}$). This corresponds to two ^4F rhodium atoms brought together with spin coupling, and shows the large 5s contribution to the metal-metal bond.

Table 5.1 *Calculated ground-state (GS) and spectroscopic constants of Rh_2.*

	Ref.	Method[a]	GS	R_e (Å)	D_e (kJ/mol)	ω_e (cm^{-1})
Norman and Kolari	25	SCF-X$_\alpha$-SW	$^5\Delta_u$	2.39	—	—
Shim	26	SCF/valence CI	$^5\Sigma_g$	2.86	82	118
Balasubramanian and Liao	27	MCSCF/CASSCF	$^5\Delta_g$	2.28	239	266
Illas, Rubio and Canellas	28	CASSCF/MRCI	$^5\Delta_u$	2.673	145	238
Mains and White	29	UHF	$^5\Sigma_u^-$	2.28	≈ -337	—
Estiu and Zerner	30	INDO	$^5\Sigma_u^-$	2.35	16	—
Estiu and Zerner	30	CAHF/CISD	$^5\Delta_g$	2.287	116	—
Goursot, Papai and Salahub	31	LCGTO-DF	$^5\Pi_g$	2.23	302	260
Yang Jinlong et al.	32	DV-LSDF	S=2	2.31	293	333
this work		LCSTO-DF	$^5\Delta_g$	2.297	330	288
Cocke and Gingerich	33	Experiment	—	2.28	282	267

[a]   SCF=self-consistent field, SW=scatterd wave, CI=configuration interaction, MCSCF=multi-configuration SCF, CASSCF=complete active space MCSCF, MRCI=multi-reference CI, UHF=unrestricted Hartree-Fock, INDO=intermediate neglect of differential overlap, CAHF=configuration average HF, CISD=singles and doubles CI, LCGTO-DF=linear combination of Gaussian type orbitals-density functional, DV-LSD=discrete variational local-spin-density-functional, and LCSTO-DF=linear combination of Slater type orbitals-DF

For five electronic states, reported by others as the groundstate of Rh_2, we obtained spectroscopic parameters (table 5.2) by calculating the potential energy curves and fit them to

$$E(r) = D_e\left(e^{-2\alpha(r-R_e)} - 2e^{-\alpha(r-R_e)}\right) + E_{r=\infty} \qquad (5.1)$$

Here r is the Rh-Rh separation, D_e the dissociation energy, and R_e the equilibrium distance.

Table 5.2 Calculated spectroscopic properties for five states of the rhodium dimer.

Electronic configuration	Term	D_e (kJ/mol)	α ($\mathring{A}^{-1}$)	R_e ($\mathring{A}$)	$E_{r=\infty}$ (kJ/mol)	T_e (kJ/mol)
$1\sigma_g^2\,2\sigma_g^2\,1\sigma_u^1\,\pi_g^2\,\pi_u^4\,\delta_g^4\,\delta_u^3$	$^5\Delta_g$	383.3	1.334	2.313	46.95	=0.0
$1\sigma_g^2\,2\sigma_g^2\,1\sigma_u^1\,\pi_g^2\,\pi_u^4\,\delta_g^3\,\delta_u^4$	$^5\Delta_u$	332.2	1.337	2.402	46.70	51.1
$1\sigma_g^2\,2\sigma_g^1\,1\sigma_u^1\,\pi_g^2\,\pi_u^4\,\delta_g^4\,\delta_u^4$	$^5\Sigma_u^-$	292.4	1.331	2.385	0.00	90.9
$1\sigma_g^2\,2\sigma_g^2\,1\sigma_u^1\,\pi_g^4\,\pi_u^3\,\delta_g^4\,\delta_u^2$	$^5\Pi_g$	186.0	1.319	2.692	38.72	197.3
$1\sigma_g^2\,2\sigma_g^2\,1\sigma_u^2\,\pi_g^3\,\pi_u^3\,\delta_g^3\,\delta_u^3$	$^5\Sigma_g^+$	158.5	1.325	2.777	38.98	224.8

5.3.3 Linear chain of rhodium atoms

The first kind of bare clusters we investigated consists of a linear chain of rhodium atoms. It is relatively easy to investigate the behavior of various properties for this kind of clusters. The Rh-Rh distance is first set to the distance in bulk rhodium, i.e., 2.6901 $\mathring{A}$ [34]. Intermediate neglect of differential overlap (INDO) calculations by Estiu and Zerner [30] for linear chains of rhodium atoms showed a preference for high multiplicity, M = 2S+1, of those chains. They found that number of unpaired electrons was almost constant, around seven or eight. We calculated, using DFT, the formation energy for various spin-multiplicity's of the linear chains. The energies relative to the most stable state are shown in table 5.3. Also we see that these linear chains prefer high spin multiplicities. The difference in the number of α and β electrons for all the chains we calculated is around two electrons per atom. Except for the Rh$_4$ chain, we find a different multiplicity for the ground-state than Estiu an Zerner. Also the relative energies differ considerably. As we increase the chain size it becomes more difficult to determine precise ground states and excitation energies.

Table 5.3 Energies (kJ/mol) relative to the most stable state for different multiplicities (M) of linear clusters. In between brackets are the INDO values found by Estiu and Zerner [30].

	M=3	M=4	M=5	M=6	M=7	M=8	M=9	M=10	M=11
Rh$_2$	95 (79)	—	0 (102)	—	112 (0)	—	564 (373)	—	X
Rh$_3$	—	40 (74)	—	0 (58)	—	20 (0)	—	271 (129)	—
Rh$_4$	—	60 (79)	—	20 (50)	—	0 (0)	—	80 (236)
Rh$_5$	—	(95)	—	82 (89)	—	59 (0)	—	0 (108)	—

For the most stable state of chains up to 13 rhodium atoms we calculated Fermi level (E_F), formation energy per bond (BE) and per atom (CE), and the ionization potential (IP). The results are shown in table 5.4 and fig. 5.1. We also present values for an 'infinitive chain'. These results were obtained with calculations on Rh_{39} through Rh_{43}. For those five chains we found a BE of -175±1 kJ/mol, and a CE -179±1 kJ/mol. In principle BE and CE should become equal for a real infinitive system, since the number of bonds becomes equal to the number of atoms in large chains. For E_F we obtained a value of -465±1 kJ/mol, and for the IP a value of 510±5 kJ/mol. Again, for large systems -E_F and IP should become equal. The IP values decrease as the chain size increases, a well known behavior due to the possibility to delocalize the positive charge over more metal centers. From fig. 5.1 we can easily see all properties converge to the values obtained with the much larger chains, and that the preference for high multiplicity solutions remains, even for very long rhodium chains.

Table 5.4 *Groundstate properties of rhodium chains. Fermi level (E_F), formation energy per bond (BE) and per atom (CE), average magnetic moment per atom (MM) and ionization potential (IP).*

Chain Rh_n	M	E_F (kJ/mol)	Bonds	BE (kJ/mol)	Atoms	CE (kJ/mol)	MM (μ_B)	IP (kJ/mol)	M Rh_n^+
Rh_2	5	-431	1	-263	2	-131	2.00	684	6
Rh_3	6	-413	2	-224	3	-149	1.67	650	7
Rh_4	9	-428	3	-206	4	-155	2.00	634	10
Rh_5	10	-432	4	-199	5	-159	1.80	608	11
Rh_6	13	-426	5	-195	6	-162	2.00	606	14
Rh_7	14	-428	6	-188	7	-161	1.86	590	15
Rh_8	17	-435	7	-190	8	-167	2.00	587	18
Rh_9	18	-447	8	-188	9	-167	1.89	571	19
Rh_{10}	21	-448	9	-192	10	-173	2.00	571	22
Rh_{11}	22	-437	10	-192	11	-174	1.91	566	23
Rh_{12}	25	-445	11	-191	12	-175	2.00	559	26
Rh_{13}	26	-446	12	-190	13	-175	1.92	558	27
Rh_{39-43}	∞	-465±1	∞	-175±1	∞	-179±1	2.00	510±5	∞

For some of the smaller chains we roughly optimized the Rh-Rh distance. We found equilibrium distances between 2.39 and 2.46 Å. Starting from Rh_4, a full geometry optimization within the D_{lin} symmetry gives different interatomic separations within a chain.

For the longer chains we did not try to optimize the Rh-Rh distance anymore, but it seems likely that also for those longer chains the Rh-Rh distance will be smaller than the bulk value.
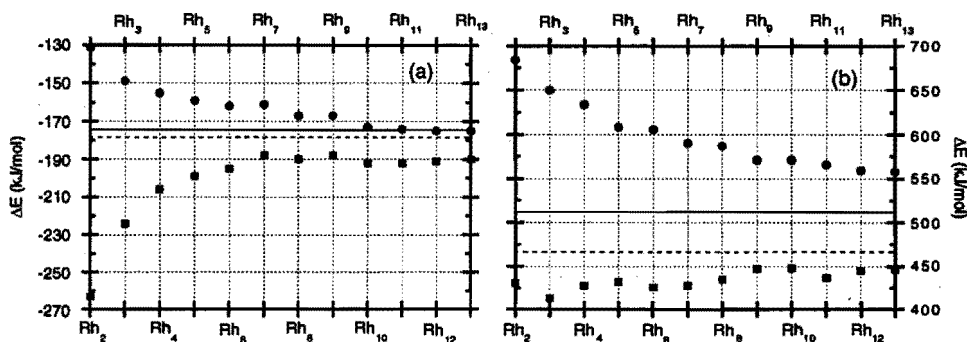

Fig. 5.1   Convergence behavior as a function of chain size. (a) CE (circles) and BE (squares), (b) IP (circles) and $-E_F$ (squares). Solid and dashes lines are computed from Rh_{39} through Rh_{43}.

The density of states (DOS) curves for all chains have been determined by Gaussian broadening of the discrete one-electron spectrum of spin-up and spin-down energy levels. For a number of chains the results are shown in fig. 5.2(a). The broadening was done with a value of 0.05 eV for the Gaussian half width, a rather small value. The analysis of the DOS curves as function of cluster size allows us to follow the evolution of the one-electron energy spectrum from the sparse and discrete spectrum typical of small (molecular) chains, to a near-continuum for the largest (metallic) chains.

The cluster calculations seem to converge towards a magnetic moment of $2\mu_B$ per atom. ADF-BAND calculations on a one-dimensional chain confirm the preference for the high spin-multiplicities. A periodic chain, with Rh-Rh separation of 2.6901 Å, shows a magnetization of 1.88 μ_B per atom. Mulliken population analysis gives $4d^{8.42} 5s^{0.54} 5p^{0.04}$, for the majority spin $4d^{4.97} 5s^{0.44} 5p^{0.04}$, and for the minority spin $4d^{3.46} 5s^{0.10} 5p^{0.01}$. The BE or CE for such an one-dimensional chain is 192, 121, and 157 kJ/mol, respectively at the LDA, LDA+Becke, and LDA+Becke+Perdew level. The Fermi level is at -476 kJ/mol, close to the value we found for our largest cluster chains. Comparison between the BE or CE from a cluster and a periodic calculation is more difficult, since the first is only done at the LDA+Stoll and LDA+Stoll+Becke level. The magnetic moment decreases somewhat as we optimize the Rh-Rh distance. At the LDA level we find an optimum at a Rh-Rh separation of 2.28 Å (226 kJ/mol), where the magnetization is 0.88 μ_B per atom. Adding Becke's correction increases the Rh-Rh distance to 2.54 Å (127 kJ/mol), with a magnetization of 1.83 μ_B per

atom. Also including Perdew's correction, results in a Rh-Rh of 2.47 Å (171 kJ/mol), and a magnetization of 1.82 μ_B per atom. The density of states for a large chain (Rh$_{37}$), and from a one-dimensional periodic calculation are shown in fig. 5.2(b). The calculated DOS from both systems is very similar, as is the integrated DOS. Both curves clearly show a difference between majority ($\uparrow$) and minority ($\downarrow$) density of states.
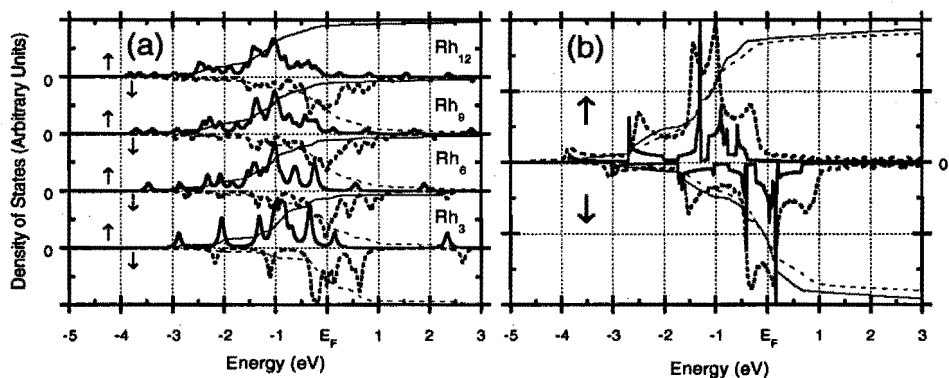

Fig. 5.2 *Density of states for different linear rhodium chains Majority ($\uparrow$) and minority ($\downarrow$) spin. (a) different chain lengths, and (b) largest chain (- - - - -) and 1D periodic calculation (———).*

5.3.3 Small model rhodium clusters

For 21 small highly symmetrical rhodium clusters, all shown in fig. 5.3, we determined a number of physical properties. We started, at Rh-Rh = 2.6901 Å, by calculating the formation energy for various spin-multiplicity's for each cluster. For the most stable state we present Fermi level (E$_F$), bond strength (BE), cohesive energy (CE), average magnetic moment per atom (MM) and the ionization potential (IP) in table 5.5. These results are discussed in some detail and, where possible, compared with earlier results. For some of the clusters, we also optimized the Rh-Rh distance.

The calculated values for E$_F$, BE, CE, MM and IP all change with respect to cluster size. For the Fermi level we see that, except for Rh$_6$, all values lie within 10% of the average value of all clusters (-367 kJ/mol). A bond in a cluster is defined as a Rh-Rh distance of 2.6901 Å. Shorter Rh-Rh separations are not present, (somewhat) longer ones are not counted as a bond. The cohesive energy is thus a better value to determine convergence with respect to cluster size. For the clusters with more than four atoms most of the calculated CE lie within 10% of the average value (-248 kJ/mol). Rhodium has a bulk cohesive energy of 555 kJ/mol. The work function of polycrystalline rhodium is 480 kJ/mol [34]. Unlike bulk rhodium, which is

non magnetic, almost all cluster have non zero magnetic moments. The average value of MM is around 1.2 μ_B. The reduced coordination number and higher symmetry narrows the electronic bands, enhancing magnetization in already ferromagnetic materials or causing magnetization in non magnetic materials. Experimentally this behavior was confirmed for small rhodium clusters [35]. The smallest measured cluster, Rh_9, showed a moment of 0.8 ± 0.2 μ_B. Especially Rh_{15}, Rh_{16}, and Rh_{19} showed strong magnetic moments per atom. While we found particular strong moments for Rh_{13}, experimentally only a value of 0.48 ± 0.13 μ_B was observed. The magnetic moment becomes approximately zero for clusters of more than 60 atoms. The cluster structure itself is important in the enhancement of the magnetic moment. IP values tend to decrease as the cluster size increase. However, the decrease is not monotonic and some clusters exhibit particular high IPs, e.g., tetrahedral Rh_{10}.

| Rh_3 | D_{3h} | Rh_4 | T_d | Rh_4 | D_{4h} | Rh_4 | D_{3h} | Rh_5 | D_{3h} | Rh_5 | C_{4v} |

| Rh_6 | O_h | Rh_7 | D_{5d} | Rh_8 | T_d | Rh_8 | C_{4v} | Rh_9 | O_h | Rh_9 | D_{4h} |

| Rh_{10} | T_d | Rh_{10} | C_{4v} | Rh_{11} | D_{3h} | Rh_{12} | I_h | Rh_{12} | D_{3d} |

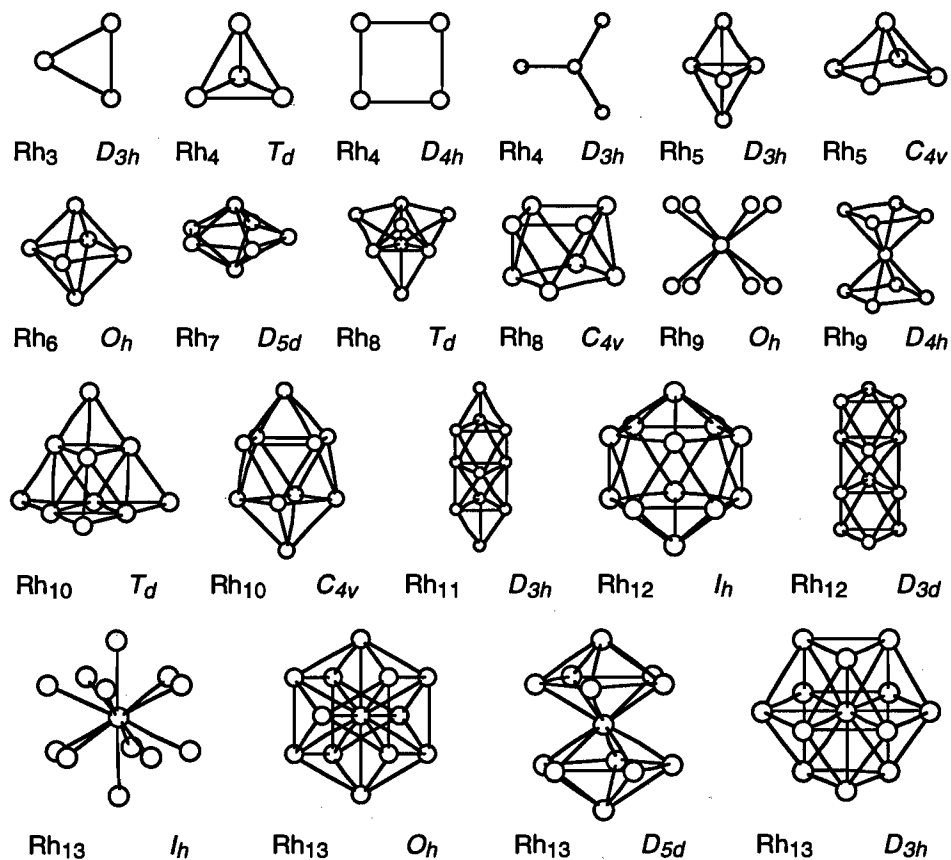| Rh_{13} | I_h | Rh_{13} | O_h | Rh_{13} | D_{5d} | Rh_{13} | D_{3h} |

Fig. 5.3   *The topologies of 21 small rhodium clusters. Drawn lines correspond to Rh-Rh bonds.*

Table 5.5 *Groundstate properties of rhodium clusters. Fermi level (E_F), formation energy per bond (BE) and per atom (CE), average magnetic moment per atom (MM) and ionization potential (IP).*

Cluster		M Rh_n	E_F (kJ/mol)	Bonds	BE (kJ/mol)	Atoms	CE (kJ/mol)	MM (μB)	IP (kJ/mol)	M Rh_n^+
Rh_3	D_{3h}	6	-372	3	-193	3	-193	1.67	672	6
Rh_4	T_d	1	-355	6	-149	4	-223	0.00	637	2
Rh_4	D_{4h}	7	-361	4	-211	4	-211	1.50	611	8
Rh_4	D_{3h}	7	-381	3	-222	4	-167	1.50	596	8
Rh_5	D_{3h}	8	-348	9	-134	5	-241	1.40	591	7
Rh_5	C_{4v}	8	-336	8	-151	5	-242	1.40	586	9
Rh_6	O_h	9	-314	12	-126	6	-252	1.33	529	10
Rh_7	D_{5h}	10	-346	15	-119	7	-255	1.29	546	11
Rh_8	T_d	13	-377	18	-113	8	-255	1.50	546	12
Rh_8	C_{4v}	13	-383	16	-133	8	-265	1.50	591	14
Rh_9	O_h	10	-389	8	-259	9	-230	1.00	548	9
Rh_9	D_{4h}	8	-359	16	-139	9	-247	0.78	549	9
Rh_{10}	T_d	7	-405	24	-107	10	-256	0.60	604	8
Rh_{10}	C_{4v}	15	-390	24	-113	10	-272	1.40	553	14
Rh_{11}	D_{3h}	10	-367	27	-109	11	-267	0.82	536	11
Rh_{12}	I_h	15	-402	30	-109	12	-274	1.17	571	16
Rh_{12}	D_{3h}	13	-358	30	-107	12	-267	1.00	523	12
Rh_{13}	I_h	22	-360	12	-299	13	-276	1.62	522	23
Rh_{13}	O_h	20	-364	36	-98	13	-268	1.46	520	21
Rh_{13}	D_{5d}	22	-374	30	-118	13	-273	1.62	540	23
Rh_{13}	D_{3h}	20	-363	36	-100	13	-276	1.46	527	21

• **Rh$_3$**   The triangular structure of the rhodium trimer has been studied before with theoretical [29, 36], and experimental [37] methods. Mains and White investigated a similar system as we did, and found the lowest energy for a $^8A_1$ state, with a fixed bond length of 2.94 Å between the apex atom and one of the two equivalent base atoms (3.745 Å, 80 deg.). Das and Balasubramanian found 2.535 Å, (2.596 Å, 61.6 deg.). Due to Jahn-Teller distortion their lowest states are of C_{2v} symmetry. Their atomic configurations are $4d^{7.92} 5s^{0.86} 5p^{0.12}$ (apex) and $4d^{8.24} 5s^{0.67} 5p^{0.14}$ (base). Consistent with our findings, recent studies reveal a sextet as the groundstate. The optimized Rh-Rh distance we obtained (2.465 Å), however, is somewhat smaller. The atomic configuration we found for each atom is $4d^{8.18} 5s^{0.76} 5p^{0.06}$.

• Rh$_4$ The tetrahedral Rh$_4$ cluster is the only one for which we did not find a high spin multiplicity for the ground state. Others found also for this cluster high multiplicities. Mains and White found the lowest energy for ^{7}A", but they did not optimize the Rh-Rh distance (3.062 Å). They found an atomization energy of only 65 kJ/mol. The tetrahedral Rh$_4$ cluster has been used in two other studies of the CO adsorption on rhodium [31, 38]. Goursot *et al.* found also for this cluster a high spin multiplicity, a septet, as the groundstate [31]. Without the Becke non-local correction we find that this state is 6 kJ/mol lower in energy, but with this correction it is 15 kJ/mol higher in energy. Our calculated binding energy per atom (CE) for this cluster is almost the same as their value of 224 kJ/mol. The total Mulliken population analysis resulted in an atomic configuration for rhodium of 4d$^{8.27}$ 5s$^{0.64}$ 5p$^{0.09}$, almost the same as the one found by Goursot *et al.* 4d$^{8.24}$ 5s$^{0.59}$ 5p$^{0.17}$. Estiu and Zerner reported as atomic configuration 4d$^{7.94}$ 5s$^{0.59}$ 5p$^{0.54}$. This has a rather high population for the p orbitals.

Mains and White also performed calculations on a planar rhombohedral configuration, showing that ^{9}A" was the lowest in energy. Their structure, with a Rh-Rh of 3.265/3.115 Å, was not optimized. They found that this structure is much more tightly bound than their tetrahedral structure. For their structure they report an UHF atomization energy of 226 kJ/mol. Estiu and Zerner [39] found close-shell solutions for full optimized square planar (Rh-Rh = 2.106 Å) and tetrahedral (Rh-Rh = 2.273 Å) geometries. For the distance observed in the bulk they found the septet to be 18 kJ/mol more stable than the singlet, the same ground state we found for the bulk Rh-Rh interatomic distance. The atomic configuration we found from a total Mulliken population analysis is 4d$^{8.24}$ 5s$^{0.69}$ 5p$^{0.07}$.

The IP is an important parameter, which is usually strongly dependent of the clusters size. Instead of removing one electron from a cluster, removing only a small fraction (say 1.10^{-5}) of electrons was suggested to reduce this dependency [7]. We applied this to tetrahedral Rh$_4$, using accurate numerical integration, and a strong convergence criterion. For these clusters we could obtain highly accurate and well converged solutions. The work function of Rh(111) is 540±4 kJ/mol [40] This is much smaller than the IP of tetrahedral Rh$_4$, 637 kJ/mol. Calculating the IP by removing 1.10^{-4} electrons resulted in 371 kJ/mol, while removal of 1.10^{-5} yields 370 kJ/mol ($\approx E_F$). Removing fewer electrons gives too small energy differences.

• Rh$_{5-9}$ These medium sized rhodium clusters are not so commonly studied as the smaller clusters. A recent first-principles DF study [32] showed that bond lengths for most clusters are shorter than the bulk interatomic spacing. This dramatically changed the magnetic properties of some clusters. Our results seem to indicate that the systems seem to prefer higher-dimensional geometries with more nearest-neighbor bonds. Crude optimization of the interatomic spacing for our clusters shows a bond length contraction for clusters. The value of the contractions varies from about 10% for the smaller, to 5% for the larger clusters.

From table 5.5 one can see that all of these small clusters have magnetic ground states. The computed average magnetic moment per atom for the small rhodium clusters varies from 0.8 μ_B to 1.5 μ_B. However, bond length contractions seem to decrease the total magnetic moment [32]. The experimental magnetic moment per atom for Rh_9 is 0.8 μ_B ± 0.2 μ_B [35].

• Rh_{10} As far as we know there exists no previous theoretical study on the tetrahedral Rh_{10} cluster, but it is comparable with the tetrahedral Ir_{10} studied by Ravenek *et al.* [41]. That DF study demonstrated the same behavior of the iridium atoms in Ir_4, Ir_{10}, and surface atoms. Neutral particles with the smaller average number of neighbors have the higher d valence electron band occupation, as is the case for surfaces. In the M_{10} cluster we can identify atoms with three and six nearest neighbors (3nn and 6nn). Mulliken population analysis for neutral Ir_{10} showed that the configuration for Ir(3nn) atoms is $s^{0.93} p^{0.10} d^{8.24}$, while Ir(6nn) atoms have $s^{0.82} p^{-.04} d^{8.05}$. The average is $s^{0.86} p^{0.01} d^{8.13}$. The charge for Ir(3nn) is -0.27, and for Ir(6nn) +0.17. For Rh_{10} we find for Rh(3nn) $s^{0.85} p^{0.08} d^{8.15}$, and $s^{0.73} p^{0.22} d^{7.99}$ for Rh(6nn). So Rh(3nn) has the higher d valence electron band occupation. The average for rhodium is $s^{0.78} p^{0.16} d^{8.06}$. Which means that the charge on Rh(3nn) is -0.08, and for Rh(6nn) it is +0.06. The difference between both kinds of atoms is less for rhodium than for iridium. Tetrahedral Rh_{10} has the highest CE, and almost the lowest BE of all the small clusters we examined. The experimental magnetic moment per atom for Rh_{10} is 0.8 μ_B ± 0.2 μ_B [35]. This is close to the value we found for tetrahedral Rh_{10}, 0.6 μ_B.
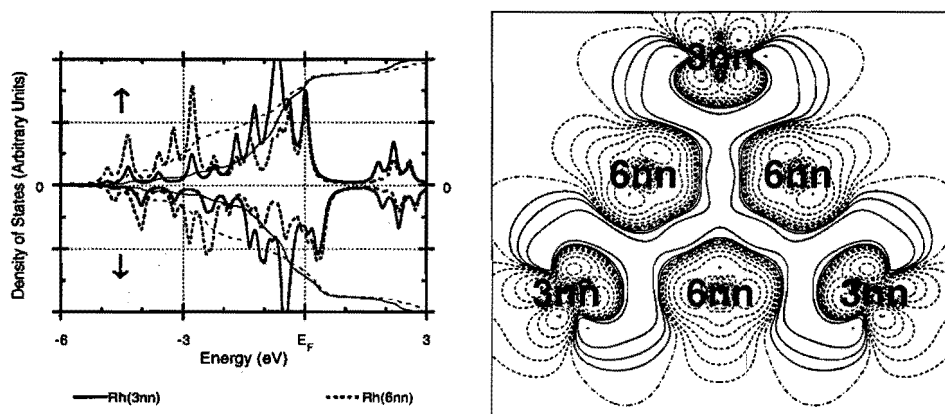

Fig. 5.4   *Tetrahedral Rh_{10}. (a) Density of states, solid lines Rh(3nn) and dashed lines Rh(6nn). (b) Contour map of the density difference $\rho(Rh_{10}) - 10\rho(Rh_{10})$. Dashed lines show a decrease and solid lines an increase of the electron density, the dashed-dotted lines depict nodal surfaces. Subsequent contours correspond to 0.00, ±0.01, ±0.02, ±0.04, ±0.08, ±0.16, ±0.32, and ±0.64 e/$Å^3$.*

In tetrahedral Rh_{10} the four rhodium atoms at the corner have three nearest neighbors (3nn), while the six inner atoms have 6nn. This difference should show up in the population and total density of states for each of the different atoms. According to a band width argument, atoms that have more neighbors should have fewer electrons. The Mulliken population analysis (table 5.6) shows that this is indeed true for tetrahedral Rh_{10}. In this cluster each atom with 3nn has 9.09 electrons while each atom with 6nn has only 8.95 electrons. We see this also from the total density of states and contour map of the density difference, as shown in fig. 5.3.

• **Rh_{13}**   From the standpoint of many chemical reactions, the transition from molecule to bulk properties appear to occur around 13 atoms. The relative stabilities of icosahedral (I_h), cubooctahedral (O_h), D_{5d} and D_{3d} symmetries (see fig. 5.3) have been compared. The most stable structure is the D_{5d} cluster, a distorted icosahedral. The ground state of Rh_{13} was found to have 19 or 21 unpaired electrons, resulting in a giant magnetic moment.

The electronic structure of 13-atom rhodium clusters has been studied before using a linear combination of atomic orbitals approach within the density functional formalism [42]. The ground state of Rh_{13} was found to have 21 unpaired electrons. For the cubo geometry an interatomic spacing of 2.59 Å was found, with a cohesive energy of 307 kJ/mol and a magnetic moment of 1.54/1.45 μ_B per (center/surface) atom. The icos geometry was a little more stable, 316 kJ/mol at 2.56 Å with a magnetic moment of 1.58/1.62 μ_B per atom. All calculated moments are much larger than the experimental magnetic moment per atom for Rh_{13}, 0.48 μ_B ± 0.13 μ_B [35].
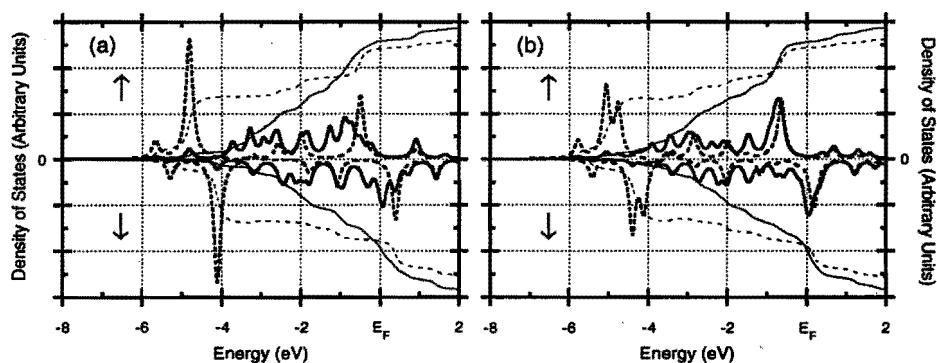

Fig. 5.5   *Density of states of two Rh_{13} clusters. (a) Icosahedral and (b) cubooctahedral Rh_{13}. A solid line is a contribution from an inner rhodium atom, a dashed line is a contribution from an outer rhodium atom. The thinner lines indicate the integration of the density of states.*

Another density functional study [43] shows comparable results. The total magnetic moment of the icosahedral Rh_{13} cluster is smaller than that of two lower-symmetry clusters. The ground state of Rh_{13} was found to have 18 (O_h and D_{3h}) or 14 (I_h) unpaired electrons. For the cubo geometry an interatomic spacing of 2.62 Å was found, with a cohesive energy of 377 kJ/mol and a magnetic moment of 1.04/1.50 μ_B per (center/surface) atom. The icos geometry was a little more stable, 387 kJ/mol at an interatomic separation of 2.56 Å with a magnetic moment of 1.12/1.16 μ_B per atom. The D_{3h} geometry was a little more stable, 384 kJ/mol at an interatomic spacing of 2.62 Å with a magnetic moment of 1.06/1.48/1.51 μ_B per atom. Both previous theoretical studies are in reasonable agreement with ours. While Reddy *et al.* [42] found slightly larger magnetic moments and weaker cohesive energies, Yang Jinlong *et al.* [43] found lower magnetic moments but larger cohesive energies.

Table 5.6 shows the Mulliken population analysis of al four Rh_{13} clusters we examined. Difference in the number of nearest neighbors should show up in the Mulliken population and total density of states. The Mulliken population analysis (table 5.6) shows that this is indeed true, atoms that have more neighbors have fewer electrons. We see this also from the total density of states, as shown in fig. 5.5 for two Rh_{13} clusters.

Table 5.6   *Mulliken population analysis by atomic orbitals.; MM is magnetic moment (in μ_B).*

	Rh_{10} T_d		Rh_{13} I_h		Rh_{13} O_h		Rh_{13} D_{5d}			Rh_{13} D_{3h}		
	3 nn	6 nn	1nn	12nn	5 nn	12 nn	4nn	5nn	10nn	5nn	5nn	12nn
#	4	6	12	1	12	1	10	2	1	6	6	1
s	0.85	0.73	0.69	0.75	0.72	0.72	0.71	0.76	0.71	0.71	0.72	0.72
p	0.09	0.22	0.24	-.19	0.19	-.06	0.23	0.18	-.11	0.19	0.21	-0.08
d	8.15	8.00	8.11	7.99	8.11	8.03	8.15	7.98	8.03	8.12	8.10	8.07
Σ	9.09	8.95	9.04	8.55	9.02	8.69	9.09	8.92	8.63	9.02	9.03	8.71
q	-.09	0.05	-.04	0.45	-.02	0.31	-.09	0.08	0.37	-.02	-.03	0.29
MM	0.32	0.79	1.63	1.46	1.47	1.33	1.63	1.65	1.42	1.48	1.46	1.36

5.3.4   The Rh(111) surface

We examined a number of clusters that are representations of the Rh(111) surface. The smallest is the Rh(7) cluster, seven atoms in one layer. The largest is the Rh(19, 12, 12) cluster, 43 atoms in three layers. $Rh(n_1, n_2, n_3)$ indicates a rhodium cluster bearing $n_1 + n_2 + n_3$ atoms of which n_1 are in the first layer, n_2 in the second layer and n_3 in the third layer. The results of our calculations are shown in table 5.7.

Table 5.7 Groundstate properties of Rh(111) models. Fermi level (E_F), formation energy per bond (BE) and per atom (CE), average magnetic moment per atom (MM) and ionization potential (IP).

Cluster	M Rh_n	E_F (kJ/mol)	Bonds	BE (kJ/mol)	Rh	CE (kJ/mol)	MM (μB)	IP (kJ/mol)	M Rh_n^+
1-layer									
Rh(7)	14	-395	12	-135	7	-231	1.86	621	15
Rh(10)	15	-413	18	-130	10	-234	1.40	585	14
Rh(13)	18	-390	24	-129	13	-238	1.31	546	19
Rh(16)	23	-413	33	-120	16	-247	1.44	566	24
Rh(19)	26	-415	42	-116	19	-256	1.32	562	27
Rh(31)	42	-420	72	-112	31	-261	1.35	531	43
Rh(37)	50	-423	90	-109	37	-265	1.35	534	51
2-layers									
Rh(7, 3)	15	-369	24	-109	10	-261	1.40	552	16
Rh(7, 6)	12	-375	36	-101	13	-280	0.85	530	15
Rh(13, 3)	21	-386	36	-113	16	-254	1.25	536	22
Rh(13, 6)	20	-374	51	-99	19	-265	1.00	522	19
Rh(13, 12)	18	-378	78	-90	25	-281	0.68	517	19
Rh(19, 3)	27	-402	54	-109	22	-267	1.18	536	27
Rh(19, 6)	22	-392	69	-99	25	-274	0.84	526	22
Rh(19, 12)	22	-387	102	-92	31	-305	0.68	516	23
3-layers									
Rh(7, 3, 3)	14	-376	33	-107	13	-273	1.00	545	15
Rh(7, 6, 6)	10	-387	57	-93	19	-278	0.47	535	9
Rh(13, 3, 3)	18	-374	45	-111	19	-263	0.89	517	19
Rh(13, 6, 6)	14	-373	72	-94	25	-271	0.52	512	15
Rh(13, 12, 12)	18	-375	132	-82	37	-292	0.46	505	17
Rh(19, 3, 3)	26	-400	63	-108	25	-271	1.00	532	27
Rh(19, 6, 6)	20	-392	90	-96	31	-278	0.61	502	21
Rh(19, 12, 12)	20	-377	156	-82	43	-299	0.44	493	19

Here, we will not discuss the results presented in table 5.7 in much detail. It seems that none of the calculated properties have really converged. The magnetic moments become smaller for the larger clusters, but do not completely disappear.

Experimentally the magnetic moment of Rh(001) surface atoms was recently estimated, using spin-polarized photoemission techniques to lie somewhere between 0.1 and 0.2 μ_B [44]. Previous theoretical calculations [45] already predicted the observed ferromagnetic behavior. Tight-binding calculation yielded a magnetic moment of 1.2 μ_B, while linear muffin-tin orbital (LMTO) calculations resulted in a somewhat smaller magnetic moment of 0.7 μ_B. Both the tight-binding and the LMTO calculations resulted in non magnetic rhodium bilayers.

Table 5.8 *Cohesive energy of Rh(111) slabs for optimized Rh-Rh and (at Rh-Rh = 2.6901 Å).*

LDA				Becke		Becke+Perdew	
#layers	a	Rh-Rh (Å)	CE (kJ/mol)	Rh-Rh (Å)	CE (kJ/mol)	Rh-Rh (Å)	CE (kJ/mol)
1	u	2.595	-391 (-385)	2.749	-199 (-198)	2.671	-292 (-292)
2	u	2.633	-528 (-525)	2.800	-277 (-270)	2.709	-398 (-398)
3	u	2.655	-565 (-563)	2.807	-298 (-287)	2.727	-428 (-426)
4	u	2.675	-592 (-592)	2.874	-332 (-305)	2.774	-451 (-450)
4	r	2.666	-589 (-589)	2.817	-317 (-304)	2.746	-451 (-449)
5	r	2.674	-597 (-597)	2.821	-316 (-304)	2.746	-455 (-453)
6	r	2.624	-608 (-605)	2.844	-320 (-307)	2.729	-459 (-458)
∞	u	2.690	-639 (-638)	2.844	-344 (-321)	2.768	-490 (-483)

a u = spin-unrestricted calculation, r = spin-restricted calculation.

We investigated two-dimensional Rh(111) layers or slabs and the three-dimensional Rh(111) crystal by using the ADF-BAND program. This program does not include the corrections as we used them for the cluster calculations (relativistic and Stoll), which makes direct comparison between ADF and ADF-BAND difficult. In contrast to the cluster calculations, we now optimized the Rh-Rh distance. The results are shown in table 5.8.

The magnetic moment for a one-layer slab depends on the Rh-Rh distance. At the LDA optimum it is 1.3 μ_B, while it is 1.4 μ_B at both the LDA+Becke and LDA+Becke+Perdew level. From the Mulliken population analysis we found $4d^{4.70}$ $5s^{0.46}$ $5p^{0.04}$ for the majority spin and $4d^{3.46}$ $5s^{0.33}$ $5p^{0.02}$ for the minority spin. The calculation magnetic moment goes rapidly to zero around the bulk Rh-Rh distance as the number of layers increases. A two layer slab shows no significant magnetic moment for distances below 2.8 Å. The Mulliken population analysis shows $4d^{4.08}$ $5s^{0.36}$ $5p^{0.07}$ for each rhodium atom. For a one-layer slab the difference between the spin restricted and unrestricted cohesive energy is small. When we increase the number of rhodium layers in the slab this difference seems to become negligible. The three layer slab is the first that really represents the face-centered-cubic Rh(111) surface.

The calculated cohesive energy seems to have converged with respect to the number of rhodium layers in the slab. Although, if we perform a calculation for the three-dimensional Rh(111) surface a cohesive energy, a value that is still higher than the value found for our largest slab. The LDA level overestimates the cohesive energy by 15%, while CE is underestimated by 38% and 12%, respectively at the LDA+Becke and LDA+Becke+Perdew level compared to the bulk cohesive energy of 555 kJ/mol. This is much better than the values we found with the cluster calculations.

Fig. 5.6 shows the density of states for a number of rhodium systems. The DOS of the largest one-layer cluster shows close resemblance to the one-layer slab calculation, while the three-layer slab result already comes quite close to the three-dimensional calculation. From fig. 5.6 we notice some exchange splitting for both the one-layer cluster and slab.
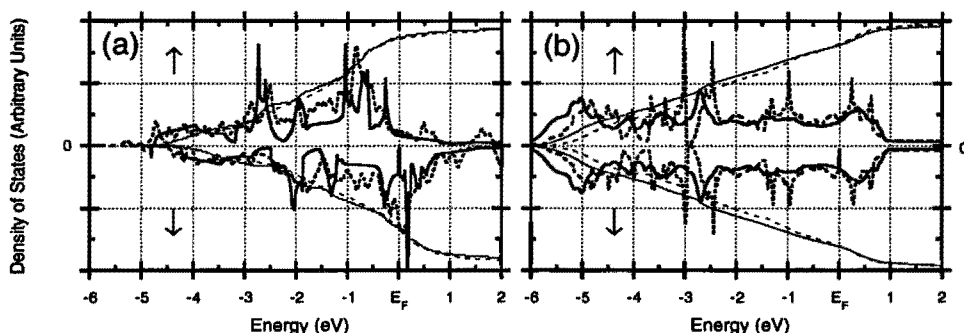
Fig. 5.6 *Density of states for different rhodium (111) models Majority (↑) and minority (↓) spin. (a) largest 1-layer cluster (- - - - -) and periodic 1-layer calculation (———), and (b) 3-layer periodic calculation (- - - - -) and 3D periodic calculation (———).*

5.4   CONCLUSIONS

Using DF theory in the LDA we calculated various properties for a number of bare rhodium clusters. Almost all clusters are found to have non zero magnetic moments. These magnetic moments are most likely a result of the reduced dimensionality and the enhanced electronic degeneracy due to the symmetry of the cluster. Although we used clusters of as large as 43 atoms, properties like cohesive energy and ionization potential seem not to have converged with respect to cluster size. Larger clusters become computationally too demanding to perform calculations within a reasonable time. Cluster of more than thirteen rhodium atoms will at this moment be probably too large for chemisorption studies.

Slab calculations seem to be much more promising than clusters. Convergence to bare transition metal bulk properties seems to be possible at a reasonable computational cost. For rhodium, the Rh-Rh distance is already predicted well at the LDA level. However, including non-local corrections is essential in order to obtain the cohesive energy to fair accuracy. This result encourages the use of slabs in the study of the interaction of adsorbates with surfaces, although for chemisorption studies the computational demands will grow rapidly.

5.5   REFERENCES

[1]   P. Jena, B.K. Rao and S.N. Khanna, eds., Physics and chemistry of small clusters, NATO ASI Series B, Vol. 158 (Plenum, New York, 1987).

[2]   H.P. Cheng, R.S. Berry and R.L. Whetten, *Phys. Rev. B* **43** (1991) 10647

[3]   D.M. Cox, D.J. Trevor, R.L. Whetten and A. Kaldor, *J. Phys. Chem.* **92** (1988) 421.

[4]   N. Rösch, L. Ackermann and G. Pacchioni, *Chem. Phys. Lett.* **199** (1992) 275.

[5]   C. Bureau, M. Defranceschi and J. Delhalle, *Int. J. of Quantum Chem.* **46** (1993) 87.

[6]   G. Pacchioni, Sai-Cheong Chung, S. Krüger and N. Rösch, *Chem. Phys.* **184** (1994) 125.

[7]   G.L. Estiú and M.C. Zerner, *J. Phys. Chem.* **98** (1994) 9972.

[8]   M. B. Knickelbein, S. Yang and S.J. Riley, *J. Chem. Phys.* **93** (1990) 94.

[9]   V. Russier, D.R. Salahub and C. Mijoule, *Phys. Rev. B* **42** (1990) 5046.

[10] W. Biemolt and A.P.J. Jansen, *J. Comp. Chem.* **15** (1994) 1053 (chapter 4 of this thesis).

[11] S.H. Vosko, L. Wilk, and M. Nusiar, *Can. J. Phys.* **58** (1980) 1200.

[12] (a) E.J. Baerends, D.E. Ellis and P. Ros, *Chem. Phys.* **2** (1973) 41;
      (b) P.M. Boerrigter, G. te Velde and E.J. Baerends, *Int. J. Quantum Chem.* **33** (1988) 87.

[13] G. te Velde, and E.J. Baerends, *J. Comput. Phys.* **99** (1992) 84.

[14] T. Ziegler and A. Rauk, *Theoret. Chim. Acta* **46** (1977) 1.

[15] (a) P.M. Boerrigter, Ph.D. thesis, Free University of Amsterdam, Amsterdam (1987);
      (b) J.G. Snijders and E.J. Baerends, *Mol. Phys.* **36** (1978) 1789;
      (c) J.G. Snijders, E.J. Baerends and P. Ros, *Mol. Phys.* **38** (1979) 1909;
      (d) T.Ziegler, V.Tschinke, E.J.Baerends, J.G.Snijders and W.Ravenek, *J. Phys. Chem.* **93** (1989) 3050.

[16] A.D. Becke, Int. J. of Quant. Chem. **23** (1983) 1915; A.D. Becke, *Phys. Rev. A* **38** (1988) 3098.

[17] (a) H. Stoll, C.M.E. Pavlidou and H. Preuß, *Theor. Chim. Acta* **49** (1978) 143;
      (b) H. Stoll, E. Golka and H. Preuß, *Theor. Chim. Acta* **55** (1980) 29.

[18] J.P. Perdew, and A. Zunger, *Phys. Rev. B* **23** (1981) 5048.

[19] G. te Velde and E.J. Baerends, *Phys. Rev. B* **44** (1991) 7888.

[20] G. te Velde, PhD. thesis, Vrije Universiteit Amsterdam (1990).

[21] F. Hermann and S. Skillman, Atomic structure calculations (Prentice-Hall, Englewood Cliffs, 1963).

[22] I. Pápai, A. Goursot, A. St-Amant, and D.R. Salahub, *Theoret. Chim. Acta* **84** (1992) 217.

[23] F.W. Kutzler and G.S. Painter, *Phys. Rev. Lett.* **59** (1987) 1285.

[24] T. Ziegler, A. Rauk, and E.J. Baerends, *Theoret. Chim. Acta* **43** (1977) 261.

[25] J.G. Norman Jr. and H.J. Kolari, *J. Am. Chem. Soc.* **100** (1978) 791.

[26] I. Shim, *Matematisk-Fysike Meddelelser-Kongelige Danske Videnskabernes Selskab* **41** (1985) 147.

[27] K. Balasubramanian and D. Liao, *J. Phys. Chem.* **93** (1989) 3989.

[28] F. Illas, J. Rubio, and J. Canellas, *J. Chem. Phys.* **93** (1990) 2603.

[29] G. Mains and J.M. White, *J. Phys. Chem.* **95** (1991) 112.

[30] G. L. Estiu and M.C. Zerner, *Int. J. of Quantum Chem.: Quantum Chem. Sym.* **26** (1992) 587.

[31] A. Goursot, I. Papai and D.R. Salahub, *J. Am. Chem. Soc.* **114** (1992) 7452.

[32] Yang Jinlong, F. Toigo, and Wang Kelin, *Phys. Rev. B* **50** (1994) 7915

[33] D.L. Cocke and K.A. Gingerich, *J. Chem. Phys.* **60** (1974) 1958.

[34] D.R. Lide, ed., Handbook of Chemistry and Physics, 71st Ed. (CRC Press, Boca Raton, 1990).

[35] (a) A.J. Cox, J.G. Louderback and L.A. Bloomfield, *Phys. Rev. Lett.* **71** (1993) 923;

(b) A.J. Cox, J.G. Louderback S.E. Aspel and L.A. Bloomfield, *Phys. Rev. B* **49** (1994) 12295.

[36] K.K. Das and K. Balasubramanian, *J. Chem. Phys.* **93** (1990) 625;

D. Dai and K. Balasubramanian, *Chem. Phys. Lett.* **195** (1992) 207.

[37] R.J. van Zee, Y.M. Hamrick, S. Li and W. Weltner Jr., *Chem. Phys. Lett.* **195** (1992) 214.

[38] G. L. Estiu and M.C. Zerner, *J. Phys. Chem.* **97** (1993) 13720.

[39] G. L. Estiu and M.C. Zerner, *Int. J. of Quantum Chem.: Quantum Chem. Sym.* **27** (1993) 195.

[40] T. Janssens, G.R. Castro, H. Busse, U. Schneider and K. Wandelt, *Surf. Sci.* **269/270** (1992) 664.

[41] W. Ravenek, A.P.J. Jansen, and R.A. van Santen, *J. Phys. Chem.* **93** (1989) 6445.

[42] B.V. Reddy, S.N. Khanna and B.I. Dunlap, *Phys. Rev. Lett.* **70** (1993) 3323.

[43] Yang Jinlong, F. Toigo Wang Kelin and Zhang Manhong, *Phys. Rev. B* **50** (1994) 7173.

[44] S.C. Wu, K. Garrison, A.M. Begley, F. Jona and P.D. Johnson, *Phys. Rev. B* **49** (1994) 14081.

[45] G. Fabricius, A.M. Llois, M. Weissmann and M.A. Khan, *Phys. Rev. B* **49** (1994) 2121.

6

A density functional study of the Rhodium-CO interaction.

ABSTRACT

The interaction of carbon monoxide with small rhodium clusters is analyzed by means of density functional calculations. Chemisorption of carbon monoxide on the onefold, twofold, threefold and fourfold position has been studied and compared for the various sites. Adsorption energies, optimized geometries and Rh-C stretch frequencies are reported. It is shown that interactions of both σ and π type contribute to the rhodium-CO bond formation. In general four-metal-atom clusters define the minimum size for a reasonable qualitative description of the interactions involved in the CO-metal surface bond. However, larger clusters are necessary to reproduce experimental findings on surfaces. We found that the ten-metal-atom cluster gives an acceptable description. With the use of Becke's gradient correction to the exchange we even were able to reproduce the correct, onefold, site preference. Previously we developed a potential energy surface (PES) from density functional calculations for the interaction of a carbon monoxide molecule with one single rhodium atom. We here present a comparison between predictions based on this PES and actual calculations on the interaction of a carbon monoxide molecule with small rhodium clusters. It is found that the PES has a too strong preference for the higher coordination sites

6.1   INTRODUCTION

The interaction of carbon monoxide (CO) with a transition metal (TM) surface is of great catalytic interest. An example where this interaction plays a crucial role is the industrial production of hydrocarbons from synthesis gas, the Fischer-Tropsch synthesis [1, 2]. Another example, and nowadays perhaps the best known, is in automobile exhaust catalysis [3, 4]. Assuming that the interaction between CO and the surface is mainly of a local nature, chemisorption has been studied for different TM clusters by various methods. It has been possible to gain considerable understanding at a qualitative level about the features that determine chemisorption. The bonding of a CO molecule to a TM surface, although still not fully understand, is generally described by the model suggested by Blyholder in 1964 [5]. In this model the bonding is the result of the donation of the CO 5σ orbital to empty metal levels and the backdonation from the metal to the CO $2\pi^*$ orbital. The metal valence s, p and d electrons are involved in the bonding.

We choose to concentrate on the interaction of CO with rhodium, because of its catalytic importance (for example hydrogenation and oxidation by NO). On rhodium, CO adsorbs molecularly at room temperature, but dissociative adsorption occurs at reaction temperatures. Because of this rhodium is a catalyst for the synthesis of hydrocarbons as well as oxygenated compounds. Particular promoters enhance the selectivity to oxygenated compounds [6]. Experimental studies gave us much insight in the influence of the rhodium particle size, surface structure and surface composition on the reactivity. On the other hand, theoretical investigations prove sometimes to be much more difficult. The incomplete d shell of rhodium, which causes interesting catalytic properties, often leads to great number of low lying states and associated structures. When self-consistent field (SCF) techniques are applied this can result in problems with convergence. A related problem is the difficulty of finding the right electronic configuration amongst the many plausible ones. In some cases an incorrect electronic configuration after adsorption yields repulsion, whereas the proper electron configuration produces a strong bonding [7, 8]. The difficulty of finding the right electronic configuration seems also closely related to the problem of the oscillatory behavior of adsorption energies calculated for various clusters.

From a theoretical point of view, among the quantum chemical methods, the density functional theory (DFT) enables us to consider a wide range of systems at the same level of approximation. Therefore it gives a good opportunity to model chemisorption on TM clusters. In general it is possible to obtain molecular properties that compare well with the measured properties. It can be used to analyze separate interactions in detail. However when one is

interested in quantitative correct adsorption energies the cluster model generally used to represent the metal surface shows its limitations. The results will depend largely on cluster size and shape. The convergence as function of cluster size is usually slow. Considerable effort has been devoted to finding solutions to this problem. One method involves "preparing" the cluster for bonding by specific excitations [9]. Another method applies fractional occupation numbers around the Fermi level (E_F) to suppress the finite size effects of discrete level spacing in clusters [10]. Recently a scheme was developed that breaks the process of chemisorption down into a number of steps. [11, 12]. One of the steps is the removal of an electron from the cluster. The oscillatory behavior of this energy term is then suppressed by replacing it by the experimental work function of the extended substrate. In spite of these efforts, the problem seems not completely satisfactory solved.

Another problem with cluster models is that they sometimes predict a strong preference for the wrong (higher coordination) adsorption site. Carbon monoxide for example is known to bind preferably onefold on rhodium surfaces [13]. *Ab initio* calculations on Rh_n-CO however tend to show a preference for the higher coordination. Finite cluster effects, rather than the method used, seem to be the primary source of the strong overbinding for higher coordination sites. Slab calculations, with good convergence for the chemisorption energy with the number of substrate layers and with the adsorbate-adsorbate distance, can yield the correct coordination site [14]. However, due to the enormous computational effort as well as disk storage requirements this kind of calculations is not (yet) easily performed.

6.2 COMPUTATIONAL DETAILS

We used the Amsterdam density-functional (ADF) program package developed in the group of Baerends [15]. All calculations we report are local spin density (LSD) approximation calculations using the parametrization of Vosko-Wilk-Nusair (VWN) [16] for the exchange-correlation potential. The Stoll correction [17] to use only correlation between electrons of different spin has been added to the VWN potential. For energy calculations we used relativistic corrections [18] and Becke's gradient or non-local (NL) correction [19].

For carbon and oxygen the 1s core, and for rhodium the electrons up to and including the 4p core are kept frozen. Single-ζ functions are used for core orthogonalization. The valence functions are of double-ζ quality with a triple-ζ d for rhodium. For all atoms polarization functions have been added. The exponents of the STO basis sets can be found elsewhere [20]. In most of our calculations we fixed the Rh-Rh and C-O distance to 2.6901 Å (bulk) [21] and 1.128 Å (free gas geometry) [22] respectively. The Rh-C distance was always optimized.

ADF represents the molecular orbitals as linear combinations of atomic Slater type orbitals (STO's). The integrals are computed numerically [23]. The adsorption energy ΔE_{ads} is calculated with the Ziegler transition state method [24], and defined as the energy difference between the fragments A and B and the overall molecule AB:

$$\Delta E_{ads} = E(AB) - E(A) - E(B). \tag{6.1}$$

It can be separated into contributions that derive from electrostatic interactions and exchange repulsion, this results in a steric repulsion, and a part that derives from orbital interaction.

$$\Delta E_{ads} = \Delta E_{steric} + \Delta E_{int}. \tag{6.2}$$

Here ΔE_{steric} is the energy change due to superposition of the fragments A and B without changing their molecular orbitals, and ΔE_{int} the energy change upon the formation of the molecular orbitals of A-B. We will use this decomposition to analyze the interaction of carbon monoxide with rhodium in more depth, together with the overlap population density of states (OPDOS) [25] or crystal orbital overlap population (COOP) [26].

6.3   RESULTS AND DISCUSSION

6.3.1   CO chemisorption on a rhodium atom

We reported before [18] that the ground state of Rh-CO is $^2\Sigma^+$ for small, and $^4A'$ for larger Rh-C distances. Corresponding respectively to the $4d^9$, and $4d^8 5s^1$ configuration of rhodium. The latter is the ground state of rhodium and CO separated at infinity. The $^4A'$ state is a bent structure. In contrast to some of the earlier calculations [27, 28, 29, 30] we find the quartet states bonding. Calculated properties for four different states of CO chemisorption on a single rhodium atom are summarized in table 6.1. We see that as the charge on CO decreases as the adsorption decreases and the distance between Rh and CO increases. This increased distance lowers the steric repulsion, but on the same time the interaction energy.

Table 6.1   *Geometry parameters, energies and atomic charges for Rh-CO*

state	Rh-C (Å)	Θ (deg.)	ΔE_{steric} (kJ/mol)	ΔE_{int} (kJ/mol)	ΔE_{ads} (kJ/mol)	q (Rh)	q (C)	q (O)	q(CO)
$^2\Sigma^+$	1.85	0	604	-809	-205	0.21	0.26	-0.47	-0.21
$^2\Delta$	1.88	0	554	-753	-199	0.20	0.25	-0.45	-0.20
$^4A'$	2.18	30	246	-310	-63	0.18	0.25	-0.43	-0.18
$^4\Delta$	2.23	0	215	-240	-25	0.09	0.33	-0.42	-0.09

Table 6.2 shows, in arbitrary units, the calculated overlap population density of states (OPDOS) for Rh-CO. A positive sign implies a bonding interaction, and a negative sign implies an anti-bonding interaction. We see that the interaction of Rh(4d) with the CO(5σ) and CO(2π*) is always attractive. The Rh(5s) orbital is responsible for a bonding interaction with CO(5σ) for the doublet states, but anti-bonding for the quartet states. The bent structure is the only geometry with an interaction between Rh(5s) and CO(2π*). This interaction significantly increases the bonding between the rhodium atom and the CO molecule. The Rh(5p) orbital shows an opposite behavior as the Rh(5s), slightly anti-bonding for the doublet states and slightly bonding for the quartet states.

Table 6.2 OPDOS (in arbitrary units) for four electronic configurations of Rh-CO.

state	Rh-C (Å)	Θ (deg.)	4d-5σ	4d-2π*	5s-5σ	5s-2π*	5p-5σ	5p-2π*	total
$^2\Sigma^+$	1.85	0	0.10	0.20	0.10	—	-0.02	0.00	0.37
$^2\Delta$	1.88	0	0.06	0.18	0.15	—	-0.01	0.00	0.38
$^4A'$	2.18	30	0.03	0.08	-0.03	0.05	0.07	0.00	0.20
$^4\Delta$	2.23	0	0.03	0.09	-0.05	—	0.09	0.01	0.16

6.3.2 CO chemisorption on small rhodium clusters

The results for carbon monoxide chemisorption on small (two, three and four atoms) rhodium model clusters are collected in tables 6.3 (energies) and 6.4 (OPDOS analysis). Measurements for the desorption energy of carbon monoxide from an onefold site yielded a bonding energy of about -120 kJ/mol for the (100) and -130 kJ/mol for the (111) surface [31]. Similar adsorption energies are expected for other surface sites. Our calculations give in general somewhat weaker adsorption energies. The only model for the (111) surface we studied, tetrahedral Rh₄, underestimates the adsorption energy for the onefold position by almost 100 kJ/mol. Partially, this seems to be due to fixing the C-O distance, as shown later. Comparison between the overlap population density of states (OPDOS) of different adsorption sites of each cluster is especially useful for the same rhodium-carbon distances. Table 6.4 was computed for a Rh-C distance of 2 Å. This table also shows the transition energy (ΔT, in kJ/mol) in going from the most stable adsorption site to the other adsorption site, without the inclusion of Becke's gradient correction to the exchange. Becke's correction is added after SCF to the calculated energy, and has no influence on the calculated OPDOS.

Table 6.3   *Geometry, configuration, energies, and Rh-C stretch frequency for Rh$_n$-CO (n=2,3,4).*

Cluster	Site	Rh-C (Å)	configuration	ΔE_{steric} (kJ/mol)	ΔE_{int} (kJ/mol)	ΔE_{ads} (kJ/mol)	ω_e (cm^{-1})
Rh$_2$[D_{lin}]-CO	onefold	1.951	$\sigma^{10}\pi^{11}\delta^{7}$	308	-357	-50	310
	twofold	2.028	$a_1^{12}a_2^{3}b_1^{7}b_2^{6}$	861	-1031	-169	390
Rh$_3$[D_{3h}]-CO	onefold	1.981	$a_1^{17}a_2^{4}b_1^{8}b_2^{8}$	272	-310	-38	350
	twofold	1.982	$a_1^{16}a_2^{5}b_1^{7}b_2^{9}$	838	-955	-117	370
	threefold	2.124	$a_1^{12}a_2^{3}e^{22}$	922	-1019	-98	360
Rh$_4$[T_d]-CO	onefold	2.106	$a_1^{16}a_2^{2}e^{28}$	178	-222	-33	220
	twofold	1.984	$a_1^{18}a_2^{6}b_1^{10}b_2^{12}$	836	-917	-81	380
	threefold	2.101	$a_1^{14}a_2^{3}e^{29}$	908	-947	-38	350
Rh$_4$[D_{4h}]-CO	onefold	1.955	$a_1^{20}a_2^{6}b_1^{9}b_2^{11}$	275	-376	-101	300
	twofold	2.084	$a_1^{19}a_2^{6}b_1^{10}b_2^{11}$	553	-592	-40	400
	fourfold	2.303	$a_1^{12}a_2^{2}b_1^{4}b_2^{4}e^{24}$	752	-769	-17	270

From table 6.3 we see that CO prefers the twofold position, followed by the threefold position. The onefold position is usually the most unfavorable, except for the square Rh$_4$. Although the higher adsorption sites have a much larger steric repulsion, this is more than compensated by an increased orbital interaction. The preference for higher coordination that the small rhodium clusters show is mainly due to a strong attractive interaction with the CO($2\pi^*$) orbital. The interaction between rhodium and the CO(5σ) also increases for higher coordinations. For larger clusters the delocalisation of the corresponding group-orbitals will become more important, resulting in a preference for the onefold adsorption. Analyzing the contribution of the different rhodium orbitals to the bonding with CO, we see that the bonding between Rh(4d) and CO increases going from onefold to higher coordination, while the bonding of CO with Rh(5s) and Rh(5p) almost remains constant.

Previously we developed a PES for the interaction of CO with a single rhodium atom [18], representing the potential as a spherical expansion using various types of functions. The best results we obtained with Morse functions. With this analytical PES it is possible, in crude approximation, to calculate the adsorption energy of CO on n rhodium atoms by

$$\Delta E_{ads}(Rh_n - CO) = \sum_{i=1}^{n} V(R_i, \Theta_i) \qquad (6.3)$$

Here R is the distance between Rh and the CO center-of-mass (CO$_{CoM}$), and Θ is the angle between Rh-CO$_{CoM}$ and C-O. We will compare the PES predictions with actual calculations.

Table 6.4 OPDOS (in arbitrary units) for Rh$_n$-CO The rhodium-carbon distance is fixed at 2 Å. ΔT is the energy difference (in kJ/mol) with respect to the most stable site without Becke correction.

Cluster	Site	4d-5σ	4d-2π*	5s-5σ	5s-2π*	5p-5σ	5p-2π*	total	ΔT
Rh$_2$[D$_{lin}$]-CO	onefold	0.06	0.14	0.10	—	-0.04	0.01	0.27	198
	twofold	0.12	0.21	0.11	0.03	-0.02	-0.01	0.43	0
Rh$_3$[D$_{3h}$]-CO	onefold	0.06	0.14	0.11	—	-0.07	0.01	0.25	169
	twofold	0.15	0.22	0.10	0.02	-0.04	-0.02	0.43	19
	threefold	0.17	0.25	0.05	0.06	-0.04	-0.03	0.46	0
Rh$_4$[T$_d$]-CO	onefold	0.03	0.12	0.17	—	-0.08	0.00	0.24	132
	twofold	0.15	0.22	0.11	0.03	-0.03	-0.01	0.48	4
	threefold	0.18	0.25	0.08	0.07	-0.03	-0.04	0.51	0
Rh$_4$[D$_{4h}$]-CO	onefold	0.05	0.14	0.13	—	-0.06	0.00	0.26	4
	twofold	0.11	0.20	0.10	0.02	-0.04	-0.01	0.37	0
	fourfold	0.20	0.29	0.05	0.04	-0.07	-0.07	0.43	55

• **Rh$_2$-CO.** One of the first ab initio calculations on Rh$_2$-CO, an unrestricted Hartree-Fock study without correlation effects of Mains and White [32] showed that the twofold site is favored over the onefold site by 89 kJ/mol. For their not fully optimized twofold geometry (Rh-C=1.9 Å, Rh-Rh=2.69 Å, and C-O=1.1 Å), Mains and White report an adsorption energy of -55 kJ/mol. Later Estiu and Zerner studied Rh$_2$-CO by means of intermediate neglect of differential overlap (INDO) calculations [33]. This study revealed a triplet as the most stable state with an adsorption energy of -60 kJ/mol for their onefold structure show in fig. 6.1(a), and -244 kJ/mol for their twofold structure, shown in fig. 6.2(b). The Mulliken populations of the rhodium atom(s) to which CO is bonded are 4d$^{8.26}$ 5s$^{0.51}$ 5p$^{0.33}$ and 4d$^{8.31}$ 5s$^{0.34}$ 5p$^{0.29}$.
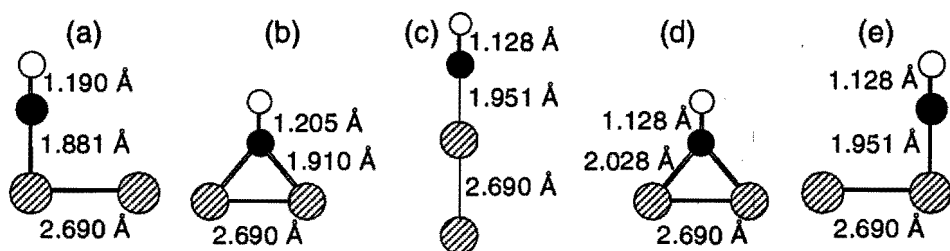
Fig. 6.1 Geometries of CO adsorption on Rh$_2$. INDO [33] results (a) onefold, and (b) twofold, and DFT results [this work] (c) onefold, (d) twofold, and (e) onefold.

We kept the Rh_2 cluster and CO adsorbate fixed, and optimized the Rh-C distance for both the onefold, fig. 6.1(c), and twofold site, fig. 6.1(d). The results are collected in table 6.3. The ground state of both geometries was a triplet. Our Rh-C distance is somewhat longer (for fixed C-O=1.128Å) than was found in both previous Rh_2-CO studies [32, 33]. The adsorption energies are comparable to those found by Estiu and Zerner [33]. The configuration of the rhodium atom(s) to which CO is bonded is $4d^{8.06} 5s^{0.81} 5p^{-.01}$ and $4d^{8.26} 5s^{0.56} 5p^{0.00}$. Both coordinations involve σ and π type interactions. The σ interactions consist of charge transfer from $CO(5\sigma)$ to empty rhodium orbitals along with a repulsive interaction between the $CO(5\sigma)$ lone pair and adjacent metal orbitals. The π interactions consist of back bonding from the metal orbitals to empty $CO(2\pi^*)$. The onefold structure of fig. 6.1(e) shows, with Rh-C fixed at 1.951 Å, a much stronger interaction between Rh_2 and CO: -141 kJ/mol. The steric repulsion increased to 450 kJ/mol, but the orbital interaction -590 kJ/mol.

The adsorption energies according eq. (6.3) are -149 kJ/mol (fig. 6.1c), -208 kJ/mol (fig. 6.1d), and -154 kJ/mol (fig. 6.1e). Comparing these PES results for Rh_2-CO with actual calculations show that, although the site preference is correct, the actual adsorption energies are much lower than the PES predictions. This can not only be explained by the fact that the rhodium atom who is the furthest away from CO is somewhat shielded by the other atom, since the latter atom contributes 99% to the total PES adsorption energy. The PES is also less sensitive to the direction CO interacts with the rhodium dimmer (compare the results for the two onefold geometries). Not only is the agreement between PES and calculated adsorption energy rather poor, also the PES prediction for equilibrium distance and Rh-CO frequency. The PES predicts 1.888 Å, 1.980 Å, and 1.888 Å as optimal Rh-C distance, respectively. The adsorption energies that belong to these structures are -151 kJ/mol, -210 kJ/mol, and -156 kJ/mol. The Rh-C stretch frequency (ω_e) 387 cm^{-1}, 341 cm^{-1}, and 406 cm^{-1}.

• *Rh$_3$-CO.* The Rh$_3$ and CO have been kept fixed, and we optimized the Rh-C distance for the onefold, twofold and threefold site. There exists, as far as we know, no other theoretical study for these systems. Of the three examined geometries, the twofold geometry is the most stable. The threefold site has a similar adsorption energy. Both are quartet states, while the onefold geometry is a doublet. The charge of CO is -0.22, -0.45, and -0.39. The total electronic population of CO thus increases from onefold to higher sites. The configuration of the atom to which CO is bonded shows an increase in the population of the d orbital and a decrease in the population of the s orbital ($4d^{8.04} 5s^{0.77} 5p^{0.01}$, $4d^{8.22} 5s^{0.59} 5p^{0.00}$, and $4d^{8.28} 5s^{0.55} 5p^{0.04}$). This is in accordance with the results in table 6.4, the interaction of Rh(4d) with both CO(5σ) and CO(2π^*) increases while the interaction between Rh(5s) and CO(5σ) decreases. The interaction between Rh(5s) and CO(2π^*), which is not present for the onefold CO adsorption, increases somewhat.
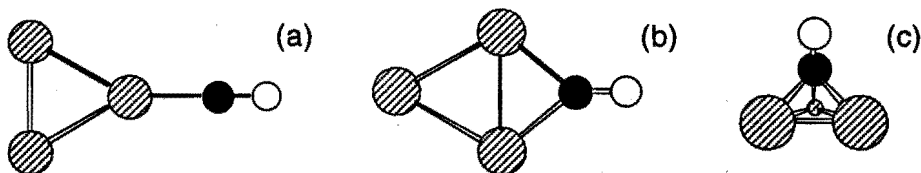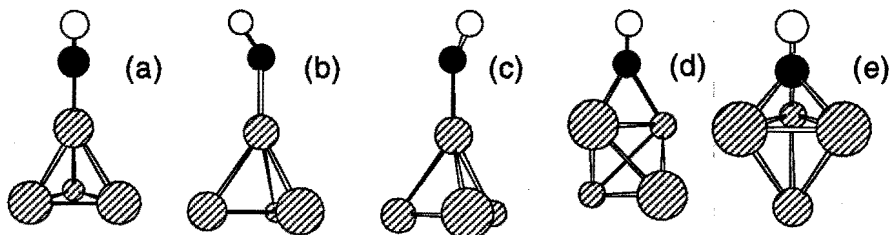
Fig. 6.2 *Geometries of CO adsorption on Rh₃[D₃ₕ]. (a) onefold, (b) twofold, and (c) threefold.*

The PES predictions according eq. (6.3) for the three geometries shown in fig. 6.2 are -148 kJ/mol, -215 kJ/mol, and -258 kJ/mol, respectively. Geometry optimization with the PES yields the following Rh-C distances: 1.886 Å (-153 kJ/mol), 1.975 Å (-215 kJ/mol), and 2.026 Å (-268 kJ/mol). The predicted energies are again too high, and the strong preference for the threefold site does not agree with the actual calculations. For the Rh-CO stretch frequencies we obtained 372 cm^{-1}, 338 cm^{-1}, and 336 cm^{-1}, respectively.

• *Rh₄-CO.* We explored a regular tetrahedral arrangement of Rh₄ with the carbon monoxide adsorbed in the onefold, twofold, and threefold position, as shown in fig. 6.3. Both Rh₄ and CO have been kept fixed, and we optimized the Rh-C distance for all three sites. Again carbon monoxide prefers the twofold site, but now the threefold coordination of CO is not of similar stability as we found for Rh₃-CO. On the onefold and threefold position CO adsorbs weakly. The charge of CO is -0.17, -0.47, and -0.46. The total electronic population of CO increase from onefold to higher sites. The configuration of the atom to which CO is bonded shows an increase in population of the d orbital and a decrease in the population of the s orbital: $4d^{8.09}\ 5s^{0.79}\ 5p^{0.06}$, $4d^{8.20}\ 5s^{0.57}\ 5p^{0.05}$, and $4d^{8.24}\ 5s^{0.54}\ 5p^{0.06}$, respectively. This is in accordance with the results in table 6.4, the interaction of Rh(4d) with both CO(5σ) and CO(2π*) increases while the interaction between Rh(5s) and CO(5σ) decreases. The interaction between Rh(5s) and CO(2π*), which is not present for the onefold CO adsorption, increases somewhat for the higher coordination sites.

Fig. 6.3 *Geometries of CO adsorption on Rh₄[Tₐ]. (a) onefold on C₃-axis, (b) onefold tilted 29° from C₃-axis to twofold, (c) onefold tilted 27° from C₃-axis to threefold, (d) twofold, and (e) threefold.*

This system, a model of the (111) surface, has been studied before by others [34, 35]. Goursot *et al.* found, using the (LCGTO) density functional formalism, that CO tilts away from the C_3-axis and becomes roughly perpendicular to the threefold site. We also noticed that CO tilts towards the twofold or threefold site. Both geometries lower the adsorption energy slightly from -33 kJ/mol to -35 kJ/mol. The atomic configuration of rhodium changes to $4d^{8.11} 5s^{0.77} 5p^{0.05}$. To allow a better comparison with the previous results we also optimized the C-O distance. The results of this optimization, together with the previous calculations, are shown in table 6.5.

Table 6.5 *Structural parameters and adsorption energies for $Rh_4[T_d]$-CO The Rh-Rh distance is 2.690 Å for DF/LCGTO (ref. [34]), 2.273 Å for INDO (ref. [35]), and 2.690 Å. for DF/LCSTO (this work).*

Rh_4-CO	Rh-C (Å)			C-O (Å)			ΔE_{ads} (kJ/mol)		
method	DF LCGTO	INDO	DF LCSTO	DF LCGTO	INDO	DF LCSTO	DF LCGTO	INDO	DF LCSTO
onefold[a]	—	1.952	2.106	—	1.186	1.159	—	-96	-48
onefold[b]	—	—	2.106	—	—	1.164	—	—	-38
onefold[c]	1.826	—	2.106	1.164	—	1.164	-223	—	-37
twofold	1.875	1.919	1.984	1.200	1.195	1.205	-228	-138	-130
threefold	1.976	1.944	2.101	1.214	1.210	1.215	-207	-100	-99

[a]CO on C_3 axis; [b]CO tilted from C_3 axis to twofold site; [c]CO tilted from C_3 axis to threefold site.

The configuration of the atom to which CO is bonded shows an increase in the population of the d orbital and a decrease in the population of the s orbital: $4d^{8.09} 5s^{0.75} 5p^{0.04}$, $4d^{8.10} 5s^{0.76} 5p^{0.04}$, $4d^{8.10} 5s^{0.76} 5p^{0.04}$, $4d^{8.18} 5s^{0.55} 5p^{0.03}$, and $4d^{8.24} 5s^{0.52} 5p^{0.05}$. Compared to the atomic rhodium configurations for the fixed C-O distance we see that both the d and s populations decrease. The charge on CO on the other hand increases.

This study, together with the two previous [34, 35], shows a preference for the twofold adsorption position (table 6.5). Our computed adsorption energies are close to the INDO results. In the latter, also the Rh-Rh distance was optimized, without symmetry constraint. This greatly increases the calculated adsorption energy for the twofold and threefold sites to respectively -215 kJ/mol and -274 kJ/mol [35]. For the twofold geometry the two atoms to which carbon monoxide bonds move away from each other, while the other two atoms move somewhat towards each other. For the threefold geometry the same happens, the three atoms to which CO bonds move away from each other, while the other atom moves towards those three atoms. The other available DF results [34] seem to overestimate the adsorption energy.

All three studies show that the C-O distance relaxes. The lengthening of C-O, when moving from onefold to twofold to threefold sites, can be related to the increased metal-$2\pi^*$ backdonation. This weakens the C-O bond. Our optimized C-O distances are close the others, our Rh-C distance on the other hand seems to be somewhat larger. Because of geometric reasons, it is expected that the metal-adsorbate bond distance increases with the number of bonded metal atoms. This is indeed true for all clusters we examined, except for the tetrahedral Rh$_4$ cluster. The related stretching frequencies should decrease.

Table 6.6   *Structural parameters and adsorption energies for Rh$_4$[T$_d$]-CO.*

Rh$_4$-CO	Rh-C (Å)	C-O (Å)	ΔE_{steric} (kJ/mol)	ΔE_{int} (kJ/mol)	ΔE_{ads} (kJ/mol)	ω_e(C-O) (cm^{-1})	Intensity (kJ/mol)	q(CO)
onefold[a]	2.106	1.159	181	-229	-48	1938	1399	-0.22
onefold[b]	2.106	1.165	187	-224	-38	1891	1292	-0.22
onefold[c]	2.106	1.164	186	-223	-37	1894	1337	-0.21
twofold	1.984	1.205	846	-976	-130	1694	544	-0.58
threefold	2.101	1.215	918	-1017	-99	1672	392	-0.58

[a]CO on C$_3$-axis; [b]CO tilted from C$_3$-axis to twofold site; [c]CO tilted from C$_3$-axis to threefold site.

In the method we employ, the SCF procedure is executed with the local density approximation (LDA) and the non-local part is only used to correct the energies afterwards. The incorporation of gradient corrections during the SCF procedure significantly increases the computing effort, while SCF effects are often small, and hardly show up in the computed energies. However, in geometry optimizations the differences can be significant. When the energy gradients are computed from the LDA energy expressions the resulting optimized geometry is the LDA minimum. Our geometries are optimized, by hand, beyond the LDA level. The geometry optimizations by Goursot *et al.* seem to be performed at the LDA level, which might explain the differences between our and their optimized structures. For all adsorption sites of CO on tetrahedral Rh$_4$, we also calculated ω_e(C-O) (see table 6.6).

Predictions according to eq. (6.3) for tetrahedral Rh$_4$ results in: -135 kJ/mol (onefold), -223 kJ/mol (twofold), and -269 kJ/mol (threefold). Geometry optimization yielded 1.883 Å (-156 kJ/mol), 1.968 Å (-223 kJ/mol), and 2.019 Å (-276 kJ/mol), respectively. The predicted energies are too high, and the predicted preference for the threefold site does not agree with the actual calculations. The Rh-CO frequencies found are: 376 cm^{-1}, 338 cm^{-1}, and 332 cm^{-1}. The bend structures are less favorable than when CO is on the C$_3$-axis, 17 kJ/mol when CO is tilted from the C$_3$-axis towards the twofold site, and 15 kJ/mol towards threefold site.

• *Rh₄-CO.* The other Rh_4 cluster we studied is a flat, square, geometry with the carbon monoxide adsorbed in the onefold, twofold, and fourfold position, as shown in fig. 6.4. There exists, at least as far as we know, no other theoretical study for this system. The onefold and twofold geometries are septets, the fourfold geometry a quintet. The onefold site is preferred by CO, followed by the twofold.
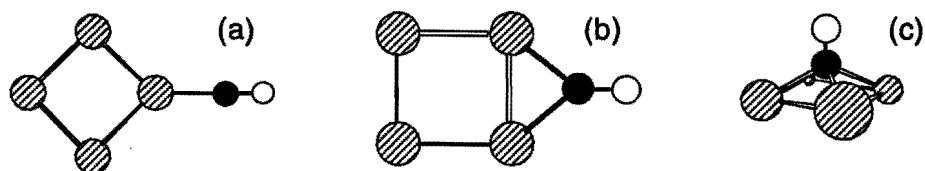

Fig. 6.4   Geometries of CO adsorption on $Rh_4[D_{4h}]$. (a) onefold, (b) twofold, and (c) fourfold.

The PES predictions according eq. (6.3) for the geometries shown in fig. 6.4 produces adsorption energies of: -152 kJ/mol, -206 kJ/mol, and -212 kJ/mol. Geometry optimization yields 1.885 Å (-155 kJ/mol), 1.976 Å (-215 kJ/mol), and 2.152 Å (-232 kJ/mol). The predicted energies are too high, and the predicted preference for the fourfold site does not agree with the actual calculations. Rh-CO frequencies are: 376 cm⁻¹, 332 cm⁻¹, and 243 cm⁻¹.

6.3.3   CO chemisorption on medium rhodium clusters

Results for CO chemisorption on a ten and thirteen atoms cluster are collected in table 6.7.

Table 6.7   Geometry, configuration, energies, and Rh-C stretch frequency for Rh_n-CO (n=10,13).

Cluster	Site	Rh-C (Å)	configuration	ΔE_{steric} (kJ/mol)	ΔE_{int} (kJ/mol)	ΔE_{ads} (kJ/mol)	ω_e (cm⁻¹)
$Rh_{10}[T_d]$-CO	onefold[a]	1.943	$a_1^{28}a_2^8e^{64}$	265	-351	-86	360
	onefold[b]	1.958	$a_1^{18}a_2^4b_1^{12}b_2^{12}$	330	-394	-65	355
	twofold	2.100	$a'^{60}a''^{40}$	689	-692	-3	375
	threefold	2.152	$a_1^{26}a_2^{10}e^{64}$	820	-805	16	360
$Rh_{13}[D_{3h}]$-CO	onefold	1.947	$a'^{74}a''^{53}$	394	-525	-132	403
	twofold[c]	2.128	$a_1^{42}a_2^{23}b_1^{32}b_2^{30}$	626	-713	-87	313
	twofold[d]	2.128	$a_1^{42}a_2^{23}b_1^{31}b_2^{31}$	611	-715	-104	338
	threefold	2.263	$a_1^{31}a_2^{12}e^{84}$	683	-746	-63	281

Rh_{10}/1-fold: on rhodium with [a] 3nn (fig. 6.5a) and [b] 6nn (fig. 6.5b). Rh_{13}/2-fold: [c] fig. 6.8b, [d] fig. 6.8c

• **Rh_{10}-CO.** The Rh_{10} cluster geometry and that of the CO molecule have been kept fixed, and we optimized the Rh-C distance for the onefold, twofold and threefold site (see fig. 6.5). There exists, as far as we know, no other theoretical study for this system. The Rh_{10} cluster is very interesting in that is possesses two different onefold adsorption sites, one with three nearest neighbors (3nn), the other with six nearest neighbors (6nn) [36].
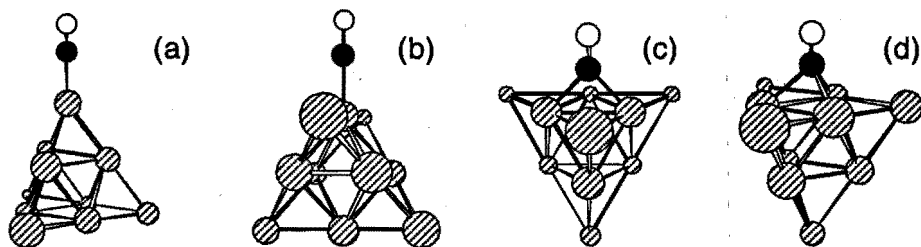

Fig. 6.5 *CO adsorption geometries on $Rh_{10}[T_d]$. (a) onefold on Rh(3nn), (b) onefold on Rh(6nn), (c) twofold, and (d) threefold.*

The charge of CO is -0.27 (both onefold), -0.46 (twofold), and -0.38 (threefold). The total electronic population of CO thus increases from onefold to higher sites. The configuration of the atom to which CO is bonded shows a small decrease in the population of the d orbital and a decrease in the population of the s orbital: $4d^{8.08} 5s^{0.97} 5p^{-.16}$, $4d^{8.06} 5s^{0.79} 5p^{-.02}$, $4d^{7.98} 5s^{0.71} 5p^{0.16}$, and $4d^{7.99} 5s^{0.70} 5p^{0.22}$. This is in accordance with OPDOS results, the interaction of Rh(4d) with both CO(5σ) and CO($2\pi^*$) increases while the interaction between Rh(5s) and CO(5σ) decreases. The interaction between Rh(5s) and CO($2\pi^*$), which is for symmetry reasons not present for the onefold CO adsorption, increases somewhat.

CO prefers the onefold site, the onefold site with three nearest neighbors above the one with six nearest neighbors. CO adsorbs only very weak on the twofold site and not at all on the threefold site. Inclusion of non-local corrections is very important, without them we found adsorption energies of -195 kJ/mol, -192 kJ/mol, -189 kJ/mol and -190 kJ/mol, respectively. We already saw that atoms with less nearest neighbors in the bare cluster have an excess of electrons [36]. Carbon monoxide seems to adsorb stronger to those atoms. Surface diffusion measurements have shown that the activation energy for diffusion increases as the size of the particle decreases. This was explained as a consequence of the larger concentration of electron deficient atomic centers in the small particles and the tighter binding of CO to those centers. This is in contrast to what we found for CO adsorption on Rh_{10}. Fig. 6.6 shows the electron density difference $\rho(Rh_{10}\text{-CO}) - \rho(Rh_{10}) - \rho(CO)$. For all four adsorption geometries there is an increase in the region between CO and the rhodium atom(s) to which it adsorbs.

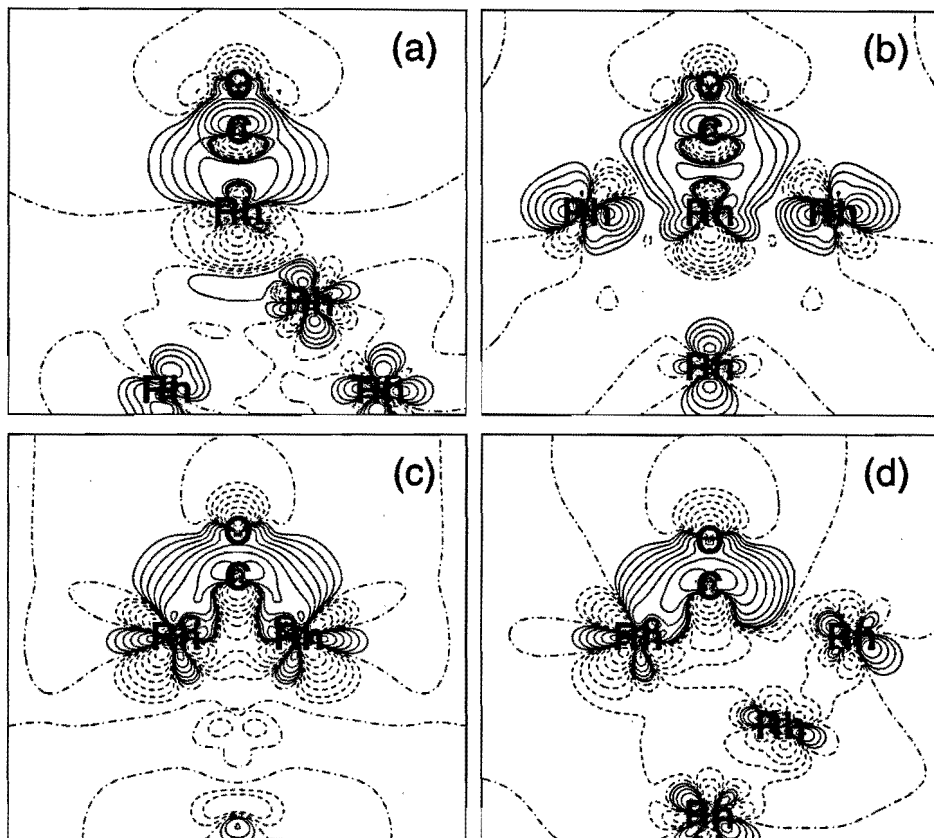**Fig. 6.6** *Contour plots of the electron density difference $\rho(Rh_{10}\text{-}CO) - \rho(Rh_{10}) - \rho(CO)$ for (a) onefold on Rh(3nn), (b)onefold on Rh(6nn) (c) twofold and (d) threefold adsorption. Dashed lines show a decrease and solid lines an increase of the electron density, the dashed-dotted lines depict nodal surfaces. Contours correspond to 0, ±0.01, ±0.02, ±0.04, ±0.08, ±0.16, ±0.32, and ±0.64 e/Å³.*

The OPDOS analysis for the interaction of the rhodium 4d orbitals of the tetrahedral Rh_{10} cluster with CO is presented in fig. 6.7. To allow a better comparison, the Rh-C distance is 2 Å for all four geometries. From these figures we see that the LDOS of rhodium 4d group orbital is quite narrow for the onefold adsorption site with three nearest neighbors compared to the three other possible adsorption sites. The overlap population appears to be a more local property of the CO site. From table 6.4 we find around 0.26 for onefold and 0.43 for twofold adsorption. It thus should reflect more accurately the experimental site preference than the adsorption energy. However the twofold and threefold sites have a higher overlap population,

in contrast to the calculated adsorption energy as well as the experimental site preference. The total overlap population for the onefold adsorption on Rh(3nn) is 0.23, and on Rh(6nn) is 0.20. This is in accordance with the relative stabilities of both onefold sites.
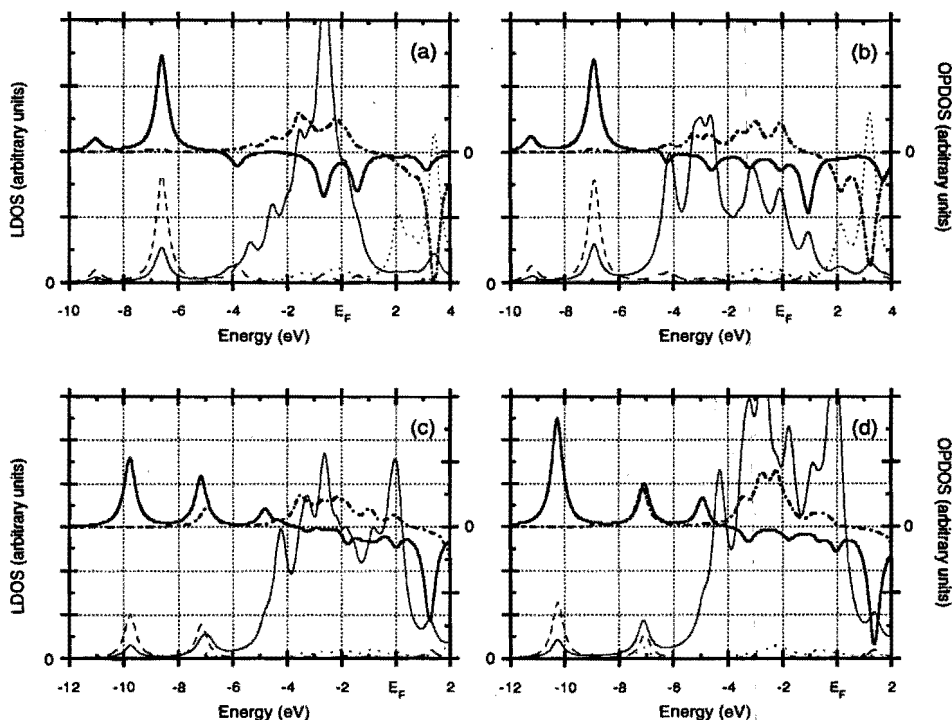
Fig. 6.7 *The LDOS and OPDOS analysis for carbon monoxide adsorption on tetrahedral Rh_{10}.* *Shown here are (———) LDOS of Rh(4d), (— — —) LDOS of CO(5σ), (· · · · ·) LDOS of CO(2π*),* *(———) OPDOS between Rh(4d) and CO(5σ), and (—·—·—) OPDOS between Rh(4d) and CO(2π*).* *for (a) onefold on Rh(3nn), (b)onefold on Rh(6nn) (c) twofold, and (d) threefold adsorption on Rh_{10}.*

• **Rh_{13}-CO.** The Rh_{13} cluster geometry and that of the CO molecule have been kept fixed, and we optimized the Rh-C distance for the onefold, twofold and threefold site (see fig. 6.8). Carbon monoxide prefers the onefold site. CO adsorbs somewhat weaker on both twofold sites and on the threefold site. Again, inclusion of Becke's non-local correction is very important, without it we found adsorption energies of -215 kJ/mol, -210 kJ/mol, -222 kJ/mol and -197 kJ/mol, respectively. The Rh_{13} cluster is interesting in that is possesses one complete saturated rhodium atom, and the electron-deficient nature of the surface atoms [36]. For this reason σ repulsive interactions become likely less important than for smaller clusters.

Our charge of CO is -0.34 (onefold), -0.30 (twofold), -0.35 (twofold) and -0.32 (threefold). The total electronic population of CO is thus approximately constant for all four geometries. Estiu and Zerner [34] found positive Mulliken charges for different one-, two- and threefold sites on a distorted Rh_{13} icosahedron as well as for tetrahedral Rh_4. The configuration of the rhodium atom to which CO is bonded shows an increase in the population of the d orbital and a decrease in the population of the s orbital: $4d^{8.08} 5s^{0.82} 5p^{-.05}$, $4d^{8.17} 5s^{0.67} 5p^{0.15}$, $4d^{8.13} 5s^{0.69} 5p^{0.11}$, and $4d^{8.11} 5s^{0.67} 5p^{0.12}$.
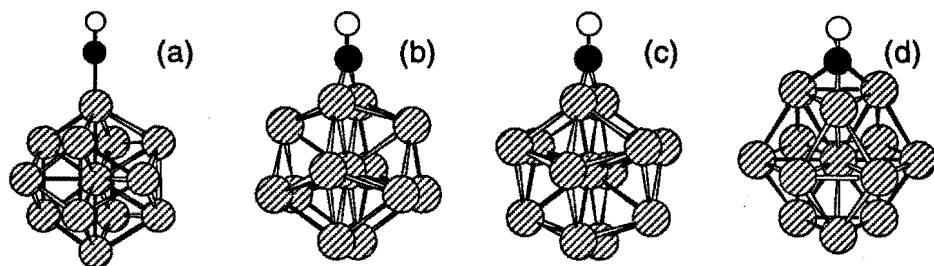
Fig. 6.8   *CO adsorption geometries on $Rh_{13}[D_{3h}]$. (a) onefold, (b, c) twofold, and (d) threefold.*

The coordination numbers of the atoms constituting cluster models must be carefully taken into account. Estiu and Zerner [37] performed calculations for thirteen atom rhodium clusters, showing the importance for complete geometry optimizations of the bare cluster. Zonnevylle *et al.* [38] already mentioned the advantages of the thirteen atom cluster on which a variety of adsorption sites can be compared. It is a highly symmetric cluster, sufficiently large to exhibit metallic characteristics and reasonably low adsorbate-to-substrate ratios while it is still sufficiently small from a computational point of view.

6.4   CONCLUSIONS

The comparison between adsorption energies predicted by our PES and actual calculated values is rather poor. Not only are the adsorption energies too high, also the site preference is not well reproduced. We were unable to improve the PES with our small cluster results.

The rhodium-CO bonding is characterized by π donation from the metal and σ donation from CO. The calculated chemisorption properties of carbon monoxide on relative small model rhodium clusters can reproduce the experimental trends. This study, together with previous calculations on CO adsorption on small rhodium clusters, demonstrates that CO adsorbs stronger on electron deficient centers.

A four-metal-atom cluster seems to define the minimum size for a good qualitative description of the interactions involved in the CO-metal bond. The, for geometric reasons expected, increased metal-CO bond distance is found. However, larger clusters are necessary to reproduce experimental findings. Both our ten and thirteen atom clusters could reproduce the experimental onefold site preference with a reasonable adsorption energy.

6.5   REFERENCES

[1] T.S. Sie, M.M.G. Senden and H.M.H. van Wechem, *Catal. Today* **8**, 371 (1991).

[2] Studies in Surface Science and Catalysis 64: *New trends in CO activation*, L. Cuczi, Ed. (Elsevier, Amsterdam, 1991);

Studies in Surface Science and Catalysis 75: *New frontiers in catalysis*, L. Cuczi, F. Solymosi and P. Tetenyi, Eds. (Elsevier, Amsterdam, 1993).

[3] N.W. Cant and W.K. Hall, *J. Catal.* **27** (1972) 80;

J.C. Schlatter and K.C. Taylor, *J. Catal.* **49** (1977) 42.

[4] Studies in Surface Science and Catalysis 30: *Catalysis and Automotive Pollution Control*, A. Crucq and A. Frennet, Eds. (Elsevier, Amsterdam, 1987);

Studies in Surface Science and Catalysis 71: *Catalysis and Automotive Pollution Control II*, A. Crucq, Ed. (Elsevier, Amsterdam, 1991).

[5] G. Blyholder, *J. Phys. Chem.* **68** (1964) 2772.

[6] T. Koerts and R.A. van Santen, *Catal. Lett.*, **6**, 49 (1990);

T. Koerts, W.J.J. Welters and R.A. van Santen, *J. Catal.*, **134**, 1 (1992);

T. Koerts and R.A. van Santen, *J. Catal.*, **134**, 13 (1992).

[7] D. Post and E.J. Baerends, *Surf. Sci.* **116** (1982) 177;

D. Post and E.J. Baerends, *J. Chem. Phys.* **78**, (1978) 5663.

[8] R.A. van Santen and E.J. Baerends, in: Theoretical models of chemical bonding, Part 4. *Theoretical treatment of large molecules and their interactions*, Z.B. Maksic, Ed. (Springer, Berlin, 1991) p. 323.

[9] I. Panas, J. Schüle, P.E.M. Siegbahn and U. Wahlgren, *Chem. Phys. Lett.* **149** (1988) 265;

J. Schüle, P.E.M. Siegbahn and U. Wahlgren, *J. Chem. Phys.* **89** (1988) 6982;

P.E.M. Siegbahn, L.G.M. Pettersson and U. Wahlgren, *J. Chem. Phys.* **94** (1991) 4024;

M.A. Nygren and P.E.M. Siegbahn, *J. Chem. Phys.* **96** (1992) 7579.

[10] N. Rösch, P. Knappe, P. Sandl and A. Görling, *Int. J. of Quantum Chem.: Quantum Chem. Sym.* **22** (1988) 275;

N. Rösch in: Cluster models for surface and bulk phenomena, NATO ASI Series B, Vol. 283, G. Pacchioni, P.S. Bagus and F. Parmigiani, Eds. (Plenum Press, New York, 1992).

[11] V. Russier and C. Mijoule, *J. Phys: Condens. Matter* **3** (1991) 3193.

[12] V. Russier, D.R. Salahub and C. Mijoule, *Phys. Rev. B* **42** (1990) 5046.

[13] R.A. Marbrow and R.M. Lambert, *Surf. Sci.* **67** (1977) 489;
      D.G. Castner, B.A. Sexton and G.A. Somorjai, *Surf. Sci.* **71** (1978) 519.

[14] G. te Velde and E.J. Baerends, *Chem. Phys.* **177** (1993) 399.

[15] E.J. Baerends, D.E. Elis, and P. Ros, Chem. Phys. **2** (1973) 41;
      P.M. Boerrigter, G. te Velde, and E.J. Baerends, *Int. J. Quantum Chem.* **33** (1988) 87.

[16] S.H. Vosko, L. Wilk, and M Nusair, *Can. J. Phys.* **58** (1980) 1200.

[17] H. Stoll, C.M.E. Pavlidou and H. Preuß, *Theor. Chim. Acta* **49** (1978) 143;
      H. Stoll, E. Golka and H. Preuß, *Theor. Chim. Acta* **55** (1980) 29.

[18] P.M. Boerrigter, Ph.D. thesis, Free University of Amsterdam, Amsterdam (1987).

[19] A.D. Becke, *Int. J. of Quant. Chem.* **23** (1983) 1915; A.D. Becke, *Phys. Rev. A* **38** (1988) 3098.

[20] W. Biemolt and A.P.J. Jansen, *J. Comp. Chem.* **15** (1994) 1053. (Chapter 4 of this thesis).

[21] D.R. Lide, Ed., *Handbook of Chemistry and Physics*, 71st ed. (CRC Press, Boca Raton, 1990).

[22] W.J. Hehre, L. Radom, P.v.R. Schleyer, J.A. Pople, *Ab Initio Molecular Orbital Theory*, (John Wiley & Sons, Chichester, 1986).

[23] G. te Velde and E.J. Baerends, *J. Comput. Phys.* **99** (1992) 84.

[24] T. Ziegler, and A. Rauk, *Theoret. Chim. Acta* **46** (1977) 1.

[25] R.A. van Santen, World Scientific Lecture and Course Notes in Chemistry, Vol. 5: *Theoretical Heterogeneous Catalysis* (World Scientific, Sigapore, 1991).

[26] R. Hoffmann, *Solids and Surfaces* (VCH Publishers, New York, 1988).

[27] J. Koutecky, G. Pacchioni and P. Fantucci, *Chem. Phys.* **99** (1985) 87.

[28] G.W. Smith and E.A. Carter, *J. Phys. Chem.* **95** (1990) 2327.

[29] R. Fournier, *J. Chem. Phys.* **98** (1993) 8041.

[30] D. Dai and K. Balasubramanian, *J. Chem. Phys.* **101** (1994) 2148

[31] P.A. Thiel, E.D. Williams, J.T. Yates Jr and W.H. Weinberg, *Surf. Sci.* **84** (1979) 54;
      H.C. Peebles, D.D. Beck, J.M. White and C.T. Cambell, *Surf. Sci.* **150** (1985) 120.

[32] G. Mains and J.M. White, *J. Phys. Chem.* **95** (1991) 112.

[33] G. L. Estiu and M.C. Zerner, *Int. J. of Quantum Chem.: Quantum Chem. Sym.* **26** (1992) 587.

[34] G. L. Estiu and M.C. Zerner, *J. Phys. Chem.* **97** (1993) 13720.

[35] A. Goursot, I. Papai and D.R. Salahub, *J. Am. Chem. Soc.* **114** (1992) 7452.

[36] Chapter 5 of this thesis.

[37] G. L. Estiu and M.C. Zerner, *Int. J. of Quantum Chem.: Quantum Chem. Sym.* **27** (1993) 195.

[38] M.C. Zonnevylle, J.J.C. Geerlings, and R.A. van Santen, *J. Catal.* **148** (1994) 417.

7 Chemisorption theory of ammonia on copper

ABSTRACT

In this chapter we[*] present local-density-approximation calculations of ammonia adsorption on copper clusters of different sizes (six to eighteen atoms) modelling the (100) and (111) surface. Using for some of the copper atoms only one instead of eleven electrons explicitly in the calculation, did not always work satisfactorily. Comparison of adsorption energies for clusters of related geometry indicates a preference for onefold adsorption. This is due to the Pauli repulsion of the lone-pair orbital of ammonia with the copper 3d electrons, which is minimal for onefold adsorption, as well as an interaction with 4s electrons, which is most attractive in the onefold geometry.

7.1   INTRODUCTION

The interaction of ammonia with copper surfaces is of considerable experimental as well as theoretical interest. From clean surfaces condensed ammonia desorbs molecularly at approximately 200 K, which assuming a pre-exponential factor of 10^{13} s^{-1} corresponds to a heat of adsorption of approximately 50-60 kJ/mol. In the presence of preadsorbed oxygen, however, ammonia remains at the surface to above 240 K, and there is some activation of the nitrogen-hydrogen bond [1]. At room temperature this interaction can lead to the rapid replacement of the oxygen by an adsorbed nitrogen-containing species. The study of the various copper clusters with ammonia presented here will serve as a reference to follow-up studies on ammonia dissociation in the presence and absence of an oxygen atom.

The local-density approximation (LDA) has proven to be a very useful tool in the study of the chemical bond between an adsorbate and a metal surface [2]. The metal surface in these kind of studies is usually modelled by (small) clusters. One question to be answered is whether a procedure can be found to simulate chemisorption to surfaces by adsorption on clusters. This general question has also been addressed by several other authors [3]. We have decided to look for trends in adsorption energies by comparing adsorption on various clusters of related geometries. As far as trends are concerned, representing a surface by a well-chosen cluster appears to be a very reasonable approximation. Slab calculations, where the surface is represented by layers with a infinite number of atoms, would be a better approach when one is interested in quantitatively more accurate results [4].

Examining the Cu/NH$_3$ system shows that chemical bonding is mainly controlled by the interaction of the doubly occupied lone-pair orbital of ammonia, directed away from the molecule, towards the copper surface. Because the energy of the lowest unoccupied molecular orbitals is high, their interaction with the metal surface is expected to be less by more than an order of magnitude. Earlier quantum-chemical studies [5] predicted that the interaction of the occupied copper d orbitals with the ammonia lone-pair orbital is onefold directing. The interaction with the lowest unoccupied ammonia orbitals, which have π symmetry, would prefer higher coordination sites, but is probably too weak. In the case of Ni(111)/CH$_3$ it was found that the interaction of the partially occupied nickel s and p orbitals with the CH$_3$ singly occupied valence orbital, which is capable of forming electron-pair bonds, prefers higher coordination sites [6-8]. We expect for ammonia a competition between the interaction with the copper d orbitals, favouring onefold adsorption, and with the copper s and p orbitals, favouring high-coordinated adsorption. In contrast to this expectation our calculations showed that the interaction with the s-valence electrons also favours the onefold position.

The method we used, enables us to separate the contributions to the adsorption energy into a repulsive part which derives from electrostatic interactions and exchange repulsion, resulting in a steric repulsion, and an attractive part that derives from orbital interaction [9]. We will analyze the changes in these two contributions for all the systems we studied.

7.2 METHOD AND CLUSTER MODELS

We performed non-relativistic, spin-restricted calculations using the local-density approximation with the Vosko-Wilk-Nusair (VWN) local-spin density (LSD) potential [10] as implemented in the Amsterdam-density-functional (ADF) program suite by Baerends and coworkers [11]. In this set of programs the molecular orbitals are represented as linear combinations of atomic Slater type orbitals (STO). Integrals are computed numerically [12], and adsorption energies are computed with the Ziegler transition state method [13].

For nitrogen the 1s core is kept frozen, and for copper the electrons up to and including the 3p core are kept frozen. In the "mixed cluster approach" for some of the copper atoms the electrons up to and including the 3d core are kept frozen. Table 7.1 shows the exponents of the STO basis sets we used in our calculations. Single-ζ functions are used for core orthogonalization. The valence functions are of double-ζ quality with a triple-ζ d for copper (when included as valence). For all the atoms polarization functions have been added.

Table 7.1 *Exponents ζ of the STO's for copper, nitrogen and hydrogen.*

type		ζ		type		ζ			type		ζ	
Cu-3d	1s	24.45	core	Cu-3p	1s	24.45	core			4p	2.00	valence
	2s	8.35	core		2s	8.35	core	N		1s	6.38	core
	3s	6.60	core		3s	6.60	core			2s	1.46	valence
	2p	11.71	core		2p	11.71	core			2s	2.38	valence
	3p	4.53	core		3p	4.53	core			2p	1.12	valence
	3d	2.43	core		3d	1.28	valence			2p	2.58	valence
	4s	1.00	valence		3d	3.10	valence			3d	2.00	valence
	4s	1.90	valence		3d	6.90	valence	H		1s	1.28	valence
	4p	1.00	valence		4s	1.00	valence			1s	0.76	valence
	4p	1.90	valence		4s	1.90	valence			2p	1.00	valence

Figs. 7.1-7.3 show all the clusters and adsorption geometries we studied. The clusters are labelled according to the number of atoms in each layer. An asterisk (*) in this notation denotes that the core for the copper atoms in that layer has been kept frozen until the 4s electrons (one valence electron). For the other copper atoms the core has been kept frozen up to and including the 3p electrons (eleven valence electrons). The copper-copper distance is set equal to the nearest-neighbour distance in the bulk: 2.556 Å [14]. For ammonia, the free gas geometry is used: the N-H bond distance is 1.008 Å and the H-N-H bond angle is 107.3° [14].

Cu(1, 4, 1)   Cu(5, 4, 1)   Cu(5, 4, 5)   Cu(9, 4, 5)
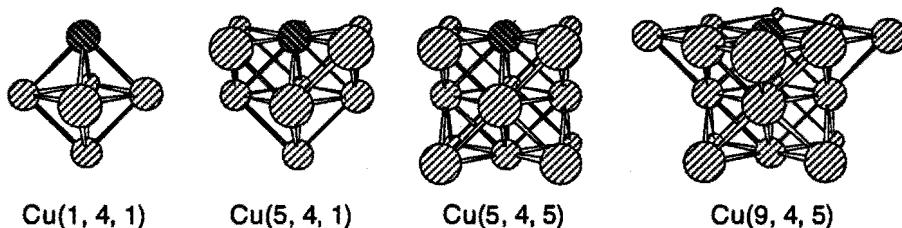
Fig. 7.1 *Clusters models for the onefold ammonia adsorption on a Cu(100) surface. The clusters are labelled according to the number of atoms in each layer, so Cu(I, J, K) refers to I copper atoms in the first layer, J in the second and K in the third. Dark atoms are "central copper atoms".*

A full geometry optimization of the Cu(1)-NH$_3$ system, when the N-H bond distance and the H-N-H bond angle are also optimized, lowers the adsorption energy by only 10 kJ/mol. This is about the same size as the error in the calculation due to numerical inaccuracies, and therefore the geometry optimization of the ammonia is ignored in this discussion. For each cluster the copper-nitrogen distance was optimized. At the optimum copper-nitrogen distance, we also included gradient or non-local corrections for the exchange [15] and correlation [16]. With these corrections, the calculated energies are in better agreement with the experimental value, but the differences between the various clusters essentially remain the same.

Cu(7, 3)   Cu(8, 3)   Cu(12, 6)
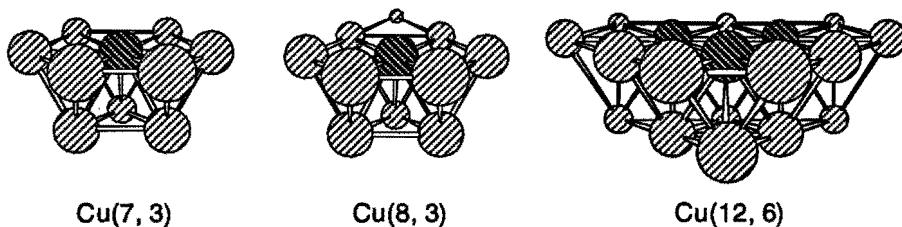
Fig. 7.2 *Clusters models for the one- and threefold ammonia adsorption on a Cu(111) surface.*

Cu(8, 6, 2)   Cu(4, 5)
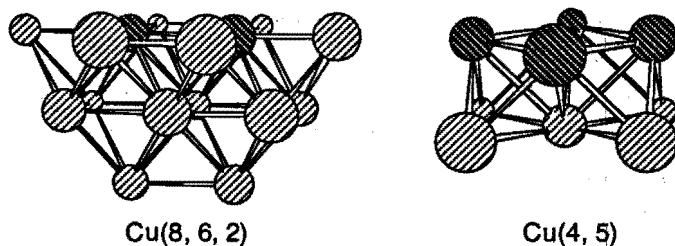
Fig. 7.3   *Clusters models for the two- and fourfold ammonia adsorption on a Cu(100) surface.*

7.3   RESULTS AND DISCUSSION

The results of the calculations made on the ammonia adsorption on all the copper clusters (figs. 7.1-7.3) are shown in tables 7.2-7.4. Here, the adsorption energy is defined as

$$\Delta E_{ads} = E(Cu_n\text{-}NH_3) - E(Cu_n) - E(NH_3). \qquad (7.1a)$$

This adsorption energy can be decomposed in two main contributions [9],

$$\Delta E_{ads} = \Delta E_{steric} + \Delta E_{int}. \qquad (7.1b)$$

where ΔE_{steric} is the energy change due to superposition of Cu_n and NH_3 without changing their molecular orbitals. This can be considered the contribution due to steric repulsion. The orbital interaction energy, ΔE_{int}, is the energy change upon the subsequent formation of the molecular orbitals of $Cu_n\text{-}NH_3$. The separate contributions are presented in the same tables.

7.3.1   Mixed cluster approach

The effect of keeping the core frozen up to and including the 3d electrons was studied for the Cu(5, 4, 1) cluster (see fig. 7.1). This approximation should result in a considerable reduction in the size of the calculations when the d valence electrons on all atoms next to those directly in contact with the adsorbate are frozen, in this case Cu(1+4*, 4*, 1*). Such kinds of calculations have given successful results earlier, especially for the adsorption of hydrogen atoms to nickel clusters [17].

We compared Cu(5, 4, 1) clusters with a different number of copper atoms that were frozen, and in various arrangements. The results have been collected in table 7.2. If we compare clusters that differ only in the second and third layer, we find that the steric repulsion, orbital interaction, adsorption energy, and optimum copper-nitrogen distance change only a little. Also the stretch frequency (ω) changes less than 10%.

Table 7.2   *The influence of using a copper 3d-frozen core in calculations on Cu_{10}-NH_3.*

Cluster geometry	Cu-N distance fixed at 2.03 Å				Cu-N distance optimized				
	ΔE_{steric} (kJ/mol)	ΔE_{int} (kJ/mol)	ΔE_{ads} (kJ/mol)	CPU time	Cu-N (Å)	ΔE_{steric} (kJ/mol)	ΔE_{int} (kJ/mol)	ΔE_{ads} (kJ/mol)	ω (cm^{-1})
Cu(5, 4, 1)	58	-135	-77	=100 %	2.13	30	-109	-80	305
Cu(5, 4, 1*)	63	-136	-73	91 %	2.14	33	-108	-76	281
Cu(5, 4*, 1)	56	-127	-71	81 %	2.15	25	-99	-74	287
Cu(1+4*, 4, 1)	82	-120	-38	85 %	2.29	20	-70	-50	168
Cu(5, 4*, 1*)	59	-128	-69	75 %	2.15	27	-99	-73	284
Cu(1+4*,4*, 1*)	82	-114	-32	63 %	2.33	14	-62	-46	174
Cu(5*, 4*, 1*)	251	-113	137	60 %	not bonding / not optimized				

The effect when first-layer atoms are kept frozen is, however, much larger, the calculated energies are very different, the optimum copper-nitrogen distance has changed significantly, and ω has now changed by more than 10%. Apparently, computed molecular orbitals of the copper clusters are different whether or not the d orbitals of the first-layer atoms are frozen. This affects the repulsion with ammonia due to the d_{z^2}-orbital of the central copper atom, the copper atom to which ammonia is directly bonded.
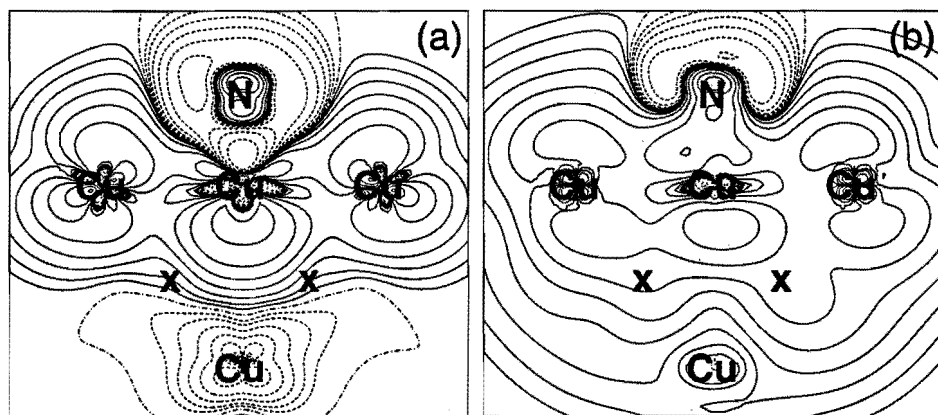
Fig. 7.4   *Contour plots of the electron density differences (a) $\rho(Cu_{10}NH_3)$-$10\rho(Cu)$-$\rho(NH_3)$ for $Cu(5, 4, 1)$-NH_3 and (b) $\rho(Cu_9Cu_1{}^*NH_3)$-$9\rho(Cu)$-$1\rho(Cu^*)$-$\rho(NH_3)$ for $Cu(5, 4, 1^*)$-NH_3. Dashed lines show a decrease, solid lines an increase of the electron density and the dashed-dotted lines depict nodal surfaces. Subsequent contours correspond to 0, ±0.001, ±0.002, ±0.004, ±0.008, ±0.016, ±0.032, ±0.064, ±0.128, ±0.256 and ±0.512 electrons/Å^3. "x" is the projection of a Cu on the plane.*

The results in table 7.2 seem to imply that freezing of the d orbitals in the second and third layer is possible. The electron-density difference (fig. 7.4) for Cu(5, 4, 1) and Cu(5, 4, 1*) indicate however, that also a cluster with only one frozen copper atom in the third layer respond differently to NH_3 adsorption. Because of this behaviour and the relative small reduction of the computational effort we decided not to use the "mixed cluster approach".

7.3.2   Onefold versus higher coordination

Table 7.3 shows for the different adsorption configurations and clusters the calculated steric repulsion (ΔE_{steric}), total orbital interaction (ΔE_{int}) and adsorption energy (ΔE_{ads}), and the total adsorption energy including non-local corrections (ΔE_{ads}/NL). Also the coordination number of ammonia, the number of nearest neighbours (nn) of the central copper atom, the optimized copper-nitrogen distance (Cu-N), and the vibrational frequency (ω) are mentioned. For the calculation of the optimum copper-nitrogen distance and ω the non-local correction is not included. Comparison is made between clusters simulating the (100) surface and (111) surface. Clusters studied vary between six and eighteen copper atoms (see figs. 7.1-7.3). Cluster sizes have been chosen such that on the clusters simulating the (100) and (111) surfaces, the copper atoms involved in the bond with ammonia, have the same number of nearest-neighbour copper atoms as on the corresponding metal surface.

Table 7.3   *Surface, number of nearest neighbours of the central copper atom (nn), geometry, energies and vibrational frequency (ω) for all Cu_n-NH_3. The clusters are sketched in figs. 7.1-7.3.*

	Cluster geometry	Surface	nn	Cu-N (Å)	ΔE_{steric} (kJ/mol)	ΔE_{int} (kJ/mol)	ΔE_{ads} (kJ/mol)	ΔE_{ads}/NL (kJ/mol)	ω (cm⁻¹)
Atom	Cu(1)	---	0	2.03	127	-212	-85	-40	335
onefold	Cu(1, 4, 1)	(100)	4	1.94	75	-233	-157	-105	400
onefold	Cu(5, 4, 1)	(100)	8	2.13	30	-109	-79	-25	305
onefold	Cu(5, 4, 5)	(100)	8	2.13	20	-111	-91	-35	293
onefold	Cu(9, 4, 5)	(100)	8	2.07	21	-132	-111	-48	344
onefold	Cu(7, 3)	(111)	9	2.15	47	-117	-69	-12	272
onefold	Cu(8, 3)	(111)	9	2.15	50	-119	-69	-10	274
twofold	Cu(8, 6, 2)	(100)	8	2.48	35	-98	-65	-11	180
threefold	Cu(12, 6)	(111)	9	2.85	20	-57	-37	4	133
fourfold	Cu(4, 5)	(100)	5	2.03	96	-58	39	—	—

The steric repulsion decreases when a single copper atom acquires neighbours. This is due to a contraction of the electron density closer to the nuclei. The steric repulsion for the various clusters that simulate the (100) surface, i.e. Cu(1, 4, 1), Cu(5, 4, 1), Cu(5, 4, 5), and Cu(9, 4, 5) (see fig. 7.1), does not seem to have converged. However, we may conclude that it is only a few kJ/mol. The clusters Cu(9, 4, 5) and Cu(8, 6, 2), both simulating the (100) surface, have about the same number of atoms in the first layer, and about the same total number of atoms. Thus they may be compared. It is interesting to note that the steric repulsion for twofold adsorption is larger than that of onefold adsorption, in accord with predictions of elementary quantum chemistry [18]. We find a significant increase in the copper-nitrogen distance when the coordination of ammonia on the (111) surface is increased from onefold to threefold; compare Cu(7, 3) and Cu(12, 6). This is due to enhanced repulsion in the high-coordination site pushing the ammonia molecule away from the surface. Table 7.3 also shows that the steric repulsion is less for the (100) surface than for the (111) surface.

If we compare the orbital interaction for the clusters Cu(1, 4, 1), Cu(5, 4, 1), Cu(5, 4, 5), and Cu(9, 4, 5), we see that there is much larger change when the number of nearest neighbours of the central copper atom than when the size of the cluster changes. This indicates that the formation of the bond with the ammonia is a local process. The decrease of the orbital interaction with the number of nearest cluster-atom neighbours relates to the increased localization energy [5]. The orbital interaction energy for the (100) surface decreases (in the absolute sense) when the coordination of ammonia is increased. This apparently unexpected behaviour can be understood, when one analyzes the electron-energy distribution in different coordination sites. As we illustrate below this is most conveniently done using the concept of group orbitals [5, 19, 20]. We have shown previously for carbon monoxide adsorption that the reduction of the Pauli-repulsion forms a large part of the orbital interaction energy [21]. We find the same here.

Fig. 7.4(a) shows that between the nitrogen atom and the central copper atom there is a decrease of electron density near the copper atom and an increase near the nitrogen atom. This latter feature can be traced back to the rehybridization of the lone-pair orbital of ammonia. A population analysis shows that this orbital gets more s character, and less p character. Note that this kind of behaviour is absent in fig. 7.4(b).

Both the steric repulsion and the orbital interaction energy drive the ammonia molecule towards the onefold site; the adsorption energy is clearly largest for the onefold site. It also seems that ammonia prefers the (100) to the (111) surface. This is mainly due to the difference in steric repulsion.

The calculated stretch frequency (ω) of ammonia on the various copper clusters shows a decrease when moving from onefold to higher coordination. For onefold coordination ω is

higher on the (100) surface clusters than on the (111) surface clusters. For the (100) surface, the calculated frequencies compare rather well with the experimental value of 360 cm^{-1} [22]. We were unable to compare the calculated frequencies for the (111) surface with earlier calculations or measurements, but the results are comparable to those obtained from various other systems.

A detailed analysis of the interaction of ammonia with Cu(9, 4, 5), Cu(8, 6, 2), Cu(7, 3), and Cu(12, 6) is presented in figs. 7.5-7.8. These figures show the local density of states (LDOS) before and after chemisorption, and the overlap population density of states (OPDOS). For higher-coordination situations the ammonia σ-orbital interaction with the local density of states of totally symmetric surface orbital fragments is shown. For example for the twofold coordination the s-atomic group orbital is

$$\Psi_g^s (\text{twofold}) = \frac{1}{\sqrt{2+2S}} [\varphi_1(s) + \varphi_2(s)]; \tag{7.2}$$

$\varphi_1(s)$ and $\varphi_2(s)$ are the atomic orbitals involved, S is their overlap. In threefold coordination, the corresponding group orbital becomes

$$\Psi_g^s (\text{threefold}) = \frac{1}{\sqrt{3+6S}} [\varphi_1(s) + \varphi_2(s) + \varphi_3(s)]. \tag{7.3}$$

As long as the Cu-N distance does not change one expects the average LDOS of the NH$_3$ σ orbital to be lower in high coordination sites than lower coordination sites. Calculation of the orbital overlap with group orbitals Ψ_g^s shows that the interaction increase with $\approx \sqrt{N}$, the number of neighbour atoms. As we will discuss below, the NH$_3$ σ-orbital density should shift downward because it forms, at low energies, part of a bonding orbital fragment. This can indeed be noted in fig. 7.5, which are computed for the same Cu-N distance for both clusters.
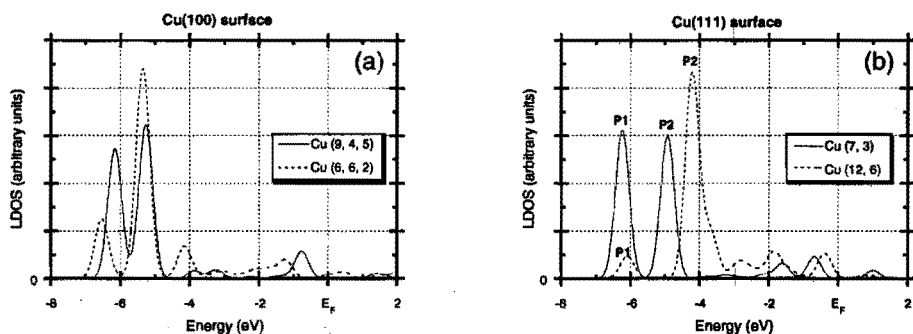
Fig. 7.5   *LDOS of the NH$_3$ σ-orbital after adsorption on (a) Cu(100) cluster models, and (b) Cu(111) cluster models. Zero energy corresponds to the Fermi level (E$_F$).*

Differences in the copper-nitrogen equilibrium distance dominate the LDOS features presented in fig. 7.5(a). Fig. 7.6(a) demonstrates the computed dependence of the position of the two lowest of the σ LDOS peaks (P1 and P2) as shown in fig. 7.5(a) as a function of copper-nitrogen. In figs. 7.5(a) and 7.5(b) the ammonia σ LDOS are compared in low and high coordination on clusters simulating the (100) and (111) surface respectively of an ammonia adsorbed in its equilibrium position. As follows from fig. 7.6(a), the larger equilibrium distance (R_0) for the higher-coordination sites dramatically affects the computed LDOS. The upwards shift of ammonia σ LDOS in threefold coordination derives from the small orbital overlap at the large equilibrium distance found. Therefore experimental information about the ammonia σ position with respect to the Fermi level should enable one to confirm the predicted preferential ammonia adsorption in the onefold position.
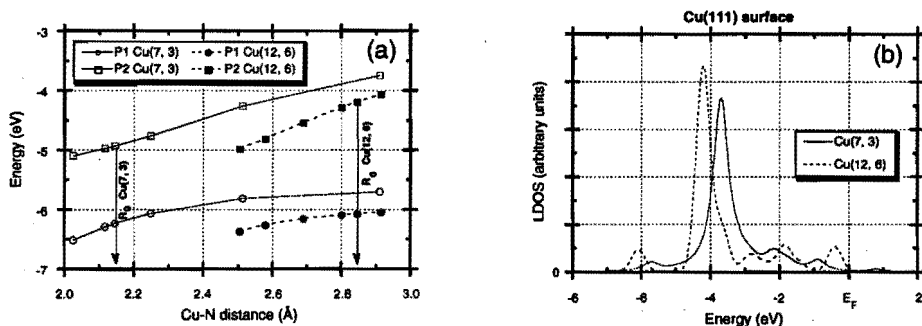
Fig. 7.6 (a) Position of P1 and P2 as a function of Cu-N and (b) LDOS of the NH_3 σ-orbital after adsorption on Cu(111) clusters. R_0 is the equilibrium distance. Zero energy corresponds to E_F.

Similarly as in usual chemical bonding, the bond strength of surface-adsorbate bonds should be related to the population of bonding and anti-bonding orbital fragments between adsorbate and surface [18, 20, 23, 24]. Computation of the OPDOS enables us to analyze this. Results of such an analysis are presented in fig. 7.7. A positive sign implies a bonding interaction, and a negative sign implies an anti-bonding interaction. The calculations in these figures refer to NH_3 adsorbed in a one- and twofold coordination site at the same Cu-N distance. Only for such a case is comparison useful. A breakdown of the interaction with valence copper 4s, as well as 3d and 4p orbitals, is given. In table 7.4, the calculated total orbital populations are presented. The interaction with the s and p orbitals appears to be bonding but that with the d orbitals anti-bonding. This shows that the Pauli repulsion derives

from the interaction with the occupied copper 3d atomic orbitals. This repulsion is larger in the high-coordination site than in the low-coordination site, as was also found in table 7.3.
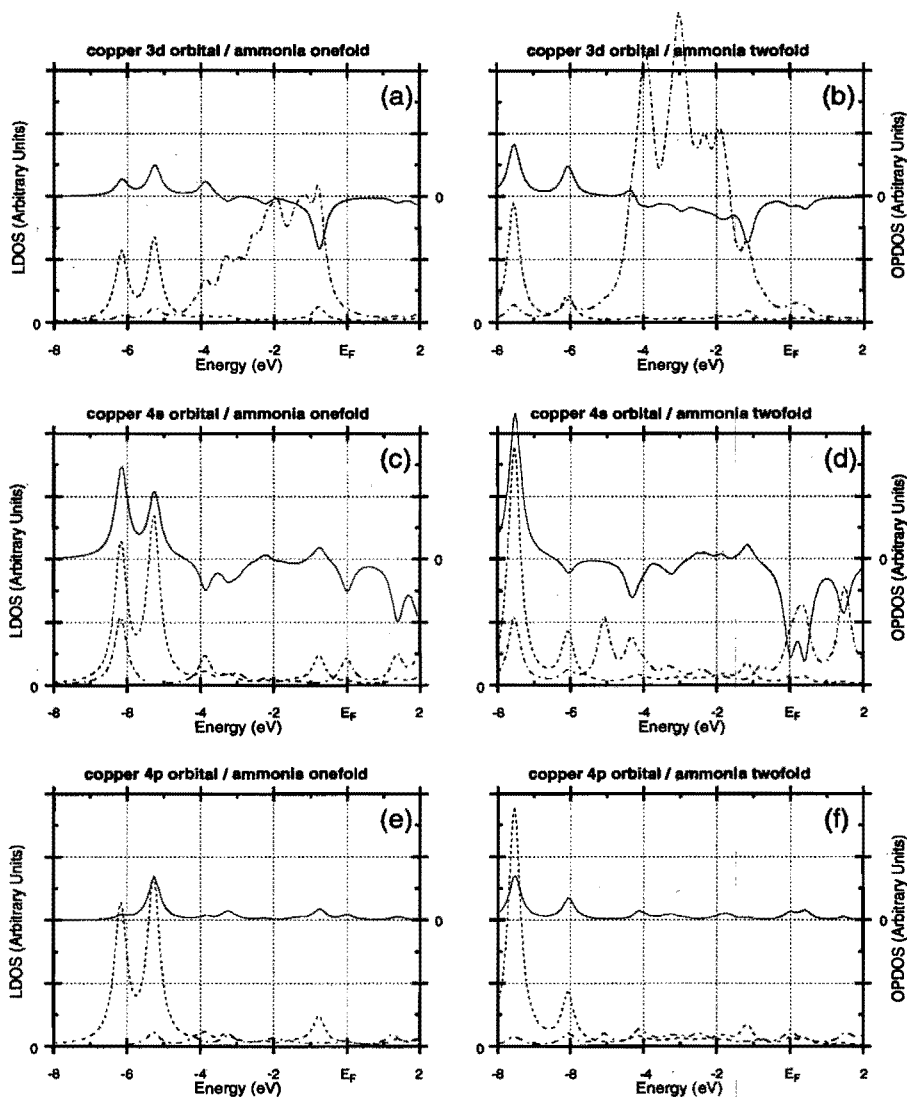

Fig. 7.7 *LDOS of NH₃ σ and copper orbitals, and OPDOS between both after NH₃ adsorption*
on Cu(100) clusters Cu(9, 4, 5), and Cu(8, 6, 2). Respectively for onefold and twofold NH₃ adsorption.
Central copper orbitals: (a, b) 3d (c, d) 4s, (e, f) 4p; NH₃ position: (a, c, e) onefold, (b, d, f) twofold.
Each graph shows - - - - -LDOS of NH₃ σ, - - - - - LDOS of central copper orbitals, and ——— OPDOS.

As the respective OPDOS indicate, there is not only a significant anti-bonding interaction with the copper d-valence orbitals, but also with the s-valence electrons. This is found notwithstanding the earlier observation that the overall interaction with the copper s-valence electrons is bonding. Note, however, that table 7.4 also shows that this bonding interaction is less in the high-coordination site than in the onefold adsorbed position. This result agrees with frontier-orbital arguments [5, 18] that predict a correlation with the σ lower local density of states of s valence group orbitals around the Fermi level in high-coordination site; the discrete nature of the group-orbital local-density of states (GDOS) in the clusters makes such a comparison useless. However, one observes from fig. 7.8 that a shift to an average lower energy is found for GDOS corresponding to high-coordination group orbitals. Returning to fig. 7.7, one sees that the peak position of the bonding σ-s adsorbate-surface s valence orbital interaction is lowest for the twofold-coordination site. This is, as mentioned earlier, partially due to the larger adsorbate-surface interaction, but also due to the lower corresponding GDOS in the higher-coordination site. This can be seen from the GDOS presented in fig. 7.8. As a consequence, the anti-bonding orbital fragments become occupied at lower energy in high-coordination sites than onefold. The weaker interaction energy with s valence atomic orbitals in high coordination then is a consequence.

Table 7.4   *Overlap population of the NH_3 σ orbital with selected copper orbitals (arbitrary units).*

cluster / copper orbital	3d	4s	4p	total
Cu(9, 4, 5)	-0.005	0.693	0.572	1.260
Cu(8, 6, 2)	-0.157	0.372	0.727	0.942
difference	0.152	0.321	-0.155	0.318

The bond strength of onefold-adsorbed ammonia on comparable copper clusters is highest on each surface, from which one concludes that ammonia prefers onefold adsorption on copper (table 7.4). As far as we know, no experimental information on the adsorption geometry of ammonia on copper surfaces is available. However, infrared adsorption spectra of CO adsorbed on copper show that CO also prefers the onefold configuration [25]. Because of the smaller back-donation contribution to the surface chemical bond, a contribution that tends to favour high-coordination sites [5], the predicted onefold adsorption geometry of ammonia is consistent with experimental observation of the adsorption site of carbon monoxide. The predicted higher adsorption-energy value of onefold-adsorbed ammonia to the (100) than on the (111) surface agrees with the more open nature of that particular surface.
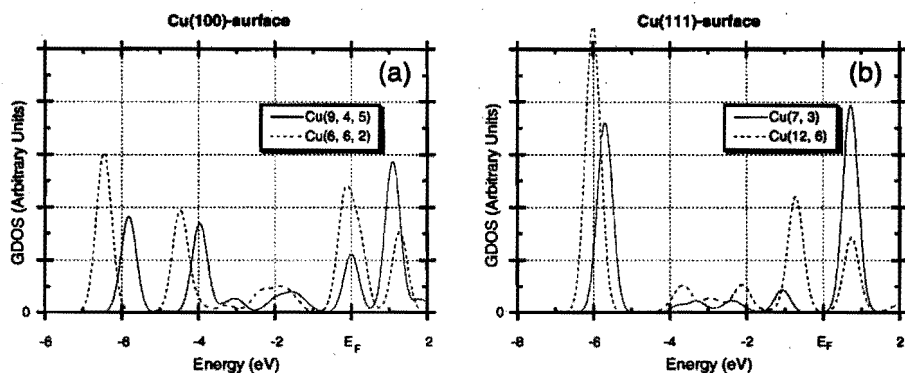
Fig. 7.8 *Group orbital density of states (GDOS) plots of the central copper 4s orbital before the adsorption of ammonia for (a) the (100) surface clusters Cu(9, 4, 5) and Cu(8, 6, 2), and for (b) the (111) surface clusters Cu(7, 3) and Cu(12, 6). Zero energy corresponds to the Fermi level (E_F).*

Chattopadhyay *et al.* [26] predict a slight preference for ammonia adsorbed onefold on the nickel (111) surface. This result of an ab initio configuration interaction (CI) calculation is consistent with our results. The partially occupied nickel d-valence electron band causes the differences in energy of ammonia adsorbed onefold or in higher-coordination sites to be less than on copper. Hermann *et al.* [27] found in cluster calculations for ammonia adsorbed on aluminium also a strong preference for onefold coordination. Pauli repulsion with the high electron-density of this s-p electron metal appears to be responsible as well as the decreased orbital-interaction energy, corresponding to the polarization energy in their calculation.

Bagus *et al.* [28] found with self-consistent field (SCF) calculations for the ammonia adsorption on the (100) model Cu(1, 4) an adsorption energy of -90 kJ/mol at Cu-N=2.3 Å. First nearest neighbors of the chemisorption site were treated at the one electron effective core potential (ECP) level. On the basis of the same kind of calculations, Bauschlicher [29] ruled out the adsorption of ammonia at the threefold site. For the (111) model Cu(12, 6) he found, for ammonia heights above the surface from 2 to 2.5 Å, a repulsive interaction from 67 to 33 kJ/mol, in qualitative agreement with our result at the non-local level.

As long as no reference can be made to larger cluster calculations or results of slab calculations, one cannot verify whether the computed bond strengths have converged to the surface-limiting value. The separate analysis of repulsive and orbital interactions indicates that the computed value for onefold adsorption of ammonia on the Cu(5, 4, 5) cluster may be close to its converged value. We have demonstrated that subdivision of clusters corresponding to models of the same surface makes useful qualitative comparisons possible.

7.4   CONCLUSIONS

Using the mixed cluster approach would at least give rise to a large error in the computed electron densities. If one wishes, nevertheless, to use this approximation, it is important to note that for a proper modelling of the copper surface, it is necessary that the atoms in the first layer are not kept frozen. The copper atoms in the second and following layers seem to play a less important role, although they will still contribute to a more proper description of the metal surface. The total number of copper atoms that is kept frozen also does not seem to determine the accuracy of the mixed cluster approximation. Thus, Cu(5, 4*, 1*), with five frozen atoms, gives a smaller error than Cu(1+4*, 4, 1), with only four frozen atoms compared to Cu(5, 4, 1).

The calculated adsorption energy is probably quantitatively not precise, since we see a rather strong dependence on the size of the cluster. Nevertheless, there is clearly a trend towards onefold adsorption. This is true for the (100) and the (111) surface. Comparing the (100) surface with the (111) surface shows that in onefold adsorption, the steric repulsion is much less for the (100) surface while the orbital interaction is about the same.

With an OPDOS analysis, we were able to show that it is the interaction of ammonia with the copper d orbitals as well as with the copper s-valence electrons which favours the onefold adsorption site, while the interaction of ammonia with the copper p orbitals favours the higher- coordination sites. Finally, we showed that it should be possible to confirm our predicted onefold adsorption geometry for ammonia on copper by determining the ammonia σ LDOS relative to the Fermi level.

7.5   REFERENCES

[1]   P.R. Davies, thesis, the University of Wales, Cardiff (1989) Chapter 4.

[2]   P.J. Feibelman, *Phys. Rev. Lett.* **54** (1985) 2627;

      W. Weinert, A.J. Freeman and S. Ohnishi, *Phys. Rev. Lett.* **56** (1986) 2295;

      D. Post, and E.J. Baerends, *Surf. Sci.* **116** (1982) 177.

[3]   Th.T. Upton and W.A. Goddard III, *CRC Crit. Rev. in Solid State and Mat. Sci.* **10** (1981) 261.

[4]   G. te Velde, thesis, the Free University, Amsterdam (1990).

[5]   R.A. van Santen, *Progr. Surf. Sci.* **25** (1987) 253;

      A. de Koster, A.P.J. Jansen, R.A. van Santen and J.J.C. Geerlings, *Faraday. Discussions Chem. Soc.* **87** (1989) 263.

[6]   C. Zheng, J. Apeloig and R. Hoffmann, *J. Am. Chem. Soc.* **110** (1988) 749.

[7]   P.E.M. Siegbahn, I. Panas, *Surf. Sci.* **240** (1990) 37.

[8]   A. de Koster and R.A. van Santen, *J. Catal.* **127** (1991) 141.

[9]   D. Post and E.J. Baerends, *J. Chem Phys.* **78** (1983) 5663;
      E.J. Baerends and A. Rozendaal in *Quantum Chemistry; The Challenge of Transition Metals and Coordination Chemistry*, A. Veillard Ed., Nato, ASI series, Reidel, Dordrecht (1986) p. 159;
      P.J. van den Hoek, A.W. Kleyn and E.J. Baerends, *Comments At. Mol. Phys.* **23** (1989) 93.

[10] S.H. Vosko, L. Wilk and M Nusair, *Can. J. Phys.* **58** (1980) 1200.

[11] E.J. Baerends, D.E. Elis and P. Ros, *Chem. Phys.* **2** (1973) 41;
      P.M. Boerrigter, G. te Velde and E.J. Baerends, *Int. J. Quantum Chem.* **33** (1988) 87.

[12] G. te Velde and E.J. Baerends, *J. Comput. Phys.* **99** (1992) 84.

[13] T. Ziegler and A. Rauk, *Theoret. Chim. Acta* **46** (1977) 1.

[14] D.R. Lide, ed., Handbook of Chemistry and Physics, 71st Ed. (CRC Press, Boca Raton, 1990).

[15] A.D. Becke, *Int. J. of Quant. Chem.* **23** (1983) 1915; A.D. Becke, *Phys. Rev. A* **38** (1988) 3098.

[16] J.P. Perdew, *Phys. Rev. B* **33** (1986) 8822; erratum ibid. **34** (1986) 7406.

[17] P.E.M. Siegbahn, M.R.A. Blomberg, C.W. Bauschlicher Jr., *J. Chem. Phys.* **81** (1984) 2103.

[18] R.A. van Santen, *Theoretical Heterogeneous Catalysis*, World Scientific lecture and course notes in chemistry, Vol. 5 (World Scientific, Singapore, 1991);
      R.A. van Santen and E.J. Baerends in *Theoretical models of chemical bonding*, Part 4, Theoretical treatment of large molecules and their interactions, Z.B. Maksic' Ed. (Springer, Berlin, 1991) p. 323.

[19] M.C. Zonnevylle, R. Hoffmann, P.J. v.d. Hoek and R.A. van Santen, *Surf. Sci.* **223** (1989) 223.

[20] R.A. van Santen, in: *New trends in CO activation* (Stud. Surf. Sci. and Catal., Vol. 64), L. Guczi Ed., (Elsevier, Amsterdam, 1991) 1.

[21] A.P.J. Jansen and R.A. van Santen, *J. Phys. Chem.* **94** (1990) 6764.

[22] P.R. Davies and M.W. Roberts, *J. Chem. Soc. Faraday Trans.* **88** (1992) 361.

[23] P.J. van der Hoek, E.J. Baerends and R.A. van Santen, *J. Phys. Chem.* **93** (1989) 6469.

[24] R. Hoffmann, *Solids and Surfaces: a chemist's view of bonding in extended structures* (VCH, Weinheim, 1988).

[25] P. Hollins and J. Pritchard, *Progr. Surf. Sci.* **19** (1985) 275.

[26] A. Chattopadhyay, H. Yang and J.L. Whitten, *J. Phys. Chem.* **94** (1990) 6379.

[27] K. Hermann, P.S. Bagus and C.W. Bauschlicher Jr., *Phys. Rev. B* **31** (1985) 6371.

[28] P.S. Bagus, K. Hermann and C.W. Bauschlicher Jr., *J. Chem. Phys.* **81** (1984) 1966.

[29] C.W. Bauschlicher Jr., *J. Chem. Phys.* **83** (1985) 2619.

8

Dissociation of ammonia on copper and the effect of preadsorbed oxygen

ABSTRACT

In this chapter we[*] present the adsorption and initial dissociation pathways of ammonia on an eleven atom model cluster of the copper (111) surface, and the effects of preadsorbed oxygen are analyzed through local density functional calculations, including non-local corrections to the final adsorption energies. The results demonstrate that the presence of oxygen increases the adsorption energy and promotes the dissociation of ammonia over copper. All examined dissociation reactions were endothermic. Dissociation in the absence of oxygen has the highest activation barrier of all steps analyzed and is the most endothermic with an overall energy change of +176 kJ/mol. In presence of oxygen, however, the energy needed for the dissociation of ammonia is considerably lower with an overall energy of +48 kJ/mol. The dissociation of ammonia in the presence of oxygen has the same overall reaction energy (+48 kJ/mol) regardless of whether the ammonia was initially adsorbed onefold or threefold. The activation energies, +132 (ammonia initially onefold) and +173 kJ/mol (ammonia initially threefold), demonstrate that system favors the pathway where ammonia is initially onefold. It is concluded that ammonia dissociation proceeds via the intermediate formation of adsorbed hydroxyl.

8.1   INTRODUCTION

The adsorption and subsequent dissociation of ammonia over copper is of considerably importance in the understanding of ammonia oxidation processes. Experimental results suggest that the adsorption energy of ammonia on the copper (100) surface is of the order of -60 kJ/mol. A summary of some of the these results are: Wu and Kevan [1] -57 ± 2 kJ/mol, Chuang and Hussla [2] -62 kJ/mol, and Davies [3] -50 to -60 kJ/mol for the copper (100), (110) and (111) surfaces. The presence of preadsorbed oxygen species on the surface has been found to increase the adsorption energy considerably. Davies [3] reported that the experimental desorption of ammonia increases from 200 K on a clean copper surface to 240 K on a surface which has been exposed to oxygen. Oxygen was also suggested to activate the nitrogen-hydrogen bond [3]. This implies that the dissociation of ammonia in the presence of oxygen becomes easier, thus resulting in the formation of adsorbed NH_2, NH, and atomic nitrogen products. The dissociation of the nitrogen-hydrogen bond on the surface generates atomic hydrogen which can subsequently bind with adsorbed oxygen atoms to form surface hydroxyl-groups or water. In the absence of oxygen, these hydrogen atoms can only adsorb onto the copper surface [4].

In this chapter, we examine the adsorption of ammonia over a number of model copper clusters and the subsequent dissociation of ammonia to form NH_2 and atomic hydrogen or, when oxygen is present, hydroxyl. In the first part, we review some of our previous results for the adsorption of ammonia over various copper clusters [5] and present new results on the role of preadsorbed oxygen on ammonia adsorption. In the second part, we examine the activation of the nitrogen-hydrogen bond. We analyze the dissociation of ammonia into NH_2 and atomic hydrogen in the absence or into NH_2 and hydroxyl in the presence of preadsorbed oxygen. Furthermore, we looked at the effects of starting with ammonia adsorbed at both onefold and threefold sites.

8.2   COMPUTATIONAL DETAILS

The local density functional calculations reported in this work were done using the Amsterdam-Density-Functional (ADF) program, developed by Baerends and coworkers [6]. In this set of programs, the Local Spin Density Approximation (LSDA) is invoked with the Vosko-Wilk-Nusair exchange-correlation energy functional [7]. Gradient or non-local (NL) corrections for the exchange [8] and correlation [9] to the final adsorption energies were

included in all the calculations. These non-local corrections resulted in a substantial improvement of the calculated energies. Since the non-local corrections are included in a non self-consistent manner the extra computational burden involved is only minimal. The molecular orbitals are represented as linear combinations of atomic Slater type orbitals (STO's). Integrals are computed numerically [10] and adsorption energies are determined by the Ziegler transition state method [11]. All the reported computations were performed using non-relativistic, spin-unrestricted, frozen-core calculations. The frozen-core approximation was invoked to help reduce the size of the calculations. For nitrogen and oxygen, the 1s core was frozen, while for copper the electrons up to and including the 3p core were kept frozen. Previous calculations showed that keeping for (some of the) copper atoms the electrons up to and including the 3d frozen gave not always satisfactory results [5]. The exponents for the STO basis set used for oxygen is presented in table 8.1. For copper, nitrogen, and hydrogen the basis sets are the same as we used before [5]. Single-ζ functions are used for core orthogonalization. The valence functions are of double-ζ quality with a triple-ζ d for copper. Polarization functions were included for all atoms.

Table 8.1   *Exponents ζ of the STO's for oxygen.*

	type	ζ		type	ζ		type	ζ	
O	1s	7.36	core	2s	2.82	valence	2p	3.06	valence
	2s	1.70	valence	2p	1.30	valence	3d	2.00	valence

Adsorption energies and activation barriers were computed by optimizing pointwise the bond distances and angles between the adsorbate or reactant and the surface bound products. The Cu-Cu distance was fixed at that of the bulk metal (2.556 Å) [12] for all copper clusters. For ammonia (NH_3) the free gas geometry was used, 1.008 Å for the N-H bond length and 107.3° for the H-N-H bond angle [12]. The error introduced by excluding NH_3 deformation was previously determined to be quite small [5] and therefore, was not considered.

8.3   THE EFFECT OF PREADSORBED O ON ADSORBED NH₃

Our previous results on ammonia adsorption over various model copper clusters demonstrated that ammonia prefers onefold adsorption on both copper (100) and copper (111) surfaces. Furthermore ammonia bonded stronger to the copper (100) than to the copper (111) surface. Computed adsorption energies and geometries without and including the non-local

corrections to the final adsorption energies are given in table 8.2. We now have also optimized the Cu-N distance on the non-local level. Earlier we only calculated the non-local corrections for the optimum Cu-N distance found for calculations without the non-local corrections [5]. Comparing the results without and with the non-local corrections we see that the calculated adsorption energies decreases and the optimum Cu-N distance increases, but on a qualitative level the results remain the same. Our calculations also demonstrate that as cluster size increases the computed adsorption energy for ammonia on copper, -52 kJ/mol for the (100) surface, approach the experimental value of approximately -60 kJ/mol [1, 2, 3]. The clusters examined, however, were still not quite large enough to accurately reproduce experimental adsorption energies. Although there exists a rather simple method to reduce the finite size effect [13] we choose not to apply it to avoid the extra computational effort involved. Therefore in the remainder of this work, the trends in energies are analyzed rather than absolute values.

Table 8.2   *Adsorption energy of ammonia on different copper clusters. The cluster designation $(n_1, n_2, ..., n_n)$ means n_1 atoms in the first layer , n_2 atoms in the second layer, etc.*

Cluster	Surface	Site	Without NL corrections		With NL corrections	
			Cu-N† (Å)	ΔE_{ads} (kJ/mol)	Cu-N† (Å)	ΔE_{ads} (kJ/mol)
atom			2.03	-85	2.17	-44
Cu(1, 4, 1)	(100)	onefold	1.94	-158	2.02	-107
Cu(5, 4, 1)	(100)	onefold	2.13	-79	2.37	-29
Cu(5, 4, 5)	(100)	onefold	2.13	-91	2.30	-39
Cu(9, 4, 5)	(100)	onefold	2.07	-110	2.23	-52
Cu(7, 3)	(111)	onefold	2.15	-69	2.38	-16
Cu(8, 3)	(111)	onefold	2.15	-68	2.41	-16
Cu(8, 6, 2)	(100)	twofold	2.48 (2.13)	-64	2.82 (2.51)	-18
Cu(12, 6)	(111)	threefold	2.85 (2.44)	-37	3.29 (2.94)	-3
Cu(4, 5)	(100)	fourfold	3.56 (3.07)	-7	– –	–

† Shortest distance between Cu and N, in parenthesis is the height of N above the copper cluster.

In the analysis of the effects of preadsorbed oxygen on the ammonia adsorption on copper, the choice of appropriate cluster geometry was important. The cluster chosen for analysis was a balance between minimal electronic structure features and achievable computational demands. Our previous results on the adsorption of ammonia on the copper (111) surface

demonstrated that the minimum structural requirements to sufficiently describe the electronic features are the copper surface atom to which the ammonia is adsorbed (the central copper atom), the six nearest copper neighbors in the surface layer, and three copper atoms in the second layer. The introduction of preadsorbed oxygen necessitated an additional copper atom in the first layer to create an additional threefold site. Oxygen adsorbs at this site, thereby reducing the repulsion between the nearby ammonia. The final cluster is labeled Cu(8, 3), thus keeping with the naming convention of $Cu(n_1, n_2, ..., n_n)$ where n_1, n_2 and n_n describe the number of copper atoms in the first, second, and nth layer. The Cu(8, 3) cluster, therefore, has eight atoms in the first layer and three in the second layer. This cluster is shown schematically in fig. 8.1(a).
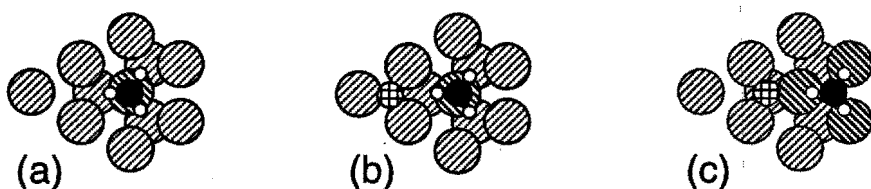
Fig. 8.1 *Top view of ammonia adsorbed on the Cu(8, 3) cluster (a) onefold, (b) onefold with threefold preadsorbed oxygen and (c) threefold with threefold preadsorbed oxygen. □=hydrogen, ■=nitrogen, ⊞=oxygen, ▨=copper and ▧=copper closest to nitrogen.*

From our local density approximation calculations including the non-local corrections to the final adsorption energy we found that ammonia adsorbs onefold to this Cu(8, 3) surface model with an optimized Cu-N distance of 2.41 Å and an adsorption energy of -16 kJ/mol. An increased adsorption energy for ammonia in the presence of oxygen is expected for the copper (100) surface. This is due to the lower degree of coordination for the metal atoms of the (100) surface than those in the (111) surface.

Bagus, Hermann and Bauschlicher [14] reported that the adsorption of ammonia on the copper surface is primarily governed by the electrostatic interaction between the large dipole moment of free ammonia and the copper surface. We computed the contribution of the dipole to the adsorption energy by replacing ammonia with point charges at the atomic positions. The interaction energy of this model dipole with the Cu(8, 3) cluster was +12 kJ/mol, which is 75% of reported adsorption energy of ammonia. This is in good agreement with the value of 76% found by Bagus, Hermann and Bauschlicher.

Rodriguez and Campbell [15] suggested that the copper orbitals which are responsible for binding NH_3 are the Cu(4s) and the Cu(4p) orbitals. They reported as the contributions to the adsorption energy: Cu(4s) = 30%, Cu(4p) = 66%, Cu(3d) = 4%. These values were obtained

by averaging over various adsorption sites. In our work, we were able to estimate the contributions of these orbitals from orbital overlap population results. For onefold adsorption of ammonia on the Cu(8, 3) cluster, we found the following contributions to bonding: Cu(4s) = 55%, Cu(4p) = 55%, Cu(3d) = -10%. The negative value for the Cu(3d) orbitals implies that the interaction with ammonia is repulsive. While there are respectable differences in absolute values, we see a similar trend with the values given by Rodriguez and Campbell.

The analysis of the adsorption of ammonia in the presence of oxygen required the optimization of the height of atomic oxygen above the bare Cu(8, 3) surface, as well as, the optimization of the Cu-N binding distance on the Cu(8, 3)-O cluster. The optimal Cu-O distance was 1.91Å which results in the adsorption energy for oxygen on copper (111) surface of -401 kJ/mol. The total energy for the binding of oxygen and ammonia on Cu(8, 3) was found to be -449 kJ/mol with the Cu-O and Cu-N bond distances of 1.95 Å and 2.28 Å respectively. The adsorption of oxygen onto the Cu(8, 3) cluster in the presence of preadsorbed NH_3 was -433 kJ/mol. This was determined by simply subtracting the base value of NH_3 on Cu(8, 3) (-16 kJ/mol) from the total binding energy (-449 kJ/mol). Similarly, the adsorption of NH_3 onto Cu(8, 3) in the presence of oxygen was -48 kJ/mol. It is noted that the adsorption energy of ammonia increased by +32 kJ/mol due to the presence of oxygen.

The origin of the differences between the Cu(8, 3)-NH_3 and Cu(8, 3)-O-NH_3 systems was studied by examining the energetic effects of the following four degrees of freedom: (I) optimizing the ammonia distance to the copper surface, (II) moving the ammonia along the copper surface towards the oxygen, (III) tilting the ammonia so that one of the hydrogen atoms is pointed more in the direction of the oxygen, and (IV) optimizing the distance between the oxygen atom and the copper surface. These four steps are depicted in fig. 8.2. The resulting adsorption energies and bond distances are also listed in table 8.3. The presence of oxygen on ammonia adsorption shortened the distance between the copper cluster and the NH_3, and lengthened the Cu-O distance. There is an overall decrease in the distance between the oxygen and NH_3 as compared to the situation in which oxygen and NH_3 do not interact.
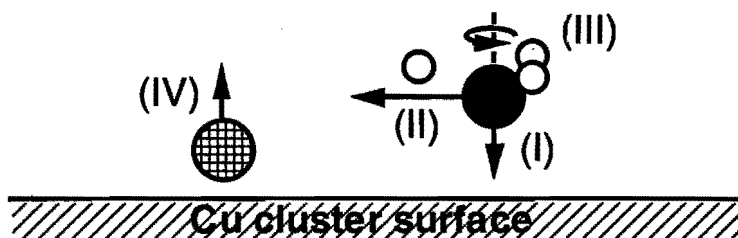

Fig. 8.2   *Optimized degrees of freedom for NH_3 adsorbed onefold with threefold adsorbed O.*

Table 8.3 *Overview of adsorption energies of different adsorbates on different sites.*

System			Cu-A	ΔE_{ads}	System			Cu-A	ΔE_{ads}
A	on	Site	(Å)	(kJ/mol)	A	on	Site	(Å)	(kJ/mol)
NH_3	Cu(8, 3)	onefold	2.41	-16	NH_2	Cu(8, 3)	onefold	1.98	-121
NH_3	Cu(8, 3)-O	onefold	2.28	-48	NH_2	Cu(8, 3)	twofold	2.14	-178
O	Cu(8, 3)	threefold	1.91	-401	NH_2	Cu(8, 3)	threefold	2.26	-164
O	Cu(8, 3)-NH_3	threefold	1.95	-433	OH	Cu(8, 3)	onefold	1.95	-181
H	Cu(8, 3)	onefold	1.57	-133	OH	Cu(8, 3)	twofold	2.08	-245
H	Cu(8, 3)	twofold	1.74	-129	OH	Cu(8, 3)	threefold	2.13	-252
H	Cu(8, 3)	threefold	1.79	-160	NH_2	Cu(8, 3)-OH	twofold	1.67	-173

The contribution of the hydrogen-bridge to the stabilization of ammonia by preadsorbed oxygen was estimated by rotating the three hydrogen atoms about the threefold ammonia axis. In the absence oxygen, the rotation barrier lies far below the accuracy of our calculation. In the presence of oxygen, however, there is a rotation barrier of approximately +7 kJ/mol. This roughly corresponds to the contribution of the hydrogen-bridge to the bonding energy.

A more important reason for the increased adsorption energy of ammonia in the presence of oxygen is that as the interaction between an atom and one of its neighbors decreases, the interaction of the neighbor atom with its other neighbors increases, and vice versa. This leads to an alternating increase and decrease in bond strengths along the O–Cu–Cu–N line when oxygen is present, as reported in table 8.4. Hence, the formation of a bond between a copper atom with the oxygen atom enhances the bonding between its copper neighbor and the nitrogen atom. This behavior is qualitatively similar to that predicted on the basis of bond order conservation as introduced by Shustorovich [16]. It also corresponds to the Friedel-type oscillating interactions of Lau and Kohn [17] to describe adsorbate-adsorbate interactions.

Table 8.4 *Overlap populations along [O-]-Cu–Cu–N and between NH_3 σ and the central Cu.*

	copper with			ammonia σ with		
	Oxygen	Copper	Nitrogen	Cu(3d)	Cu(4s)	Cu(4p)
Without Oxygen	–	0.0419	0.0785	-0.0037	0.0164	0.0160
With Oxygen	0.110	0.0375	0.0896	-0.0040	0.0193	0.0170

The increased binding between the central copper atom, the copper atom(s) closest to the nitrogen atom, and the ammonia is largely attributed to an increase in the interaction between copper orbitals and the highest occupied σ orbital of ammonia. This was confirmed by the

analysis of the differences in the calculated overlap population density of states (OPDOS) for this orbital with various orbitals of the central copper atom (table 8.4). The increase in the overlap population between Cu(4s) and $NH_3(\sigma)$ is the largest. The OPDOS-curves for the overlap between the $NH_3(\sigma)$ and the Cu(3d), Cu(4s), and the Cu(4p) of the central copper atom are shown in fig. 8.3. The differences between the oxygen-present and oxygen-absent OPDOS curves were negligible for all interactions except the $NH_3(\sigma)$ orbital with the central Cu(4s) orbital. As illustrated in fig. 8.3(b), the large anti-bonding peak near the Fermi-level (marked by the arrow) disappears in the presence of oxygen. An electron density contour plot of the molecular orbital responsible for this peak is shown in fig. 9.2. This is an anti-bonding Cu-N bond. The population of this anti-bonding orbital is decreased by 0.3 electrons when oxygen is added to the system. This reduction in anti-bonding significantly increases the copper-ammonia bond strength.
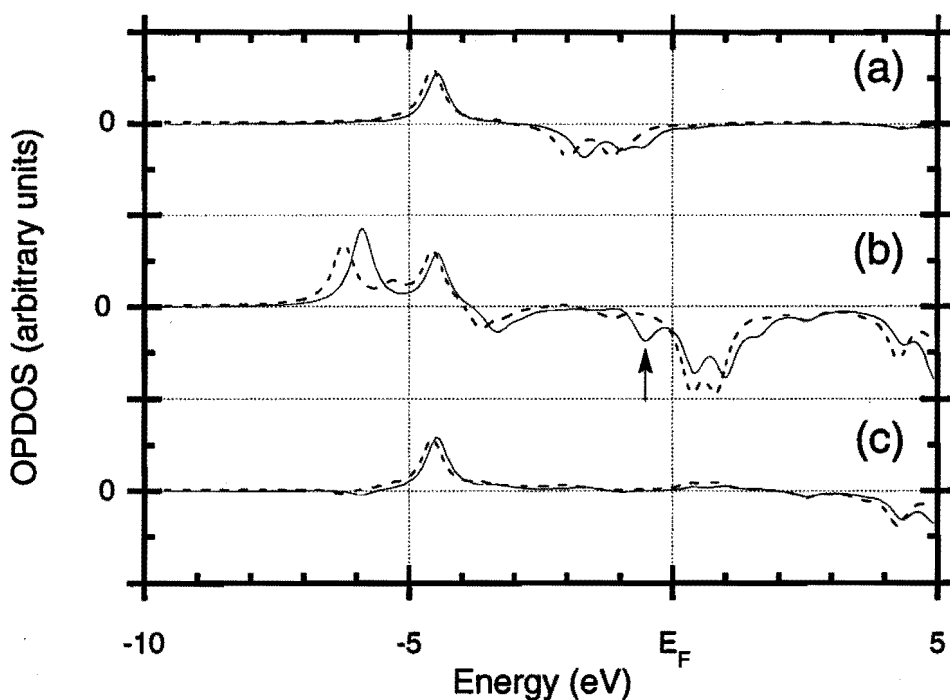
Fig. 8.3 *The overlap population density of states (OPDOS) of the ammonia σ orbital with (a) the Cu(3d), (b) the Cu(4s), and (c) the Cu(4p) orbital. The peak that disappears in the presence of oxygen is marked with an arrow. The corresponding, anti-bonding Cu-N, orbital is shown in fig. 9.2.*

8.4   DISSOCIATION OF AMMONIA ON A COPPER SURFACE

    The dissociation of ammonia to NH_2 and atomic hydrogen was analyzed by computing both the overall energy for reaction and its activation barrier. All calculations again were performed using the Cu(8, 3) cluster, fig. 8.1(a), which provided a suitable geometry for ammonia dissociation and oxygen coadsorption. Table 8.3 presents a summary of the adsorption energies for various molecular and atomic adsorbates on various adsorption sites. From this table it is evident that both NH_2 and atomic hydrogen fragments from the dissociation of ammonia favor higher coordination sites. Hydrogen clearly preferred threefold adsorption-site, whereas NH_2 opted for a twofold site. For NH_2, the p-type atomic orbital perpendicular to the NH_2 plane are stabilized by a favorable interaction with the asymmetric s-type copper group orbitals for twofold coordination [5].

    Overall reaction enthalpies were determined from both the adsorption and formation energies for the species involved. The adsorption energies are summarized in table 8.3, while the formation energies are listed in table 8.5. The dissociation of ammonia to NH_2 and atomic hydrogen was estimated to be endothermic by +176 kJ/mol.

$$\Delta E = \Delta E_{ads, H} + \Delta E_{ads, NH_2} - \Delta E_{ads, NH_3} + E_{f, H} + E_{f, NH_2} - E_{f, NH_3}$$
$$= -160 - 178 + 16 + 0 - 761 + 1259 = +176 \text{ kJ/mol} \qquad (8.1)$$

Here $\Delta E_{f, AB}$ is the energy of formation when AB is formed from the atoms A and B; i.e. the last three terms in eq. (8.1) represent the dissociation energy in the gas phase.

Table 8.5   *Formation energies (E_f) of NH_3, NH_2 and OH calculated with respect to the atoms.*

Species	Calculated E_f (kJ/mol)	Experimental E_f [12] (kJ/mol)	Difference (kJ/mol)
NH_3	-1259	-1172.6	-86
NH_2	-761	-723.3	-38
OH	-469	-427.5	-42

    In the analysis of the activation barrier for ammonia dissociation, the reaction path was divided into two steps; the first was the separation of a proton from the onefold adsorbed ammonia and the subsequent adsorption of this proton at a threefold site, and the second was the movement of the NH_2 product from the onefold position to a twofold site. The optimized Cu(8, 3)-NH_3 cluster discussed earlier was chosen as the initial starting geometry. In the calculations on this system, the hydrogen atom in the NH_3 group which is directed towards the empty threefold site at the edge of the cluster was moved in small increments toward this

site. The energy of the system was determined at each increment as the hydrogen is moved in a straight line towards the threefold site. All other atomic positions were held fixed. The transition state for this reaction step was found half way between the hydrogen's initial starting point and its final state (above the threefold site) with a corresponding activation energy of approximately +344 kJ/mol. The reaction coordinate for this step is shown in fig. 8.4. The overall energy change for this path is +248 kJ/mol. Therefore, the second step of the path is estimated to be exothermic with an energy of about -72 kJ/mol.

(a)   (b)
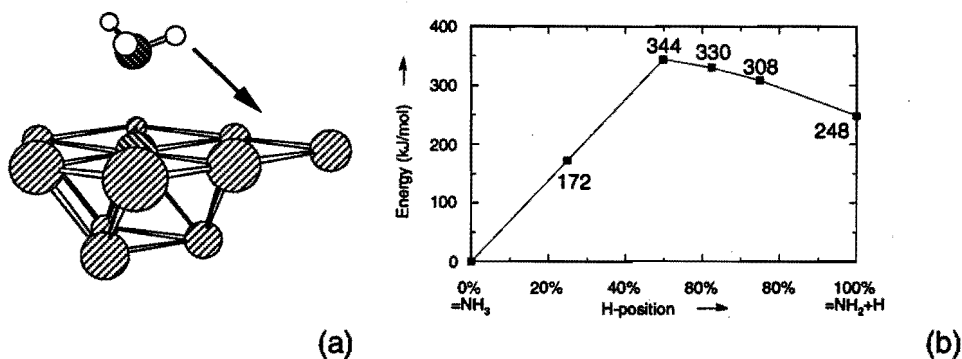
Fig. 8.4   *The dissociation of onefold adsorbed NH$_3$ on Cu(8, 3) without preadsorbed oxygen.*

The dissociation of ammonia on a copper surface in the presence of preadsorbed oxygen results in the formation of NH$_2$ and hydroxyl product fragments. The hydroxyl species is formed via the migration of a hydrogen atom from ammonia to the oxygen atom. Initially, both NH$_2$ and hydroxyl are located where the ammonia and oxygen adsorbed, onefold and threefold sites respectively. The results of subsequent calculations (see table 8.3) imply that the hydroxyl groups prefers to remain threefold coordinated.

The analysis of NH$_2$ in the presence of the product hydroxyl group was also investigated. The adsorption energies for NH$_2$ on various sites in the presence of a preadsorbed hydroxyl group were computed and are presented in fig. 8.5. The Cu-N distances used in these site screening calculations were those determined for NH$_2$ adsorbed on the bare Cu(8, 3) surface (see table 8.3). The height of the NH$_2$ above the copper surface was optimized only for site c (fig. 8.5). In all but one of the sites examined, the adsorption energy for NH$_2$ on copper in the presence of a preadsorbed hydroxyl group was less than that for the adsorption of NH$_2$ on a clean copper surface. This is possibly attributed to the repulsion between these two negatively charged surface species (NH$_2$ and hydroxyl). Therefore, upon dissociation of ammonia in the

presence of oxygen the product hydroxyl and NH_2 groups should move away from one another. The only case in which a higher adsorption energy for NH_2 in the presence of hydroxyl was noted is for site d (fig. 8.5), where the NH_2 is bonded twofold at the edge of the cluster. However, due to the low coordination of the copper atoms which bind NH_2, this site is not representative of those in a real copper (111) surface and therefore should not be considered, and thus we optimized the Cu-N distance only for site c instead of site d (fig. 8.5).
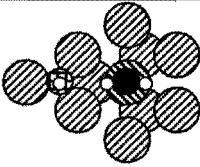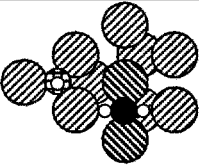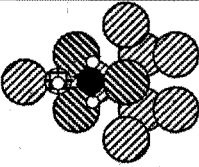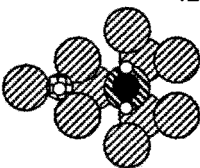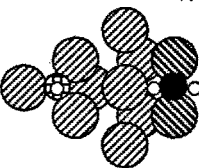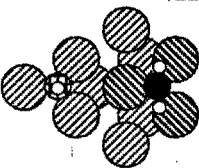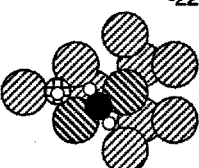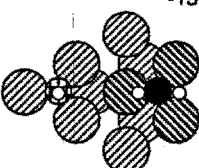
NH_2 adsorption site	onefold	twofold	threefold
	(a)	(c)	(f)
Cu-N distance (Å)	1.98	2.10	2.26
E_{ads} (kJ/mol)	-121	-173	+224
	(b)	(d)	(g)
Cu-N distance (Å)	1.98	2.14	2.26
E_{ads} (kJ/mol)	-102	-225	-156
		(e)	(h)
Cu-N distance (Å)		2.14	2.26
E_{ads} (kJ/mol)		+64	-146

☐ = H   ■ = N
⊞ = O   ▨ = Cu
▧ = Cu closest to N

Fig. 8.5   *Adsorption geometries and energies of OH and NH_2 adsorbed on the Cu(8, 3) cluster. Only for geometry c the Cu-N distance was optimized.*

Similar to the reaction over the bare copper surface, the overall dissociation energy for ammonia to NH_2 and atomic hydrogen in the presence of oxygen on a copper (111) surface was estimated from the adsorption energies and formation energies reported in tables 8.3 and table 8.5 respectively. We assumed that upon dissociation the NH_2 diffuses to a twofold site which is removed from the repulsive interaction with the neighboring hydroxyl group.

Therefore, the adsorption value for NH_2 on the bare copper surface was assumed to be more representative for this system and used in the calculation of the overall reaction energy for dissociation of ammonia by the copper-oxygen surface. This energy is endothermic by:

$$\Delta E = E_{ads, OH} + \Delta E_{ads, NH_2} - E_{ads, O} - \Delta E_{ads, NH_3} + \Delta E_{f, OH} + E_{f, NH_2} - E_{f, NH_3}$$

$$= -252 - 178 + 401 + 48 - 469 - 761 + 1259 = +48 \text{ kJ/mol} \qquad (8.2)$$

This is far less than the +176 kJ/mol found with eq. (8.1) for the dissociation of ammonia on the copper (111) surface in the absence of oxygen.

Two different reaction paths for the dissociation of ammonia in the presence of preadsorbed oxygen were examined. In the first path, ammonia is initially coordinated onefold at the central copper site and oxygen on a neighboring threefold site, fig. 8.1(b). The reaction path is composed of the following two steps: the dissociation of hydrogen from ammonia and binding of this hydrogen to the adjacent oxygen, and the subsequent movement of the product NH_2 fragment from the onefold to a twofold site. The second path also proceeds with the ammonia and oxygen adsorbed onefold and threefold. The steps of this path, however, are slightly different: The first step is the movement of ammonia from a onefold to a threefold site, resulting in the system shown in fig. 8.1(c). The second step is the simultaneous dissociation of a proton from ammonia and the binding of this proton to the preadsorbed oxygen. Finally, the last step is the movement of the NH_2 product fragment from the threefold to a twofold site.

An appropriate reaction coordinate for the first path was deduced by computing the optimal initial and final geometries of the dissociation step. The optimal structure after dissociation indicates that the hydrogen atom of the hydroxyl group is pointed toward the NH_2 fragment. Fig. 8.6 shows a plot of the energy as a function of the tilt angle, i.e., the angle that the O-H bond makes with the normal of the copper (111) surface. In the absence of preadsorbed NH_2, the O-H bond was found to be perpendicular to the copper surface. However in the presence of preadsorbed NH_2, the hydroxyl group tilts about 40° so that the hydrogen is pointing towards the NH_2 group. Therefore in computing the first step of this dissociation path, one of the hydrogen atoms from ammonia is moved from the ammonia to this final position along a linear path. The energy change associated with this reaction coordinate is depicted in fig. 8.7. The highest energy is reached when the hydrogen has moved about 60% of the distance. The activation energy is about +203 kJ/mol. The geometry which corresponded to this transition complex was determined by separately optimizing the distance of the oxygen above the surface and the orientation of the NH_2 fragment, and the height of the NH_2 fragment above the surface. Optimization of the oxygen-height significantly lowered the energy to a value of +141 kJ/mol. The optimization of the NH_2 orientation had little effect on the energy, therefore the two remaining hydrogens were left in

there original positions. The final optimization, the height of NH_2 fragment, lowered the energy by +10 kJ/mol. One concludes that the activation energy needed for this first step is about +131 kJ/mol. This energy is further reduced by the subsequent movement of NH_2 from its initial onefold site to a twofold position, as illustrated in fig. 8.5(c), and the tilting of the hydroxyl group thus allowing it to become perpendicular with the copper surface.
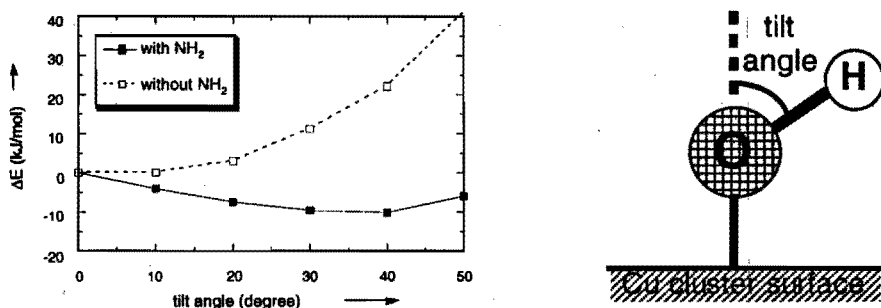

Fig. 8.6 *The energy needed to tilt OH adsorbed on the Cu(8, 3) cluster with NH_2 and without NH_2 preadsorbed. The tilt angle is the angle which O-H makes with the normal (see inset).*

The absolute value of the adsorption energy for NH_2 on Cu(8, 3)-OH increased as the distance between NH_2 and OH was increased (table 8.6). The longer the distance between NH_2 and OH the smaller their interaction was. The NH_2 and hydroxyl prefer to adsorb distant from one another to minimize this repulsion in the overall dissociation path.
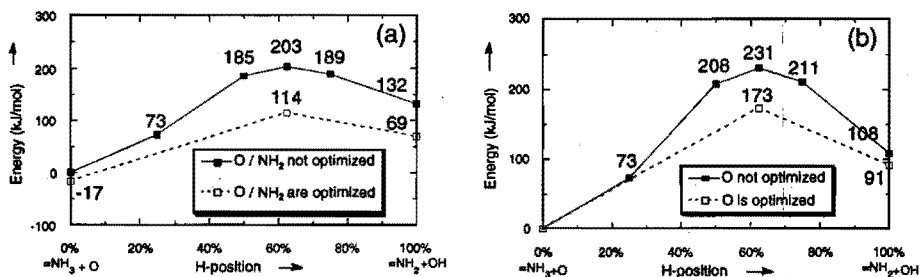
Fig. 8.7 *The dissociation of (a) onefold and (b) threefold adsorbed NH_3 on Cu(8, 3) with threefold preadsorbed oxygen. The starting geometries are shown in fig. 8.1(b) and (c) respectively. The positions of oxygen and NH_2 were not optimized, except for the initial-, transition-, and final-state.*

Table 8.6   *Energies for the reaction paths of the different dissociation reactions.*

$NH_3 \rightarrow NH_2 + [O]H$	ΔE_{act} for dissociation (kJ/mol)	ΔE for dissociation (kJ/mol)	$\Delta E_{overall}$ (kJ/mol)
In the gasphase	+498	+498	+498
Initial geometry fig. 8.1(a)	+345	+249	+176
Initial geometry fig. 8.1(b)	+132	+86	+48
Initial geometry fig. 8.1(c)	+173	+91	+48

The significant reduction in the activation energy for the dissociation of ammonia in the presence of oxygen is caused by two more or less similar effects. First, the hydrogen atom binds more strongly with oxygen than with copper. Second, the distance that the hydrogen needs to travel in the dissociation process is less when oxygen is present. Therefore, the distance between the hydrogen and the nitrogen atom is smaller for the transition state with oxygen than without oxygen, and appreciable interactions exist.

In the analysis of the second reaction path, we again assumed that the step in which the hydrogen atom is separated from nitrogen and adsorbed on oxygen is the rate determining step. The same base Cu(8, 3) cluster was used in these calculations. The new positions of the ammonia and the oxygen atom on this cluster are illustrated in fig. 8.1(c). As in the first path, the hydrogen atom was moved in a straight line towards the oxygen atom. The resulting energy profile for this coordinate is shown in fig. 8.8. In the computing the transition state for this step, only the height of the hydroxyl group above the copper surface was optimized. The relative energy changes for optimizing NH_2 in the first path were found to be small and therefore were neglected here for path 2. The activation energy for this step was +173 kJ/mol which is about +40 kJ/mol larger than the activation energy needed for the same step in the first path. The initial step in the second path required the migration of the ammonia to a threefold site prior to dissociation. The energy required for this migration is +38 kJ/mol which increases the overall activation energy to +211 kJ/mol for this path. Dissociation via this route appears to be unlikely. Activation energies, energy effects for the dissociation step and overall reaction energies for the different dissociation paths are summarized in table 8.6.

8.5   CONCLUSIONS

Oxygen and ammonia preadsorbed on a copper (111) surface demonstrate an attractive interaction. While this is in part due to the direct interaction between the oxygen and one of

the hydrogen atoms of ammonia, a greater portion of the favorable bonding is attributed to the interaction through the copper surface. The latter agrees with the predictions from the bond order conservation postulate [16]. An alternating increase and decrease in overlap population densities following the line O–Cu–Cu–N substantiates this reasoning.

Of the three reaction paths analyzed, the dissociation in the absence of preadsorbed oxygen has the highest activation energy and is the most endothermic. The dissociation of adsorbed ammonia in the presence of oxygen has a considerably lower reaction energy due to hydroxyl formation. Of the two dissociation pathways studied in the presence of oxygen, the first one in which ammonia is initially adsorbed onefold is favored over the second one in which ammonia is initially adsorbed threefold.

8.6   REFERENCES

[1] K.J. Wu and S.D. Kevan, *J. Chem. Phys.* **94** (1991) 7494.

[2] T.J. Chuang, H. Seki and Ingo Hussla, *Surf. Sci.* **158** (1985) 525.

[3] P.R. Davies, thesis, the University of Wales, Cardiff (1989) Chapter 4.

[4] C.T. Au and M.W. Roberts, *Chem. Phys. Lett.* **74** (1980) 472.

[5] W. Biemolt, G.J.C.S. van de Kerkhof, P.R. Davies, A.P.J. Jansen and R.A. van Santen, *Chem. Phys. Lett.* **188** (1992) 477 (chapter 7 of this thesis).

[6] E.J. Baerends, D.E. Ellis and P. Ros, *Chem. Phys.* **2** (1973) 41;
P.M. Boerrigter, G. te Velde and E.J. Baerends, *Int. J. Quantum Chem.* **33** (1988) 87.

[7] S.H. Vosko, L. Wilk and M. Nusiar, *Can. J. Phys.* **58** (1980) 1200.

[8] A.D. Becke, *Int. J. of Quant. Chem.* **23** (1983) 1915; A.D. Becke, *Phys. Rev. A* **38** (1988) 3098.

[9] J.P. Perdew, Phys. Rev. B **33** (1986) 8822; erratum: J.P. Perdew, *Phys. Rev. B* **34** (1986) 7406.

[10] G. te Velde and E.J. Baerends, *J. Comput. Phys.* **99** (1992) 84.

[11] T. Ziegler and A. Rauk, *Theoret. Chim. Acta* **46** (1977) 1.

[12] D.R. Lide, ed., Handbook of Chemistry and Physics, 71st Ed. (CRC Press, Boca Raton, 1990).

[13] V. Russier and C. Mijoule, *J. Phys.: Condens. Matter* **3** (1991) 3193.

[14] P.S. Bagus, K. Hermann, *Phys. Rev. B* **33** (1986) 2987;
P.S. Bagus, K. Hermann, C.W. Bauschlicher, *J. Chem. Phys.* **81** (1984) 1966.

[15] J.A. Rodriguez and C.T. Campbell, *Surf. Sci.* **197** (1988) 567.

[16] E.M. Shustorovich, *Surf. Sci. Rep.* **6** (1986) 1.

[17] K.H. Lau, W. Kohn, *Surf. Sci.* **75** (1985) 69.

9

The oxidation of ammonia by copper

ABSTRACT

We[*] present local spin density approximation calculations on the adsorption and dissociation of ammonia on a copper cluster which models the Cu(111) surface. Preadsorbed oxygen increases the adsorption energy of ammonia, and promotes the dissociation of ammonia. All examined dissociation reactions in the absence of oxygen are endothermic. Dissociation of ammonia to NH_2 with oxygen is also found to be endothermic, but less than for systems without oxygen. Subsequent dissociation to NH is thermally neutral, whereas NH dissociation to nitrogen is exothermic. The most endothermic steps in the catalytic reaction cycle of the ammonia oxidation reaction appear to be the dissociation of ammonia and the desorption of water.

9.1   INTRODUCTION

Ammonia desorbs molecularly from clean single-crystal copper surfaces with an energy of approximately +50 to +60 kJ/mol [1, 2]. In the presence of preadsorbed oxygen there is some activation of the N-H bond [3, 4]. This interaction leads to the rapid replacement of the oxygen by an adsorbed nitrogen-containing species.

We have found that the chemical bonding in the copper-ammonia system is mainly controlled by the interaction of the doubly occupied lone pair orbital of ammonia with orbitals from the copper surface [5]. Copper d-orbitals favor the onefold adsorption of ammonia, whereas the copper s- and p-orbitals favor higher coordinated adsorption sites. We found that NH_2 prefers twofold coordination [6]. NH and nitrogen are expected to prefer higher coordination sites.

Previously, we concluded that NH_2 is formed from the reaction of adsorbed oxygen with ammonia. The hydrogen atoms bind with adsorbed oxygen atoms thus resulting in the formation of adsorbed hydroxyl groups [6]. Herein we extend the previous results for the reaction of ammonia on a model Cu(111) cluster with preadsorbed oxygen and also present results for subsequent oxidation steps

9.2   COMPUTATIONAL DETAILS

We performed spin-unrestricted, non-relativistic local spin density approximation (LSDA) calculations [7] supplemented with non-local (NL) corrections for the exchange [8] and the correlation [9] as implemented in the Amsterdam-density-functional (ADF) program suite by Baerends and coworkers [10-12]. The distance of the adsorbed species to the surface, and various tilt angles were manually optimized.
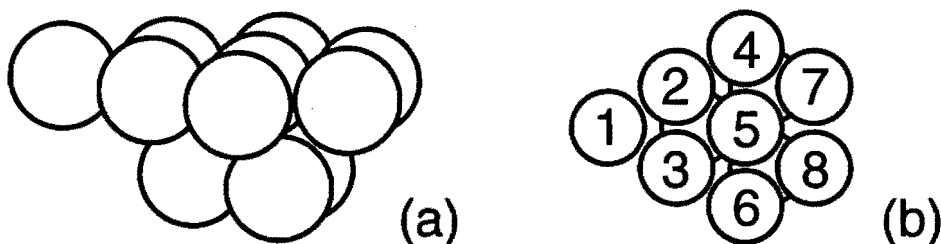

Fig. 9.1   *Perspective and top view of the Cu(8,3) cluster, used to model the Cu(111) surface. Copper atoms in the first layer are labeled with numbers to identify adsorption positions on this cluster.*

Fig. 9.1 shows the copper cluster used to model the Cu(111) surface. We limited our studies to this Cu(8, 3) cluster (i.e. eight atoms in the first and three atoms in the second layer) in order to enable comparisons with earlier calculations. Previous results demonstrated that this cluster provides a reasonable electronic description of various surface sites while minimizing the computational demand. The copper-copper distance was set equal to the nearest-neighbor distance in the bulk: 2.556 Å [13]. For ammonia the free gas geometry was used: the N-H bond distance is 1.008 Å, and the H-N-H bond angle is 107.3° [13].

9.3   RESULTS AND DISCUSSION

Table 9.1 summarizes the adsorption energies for molecular and atomic fragments formed in the reaction of ammonia with oxygen. Note that the adsorption energy of ammonia is increased by +32 kJ/mol in the presence of preadsorbed oxygen. The overlap population along the line O–Cu–Cu–N illustrates that when oxygen is present there is an alternating increase and decrease in bond strengths (table 8.4). That is, the formation of a bond between the copper atom and oxygen atom increases the interaction between its copper neighbor and the adsorbing nitrogen atom. This behavior is qualitatively similar to that predicted on the basis of bond order conservation (BOC) as introduced by Shustorovich [14].

Table 9.1   *Optimized geometries and calculated adsorption energies (kJ/mol) on Cu(8,3).*

A (†)	Site	Atoms (††)	Cu-A (Å)	ΔE_{ads} (kJ/mol)	A (†)	Site	Atoms (††)	A_p (†††)	Cu-A (Å)	ΔE_{ads} (kJ/mol)
NH_3	onefold	1	2.41	-16	O	threefold	1-2-3	—	1.91	-401
NH_2	onefold	1	1.99	-121	H	onefold	1	—	1.57	-133
NH_2	twofold	2-3	2.14	-178	H	twofold	2-3	—	1.74	-129
NH_2	threefold	2-3-5	2.25	-164	H	threefold	2-3-5	—	1.79	-160
NH	onefold	1	1.95	-210						
NH	threefold	5-7-8	2.39	-258	NH_3	onefold	1	O	2.28	-48
OH	onefold	1	1.95	-181	NH_2	twofold	5-6	OH	1.67	-173
OH	twofold	2-3	2.08	-245	NH	threefold	2-3-5	O	2.18	-46
OH	threefold	1-2-3	2.13	-252	N	threefold	2-3-5	OH	2.03	-196
N	threefold	1	1.78	-339	O	threefold	1-2-3	NH_3	1.95	-433

† A = adsorbate; †† atoms defining site (see fig. 9.1); ††† A_p = preadsorbed species.

The increased adsorption energy of ammonia on the Cu(8, 3)-O system is largely attributed to the population of the highest occupied molecular orbital shown in fig. 9.2, which is an anti-bonding Cu-N bond. The overlap population density-of-states (OPDOS) shows that this MO depopulates by 0.3 electrons when oxygen is added to the system so that the Cu-NH bond strength increases. This is the main reason for the change in NH_3 adsorption energy.
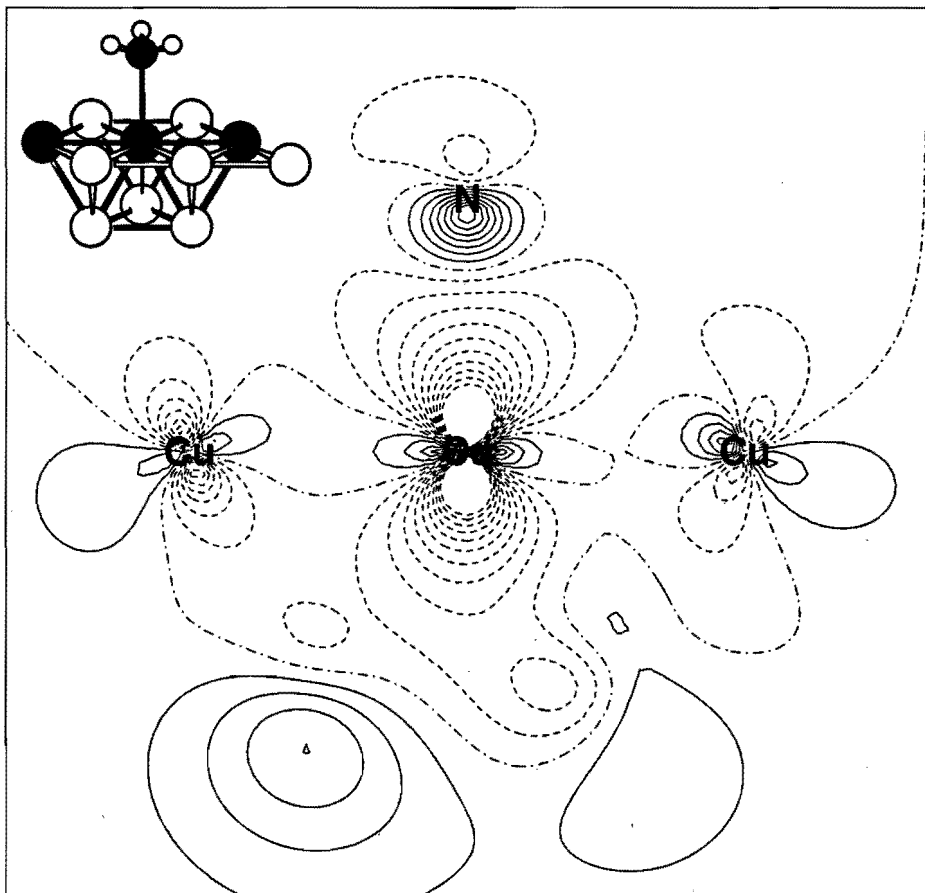

Fig. 9.2 *Contour plot of the highest-occupied orbital for NH_3 adsorbed onefold on Cu(8, 3). Dashed lines show a decrease, solid lines an increase, except for the fatter solid lines which depict nodal surfaces. Subsequent contours correspond to ± 0.0, ± 0.1, ± 0.2, ± 0.3, ± 0.4, ± 0.5, ± 0.6, ± 0.7, ± 0.8, ± 0.9 and ± 1.0 electrons per $Å^3$. The four atoms correspond to the four dark atoms shown in the inset.*

The adsorption energies presented in table 9.1 together with formation energies were used to determine reaction enthalpies. All the formation energies were computed by unrestricted non-local ADF calculations using known experimental bond lengths and angles for each of the gas phase adsorbate species. For the dissociation of ammonia in the absence of oxygen we found the reaction energy to be

$$\Delta E[NH_3(a) \rightarrow NH_2(a) + H(a)] = +176 \text{ kJ/mol} \qquad (9.1)$$
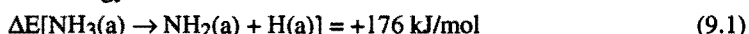
The activation barrier was computed by moving the hydrogen atom in a straight line towards a threefold site, without changing the positions of any of the other atoms. The transition state was found where the hydrogen atom had travelled about 50% of the distance. The activation energy for this step is +344 kJ/mol, whereas the energy change is +248 kJ/mol. Next NH_2 is moved to a twofold site. This step is exothermic with an energy change of -72 kJ/mol and no activation barrier.

In the presence of oxygen the hydrogen atom moves to the oxygen atom and forms an hydroxyl group at a threefold site. We find for the ammonia dissociation with oxygen

$$\Delta E[NH_3(a) + O(a) \rightarrow NH_2(a) + OH(a)] = +48 \text{ kJ/mol} \qquad (9.2)$$
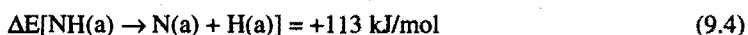
Hence the dissociation in the presence of oxygen is also endothermic, but much less than that for the dissociation without oxygen. Interestingly this result contrasts predictions based on energy estimates using the BOC method.[15] Upon dissociation the hydrogen atom moves to the oxygen atom and forms an hydroxyl group which is tilted 40° with respect to the normal toward NH_2. When no coadsorbed NH_2 is present the O-H bond is perpendicular to the copper surface. The transition state is found when the hydrogen atom has moved about 60% of the distance towards oxygen. The activation energy is +131 kJ/mol. The hydroxyl and NH_2 groups repel each other and therefore move apart after reaction. The NH_2 moves to a twofold site, and the hydroxyl group becomes perpendicular to the surface.

The lower energy transition state is the result of by two similar effects. First, the hydrogen atom binds more strongly with oxygen than with copper. Secondly, the distance that the hydrogen needs to travel in the dissociation process is less when oxygen is present. Thus in the transition state with oxygen, the distance between the hydrogen and the nitrogen atom is smaller than in the transition state without oxygen and an appreciable interaction already exists between hydrogen and oxygen.
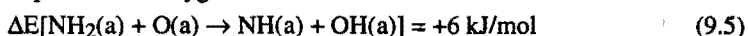
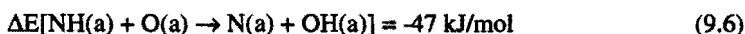Further dissociation of NH_2 leads to NH and nitrogen. We find without oxygen

$$\Delta E[NH_2(a) \rightarrow NH(a) + H(a)] = +166 \text{ kJ/mol} \qquad (9.3)$$

and

$$\Delta E[NH(a) \rightarrow N(a) + H(a)] = +113 \text{ kJ/mol} \qquad (9.4)$$

However, in the presence of oxygen we find

$$\Delta E[NH_2(a) + O(a) \rightarrow NH(a) + OH(a)] = +6 \text{ kJ/mol} \qquad (9.5)$$

and

$$\Delta E[NH(a) + O(a) \rightarrow N(a) + OH(a)] = -47 \text{ kJ/mol} \qquad (9.6)$$
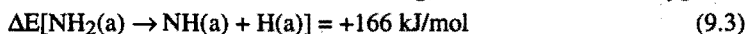
All reactions in the absence of oxygen were found to be endothermic. Reactions in the presence of oxygen were considerably less in energy than their corresponding reactions in the absence of oxygen. In fact, the reactions of NH_2 to NH and NH to nitrogen were determined to be thermally neutral and exothermic, respectively. The postulated mechanistic steps involved in the overall oxidation of ammonia by oxygen on the Cu(111) surface and their computed energy values determined here are summarized in fig. 9.3. This figure illustrates that there are two highly endothermic reaction steps in this cycle. The desorption of water by recombination of hydroxyl groups is endothermic by +39 kJ/mol. The energy to break one bond in ammonia cost +48 kJ/mol. Once ammonia has lost a hydrogen atom consecutive reactions become thermodynamically favorable. The overall change for the entire cycle (the reaction path steps in fig. 9.3) is in excellent agreement with that predicted from gas phase thermochemical analysis of the overall thermodynamics (the traversing dotted line in fig. 9.3).
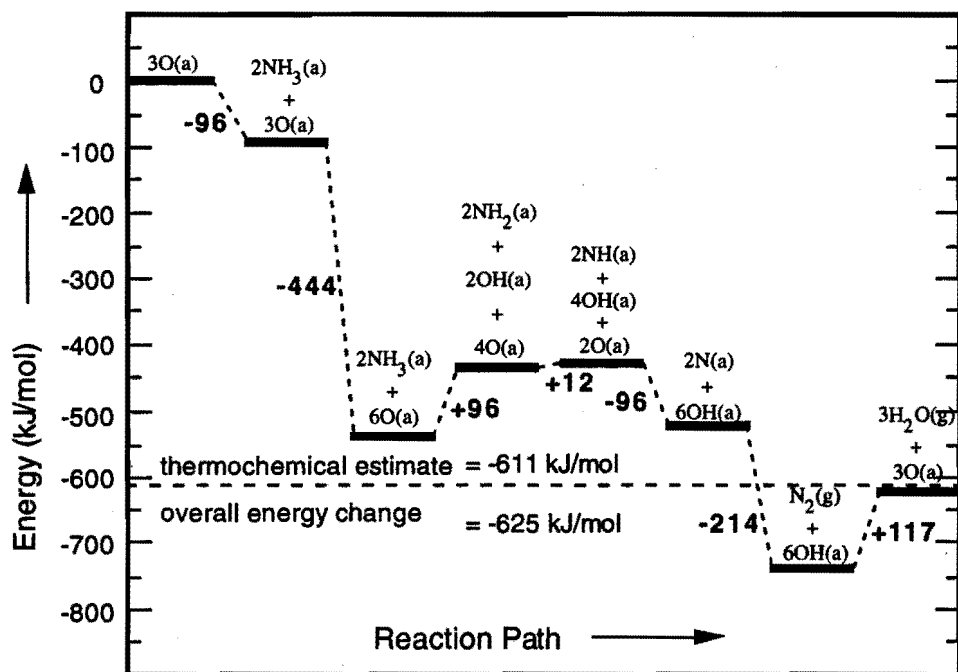

Fig. 9.3 *Schematic view of the energetics for the oxidation of NH_3 by copper to $N_2(g)$ and $H_2O(g)$. Shown are the species adsorbed on/desorbing from Cu(8, 3) with the changes in the energy.*

9.4   CONCLUSIONS

Ammonia and preadsorbed oxygen on a Cu(111) surface have an attractive interaction, which is mainly due to interaction through the surface. Dissociation of ammonia to NH_2 in the absence of preadsorbed oxygen has a high activation energy and is endothermic. Dissociation of ammonia in the presence of preadsorbed oxygen has a much lower activation barrier due to hydroxyl formation, but is still an endothermic step. Subsequent dissociation of NH_2 and NH in the presence of oxygen help to drive the overall oxidation process. The desorption of water from the surface and dissociation of ammonia are the two most thermodynamically unfavorable steps in the overall sequence of steps.

9.5   REFERENCES

[1]   K.J. Wu and S.D. Kevan, *J. Chem. Phys.* **94** (1991) 7494.

[2]   T.J. Chuang, H. Seki and Ingo Hussla, *Surf. Sci.* **158** (1985) 525.

[3]   C.T. Au and M.W. Roberts, *Chem. Phys. Lett.* **74** (1980) 472.

[4]   P.R. Davies, thesis, the University of Wales, Cardiff (1989) Chapter 4.

[5]   W. Biemolt, G.J.C.S. van de Kerkhof, P.R. Davies, A.P.J. Jansen and R.A. van Santen, *Chem. Phys. Lett.* **188** (1992) 477 (chapter 7 of this thesis).

[6]   G.J.C.S. van de Kerkhof, W. Biemolt, A.P.J. Jansen and R.A. van Santen, *Surf. Sci.* **284** (1993) 361 (chapter 8 of this thesis).

[7]   S.H. Vosko, L. Wilk and M. Nusair, *Can. J. Phys.* **58** (1980) 1200.

[8]   A.D. Becke, *Int. J. Quantum Chem.* **23** (1983) 1915; A.D. Becke, *Phys. Rev. A* **38** (1988) 3098.

[9]   J.P. Perdew, *Phys. Rev. B* **33** (1986)8822; erratum *Phys. Rev. B* **34** (1986) 7406.

[10] E.J. Baerends, D.E. Elis and P. Ros, *Chem. Phys.* **2** (1973) 41; P.M. Boerrigter, G. te Velde and E.J. Baerends, *Int. J. Quantum Chem.* **33** (1988) 87; G. te Velde and E.J. Baerends, *J. Comput. Phys.* **99** (1992) 84.

[11] T. Ziegler and A. Rauk, *Theoret. Chim. Acta* **46** (1977) 1.

[12] D. Post and E.J. Baerends, *J. Chem. Phys.* **78** (1983) 5663; E.J. Baerends and A. Rozendaal in *Quantum Chemistry: The Challenge of Transition Metals and Coordination Chemistry*, A. Veillard, Ed., Nato ASI Ser (Reidel, Dordrecht, 1986) p. 159; P.J. van den Hoek, A.W. Kleyn and E.J. Baerends, *Comments Atom. Molec. Phys.* **23** (1989) 93.

[13] D.R. Lide, Ed., Handbook of Chemistry and Physics , 71st ed. (CRC Press, Boca Raton, 1990).

[14] E.M. Shustorovich, *Surf. Sci. Rep.* **6** (1986) 1.

[15] E. Shustorovich, A.T. Bell, *Surf. Sci.* **268** (1992) 397.

10 Oxygen as chemical precursor in the oxidation of ammonia by copper

ABSTRACT

In this chapter we[*] analyze the role of O and O_2 precursors in the overall catalytic cycle for NH_3 dissociation using density functional theory. Energetics were computed from geometry optimizations on a cluster model of Cu(111). The calculations systematically underpredict experimental results due to the finite cluster size. Attractive and repulsive lateral interactions were important in accessing accurate adsorption energies. O enhances N-H bond activation, however, it also acts to poison active surface sites and inhibit NH_3 dissociation kinetics. Transient O_2 adsorbs weakly in parallel (precursor for O_2 dissociation) and perpendicular (precursor for NH_3 dissociation) orientation. The mechanism in which H atoms are abstracted sequentially to form an OOH[*] intermediate is favored over that in which two H atoms are simultaneously transferred to form water directly. The non-activated transient molecular path in which H is abstracted sequentially is the most favored of all of the four paths studied. In light of the experimental O_2 dissociation energy over Cu(111), transient O_2 is more likely than "hot" O as the dominant chemical precursor for NH_3 dissociation. Subsequent dissociation of the NH_x fragments lead to N[*]. While enthalpy considerations favor recombinative desorption of N_2, at reaction conditions the most abundant reaction intermediate (MARI) is O, making the recombinative desorption of NO a more likely reaction path.

10.1 INTRODUCTION

Both atomic and molecular oxygen surface species have been speculated as precursors for several important transition metal catalyzed reactions. On silver weakly bound atomic oxygen, stabilized by subsurface oxygen, was cited as the dominant precursor in ethylene epoxidation [1-3], whereas molecular oxygen was found to control the oxidation of SO_2 and CO [4]. In addition, there has been support for both oxygen species in mediating the same catalytic reaction paths. For example, Roberts et al. cited both atomic and molecular precursors as controlling the oxidation of ammonia over Mg [5-8], Zn [9, 10] and Cu [11-14]. Clearly, the role of both atomic and molecular oxygen species as precursor is of considerable importance in understanding different selective oxidation reaction pathways.

The transient nature of chemical precursors, however, makes it difficult to experimentally resolve their role in the mechanism. For example, oxygen has been shown to activate strong nitrogen-, sulfur-, and carbon- hydrogen bonds on transition metal surfaces [13, 15] and also inhibit dissociation [11, 12, 14]. While it is generally agreed that the formation of strong adsorbed atomic oxygen overlayers poisons active surface sites and is responsible for inhibition, the nature of the activation process is still unclear. In this work we present a theoretical analysis of the dissociation of ammonia over copper and elucidate the role of both adsorbed atomic and molecular oxygen species. We first provide a short background of the experimental literature on ammonia oxidation before outlining the specifics of this study.

Roberts and coworkers have experimentally investigated the role of oxygen in the dissociation of ammonia on both Cu(110) [11, 12] and Cu(111) [13, 14]. On Cu(110) they found that both the activity and the selectivity toward different NH_x products were highly sensitive to the reaction conditions and to the order in which the reactants were introduced to the surface. When oxygen was preadsorbed on the surface, a very slow exchange of oxygen and ammonia was required prior to any subsequent dissociation of ammonia to different NH_x species. The surface amide (NH_2^*) was favored at low temperatures and coverages, whereas the surface imide (NH^*) and surface nitrogen (N^*) were favored at higher temperatures and coverages. The activity was attributed to only a small fraction of the preadsorbed oxygen species. The remaining oxygen was thought to poison surface and inhibit the kinetics.

When oxygen and ammonia were coadsorbed (in a regime of excess ammonia), however, there was rapid dissociation of the ammonia with a high selectivity for NH^* formation. The initial speculation was that a molecularly adsorbed transient oxygen precursor, similar to that which was found on Zn(001) surface [9, 10], was responsible for the chemistry.

On Cu(111) Roberts et al. [13, 14] once again found that NH_3 readily dissociates in the presence of oxygen. Based on their results and the ideas proposed by Ertl for the dissociation of oxygen on platinum [16], they suggested that the mechanism for the initial dissociation might be controlled by a "hot" transient atomic oxygen species. It is speculated that these species rapidly diffuse across the surface and abstract hydrogen from the coadsorbed NH_3 before becoming thermally equilibrated with the surface. At high oxygen partial pressures, they found that the rate was inhibited by the presence of adsorbed oxygen overlayers.

Clearly, the chemistry of these systems and the role of oxygen is a complex function of competing elementary reaction steps. Both the overall catalytic cycle and details of the mechanism and activation barriers are, therefore, essential for a more complete and fundamental understanding of the chemistry. Herein, we report the results of a theoretical analysis of the mechanism of oxygen-assisted ammonia dissociation on model copper clusters of the Cu(111) surface. We draw upon some of our previous results which were aimed at deducing the electronic features responsible for the interaction of ammonia at various different adsorption sites on Cu(111) surface [17], the effects of cluster size and frozen core approximation on the computed ammonia adsorption energy [17] and the role of preadsorbed atomic oxygen on the activation of the NH bond [18, 19].

In this work we analyze five paths as plausible controlling mechanistic steps in the dissociation of ammonia in the presence of oxygen. In the first two paths, adsorbed atomic oxygen is proposed as being responsible for ammonia dissociation.

(path 1)	$NH_3(a) + O(a)$	$\rightarrow$	$NH_2(a) + OH(a)$	(10.1)
(path 2)	$NH_3(a) + O(a)$	$\rightarrow$	$NH(a) + H_2O(g)$	(10.2)

In path 1 a single N-H bond is activated by the adsorbed oxygen, whereas in path 2 the NH_3 is situated on the surface such that two N-H bonds can simultaneously be activated and water is formed directly. In the next two paths, molecular oxygen is considered to be active precursor responsible for the dissociation of ammonia.

(path 3)	$NH_3(a) + O_2(a)$	$\rightarrow$	$NH_2(a) + OOH(a)$	(10.3)
(path 4)	$NH_3(a) + O_2(a)$	$\rightarrow$	$NH(a) + H_2O(g)$	(10.4)

In path 3, a single hydrogen is abstracted to form the OOH^* intermediate, whereas in path 4 two hydrogens are simultaneously transferred to form water. In the final path, proposed by Roberts, a "hot" transient atomic oxygen surface species (O^h) which has not been thermally equilibrated with the surface, controls the NH bond activation [5-7, 12, 14].

(path 5)	$NH_3(a) + O^h(a)$	$\rightarrow$	$NH(a) + H_2O(g)$	(10.5)

We analyzed in detail the activation barriers and corresponding catalytic reaction cycles associated with the first four of these paths. Based on these results we speculate as to which is the dominant path and access the plausibility of the final "hot" oxygen-mediated path.

10.2   METHODS

Density functional theory (DFT) calculations were performed to determine formation, adsorption, dissociation and activation energies. Nearly all of the results reported here were derived from the Amsterdam Density Functional (ADF) program of Baerends et al. [20-22]. Supplementary calculations of transition barriers were determined with the DGauss program from Cray Research Inc. [23]. A difference between these two programs is that ADF uses Slater type orbitals, whereas DGauss utilizes Gaussian type orbitals. Adsorption energies for ammonia and other adsorbates computed with both programs were shown to be equivalent to within ±10 kJ/mol. Both programs invoke the local density approximation using the parameterization of Vosko-Wilk-Nusair for the exchange correlation energy functional [24]. Nonlocal gradient corrections for the exchange [25] and correlation [26] were added. All reported calculations are non-relativistic and spin-unrestricted. ADF kept for nitrogen and oxygen the 1s electrons frozen, and for copper the electrons up to and including 3p. In the DGauss calculations all electrons were explicitly included. The basis sets used in both ADF and DGauss were of single-ζ quality for core orthogonalization, and double-ζ for nitrogen and oxygen and triple-ζ quality for copper. Polarization functions were included for all atoms. The basis sets used by ADF are discussed in more detail elsewhere [17, 18], those used in the DGauss program were reported by Andzelm [23, 27]. Analytical gradient algorithms [23, 28] employed in both programs enabled geometries to be optimized.

Adsorption energies were determined by optimizing the adsorbate geometry on a model cluster of the Cu(111) surface (Cu-Cu bond length of 2.556 Å) and computing the energy change between the cluster-adsorbate complex and the energies for the free cluster and adsorbate. All reported adsorption energies were computed with ADF, whereby the adsorption energy is determined as the energy difference of the overall complex minus its respective fragments via the Ziegler transition state method [29].

Activation barriers were computed by choosing an appropriate reaction coordinate and optimizing the geometry of the adsorbates on the cluster at fixed points along the coordinate. The Cu(6) cluster (fig. 10.1a) was used as an initial scooping tool. The central copper in Cu(6) is coordinatively unsaturated and as a result overestimates the nitrogen atom binding to this site. This subsequently leads to the prediction of a much weaker N-H bond. Thus, the Cu(6) cluster provides a significant lower bound on activation energies for hydrogen abstraction. Nevertheless calculations based on this cluster allowed us to judiciously choose which geometry optimizations and reaction coordinate calculations to perform on the larger Cu(8, 3) cluster (fig. 10.1b).
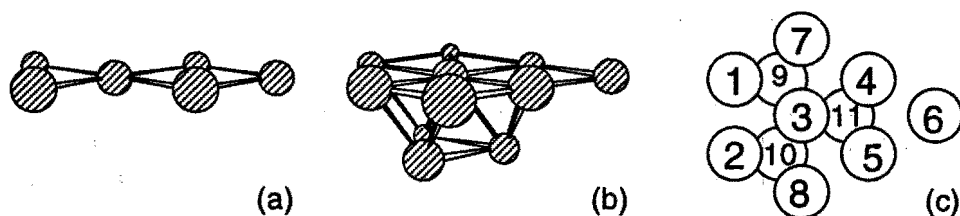
Fig. 10.1 *The Cu(111) surface models (a) Cu(6), (b) Cu(8, 3) and (c) Cu(8, 3) with numbered atoms to identify adsorption positions. The nomenclature $Cu(n_1, n_2)$ refers to the arrangement of the atoms, there are n_1 copper atoms in the surface and n_2 copper atoms in the layer beneath.*

The Cu(8, 3) cluster was chosen to mimic the essential electronic features of the Cu(111) surface while maintaining reasonable CPU expenditures. We have shown the effects of cluster size and configuration on computed adsorption energies for ammonia elsewhere [17]. Comparing computed adsorption energies over the Cu(8, 3) cluster with experimental values for H [15], O [15], ammonia [30, 31] and water [32, 33] on Cu(111) show that the absolute values are slightly off (±30 kJ/mol), but the deviation appears to be systematic which indicates that the relative trends are quite good. While larger clusters gave slightly more accurate adsorption energies [17], they also required considerably greater CPU times, which when coupled with demanding geometry optimization becomes computationally prohibitive.

10.3   RESULTS

In this section we present adsorption energies, lateral interactions, overall catalytic energy cycles and activation barriers for the four mechanistic paths outlined in eqs. (10.1)-(10.4). A substantial portion of the formation and adsorption energies, was described earlier [17-19]. We therefore only give a short review on the important features, and concentrate more heavily on lateral interactions, overall catalytic energy cycles and activation barriers.

10.3.1   Adsorption energies

Computed adsorption energies for relevant adatoms, intermediates and molecules on Cu(8, 3) are summarized in table 10.1. Also the sites and optimized copper-adsorbate bond distances are reported. Ziegler [34] has recently reported that DFT typically predict structural bond lengths to within 0.01 Å, and organometallic bond energies within about 20 kJ/mol.

Table 10.1   Calculated adsorption energies for molecules, intermediates and adatoms on Cu(8, 3).

A (†)	Site	Atoms (††)	Cu-A (Å)	ΔE_{ads} (kJ/mol)	A (†)	Site	Atoms (††)	Cu-A (Å)	ΔE_{ads} (kJ/mol)
NH_3	onefold	3	2.41	-16	NH	threefold	1-2-3	1.84	-258
O_2 (II)	onefold	3	—	+2	OH	onefold	3	1.95	-181
O_2 (II)	threefold	4-5-6	2.97	-17	OH	twofold	4-5	2.08	-245
O_2 (⊥)	threefold	4-5-6	2.23	-10	OH	threefold	4-5-6	2.13	-252
O_2 (⊥)	threefold	3-4-5	2.23	-3	OOH	threefold	4-5-6	2.14	-105
H_2O	onefold	3	2.7	+1	N	threefold	1-2-3	1.90	-339
NO	threefold	4-5-6	2.18	-83	O	threefold	4-5-6	1.91	-401
NH_2	onefold	3	1.99	-121	H	onefold	3	1.57	-133
NH_2	twofold	4-5	2.14	-178	H	twofold	4-5	1.74	-129
NH_2	threefold	3-4-5	2.25	-164	H	threefold	3-4-5	1.79	-160
NH	onefold	3	1.26	-210	H	threefold	3-4-5	1.68	-175

† A = adsorbate; †† atoms defining site (see fig. 10.1c).

One can question how cluster size and symmetry will affect the calculated energies. The result of adding an additional copper atom to the second layer to form Cu(8, 4) (fig. 10.2a) changed the adsorption energy of both atomic nitrogen and NH_2 at the center threefold site by as little as 4 kJ/mol. The local environment about a particular site was found to be much more important. Threefold sites situated directly above a copper atom in the second layer were found to be energetically less favorable for adsorption by 40-50 kJ/mol for both atomic nitrogen and NH_2 than for those threefold sites directly above a second layer threefold site.
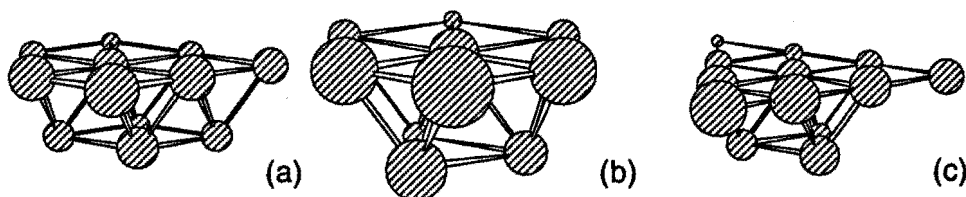
Fig. 10.2   *Large and/or symmetric Cu(111) models (a) Cu(8, 4), (b) Cu(7, 3) and (c) Cu(10, 3).*

In an effort to probe the influence of cluster symmetry, the binding of different adsorbates on two symmetric (C_{3v}) copper clusters, Cu(7, 3) (fig. 10.2b) and Cu(10, 3) (fig. 10.2c) was examined. The adsorption energy of ammonia on Cu(7, 3) was within 1 kJ/mol of the value found for the Cu(8, 3) cluster (C_s) suggesting that the symmetry of the cluster has little effect.

The adsorption energies of atomic oxygen and nitrogen on the other hand were reduced from 401 to 362 and from 339 to 288 kJ/mol, respectively in going from Cu(8, 3) to Cu(10, 3). While cluster symmetry may be responsible for the small but measurable lowering of the adsorption energies, the more likely explanation is due to changes in the cluster Fermi level.

In general, as expected, the adsorption energies reported in table 10.1 demonstrate that molecular adsorption is less strong than radical fragment adsorption, which is less strong than adatom adsorption. Molecular adsorbates have a weak electrostatic surface interaction and tend to prefer onefold coordination sites, whereby Pauli repulsion is minimized [17, 18]. Adatoms and hydrogen deficient radical fragments such as NH and OH, however, bind much stronger and prefer the higher threefold coordination sites. The overlap between the free adatom p_x and p_y orbitals with the metal surface s orbitals provides additional stabilization at the higher coordination sites which helps to increase the adsorption energy. Intermediate radical fragments, such as NH_2, prefer twofold coordination. A number of our adsorption energies correspond with bond order conservation calculations by Shustorovich [15].

The adsorption of molecular oxygen is an important step in the O_2 controlled pathways, eqs. (10.3) and (10.4), so we gave considerable attention to optimizing the binding of O_2 to the surface. Both perpendicular ($\perp$) and symmetric parallel ($\parallel$) adsorption over threefold coordination sites were found to be favorable steps and within 10 kJ/mol one another. In the parallel arrangement, the oxygen-oxygen bond is stretched from 1.21 Å to 1.43 Å and each oxygen appears to take on a considerable negative charge. This geometry is very similar to the experimental results reported by Madix for O_2 on Ag(110) where the oxygen-oxygen bond was found to bind parallel to the surface with an O-O distance of 1.41 Å [35]. The bond length follows the value reported for the gas-phase O_2^{2-} (1.41 Å) [36] which suggests that each oxygen takes on a considerable negative charge. Computed Mulliken charges for the bare Cu(8, 3) cluster and for the Cu(8, 3) cluster with adsorbed atomic and (parallel and perpendicular) molecular oxygen, are given in table 10.2. Due to arbitrariness of the Mulliken population analysis to apportion the density in a chemical bond to its representative atoms, the results in table 10.2 provide only an approximate qualitative measure of charge and charge transfer. The surface O_2^* species picks up a significant charge (-0.62) from its neighboring copper atoms (4, 5 and 6 in table 10.2), which is in good agreement with the results reported by Fischer and Whitten [37], -0.76 for O_2 bound tilted on Cu(001). This is somewhat lower than value for adsorbed atomic oxygen (-0.75). The combination of the long O-O bond and the enhanced surface charge transfer to this bond suggests that the parallel arrangement is a likely precursor state for the O_2 dissociation.

Table 10.2   *The computed Mulliken charges for the bare Cu(8, 3) cluster and for the Cu(8, 3) cluster with threefold adsorbed atomic oxygen, parallel (II) molecular oxygen and perpendicular (⊥) molecular oxygen.*

Atom	#	bare	O	O_2 (II)	O_2 (⊥)	Atom	#	bare	O	O_2 (II)	O_2 (⊥)
Cu	1	-0.060	0.016	0.005	0.036	Cu	8	-0.006	-0.077	-0.000	0.083
Cu	2	-0.066	0.016	0.005	0.036	Cu	9	0.023	0.010	0.006	-0.000
Cu	3	0.190	0.193	0.188	-0.100	Cu	10	0.023	0.010	0.006	-0.000
Cu	4	-0.029	0.240	0.148	0.033	Cu	11	0.038	-0.062	-0.004	-0.055
Cu	5	-0.029	0.240	0.148	0.033	O	12	—	-0.745	-0.341	-0.074
Cu	6	-0.098	0.235	0.117	0.061	O	13	—	—	-0.277	-0.255
Cu	7	0.006	-0.077	-0.000	0.083	ΣQ_O		—	-0.745	-0.618	-0.329
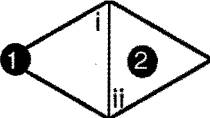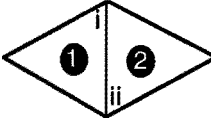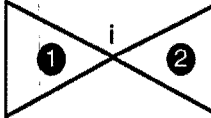
Interestingly, while both molecular oxygen surface-species and the adsorbed atomic oxygen pick up significant charge from the copper surface, the charge-transfer is not as high as two electrons (ΣQ_O in table 10.2). The value for atomic oxygen on Cu(8, 3), -0.75, is in good agreement with those reported by others for fourfold atomic oxygen on the Cu(100) surface. Illas et al. [38] found -0.96 and -0.62 (for respectively the ^2E and $^4A_2$ state), and by Mattsson et al. [39], around -0.85 (for the ^2E state) for atomic oxygen on the Cu(4, 1) cluster. Through a detailed analysis of the projection of oxygen orbitals in the Cu(4, 1)-O wave function, the dipole moment curves for oxygen and various point charges interactions with the Cu(4, 1) cluster, and the participation of the copper 3d orbitals in the copper-oxygen bond, Illas and Bagus [40] were able to extend approximate Mulliken results to find a better estimate of the charge on oxygen, -1.5 electrons. The good agreement between the Mulliken charges reported here and those determined by Illas and Bagus suggest that the actual charge of oxygen on the Cu(8, 3) cluster is closer to -1.5. This also agrees with the experimental results of Clendening et al. [41] who find small increases in the work function induced by oxygen, and hence a charge transfer from the metal to the oxygen less than two electrons.

For molecular oxygen adsorbed perpendicular to the surface, the optimized O-O distance (1.30 Å) was found to be significantly shorter then that for the parallel case. The 1.30 Å distance is close to the reported 1.36 Å for O_2^- in the gas phase. In addition, there is also a decrease in the overall charge transfer, -0.33 on O_2. While the parallel mode of molecular oxygen adsorption is slightly favored on the clean copper surface, the perpendicular mode, as we shall see, becomes favored in the presence of coadsorbed or preadsorbed ammonia species due to a reduction in the repulsive interactions.

10.3.2　　　Lateral Surface Interactions

Our previous results on the adsorption of ammonia on Cu(111) and the electronic effect of coadsorbed atomic oxygen demonstrated the significance of lateral surface interactions on calculated adsorption energies [17, 19]. Lateral interaction energies are defined here as the enhanced or diminished adsorption energy of an adsorbate on a surface due to the presence of additional surface species. The controlling enhancement or reduction should be governed predominantly by changes in the electronic surface structure, i.e. through-metal interactions rather than through-space interactions. The adsorbate arrangement on the surface for the above example is depicted in case I of table 10.3. NH_3 (A1), which prefers the onefold adsorption site (Cu3 in fig. 10.1) is stabilized by 32 kJ/mol via a through-metal attractive interaction with the neighboring threefold O adsorbate (A2). A detailed electronic analysis of this type of interaction was presented elsewhere [18, 19, 42]. The attractive interaction can be rationalized along the lines of bond order conservation [43] and least metal atom sharing principles [42]. The presence of the O adsorbate weakens the bonds between nearest-neighbor (Cu4 and Cu5) and next-nearest-neighbor metal atoms (Cu3, Cu7, Cu8 and Cu11) which subsequently strengthens the binding at next-nearest-neighbor adsorption sites, such as the onefold position for ammonia (Cu3). The adsorption of NH_3 in the presence of $O_2{}^*$ and the adsorption of NH_2 in the presence of OH^* are two similar examples of the enhanced binding effects for a case I adsorption. NH_3 binds 17 kJ/mol more strongly and NH_2 binds 5 kJ/mol more strongly in the presence of $O_2{}^*$ and OH^* respectively.

Table 10.3　　*Lateral interaction energies (in kJ/mol) for coadsorptions on Cu(8, 3). Case I refers to adsorption at a onefold site and at a next-nearest neighbor threefold site. In cases II and III, the adsorbates bind at neighboring threefold sites and share two and one metal atoms respectively.*

cluster	adsorbates		case I	case II	case III
	A1 or ①	A2 or ②			
Cu(8, 3)	O	NH_3	-32	—	—
Cu(8, 3)	O_2	NH_3	-17	—	—
Cu(8, 3)	OH	NH_2	-5	—	—
Cu(8, 3)	O	NH	—	+178	+25
Cu(8, 3)	O	N	—	—	+30
Cu(8, 3)	OH	N	—	+170	+29

The case II and case III adsorption schemes depicted in table 10.3 present situations where both adsorbates prefer higher coordination and sit at adjacent threefold sites. In the case II situation, both adsorbates share two metal atoms (i and ii) in forming adsorbate-metal bonds. This "sharing" considerably weakens the metal-adsorbate bonds and gives rise to a large repulsive interaction between the two adsorbates. For example, the adsorption of NH on the Cu(8, 3)-O cluster, where the oxygen and NH share two metal atom centers, was found to be 178 kJ/mol less favorable than for the adsorption of NH on the clean Cu(8, 3) surface. According to the principle of least metal atom sharing [42], one should expect a large repulsive interaction. The strength of the repulsive interaction, however, can be considerably reduced by moving to case III where the adsorbates share only a single metal atom center (i). This explains the results in table 10.3, where the calculated repulsive interactions for case III are reduced to 25-30 kJ/mol. These values are better in line with general experimental adsorbate-adsorbate repulsive interaction energies on transition metal surfaces. In general the results suggest that only case I and case III situations are likely on the Cu(111) surface.

Before proceeding to the overall reaction cycles, we first discuss the model used for the relative positioning of adsorbates on the cluster. We attempt to minimize artifacts of cluster size effects and establish an appropriate model of the real surface. NH_3 which binds weakly to the cluster, will be much more sensitive to location (interior vs. exterior) than the strongly adsorbed O. Therefore the more realistic arrangement of the NH_3 and O adsorbates is to have NH_3 sit onefold on the central copper site with O closer to the edge. The inverse situation, where NH_3 is placed at an edge site and O located toward the center of the cluster, will be less representative of an extended surface because of the enhanced stability of NH_3 at the unsaturated edge site. Here we analyze the analogous situation of NH_2 and O on Cu(8, 3). The binding energy was 140 kJ/mol stronger for the case where NH_2 was placed at an edge twofold site (with oxygen positioned in the center) than the case in which NH_2 was bound at a central edge site (with oxygen situated at an exterior threefold site). This increased binding energy, for NH_2 at the edge of the cluster, is directly due to the excessive stabilization of NH_2 at unsaturated metal sites. The more likely model of the extended surface is therefore the one in which O binds at the exterior with NH_3 and NH_2 occupying more central adsorption sites.

10.3.3 Overall catalytic cycles

Adsorption-, formation- and lateral interaction energies provided the basis for computing reaction enthalpies of elementary adsorption, surface reaction and desorption steps. Overall catalytic cycles were fashioned from these steps and are delineated in terms of the controlling mechanistic paths defined in eqs. (10.1)-(10.4). Each of these are described here in turn.

10.3.3.1   *Atomic oxygen controlled*

Two mechanistic paths exist for the cycles controlled by atomic oxygen. In the first, atomic oxygen abstracts a single hydrogen from neighboring ammonia to form surface amide and hydroxyl groups (eq. 10.1). In the second, two of the ammonia hydrogens are simultaneously transferred from the adsorbed ammonia to the surface oxygen to yield gaseous water directly and a surface imide (eq. 10.2). The elementary adsorption, surface reaction (SR) and desorption steps required for the two overall cycles which follow these two different paths are outlined in table 10.4. The corresponding reaction enthalpies for each of these steps are assembled into the overall energy profile for each of the two cycles, shown in fig. 10.3.

Table 10.4   *The overall steps in the dissociation of NH_3 to N_2 and H_2O via atomic oxygen through (1) sequential hydrogen abstraction steps, and (2) simultaneous transfer of two hydrogens.*

ATOMIC OXYGEN PATHS			
Sequential hydrogen abstraction steps		**Simultaneous hydrogen abstraction steps**	
$2NH_3(g) + 2^*$ $\rightarrow$ $2NH_3^*$		$2NH_3(g) + 2^*$ $\rightarrow$ $2NH_3^*$	
$3O_2(g) + 6^*$ $\rightarrow$ $6O^*$		$2O_2(g) + 4^*$ $\rightarrow$ $4O^*$	
SR1 $2NH_3^* + 2O^*$ $\rightarrow$ $2NH_2^* + 2OH^*$		**SR4** $2NH_3^* + 2O^*$ $\rightarrow$ $2NH^* + 2H_2O(g)$	
SR2 $2NH_2^* + 2O^*$ $\rightarrow$ $2NH^* + 2OH^*$		**SR3** $2NH^* + 2O^*$ $\rightarrow$ $2N^* + 2OH^*$	
SR3 $2NH^* + 2O^*$ $\rightarrow$ $2N^* + 2OH^*$			
$2N^* + 2O^*$ $\rightarrow$ $2NO^*$		$2N^* + 2O^*$ $\rightarrow$ $2NO^*$	
$2N^*$ $\rightarrow$ $N_2(g)$		$2N^*$ $\rightarrow$ $N_2(g)$	
$6OH^*$ $\rightarrow$ $3/2\ O_2(g) + 3H_2O(g)$		$2OH^*$ $\rightarrow$ $1/2\ O_2(g) + H_2O(g)$	

In the first step in fig. 10.3a, ammonia is adsorbed on the surface in the presence of oxygen at -48 kJ/mol. The negative sign simply indicates that the step is exothermic. Additional oxygen, which is required for the overall cycle, is dissociatively adsorbed leading to a strongly bound atomic oxygen (-148 kJ/mol). The high exothermicity of this step indicates that any ad-oxygen that is formed on the surface will be very difficult to remove, and thus acts to poison active surface sites. The initial ammonia dissociation step, SR1, was found to be 128 kJ/mol more likely in the presence of oxygen than on the clean Cu(111) surface, however, at +48 kJ/mol some form of thermal energy is still required for this endothermic step. Subsequent dissociation steps, SR2 (+6 kJ/mol) and SR3 (-48 kJ/mol), to form NH^* and N^* help to drive the energetics of the overall cycle. Thermodynamics, indicate that the final nitrogen surface species favor recombination with additional N^* and desorption as N_2 (-214 kJ/mol) over recombination with oxygen and desorption as NO (+46 kJ/mol).

However under steady state reaction conditions, adsorbed oxygen, which is strongly bound to the surface, will be the most abundant reaction intermediate (MARI). The number of N-O collisions will, therefore, be far greater than the number of N-N collisions, thus implying that NO formation will dominate over N_2 formation. Lastly, the recombination of surface hydroxyl groups to form water and adsorbed atomic oxygen was found to be highly endothermic and is speculated as a plausible rate controlling step. The overall reaction energy for the complete catalytic cycle was computed to be -625 kJ/mol which is in very good agreement with the estimate of -611 kJ/mol from thermochemical data.
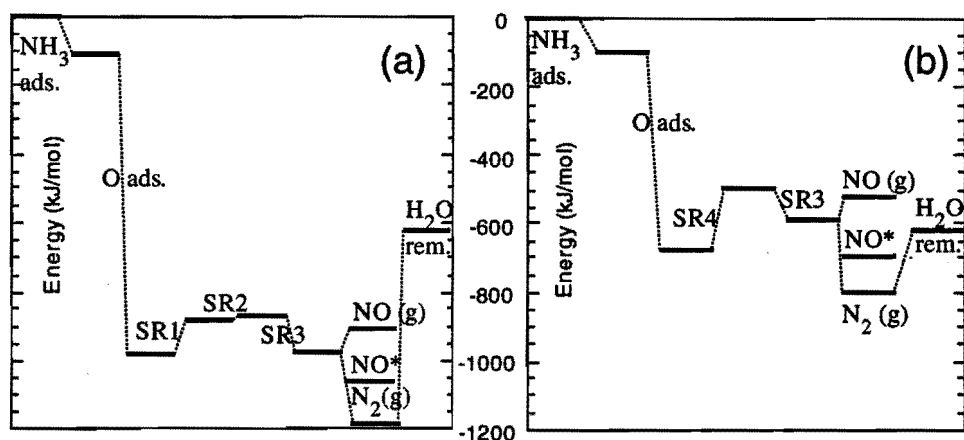
Fig. 10.3 *The energetics of $2NH_3(g) + O_2(g) \rightarrow N_2(g) + H_2O(g)$ controlled by atomic oxygen. (a) sequential H transfer to form NH_2^*, NH^*, N^* and OH^*, and (b) simultaneous transfer of 2H to form $H_2O(g)$ directly and NH^* followed by a final H-abstraction to form N^*. The first two steps in both cycles refer to NH_3 and O adsorption. Steps SR1-SR4 are depicted in table 10.4. The final steps, N_2 (g), NO^*, NO(g), and H_2O rem., refer to recombinative desorption of N to $N_2(g)$, recombinative desorption of NO, reaction of N^* and O^* to form NO^*, and recombination of OH to form $H_2O(g)$, respectively.*

Fig. 10.3b represents the overall energy diagram for the atomic oxygen mediated path in which two hydrogens are simultaneously transferred in the surface dissociation step and water is formed directly. This cycle is identical to that in fig. 10.3a with the exceptions that less atomic oxygen is required to carry out the overall reaction and the number of surface reactions is reduced from two to three due to the simultaneous transfer of two hydrogens in the initial dissociation step. The most striking feature of the cycle is the considerable energy required to dissociate the two hydrogens from ammonia. At +92 kJ/mol, this step is now +44 kJ/mol more endothermic than that for the abstraction of a single hydrogen (fig. 10.3a).

10.3.3.2   Molecular oxygen controlled

The overall cycles for the molecular paths, eqs. (10.3) and (10.4), are reported in table 10.5, and their corresponding energy profiles depicted in fig. 10.4. The path mediated by a single hydrogen transfer to form the OOH^* intermediate is shown in part a. In this scheme, ammonia and molecular oxygen are coadsorbed and react to form OOH^* and NH_2^*. A series of ammonia adsorption calculations at various O-O-surface angles indicated that the coadsorbed molecular oxygen prefers to sit perpendicular to the surface. This angle decreases somewhat as the hydrogen abstraction reaction proceeds to help shorten the distance that the hydrogen must travel. Subsequent dissociation steps lead to O^*, OH^*, and NH^* products. To complete the series of abstraction steps, one mole of dissociated O_2 was required for the final step: $NH^* + O^* \rightarrow N^* + OH^*$. The initial surface dissociation step for this scheme, SR5, is now exothermic, and appears more likely than the considerable endothermic steps reported for dissociation on the clean Cu(111) surface and the atomic-oxygen-assisted dissociation. The desorption steps are the same as those reported in table 10.4 and fig. 10.3a.

Table 10.5   *The overall steps in the dissociation of NH_3 to N_2 and H_2O via molecular oxygen through (1) sequential transfer of hydrogen, and (2) simultaneous transfer of two hydrogens.*

MOLECULAR OXYGEN PATHS		
Sequential hydrogen abstraction steps	**Simultaneous hydrogen abstraction steps**	
$2NH_3(g) + 2^* \rightarrow 2NH_3^*$	$2NH_3(g) + 2^* \rightarrow 2NH_3^*$	
$2O_2(g) + 2^* \rightarrow 2O_2^*$	$2O_2(g) + 2^* \rightarrow 2O_2^*$	
$O_2(g) + {}^* \rightarrow 2O^*$		
SR5 $2NH_3^* + 2O_2^* \rightarrow 2NH_2^* + 2OOH^*$	**SR6** $2NH_3^* + 2O_2^* \rightarrow 2NH^* + 2O^* + 2H_2O(g)$	
SR2 $2NH_2^* + 2O^* \rightarrow 2NH^* + 2OH^*$	**SR3** $2NH^* + 2O^* \rightarrow 2N^* + 2OH^*$	
SR3 $2NH^* + 2O^* \rightarrow 2N^* + 2OH^*$		
$2N^* + 2O^* \rightarrow 2NO^*$	$2N^* + 2O^* \rightarrow 2NO^*$	
$2N^* \rightarrow N_2(g)$	$2N^* \rightarrow N_2(g)$	
$6OH^* \rightarrow 3/2\ O_2(g) + 3H_2O(g)$	$6OH^* \rightarrow 3/2\ O_2(g) + 3H_2O(g)$	

The final path analyzed, eq. (10.4), was that for molecular-mediated oxygen dissociation and the simultaneous abstraction of two hydrogens to form gaseous water. The steps required for this scheme are outlined in table 10.5 and depicted in fig. 10.4b. The overall energy profile is the most appeasing of all those studied. The cycle moves to lower energies at each subsequent elementary step until the final endothermic recombinative desorption steps. In addition, this path completely eliminates the highly exothermic oxygen dissociation step

which leads to strong adsorbed atomic oxygen that poison active surface sites. The initial surface dissociation step, $NH_3(a) + O_2(a) \rightarrow NH(a) + O(a) + H_2O(g)$, is now thermodynamically quite favorable at -184 kJ/mol.
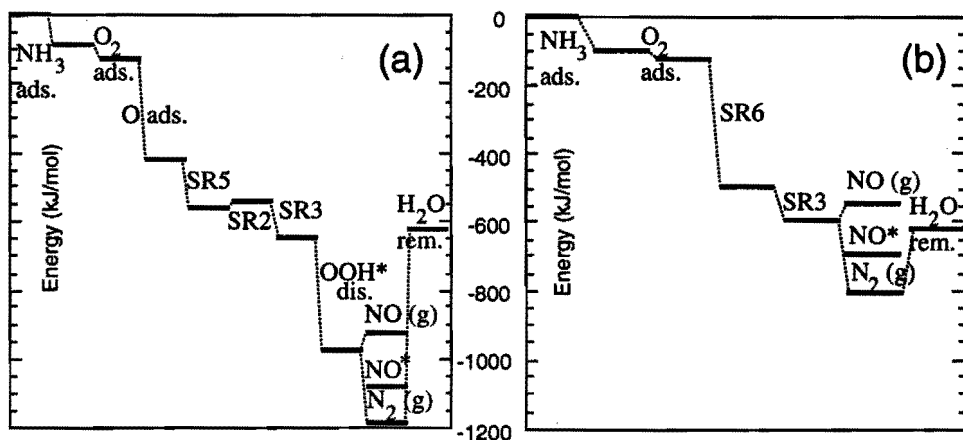
Fig. 10.4 *The energetics of $2NH_3(g) + O_2(g) \rightarrow N_2(g) + H_2O(g)$ controlled by molecular oxygen. (a) the sequential H transfer steps to form NH_2^*, NH^*, N^* and OOH^*, and (b) the simultaneous transfer of 2H to form $H_2O(g)$ directly and NH^* followed by a final H-abstraction to form N^*. The first two steps in both cycles refer to NH_3 and O_2 adsorption. Steps SR2-SR6 are depicted in table 10.5. The final steps, $N_2(g)$, NO^*, $NO(g)$, OOH^* dis., and H_2O rem., refer to recombinative desorption of N to $N_2(g)$, recombinative desorption of NO, reaction of N^* and O^* to form NO^*, dissociation of OOH^* to form O^* and OH^*, and recombination of OH to form $H_2O(g)$, respectively.*

10.3.4   Activation energies and reaction mechanism

In general, the overall reaction energies for each step suggest that recombinative hydroxyl removal as water and the initial hydrogen abstraction step are the most likely candidates for rate-controlling. While the former process is the more endothermic, entropy is an important factor. At higher temperatures, recombinative desorption is considerably enhanced due to the entropic contributions, and the surface reaction steps become more predominant in controlling the mechanism. We, therefore, analyzed the activation barriers for each of the initial surface reaction steps shown in eqs. (10.1)-(10.4).

10.3.4.1   Atomic oxygen

We reported the activation barrier for ammonia dissociation in the presence of atomic oxygen in a previous communication [18]. The dissociation was modeled as a two-step process: N-H bond activation with the nitrogen fixed at the onefold site, and surface diffusion of the NH_2^* product to the stable twofold binding site. The initial N-H activation step was found to be controlling with an activation barrier of +132 kJ/mol. The surface reactants, transition complex, and surface products for this reaction along with the associated activation energy and overall reaction energy are depicted in fig. 10.5.
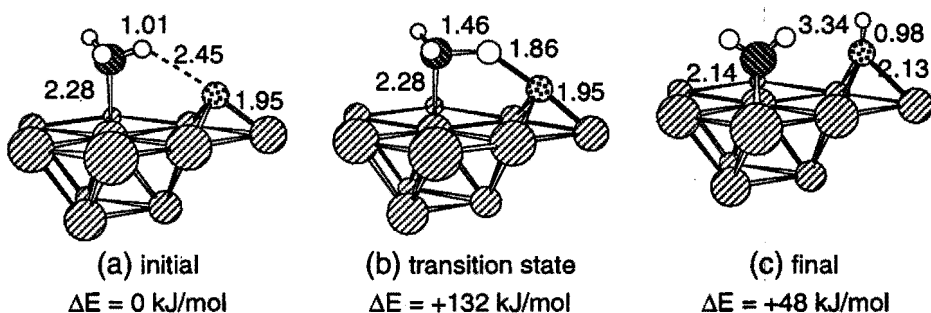

(a) initial	(b) transition state	(c) final
ΔE = 0 kJ/mol	ΔE = +132 kJ/mol	ΔE = +48 kJ/mol

Fig. 10.5   *The main structural and energetic results for path 1 dissociation of NH₃ over Cu(8, 3). Atomic oxygen acts to abstract a single hydrogen from NH₃ on Cu(8, 3). Bond lengths are in Å.*

The detailed reaction coordinate for the simultaneous activation of two NH bonds by atomic oxygen was analyzed here on the Cu(6) cluster. The N-H bond stretch was chosen as the reaction coordinate. All other adsorbate-surface variables were optimized at each position along this coordinate. The important results are shown in fig. 10.6.
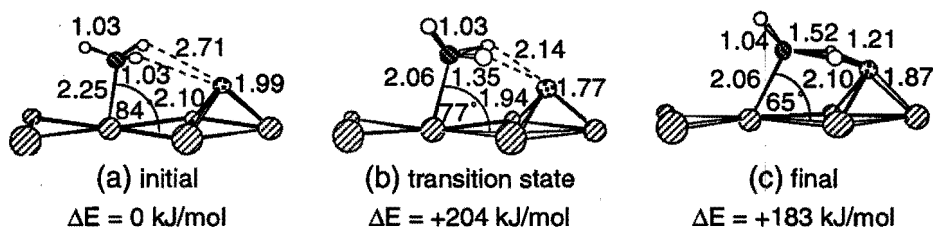

(a) initial	(b) transition state	(c) final
ΔE = 0 kJ/mol	ΔE = +204 kJ/mol	ΔE = +183 kJ/mol

Fig. 10.6   *The main structural and energetic results for path 2 dissociation of NH₃ over Cu(6). Atomic oxygen acts to abstract two hydrogens from the coadsorbed ammonia which results in NH* and the formation of gaseous water. The N-H stretch is the reaction coordinate. Bond lengths are in Å.*

As the two N-H bonds stretch, the resulting NH* fragment rotates toward the threefold site which is adjacent to the H₂O species that is being formed. This is illustrated by the decreasing N-H-surface angle along the reaction coordinate in fig. 10.6. All three copper-oxygen bonds elongate as gaseous water is formed. The two Cu-O bonds closest to the nitrogen-bound adsorbate, however, increase somewhat more substantially. In the final situation (fig. 10.6c), for example, the Cu-O distances are 2.10 Å for Cu4-O and Cu5-O and 1.87 Å for Cu6-O. This increase in the bond distance is attributed to the repulsive interaction between the oxygen which still maintains some interaction with the surface and the neighboring NH fragment which is forming. The release of water to the gas phase essentially removes this repulsive interaction and thus allows the surface imide to be formed toward the front of the cluster. Had the water remained adsorbed, the NH* species would have more likely moved toward back of the cluster which is in accord with the principle of least metal atom sharing. The transition-state occurs as the N-H bond is stretched 0.32 Å from its original equilibrium distance (1.03 Å). This corresponds to an activation barrier of 204 kJ/mol. However, as was discussed earlier, this simple Cu(6) cluster underpredicts the N-H bond strength, and therefore provides only a lower bound on the energy barrier. The true activation energy is therefore > 204 kJ/mol, which makes this an unlikely reaction path.

10.3.4.2   Molecular oxygen

The N-H bond stretch was also chosen as the reaction coordinate for the abstraction of a single hydrogen by molecular oxygen to form OOH*. Reaction coordinate calculations were performed on both the Cu(6) and Cu(8, 3) clusters, and the results are shown in fig. 10.7 and fig. 10.8, for the two respective clusters.
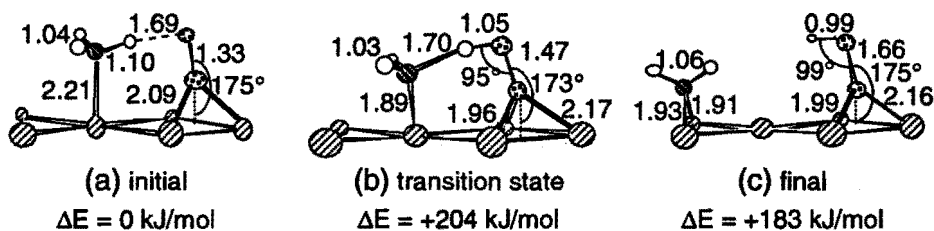

| (a) initial | (b) transition state | (c) final |
| ΔE = 0 kJ/mol | ΔE = +204 kJ/mol | ΔE = +183 kJ/mol |

Fig. 10.7   The main structural and energetic results for path 3 dissociation of NH₃ over Cu(6). Molecular oxygen acts to abstract a single hydrogen from the coadsorbed ammonia to form NH₂ and OOH* intermediates. The N-H stretch is the reaction coordinate. Bond lengths are in Å.*

(a) initial
ΔE = 0 kJ/mol

(b) transition state
ΔE = +67 kJ/mol

(c) final
ΔE = -25 kJ/mol

Fig. 10.8 *The main structural and energetic results for path 3 dissociation of NH_3 over Cu(8, 3). Molecular oxygen acts to abstract a single hydrogen from the coadsorbed ammonia to form NH_2^* and OOH^* intermediates. The N-H stretch is the reaction coordinate. Bond lengths are in Å.*
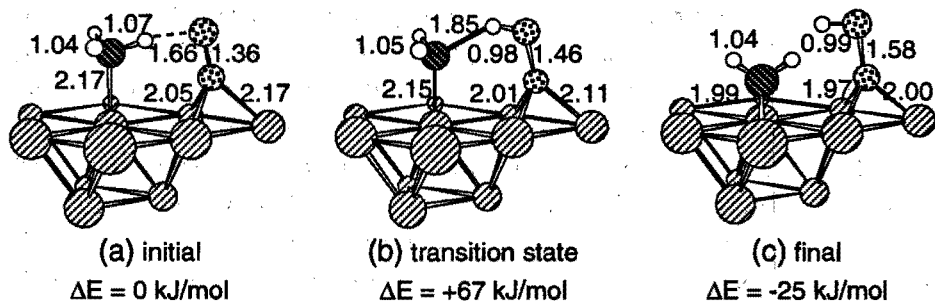
Molecular oxygen initially prefers the near-perpendicular adsorption geometry in the presence of ammonia. The O-O-surface angle decreases very slightly as the reaction proceeds to shorten the distance the hydrogen must travel to the neighboring oxygen. However, once the hydrogen begin binding with the oxygen, the O-O-surface angle returns to the perpendicular state. In general the results in figs. 10.7 and 10.8 demonstrate that as the N-H bond is elongated the Cu-N distance decreases, the Cu-O distance decreases and the O-O distance increases. This corresponds with the development of a stronger Cu-N, Cu-O bonds and a weaker O-O bond, consistent with the BOC principle. The low activation energy (+29 kJ/mol) and the shorter Cu-N bonds on Cu(6) are clear evidence of the overprediction by Cu(6) for Cu-N binding and hence underprediction for N-H bond breaking. This helps to establish the role of Cu(6) for providing lower limits on N-H dissociation barrier. Cu(8, 3) yields a much more accurate representation and predicts an activation energy of +67 kJ/mol. The results presented in fig. 10.8 were obtained with DGauss. The activation energy was also calculated with ADF, and found to be +62 kJ/mol. Path 3 is quite late in the N-H stretch. It is not until NH^* diffuses to the more favorable twofold site and rotates about the Cu-N bond to a more favorable arrangement where the remaining N-H bonds are perpendicular to the surface (fig. 10.8c) that the reaction becomes favorable. NH_2 prefers the twofold site which is one Cu removed from the binding of the OOH^* species (fig. 10.?), similar to case I whereby the through-metal interaction stabilizes the binding of both adsorbates. One last point worth noting is the difference between the three Cu-O bond lengths. In path 2, where O abstracted two hydrogens, the water and NH^* species were in close proximity, and therefore repulsive interactions lead the Cu4-O and Cu5-O to be somewhat longer. In path 3 the through-metal interaction increases the binding and hence decreases the Cu4-O and Cu5-O bond lengths.

In the final mechanistic path, eq. (10.4), molecular oxygen acts to simultaneously abstract two hydrogens from the coadsorbed ammonia to form water directly. The N-H bond stretch was once again chosen as the reaction coordinate. The results are depicted in fig. 10.9 on the Cu(6) cluster, and suggest that the activation energy for this path is greater than +172 kJ/mol. The activation barrier for this path is considerably higher than that for the abstraction of a single hydrogen. This is attributed to the longer initial N-H distances (1.66 Å versus 2.41 Å for path 4) and the necessity to activate two bonds rather than one. In fact, if one compares the N-H bond length for the initial adsorbates in path 3, 1.10 Å on Cu(6) and 1.07 Å on Cu(8, 3), to those for path 4, 1.02 Å on Cu(6) and 1.03 Å on Cu(8, 3), it appears that the NH bond for path 3 is initially activated as a result of the short initial O-H distance. There is no initial activation, however, for path 4.
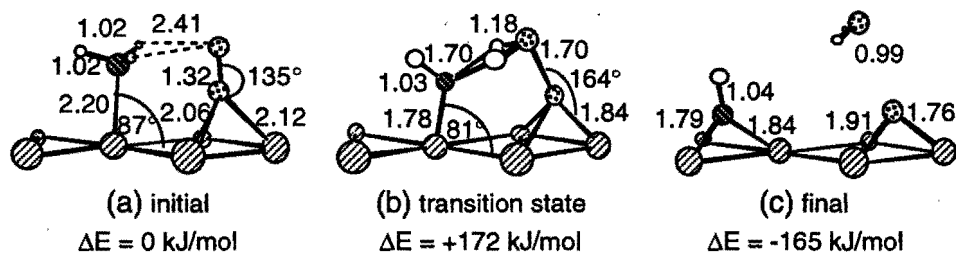

(a) initial	(b) transition state	(c) final
ΔE = 0 kJ/mol	ΔE = +172 kJ/mol	ΔE = -165 kJ/mol

Fig. 10.9 *The main structural and energetic results for path 4 dissociation of NH_3 over Cu(6). Molecular oxygen acts to abstract a two hydrogen from the coadsorbed ammonia to form NH^*, O^* and gaseous water. The N-H stretch is chosen as the reaction coordinate. Bond lengths are in Å.*

An energetically more favorable reaction coordinate for this path was found to be the stretch of the weak O-O bond. A summary of the reaction coordinate results for this step are provided in fig. 10.10. The activation energy for this path is +134 kJ/mol and the transition state appears to be early in the N-H stretch (+0.03 Å) but late with respect to the O-O stretch (+1.02 Å). As the O-O bond is stretched the Cu-O bond becomes shorter and the two hydrogens are separated from the adsorbed ammonia to form water in the gas phase and a surface imide which sits threefold. The results from path 2 (fig. 10.6) demonstrated that the NH^* preferred to move forward on the cluster toward the releasing water. However, in path 4, as is shown here in fig. 10.10, the surface imide actually prefers to move toward the threefold site at the back of the cluster, away from the threefold adsorbed oxygen. Had the NH^* moved to the threefold site directly in front of it both the NH^* and O^* would share two metal atom neighbors, a case II scenario, which was found to be considerably repulsive.
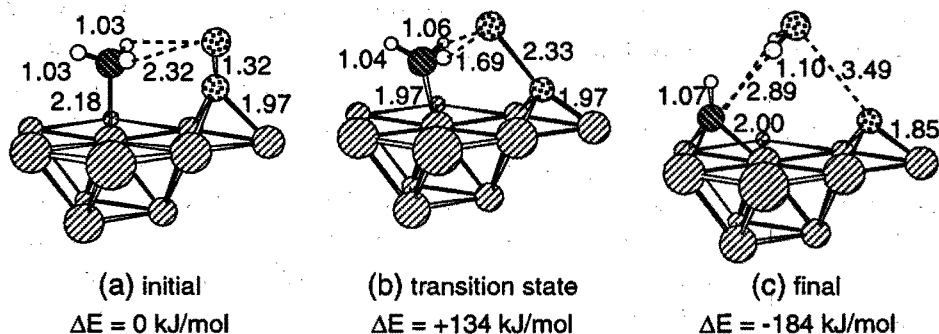
(a) initial
ΔE = 0 kJ/mol

(b) transition state
ΔE = +134 kJ/mol

(c) final
ΔE = -184 kJ/mol

Fig. 10.10 *The main structural and energetic results for path 4 dissociation of NH₃ over Cu(8, 3). Molecular oxygen acts to abstract a two hydrogen from the coadsorbed ammonia to form NH*, O* and gaseous water. The O-O stretch is chosen as the reaction coordinate. Bond lengths are in Å.*

10.3.5   Nitric oxide formation

While recombination of nitrogen and oxygen adatoms and desorption as nitric oxide (NO) is thermodynamically less favorable than recombinative desorption of N_2, the substantially higher oxygen surface coverages make the NO path much more likely. To further investigate this we computed the detailed energy profile for the adsorption and dissociation of NO over the Cu(8, 4) cluster. Fig. 10.11 depicts the important structural results and a summary of the corresponding energetics, while fig. 10.12 provides a more complete energy profile.
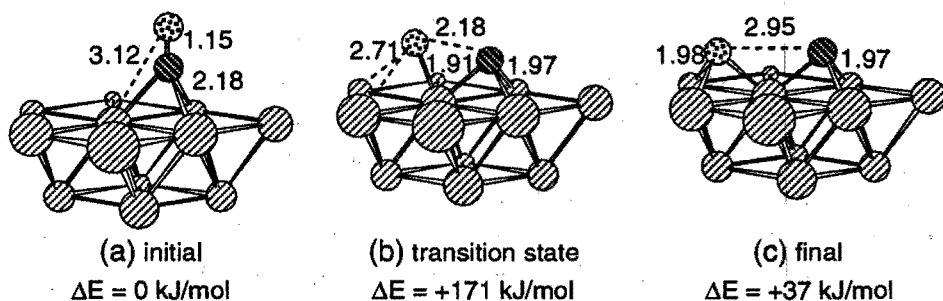

(a) initial
ΔE = 0 kJ/mol

(b) transition state
ΔE = +171 kJ/mol

(c) final
ΔE = +37 kJ/mol

Fig. 10.11 *A summary of structural and energetic results for dissociation of NO over Cu(8, 4). Initial refers to the adsorption of NO, the transition state and the overall reaction energy are measured with respect to the gas phase, i.e. NO(g) and clean Cu(8, 4). Bond lengths are in Å.*

Our calculations revealed that nitric oxide adsorbs molecularly at the threefold adsorption site (with Cu-N and N-O bond distances of 2.18 Å and 1.15 Å respectively). The calculated adsorption energy was found to be -83 kJ/mol (table 10.1). This agrees quite well with the experimental value of -105 kJ/mol reported by Conrad et al. for NO on Ni(111) [44]. Nickel is expected to be more active than copper due to vacancies in its valence electron band, and thus the adsorption energy on Ni(111) should be somewhat greater. The computed adsorption energy also follows the ab initio MCSCF results of Bagus et al. [45] for NO adsorbed onefold on Cu(1, 4) which indicate adsorption energies between -80 kJ/mol and -100 kJ/mol.
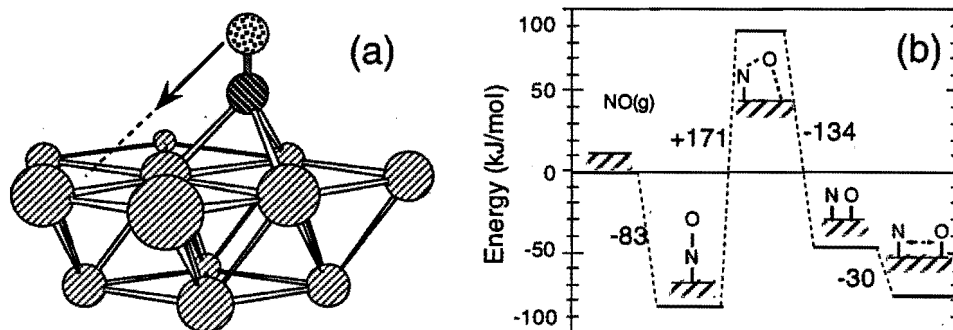

Fig. 10.12 *NO dissociation over Cu(8, 4), (a) reaction path and (b) calculated overall energetics. The first step is the adsorption of NO(g), followed by the activation barrier for NO dissociation, the intermediate surface products (N^* and O^*) and the final "diffused" state for low surface coverage.*

A linear transient between the optimized NO reactant and the dissociated product state was chosen as the reaction coordinate for NO dissociation. The activation barrier was computed by optimizing surface-N-O interactions at a number of points along the reaction coordinate. The resulting barrier is +88 kJ/mol with respect to the gas phase (or +51 kJ/mol for the reverse reaction N-O recombination). The associated transition state shown in fig. 10.11 appears to be quite late with respect to the N-O stretch (+1.03 Å) and close in proximity to the dissociated product state. The reaction proceeds over a single copper atom, thus resulting in N^* and O^* products in a case III situation. The barrier to dissociate NO over a twofold site, i.e. a case II situation, would have been much more costly in terms of energy.

At low coverages, the N^* and O^* products diffuse apart (final step in fig. 10.12) to remove the 30 kJ/mol repulsive interaction. The dissociative adsorption energy to the intermediate state, where N^* and O^* share a single metal center, is -46 kJ/mol, while that to the separated N^* and O^* products is -76 kJ/mol. The reverse reaction of N^* and O^* recombination to molecularly bound NO is slightly exothermic. When this step is coupled with the desorption of NO from the surface, the overall recombinative desorption process becomes endothermic.

10.4   DISCUSSION

The various reaction paths for the dissociation of ammonia studied herein are summarized in table 10.6. While the Cu(111) surface helps to lower both the endothermicity and the activation barrier for ammonia dissociation considerably, the substantial activation barrier and reaction enthalpy indicate that little dissociation will occur over the clean Cu(111) surface. The presence of atomic oxygen decreases the activation barrier and the endothermicity even further. The activation energy is now low enough that moderate dissociation is likely at high temperatures and very low surface coverages. The high exothermicity which accompanies the dissociative adsorption of oxygen, however, indicates that adsorbed oxygen will poison the surface and impede ammonia dissociation kinetics. All of these results are consistent with the experimental findings presented by Roberts and his colleagues on Cu(110) [11, 12] and Cu(111) [14] where at low coverages of preadsorbed oxygen, ammonia dissociation occurs but at a rather slow rate. At higher coverages the ammonia dissociation path shuts down, and adsorbed oxygen overlayers poison the surface.

Table 10.6   Summary of activation- and overall energies for various paths for NH_3 dissociation

	Reaction			Activation energy (kJ/mol)	Overall energy (kJ/mol)
gas phase	$NH_3(g)$	$\rightarrow$	$NH_2(g) + H(g)$	+498	+498
surface	NH_3^*	$\rightarrow$	$NH_2^* + H^*$	+344	+176
path 1 (eq. 10.1)	$NH_3^* + O^*$	$\rightarrow$	$NH_2^* + OH^*$	+132	+48
path 2 (eq. 10.2)	$NH_3^* + O^*$	$\rightarrow$	$NH^* + H_2O(g)$	> +204	+92
path 3 (eq. 10.3)	$NH_3^* + O_2^*$	$\rightarrow$	$NH_2^* + OOH^*$	+67	-84
path 4 (eq. 10.4)	$NH_3^* + O_2^*$	$\rightarrow$	$NH^* + O^* + H_2O(g)$	+134	-184

Of the two candidates for atomic-oxygen-assisted dissociation, we find that the sequential hydrogen dissociation path (eq. 10.1) is more likely. In this path, the ammonia H and surface O^* are significantly closer, only one N-H bond needs to be cleaved and the strong Cu-O bond does not have to be broken. The activation barrier is over 72 kJ/mol lower in energy and the overall reaction energy 44 kJ/mol more exothermic for the mechanism based on single hydrogen transfer steps over the mechanism for the simultaneous transfer of two hydrogens.

The results presented above and summarized in table 10.6, clearly indicate that molecular oxygen acts as chemical precursor in the dissociation of ammonia. Both the sequential and simultaneous hydrogen abstraction paths (eqs. 10.3 and 10.4) are largely exothermic.

Molecular oxygen is weakly bound perpendicular to the copper surface with an adsorption energy of -10 kJ/mol. Electron back donation from the surface to the π^* orbital of O_2, weakens the O-O bond which is reflected by the longer O-O distance ($O_2^* = 1.36$ Å versus $O_2(g) = 1.21$ Å). The weakly bound O_2 can then readily abstract hydrogen from the coadsorbed NH_3. The initial distance between the ammonia hydrogen and O that is transferred to is now only 1.66 Å for path 3, whereas for the O abstraction the distance was 2.45 Å. While the overall thermodynamics favor the simultaneous hydrogen abstraction to form water directly, the activation barriers indicate that the sequential path which is 67 kJ/mol less costly, predominates. The initial O-H distance, and the need to break only a single N-H bond once again are likely explanations why path 3 is favored over path 4. In addition, these explanations help to clarify the change in the reaction coordinate in going from path 3 (controlled by the N-H stretch) to path 4 (controlled by O-O stretch). In path 3, the N-H stretch is activated by the close proximity N-H hydrogen and the neighboring oxygen. In path 4, however, the O-H distance is significantly longer thus reducing N-H bond activation. NH bond scission is therefore much more costly than stretching of the weak O-O bond. In the end, the energy required for the significant O-O stretch in path 4 is greater than the energy needed to cleave the activated N-H bond in path 3.

Under the typical UHV conditions of Roberts [11-14] and at low oxygen partial pressures, the apparent activation energy for ammonia dissociation is really a measure of both the intrinsic N-H bond scission and equilibrium adsorption constants for ammonia and molecular oxygen. For path 4 the apparent activation barrier is +67 kJ/mol whereas for the more likely path 3 the apparent activation barrier is 0 kJ/mol. Path 3 is essentially a non-activated route for molecular oxygen dissociation of ammonia under these conditions. Molecular oxygen dissociation may be in direct competition with this path for the consumption of O_2. However, Habraken et al. [46] determined that the apparent activation for O_2 dissociation over Cu(111) is an activated process with a barrier of 8-17 kJ/mol. Ammonia dissociation by O_2 is therefore the favored route. All of these results directly correspond to the experimental evidence from Boronin et al. [14] who demonstrated that ammonia readily dissociates in the presence of coadsorbed oxygen, and confirm the role of a transient oxygen precursor. At higher partial pressures of oxygen the surface essential becomes poisoned by adsorbed oxygen species and the rate severely inhibited. This is also consistent with findings of Boronin et al. [14].

The "hot" atomic oxygen mediated mechanism proposed by Boronin et al. [14] (path 5) which cannot be completely ruled out is somewhat inconsistent with our findings. The scission of the N-H bond by reaction with O^h requires that energy from the transient oxygen be transferred to the N-H bond. The time scale for this step is comparable with that required for thermal equilibration. Thus, the reaction via the O_2 precursor path appears more likely.

10.5   CONCLUSIONS

Ammonia adsorbs on a model of the Cu(111) surface at -32 kJ/mol. In the absence of coadsorbed oxygen species, the dissociation of ammonia over copper is energetically an unfavorable process with an activation barrier of +344 kJ/mol and an overall reaction enthalpy of +176 kJ/mol. In the presence of coadsorbed oxygen species the dissociation of ammonia over copper is energetically less unfavorable (in the case of atomic oxygen) or a favorable process (in the case of molecular oxygen). Lateral interactions are important in determining both the adsorption and the activation energies. Oxygen promotes N-H bond activation, by lowering the activation energy to +132 kJ/mol. The strong atomic oxygen surface bond, however, leads to poisoning of surface sites which inhibits the overall dissociation kinetics. The atomic pathway in which hydrogen is transferred sequentially to form OH* is favored over the simultaneous path leading to the direct formation of water.

O_2 adsorbs favorably to Cu(111) both in parallel and perpendicular orientations to the surface. The parallel mode is a precursor state for O_2 dissociation where a significant charge transfer from the surface to O_2 π^* orbital weakens the O-O bond as is demonstrated by the long O_2 bond (1.43 Å). The perpendicular mode, on the other hand, is the precursor state for ammonia dissociation. Coadsorbed O_2 enhances the adsorption of ammonia by 17 kJ/mol and acts to lower the barrier for N-H bond activation. The sequential hydrogen abstraction pathway, which leads to the OOH* intermediate, while 100 kJ/mol less exothermic than the path for the simultaneous hydrogen transfer, is kinetically favored by 67 kJ/mol.

The sequential-hydrogen-transfer-transient-molecular-oxygen path is the most likely of all those studied. Its apparent activation energy is zero, i.e. a non-activated process. All paths controlled by transient atomic oxygen, including the "hot" transient oxygen case proposed by Roberts require at least an initial activation barrier of +17 kJ/mol. At low to moderate temperatures the "hot" atomic oxygen path will be kinetically insignificant in comparison with the molecular path. As the temperature increases, however, these other pathways also become feasible. Adsorbed atomic oxygen is formed, which in turn inhibits ammonia dissociation kinetics. At high enough temperatures or coverages the dissociation reaction eventually shuts down due to the formation of strong adsorbed oxygen overlayers.

Finally, based solely on overall enthalpy, recombination of N adatoms and desorption of N_2 was found to be favored over the recombinative removal of NO. However, under reaction conditions both the entropy and the selective collision frequency favor NO formation.

10.6   REFERENCES

[1]   P.J. van den Hoek, E.J. Baerends and R.A. van Santen, *J. Phys. Chem.* **93** (1989) 6469.

[2]   R.A. van Santen, *J. Mol. Catal.* **54** (1989) 288.

[3]   M.C. Zonnevylle, R.H. Hoffman, P.J. van den Hoek and R.A. van Santen, *Surf. Sci.* **223** (1989) 233.

[4]   A.J. Capote, J.T. Roberts and R.J. Madix, *Surf. Sci.* **209** (1989) L151.

[5]   C.T. Au and M.W. Roberts, *Nature* **319** (1986) 206.

[6]   C.T. Au and M.W. Roberts, *J. Chem. Soc. Faraday Trans.* **83** (1987) 2047.

[7]   P.G. Blake and M.W. Roberts, *Catal. Lett.* **3** (1989) 379.

[8]   M.W. Roberts, *J. Molec. Catal.* **74** (1992) 11.

[9]   A.F. Carley, Song Yan and M.W. Roberts, *J. Chem. Soc. Faraday Trans.* **86** (1990) 2701.

[10]   A.F. Carley, M.W. Roberts and M. Tomellini, *J. Chem. Soc. Faraday Trans.* **87** (1991) 3563.

[11]   B. Afsin, P.R. Davies, A. Pashuski and M.W. Roberts, *Surf. Sci.* **259** (1991) L724.

[12]   B. Afsin, P.R. Davies, A. Pashusky , M.W. Roberts and D. Vincent, *Surf. Sci.* **284** (1993) 109.

[13]   C.T. Au and M.W. Roberts, *Chem. Phys. Lett.* **74** (1980) 472.

[14]   A. Boronin, A. Pashusky and M.W. Roberts, *Catal. Lett.* **16** (1992) 345.

[15]   E. Shustorovich and A.T. Bell, *Surf. Sci.* **268** (1992) 397.

[16]   H. Brune, J. Wintterlin, R.J. Behm and G. Ertl, *Phys. Rev. Lett* **68** (1992) 624.

[17]   W. Biemolt, G.J.C.S. van de Kerkhof, P.R. Davies, A.P.J. Jansen and R.A. van Santen, *Chem. Phys. Lett.* **188** (1992) 477 (chapter 7 of this thesis).

[18]   G.J.C.S. van de Kerkhof, W. Biemolt, A.P.J. Jansen and R.A. van Santen, *Surf. Sci.* **284** (1993) 361 (chapter 8 of this thesis).

[19]   W. Biemolt, A.P.J. Jansen, Neurock, M., G.J.C.S. van de Kerkhof and R.A. van Santen, *Surf. Sci.* **287** (1993) 183 (chapter 9 of this thesis).

[20]   E.J. Baerends, D.E. Elis and P. Ros, *Chem. Phys.* **2** (1973) 41.

[21]   E.J. Baerends and P. Ros, *Int. J. Quantum Chem.: Quantum Chem. Sym.* **12** (1978) 169.

[22]   P.M. Boerrigter, G. te Velde and E.J. Baerends, *Int. J. Quantum Chem.* **33** (1988) 87.

[23]   J. Andzelm and E. Wimmer, *J. Chem. Phys.* **96** (1992) 1280.

[24]   S.H. Vosko, L. Wilk and M. Nusair, *Can. J. Phys.* **58** (1980) 1200.

[25]   A.D. Becke, *Phys. Rev. A* **38** (1988) 3098; A.D. Becke, *ACS Symp. Series* **394** (1989) 165.

[26]   J.P. Perdew, *Phys. Rev. B* **33** (1986) 8822.

[27]   J. Andzelm, E. Radzio and D.R. Salahub, *J. Comp. Chem.* **6** (1985) 520.

[28]   L. Versluis and T. Ziegler, *J. Chem. Phys.* **88** (1988) 322.

[29]   T. Ziegler and A. Rauk, *Theoret. Chim. Acta* **46** (1977) 1.

[30]   K.J. Wu and S.D. Kevan, *J. Chem. Phys.* **94** (1991) 7494.

[31] T.J. Chuang, H. Seki and I. Hussla, *Surf. Sci.* **158** (1985) 525.

[32] B.J. Hinch and L.H. Dubois, *J. Chem. Phys.* **96** (1992) 3262.

[33] J.M. Heras, M.C. Asensio and L. Viscido, Z. Phys. Chem. Neue Folge **160** (1988) 199.

[34] T. Ziegler, *Chem. Rev.* **91** (1991) 651.

[35] D.A. Outka, J. Stöhr, W. Jark, P. Stevens, J. Solomon and R.J. Madix, *Phys. Rev. B* **35** (1987) 7891.

[36] D.R. Lide, Ed., *Handbook of Chemistry and Physics*, 71st ed. (CRC Press, Boca Raton, 1990).

[37] C. Fischer and J.L. Whitten, *Phys. Rev. B.* **40** (1989) 5745.

[38] F. Illas, M. Bachs, M. Rubio and J.M. Ricart, *J. Chem. Phys.* **91** (1989) 5466.

[39] A. Mattsson, I. Panas, P. Siegbahn, U. Wahlgren and H. Åkeby, *Phys. Rev. B* **36** (1987) 7389.

[40] P.S. Bagus and F. Illas, *Phys. Rev. B* **42** (1990) 10852.

[41] W. Clendening, J.A. Rodiguez, J.A. Campbell and C.T. Campbell, *Surf. Sci.* **216** (1989) 429.

[42] R.A. van Santen, *Theoretical Heterogeneous Catalysis*, World Scientific lecture and course notes in chemistry, Vol. 5 (World Scientific, Singapore, 1991).

[43] E. Shustorovich, *Surf. Sci. Rep.* **6** (1986) 1; E. Shustorovich, *Adv. Catal.* **37** (1990) 101.

[44] H. Conrad, G. Ertl, J. Küppers and E.E. Latta, *Surf. Sci.* **50** (1975) 296.

[45] P. Bagus, C.J. Nelin and P.J. Avouris, *Vac. Sci. and Technol. A* **5** (1987) 701.

[46] F.H.P.M. Habraken, E.P. Kiefer and G.A. Bootsma, *Surf. Sci.* **83** (1979) 45.

Conclusion
and
Summary

In this thesis we studied some small catalytic systems involving the transition metals iridium, rhodium and copper with density functional (DF) calculations using the Xα method (chapter 2) or the Vosko-Wilk-Nussair exchange-correlation potential (chapters 3-10). Including non-local and (for iridium and rhodium) relativistic corrections in the calculations give a much better description when comparing our calculations with experimental results. With the work described in this thesis we showed that it is very well possible to apply an advanced quantum chemical method to various catalytic relevant problems.

The influences of cations on the adsorption of atomic hydrogen and sulphur on iridium.

Hydrogen adsorbed to a tetrahedral Ir_4 cluster shows a small decrease in hydrogen bond strength in the presence of a Mg^{2+} cation. The maximum decrease is 25 kJ/mol for onefold adsorbed hydrogen. For stronger bonded hydrogen atoms adsorbed in high coordination sites only very small changes in bond strength were found. As a result the heat of dissociative adsorption of hydrogen to tetrahedral Ir_4 particles will not change. The overall activation energy with respect to the gasphase is predicted to decrease in the presence of the Mg^{2+} cation due to the increased heat of adsorption of the hydrogen molecule.

Sulphur adsorbed on tetrahedral Ir_4 cluster without a Mg^{2+} cation shows adsorption energies that are in good agreement with values found from equilibrium measurements. Bonding is mainly due to the interaction with the p orbitals of sulphur. The effect of introducing the Mg^{2+} cation is geometry dependent. The interaction for onefold geometry is weakened, that of the twofold is unchanged, whereas that of the threefold is strengthened. For the onefold geometry the Ir-S bond length remains almost unchanged, for the twofold and threefold it decreases. The influence of a Mg^{2+} cation on CO, H_2 and H adsorption could be explained with a simple electrostatic model because the Mg^{2+} electrostatic field was dominating the changes. For sulphur the influence of the cation is similar for the onefold and the twofold geometry. For the threefold geometry however, chemical bonding effects are of more importance. The bond strengthening can be explained using a promoted sulphur atom which has for this geometry a more favorable π interaction with Ir_4 when Mg^{2+} is present. This indicates an increased sulphur sensitivity of metal particles in close contact with a cation.

Bare rhodium systems and the interaction of carbon monoxide with rhodium.

We calculated various properties for a large number of bare rhodium clusters. Most clusters have non zero magnetic moments. These magnetic moments are most likely a result of the reduced dimensionality and the enhanced electronic degeneracy due to the symmetry of the cluster. Although we used clusters as large as 43 atoms, properties as cohesive energy and ionization potential have not converged with respect to cluster size. Larger clusters become computationally too demanding to perform calculations within a reasonable time. Cluster of more than thirteen rhodium atoms will at this moment be probably too large for chemisorption studies. Slab calculations seem to be much more promising than clusters. Convergence to bare transition metal bulk properties seems to be possible at a reasonable computational cost. The Rh-Rh distance is already predicted well at the LDA level. However, inclusion of non-local corrections is essential to obtain the cohesive energy to fair accuracy. This result encourages the use of slabs in the study of the interaction of adsorbates with surfaces, although the computational demands will grow very rapidly.

We developed two PESs for the interaction of CO with a rhodium atom, corresponding to the electronic ground state at short and large Rh-CO distances, respectively. At short distances the system is a doublet, and at large distances it is a quartet. It could be proven that atom-atom potentials were not appropriate to describe this system. The PESs could be fitted best with a spherical expansion and Morse forms for the expansion coefficients. We found somewhat larger bonding energies than most previous calculations. This may be due to the common overestimation of bonding energies in DFT, even though we have included non-local corrections. Our results agree reasonably well with previous DFT calculations on Rh-CO. The calculations on the interaction of CO with small rhodium clusters show reasonable agreement with experimental values. Comparing the same cluster calculations with predictions by the PESs, it seems that our PESs are not anisotropic enough (the site preference is not well reproduced), and give too high adsorption energies. Unfortunately, we were unable to improve the PESs with results from our small cluster calculations. The rhodium-CO bonding itself is characterized by π donation from the metal and σ donation from CO. The calculated chemisorption properties of CO on relative small model rhodium clusters can only reproduce the experimental trends. A four-metal-atom cluster defines the minimum size for a good qualitative description of the interactions involved in the CO-metal bond. However, larger clusters are necessary to reproduce experimental findings. Both our (T_d) ten and (D_{3h}) thirteen atom clusters could reproduce the experimentally observed preference for the onefold site with a reasonable adsorption energy. Carbon monoxide adsorbed stronger on the onefold site with three nearest neighbors than on the onefold site with six nearest neighbors in tetrahedral Rh_{10}.

The chemisorption and oxidation of ammonia over copper and the role of oxygen.

Our calculated adsorption energies for ammonia on copper showed a rather strong dependence on the size of the cluster. Nevertheless, there was clearly a trend towards onefold adsorption for the (100) and the (111) surface. Comparing both surfaces shows that in onefold adsorption, the steric repulsion is much less for the (100) surface while the orbital interaction is about the same. With an OPDOS analysis, we were able to show that it is the interaction of NH_3 with the copper d orbitals as well as with the copper s valence electrons that favors the onefold adsorption site, while the interaction of NH_3 with the copper p orbitals favors the higher coordination sites. It is possible to confirm our predicted onefold adsorption geometry for NH_3 on copper by determining the NH_3 σ LDOS relative to the Fermi level.

Oxygen and ammonia preadsorbed on a copper (111) surface demonstrate an attractive interaction. While this is in part due to the direct interaction between the oxygen and one of the hydrogen atoms of NH_3, a greater portion of the favorable bonding is attributed to the interaction through the copper surface. The latter agrees with the predictions from the bond order conservation postulate. For the dissociation of NH_3 over copper we analyzed three reaction paths. The dissociation without preadsorbed oxygen has the highest activation energy and is the most endothermic. The dissociation of adsorbed NH_3 in the presence of oxygen has a considerably lower reaction energy due to hydroxyl formation. Of the two dissociation pathways studied in the presence of oxygen, the first one in which NH_3 is initially adsorbed onefold is favored over the second one in which NH_3 is initially adsorbed threefold. Subsequent dissociation of NH_2 and NH in the presence of oxygen help to drive the overall oxidation process. The desorption of water from the surface and the dissociation of NH_3 are the two most thermodynamically unfavorable steps in the overall sequence of steps. Although atomic oxygen promotes N-H bond activation, the strong Cu-O interaction leads to poisoning of surface sites that inhibits the overall dissociation kinetics. Sequential hydrogen transfer to form OH is favored over the simultaneous hydrogen transfer to form water directly.

Molecular oxygen adsorbs favorably both in parallel and perpendicular orientations to the surface. The parallel mode is a precursor state for O_2 dissociation where a significant charge transfer from the surface to O_2 π^* orbital weakens the O-O bond. The perpendicular mode is the precursor state for NH_3 dissociation. Preadsorbed O_2 enhances the adsorption of NH_3 and acts to lower the barrier for N-H bond activation. The sequential hydrogen abstraction, while less exothermic than the path for the simultaneous H transfer, is kinetically favored. The sequential-H-transfer-O_2 path is the most likely of all those studied. Its activation energy is zero, i.e., a non-activated process. Recombination of N adatoms and desorption of N_2 was found to be favored over the recombinative removal of NO. However, under reaction conditions both entropy and selective collision frequency favor NO formation.

Conclusie en Samenvatting

Dit proefschrift beschrijft enkele katalytische systemen met de overgangs metalen iridium, rhodium en koper met dichtheids funktionaal berekeningen: de $X\alpha$ methode (hoofdstuk 2) of de Vosko-Wilk-Nussair exchange-correlatie potentiaal (hoofdstukken 3-10). Het gebruik van niet-lokale en (voor iridium en rhodium) relativistische correcties in de berekeningen geeft veel betere beschrijvingen in vergelijking met experimenten. De resultaten zoals beschreven in dit proefschrift laten zien dat het zeer wel mogelijk is om een geavanceerde quantum-chemische methode toe te passen op relevante katalytische problemen.

De invloed van kationen op de adsorptie van atomair waterstof en zwavel op iridium.

Waterstof geadsorbeerd op een tetrahedrisch Ir_4 cluster laat een kleine afname in de waterstof bindings sterkte zien in de aanwezigheid van een Mg^{2+} kation. De maximale afname is 25 kJ/mol voor enkelvoudig geadsorbeerd waterstof. Sterker gebonden waterstof atomen geadsorbeerd op hogere coördinatie plaatsen laten enkel kleine verschillen in bindings sterkte zien. Hieruit kunnen we concluderen dat de dissociatieve adsorptie energie van waterstof op Ir_4 niet zal veranderen. Dit voorspeld dat de gehele aktiverings energie ten opzichte van de gasfase afneemt in de aanwezigheid van een Mg^{2+} kation door de toegenomen adsorptie energie van het waterstof molekuul.

Zwavel geadsorbeerd op tetrahedrisch Ir_4 zonder een Mg^{2+} kation laat adsorptie energieën zien die in goede overeenstemming zijn met experimenteel gevonden waarden. De binding wordt voornamelijk veroorzaakt door de interactie met de p orbitalen van zwavel. Het effect van de introductie van een Mg^{2+} kation is geometrie afhankelijk. De interactie voor enkelvoudige adsorptie wordt verzwakt, dat van de tweevoudige blijft onveranderd, terwijl dat van de drievoudige wordt versterkt. Voor de enkelvoudige geometrie blijft de Ir-S bindings lengte bijna gelijk, voor de tweevoudige en drievoudige neemt het af. De invloed van een Mg^{2+} kation op CO, H_2 en H adsorptie kon worden verklaard met een eenvoudig electrostatisch model omdat het Mg^{2+} electrostatisch veld de veranderingen domineerde. Voor zwavel is de invloed van het kation identiek voor de enkelvoudige en de tweevoudige geometrie. Voor de drievoudige geometrie echter zijn chemische bindings effecten van meer belang. De sterkere binding kan worden verklaard met een geëxciteerd S atoom dat voor deze geometrie een gunstiger π interactie met Ir_4 heeft in de aanwezigheid van Mg^{2+}. Dit wijst op een toegenomen zwavel gevoeligheid van metaal deeltjes in de nabijheid van een kation.

Rhodium clusters en de interactie van koolmonoxyde met rhodium.

Wij berekenden verschillende eigenschappen voor een aanzienlijk aantal rhodium clusters. De meeste clusters bezitten magnetische momenten ongelijk nul. Deze magnetische momenten zijn waarschijnlijk het resultaat van de gereduceerde dimensie en de vergrote electronische ontaarding door de symmetrie van het cluster. Ondanks clusters van wel 43 atomen waren eigenschappen als cohesie energie en ionisatie potentiaal niet geconvergeerd naar de bulk. Berekeningen aan grotere clusters worden te groot om binnen een redelijke tijd te doen. Clusters van meer dan dertien rhodium atomen zijn op dit moment waarschijnlijk te groot voor chemisorptie studies. Slab berekeningen lijken veelbelovender dan clusters. Convergentie naar overgangs metaal bulk eigenschappen lijkt mogelijk te zijn tegen een redelijke reken inspanning. De Rh-Rh afstand wordt al goed voorspeld op LDA niveau. Het meenemen van niet-lokale correcties is echter essentieel om de cohesie energie redelijk te kunnen bepalen. Dit moedigt het gebruik van slabs in de studie van de interactie van adsorbaten met oppervlakken aan, hoewel de reken inspanning zeer snel zal toenemen.

We ontwikkelden twee PESen voor de interactie van CO met een rhodium atoom, behorende bij de elektronische grond toestand op korte en lange Rh-CO afstand. Op korte afstand is het systeem een doublet, op langere afstand een quartet. Aangetoond kon worden dat atoom-atoom potentialen niet geschikt zijn om dit systeem te beschrijven. De PESen konden het beste worden gefit d.m.v. een sferische expansie en Morse functies voor de expansie coëfficiënten. We vonden iets grotere bindings energieën dan de meeste eerdere berekeningen. Dit kan worden veroorzaakt door de gebruikelijke overschatting van bindings energieën in DFT, hoewel we niet-lokale correcties hebben meegenomen. Onze resultaten stemmen redelijk overeen met eerdere DFT berekeningen aan Rh-CO. Berekeningen aan de interactie van CO met kleine rhodium clusters geeft redelijke overeenstemming met experimentele waarden. Vergelijken we dezelfde berekeningen met voorspellingen van de PESen, dan lijkt het erop dat deze niet anisotropisch genoeg zijn (de adsorptie geometrie wordt niet goed gereproduceerd), en te hoge adsorptie energieën geven. Helaas zijn we niet in staat geweest om de PESen te verbeteren met resultaten van onze cluster berekeningen. De rhodium-CO binding wordt gekenmerkt door π donatie van het metaal en σ donatie van CO. De berekende chemisorptie eigenschappen van CO op relatief kleine rhodium clusters kan enkel de experimentele trends reproduceren. Een vier-metaal-atoom cluster definieert de minimum afmeting voor een goede kwalitatieve beschrijving van de interacties betrokken bij de CO-metaal binding. Grotere clusters zijn noodzakelijk om experimentele waarnemingen te reproduceren. Tien (T_d) en dertien (D_{3h}) atoom clusters geven de experimenteel gevonden voorkeur voor de enkelvoudige adsorptie met redelijke adsorptie energieën. CO adsorbeerd sterker op de enkelvoudige positie met drie dan met zes naaste buren in tetrahedrisch Rh_{10}.

De chemisorptie en oxydatie van ammonia over koper en de rol van zuurstof.

De berekende adsorptie energie voor ammonia op koper is sterk afhankelijk van de afmeting van het cluster. Niet te min is er duidelijk een trend naar enkelvoudige adsorptie voor het (100) en (111) oppervlak. Vergelijking van beide oppervlakken laat zien dat voor enkelvoudige adsorptie de sterische repulsie veel minder is voor het (100) oppervlak terwijl de orbital interactie ongeveer gelijk is. Met een OPDOS analyse konden we aantonen dat de interactie van NH_3 met de koper d orbitalen en s valentie elektronen de enkelvoudige adsorptie begunstigd, terwijl de interactie met de koper p orbitalen de hogere coordinatie bevoordeeld. Het is mogelijk om de voorspelde enkelvoudige adsorptie geometrie voor NH_3 op koper te bevestigen door de NH_3 σ LDOS ten opzichte van het Fermi niveau te bepalen.

Zuurstof en ammonia geadsorbeerd op koper (111) laten een gunstige interactie zien. Dit komt gedeeltelijk door de directe interactie tussen het zuurstof en één van de H atomen van NH_3. Een groter gedeelte van de binding wordt veroorzaakt door de interactie door het koper oppervlak. Dit is in overeenstemming met voorspellingen van het bond order conservatie postulaat. Voor de dissociatie van NH_3 over koper hebben we drie reactie paden geanalyseerd. De dissociatie zonder gepreadsorbeerd zuurstof had de hoogste activerings energie en is het meest endotherm. De dissociatie in de aanwezigheid van zuurstof heeft een aanzienlijk lagere reactie energie door de OH formatie. Van de twee bestudeerde dissociatie paden in de aanwezigheid van zuurstof wordt de eerste, waar NH_3 enkelvoudig is geadsorbeerd, geprefereerd over de tweede, waar NH_3 drievoudig is geadsorbeerd. Verdere dissociatie van NH_2 en NH in de aanwezigheid van zuurstof helpt het gehele oxydatie proces verlopen. Water desorptie en de dissociatie van NH_3 zijn de twee thermodynamisch meest ongunstige stappen in de gehele reeks van stappen. Hoewel atomair zuurstof de N-H binding activering begunstigd, leidt de sterke Cu-O interactie tot de vergiftiging van oppervlakte plaatsen die de gehele dissociatie kinetiek verhinderen. Opeenvolgende H overdracht om OH te vormen is gunstiger dan de gelijktijdige H overdracht om direct water te vormen.

Moleculair zuurstof adsorbeerd op Cu(111). De parallelle geometrie is een voorloper voor O_2 dissociatie waar een significante ladings overdracht van het oppervlak naar de O_2 π^* orbital de O-O binding verzwakt. De loodrechte geometrie is de voorloper van NH_3 dissociatie. Gepreadsorbeerd O_2 verhoogd de adsorptie van NH_3 en verlaagd de barrière voor N-H bindings activering. De opeenvolgende waterstof abstractie, hoewel minder exotherm dan het pad voor de gelijktijdige H overdracht, is kinetisch gunstiger. Van alle bestudeerde paden is het opeenvolgende-H-overdracht-O_2 pad de meest waarschijnlijke De activerings energie hiervan is nul, een niet-geactiveerd proces. De recombinatie van N atomen en de desorptie van N_2 was gunstiger dan de recombinatieve verwijdering van NO. Onder reactie condities begunstigen zowel entropie als selectieve botsings frequentie NO formatie.

Conclusão e Sumário

Nesta tese estudou-se pequenos sistemas catalíticos (*clusters*) envolvendo os metais de transição irídio, ródio e cobre por meio de cálculos do tipo funcional densidade (DF), usando o método Xα (capítulo 2) ou o potencial de correlação de troca Vosko-Wilk-Nusair (capítulos 3-10). A inclusão de correções não-locais e (para irídio e ródio) correções relativísticas fornece muito melhor descrição dos sistemas estudados, se comparado com o experimento. Com o trabalho desenvolvido nesta tese mostrou-se que é possível aplicar um método químico quântico avançado a vários problemas catalíticos relevantes.

A influência de cátions na adsorção de hidrogênio atômico e enxofre sobre irídio.

A força da ligação de hidrogênio adsorvido em *clusters* tetraédricos de Ir_4 sofre um pequeno decréscimo quando da presença do cátion Mg^{+2}. O máximo decréscimo observado foi de 25 kJ/mol para hidrogênio mono-coordenado à superfície. Para átomos de hidrogênio adsorvidos fortemente em mais alta coordenação, observou-se apenas uma pequena variação na força da ligação H-Ir. Como resultado, a entalpia de adsorção dissociativa de hidrogênio em partículas de Ir_4 tetraédrico não se altera. Prevê-se então que a energia de ativação total com respeito aos reagentes na fase gasosa decrescerá na presença de Mg^{+2} devido ao aumento do calor de adsorção da molécula de H_2.

As energias de adsorção do enxofre em *clusters* tetraédricos de Ir_4 na ausência de Mg^{+2} concordam bem com os resultados experimentais. A ligação se deve principalmente à interação com os orbitais p do enxofre. A geometria do sistema é dependente da introdução de Mg^{+2}. A interação para a geometria mono-coordenada decresce, bi-coordenada não se altera e tri-coordenada, aumenta. O comprimento da ligação Ir-S quase não se altera para o modo de adsorção mono-coordenado enquanto que para bi-coordenado e tri-coordenado, ela diminui. A influência da presença de Mg^{+2} na adsorção de CO, H_2 e H pode ser explicada como sendo simples interação eletrostática, uma vez que o campo eletrostático do Mg^{+2} domina as mudanças. Para enxofre a influência do cátion é similar para os modos de adsorção mono e bi-coordenado. Já para o tri-coordenado, efeitos sobre as ligações químicas são mais importantes. O aumento da força de ligação pode ser explicado usando-se um átomo de enxofre excitado, o qual para esta geometria apresenta interação π mais favorável com Ir_4 quando Mg^{+2} está presente. Isto indica um aumento na sensitividade do enxofre à partículas metálicas quando em contato com um cátion.

Sistemas de ródio e interação de monóxido de carbono com ródio.

Calculou-se diversas propriedades para diferentes *clusters* de ródio. A maioria tem momento magnético diferente de zero. Isto é, muito provavelmente, resultado da reduzida dimensão bem como aumento na degenerescência eletrônica devido à simetria do *cluster*. Apesar de ter-se usado *clusters* de até 43 átomos, propriedades tais como energia de coesão e potencial de ionização não são convergentes com relação ao tamanho do *cluster*. Grandes *clusters* exigem considerável esforço computacional dificultando a realização dos cálculos em tempo razoável. *Clusters* com mais de 13 átomos são, no momento, provavelmente muito grandes para o estudo de adsorção química. Cálculo de sistemas periódicos bidimensionais (*slabs*) parece mais promissor do que simples *clusters*. A convergência de propriedades *bulk* de metais de transição parece ser possível em um custo computacional razoável. A distância da ligação Rh-Rh pode ser predita relativamente bem usando-se correções do tipo local. Em cálculos de energia de coesão, no entanto, é indispensável o uso de correções do tipo não-local. Tais resultados encorajam o uso de *slabs* no estudo da interação de adsorbatos em superfícies, muito embora a demanda computacional cresça muito rapidamente.

Desenvolveu-se duas diferentes superfícies de energia potencial (PES) para a interação de CO com um átomo de ródio, relativas ao estado eletrônico fundamental, para pequenas e grandes distâncias Rh-CO. A pequenas distâncias o sistema é um dublete enquanto que a grandes distâncias, um quarteto. É possível provar que o potencial átomo-átomo não é apropriado para descrever tal sistema. O ajuste da PES é mais adequado usando-se as formas de potencial de expansão esférica e Morse. Encontrou-se mais alta energia de ligação se comparado com a maioria dos resultados anteriores. Isto pode ser devido à comum superestimativa de energias de ligação em DFT, apesar da inclusão de correções do tipo não-local. Os resultados estão em razoável acordo com cálculo DFT anterior para Rh-CO bem como com o experimento. Comparando cálculos para *clusters* com predições de PES's, parece que estas últimas não são suficientemente anisotrópicas (o modo de adsorção preferido não é bem reproduzido) e apresentam energias de adsorção muito altas. Não foi possível melhorar as PES's apenas com resultados obtidos nos cálculos com pequenos *clusters*. A ligação Rh-CO é caracterizada por doação π do metal e doação σ do CO. As propriedades de quimissorção de CO em pequenos *clusters* de ródio podem reproduzir apenas tendências obtidas experimentalmente. *Clusters* com no mínimo quatro átomos são necessários para boa descrição qualitativa das interações envolvidas na ligação CO-metal. *Clusters* maiores são necessários para reproduzir resultados experimentais. Ambos os *clusters*, com dez (T_d) e treze (D_{3h}) átomos reproduzem a preferência para mono-coordenação observada experimentalmente com razoável energia de adsorção. CO adsorve mais fortemente mono-coordenado com três vizinhos mais próximos do que com seis, R_{10} tetraédrico.

Quimissorção e oxidação de amônia sobre cobre e influência da presença de oxigênio.

A energia de adsorção calculada para a amônia em *clusters* de cobre é fortemente dependente do tamanho do *cluster*. Existe clara tendência para a adsorção mono-coordenada para as superfícies (100) e (111). Comparando ambas as superfícies percebe-se que na adsorção mono-coordenada a repulsão estérica é muito menor para a superfície (100) enquanto a interação orbital é quase a mesma. Por meio de análise OPDOS, pode-se mostrar que a interação de NH$_3$ com os orbitais d bem como elétrons de valência s do cobre favorece o modo de adsorção mono-coordenado, enquanto que a interação com orbitais p favore modos de adsorção de mais alta coordenação. É possível confirmar a geometria de adsorção mono-coordenada para NH$_3$ sobre cobre determinando o NH$_3$ σ LDOS relativo ao nível de Fermi.

Oxigênio e amônia pré-adsorvidos em superfície de Cu (111) mostram interação atrativa. Isso é, em parte, devido à interação direta entre oxigênio e um dos átomos de hidrogênio da amônia. Grande parte da ligação favorável é, entretanto, atribuída à interação com a superfície de Cu. Isto concorda com as predições do postulado da conservação da ordem de ligação. Para a dissociação de NH$_3$ sobre Cu, três diferentes mecanismos de reação foram analisados. Dissociação na ausência de O pré-adsorvido tem a mais alta energia de ativação e é a mais endotérmica. Dissociação em presença de O tem energia de reação consideravelmente mais baixa devido à formação de hidroxila. Dos dois diferentes caminhos de reação estudados em presença de O, o primeiro no qual a adsorção de NH$_3$ é inicialmente mono-coordenada é favorecido sobre o segundo, no qual ela é inicialmente tri-coordenada. Subsequente dissociação de NH$_2$ e NH na presença de O ajuda no processo oxidativo como um todo. Dessorção de água de superfície e dissociação de NH$_3$ são as duas etapas termodinamicamente mais desfavoráveis da reação. Apesar de oxigênio atômico promover a ativação da ligação N-H, a forte interação Cu-O promove o envenenamento dos sítios que inibem a cinética total de dissociação. Transferência sequencial de hidrogênios para formar hidroxilas é favorecido sobre transferência simultânea para formar água diretamente.

O$_2$ adsorve favoravelmente em ambas as orientações, paralela e perpendicular à superfície. O modo paralelo é precursor para dissociação de O$_2$ com razoável transferência de carga da superfície para os orbitais π* do O$_2$, enfraquecendo a ligação O-O. A adsorção perpendicular é precursora da dissociação de NH$_3$. O$_2$ pré-adsorvido facilita a adsorção de NH$_3$ e atua baixando a energia de ativação da ligação N-H. Abstração de H sequencial, apesar de menos exotérmica do que a tranferência simultânea, tem uma cinética favorável. Dentre os estudados, o caminho de reação mais provável parece ser a transferência sequencial de H para O$_2$. Sua energia de ativação é zero. Recombinação de átomos de N adsorvidos na superfície e dessorção de N$_2$ é favorável sobre remoção recombinativa de NO. Nas condições de reação ambos, entropia e frequência de colisão seletiva favorecem à formação de NO.

Dankwoord

Tot slot van dit proefschrift wil ik graag allen bedanken die van cruciaal belang zijn geweest bij de totstandkoming van dit proefschrift. Voor de deskundige hulp bij o.a. het gebruik van ADF en/of ADF-BAND ben ik prof. Baerends, Eric Kirchner, Bert te Velde, Pieter Vernooijs, Gijsbert Wiesenekker en Egbert van Wezenbeek veel dank verschuldigd. Zonder jullie programma's zou dit proefschrift nooit geschreven hebben kunnen worden. Mijn copromotor Tonek Jansen voor de dagelijkse begeleiding. Dat het misschien niet allemaal precies geworden is wat we hoopten heeft zeker niet aan jou gelegen. Phil Davies, who started the density functional calculations on the chemisorption of ammonia on copper. De afstudeerders Ton van Daelen en Gerard van de Kerkhof. Met name Gerard heeft tijdens zijn afstuderen een ongelovelijke hoeveelheid berekeningen voor mij gedaan, en me daarnaast ook nog eens geholpen bij het visualiseren van de vele resultaten. Matthew Neurock, who worked together with me on the copper project, and completed it almost on his own. Your work not only improved the quantity but certainly also the quality of the copper project. I really enjoyed the time we worked together. De vele (ex-)leden van de vakgroep TAK wil ik graag bedanken voor de goede sfeer binnen de vakgroep. In het bijzonder geldt dit voor alle (ex-)leden van de theorie groep. Tenslotte dank ik mijn ouders en Solange voor hun steun, en voor het feit dat ze altijd klaar stonden om mij door deze promotie heen te helpen.

Stellingen

behorende bij het proefschrift

Quantum Chemical Studies in Catalysis

W. Biemolt

1 Het gebruik van "metallische atomen" levert, gezien de veel te hoge adsorptie energie, geen betrouwbaar(der) theoretisch model voor de bestudering van chemisorptie.

X. Xu, N. Wang en Q. Zhang, Surf. Sci. 274 (1992) 378.

2 Hoewel de conclusie van Jentys en Catlow juist is dat "edge sharing" tetraedra niet in Ti-zeolieten zullen voorkomen, kan dat niet worden gebaseerd op hun quantumchemische berekeningen waarin een onwaarschijnlijke Si-O afstand van 1.987 Å wordt gevonden.

A. Jentys en C.R.A. Catlow, Catal. Lett. 22 (1993) 251.

3 De dichtheids functionaal theorie, een grondtoestands theorie, is zeer wel toepasbaar voor toestanden anders dan de grondtoestand.

Dit proefschrift

4 Het is verwonderlijk dat Bates et al., in overeenstemming met eerdere berekeningen van Sauer et. al., concluderen dat de overdracht van een zuur proton naar methanol gunstig is terwijl ze vinden dat de formatie van een methoxonium ion op een zure zeoliet ongunstig is.

S. Bates en J. Dwyer, J. Molec. Struc. (Theochem) 306 (1994) 57.

J. Sauer, C. Kölmel, F. Haase en R. Ahlrichs: Proceedings from the 7th international zeolite conference, Montreal 1992, R. von Ballmoos, J.B. Higgins and M.M.J. Treacy (eds.) (Butterworths, London, 1993) p. 679.

F. Haase en J. Sauer, J. Phys. Chem. 98 (1994) 3083.

5 Het gebruik van als maar grotere clusters als model voor oppervlakken, in de hoop dat deze clusters naar de bulk eigenschappen van het oppervlak convergeren, is zinloos omdat de meeste grote clusters überhaupt niet convergeren.

6 De kristallografische voorkeurspositie van titanium in zeolieten kan niet quantumchemisch onderzocht worden met behulp van pentamerische modelstructuren waarvan alle T-O-T en O-T-O hoeken vast worden gehouden.

R. Millini, G. Perego en K. Seiti : *Zeolites and related microporous materials: state of the art 1994*, J. Weitkamp, H.G. Karge, H. Pfeifer, en W. Hölderich (eds.) Studies in Surf. Sci. and Catal. 84 (Elsevier, Amsterdam, 1994) p. 2123.

7 Een te lange promotie moet niet alleen financiële consequenties hebben voor een OiO maar ook voor de instelling waar het promotie onderzoek werd uitgevoerd.

8 De schatting dat 99% van de Nederlandse bevolking kan lezen en schrijven lijkt, gezien het aantal mensen dat niet in staat is om een tekst als "verboden te roken" te begrijpen, aan de ruime kant.

http://www.ic.gov/94fact/171.html.

9 Dichtheids functionaal methoden waren al van belang ver voordat GAUSSIAN92 een dichtheids functionaal module had.

J. Simons, J. Phys. Chem. 95 (1991) 1017.
B.G. Johnson, P.M.W. Gill en J. A. Pople, J. Chem. Phys. 97 (1992) 7846.
B.G. Johnson, P.M.W. Gill en J. A. Pople, J. Chem. Phys. 98 (1993) 5612.

10 Bestudering van reakties tussen ammonia en zuurstof met semi-empirische MNDO berekeningen geeft enkel kwalitatieve resultaten, zeker als het oppervlak waarop deze reakties plaats vinden niet in de berekeningen mee neemt.

E. Broclawik en J. Haber, J. Molec. Catal., 82 (1993) 353.

11 De conclusie dat zwavel desorptie van nikkel sterk endotherm is omdat zwavel adsorptie op nikkel sterk exotherm is mag gedurfd worden genoemd.

M. Neurock en R.A. van Santen, J. Am. Chem. Soc. 116 (1994) 4427.